AB INITIO DEFECT ENGINEERING AND GREEN SYNTHESIS OF Ca-Mg CODOPED TITANIA AND ZIRCONIA FOR PHOTOCATALYTIC APPLICATIONS

JANE KATHURE MBAE

A Thesis Submitted to the Graduate School in Partial Fulfilment of the Requirements for the Award of the Degree of Doctor of Philosophy in Physics of Chuka University

CHUKA UNIVERSITY

OCTOBER, 2025

DECLARATION AND RECOMMENDATION

Declaration

This thesis is my own original work and has not been presented for an award of a degree or a diploma in any other University or institution.

Signature..... Date..14/10/25.....
Mbae Jane Kathure
SD19/58026/22

Recommendation

The thesis has been examined, passed and submitted with our approval as the University supervisors.

Signature..... Date..14/10/2025.....
Dr. Zipporah Muthui, PhD,
Chuka University

Signature..... Date..14/10/25.....
Prof. Eric Njagi, PhD,
Chuka University

COPYRIGHT

DEDICATION

This work is dedicated to the Almighty God for the divine help to successfully carry out this research work.

ACKNOWLEDGEMENT

First I thank Almighty God for grace, strength and wisdom to successfully carry out this research. All honour and glory belongs wholly to Him.

A successful research like this is not possible without help of many others. I acknowledge the enormous input of my supervisors; Dr. Zipporah Muthui and Prof. Eric Njagi of Chuka University for their supervisory work, expertise, exceptional advice and availability. They have challenged my thinking, supported my wild ideas and said no when I was going in the wrong direction. I appreciate the effort they made to read and make corrections on the proposal of this project and the thesis of this research.

I would like to express my heartfelt gratitude to Prof. Ochieng Ombaka, Chairman of the Department of Physical Sciences, for his unwavering support and leadership throughout the course of my research. His guidance, encouragement, and dedication to academic excellence have greatly contributed to the successful completion of this thesis. I am really appreciative for the opportunities and resources provided under his leadership, which have played a vital role in shaping my academic journey.

My sincere appreciation to the laboratory technologists; Eric and Juliet of the Chemistry laboratory, and Mutunga of the Physics laboratory, for their invaluable technical support and assistance throughout my research. I greatly appreciate their attention and willingness to assist at all stages of the experimental process.

I am indebted to my dad, David, and mum, Charity, for my earlier upbringing and education, as well as the support of my older sister Betty, who has been a special pillar in this scholastic journey.

Special thanks to my husband Josphat, who has greatly supported and encouraged me to move on even in the most tough situations. Last but not least, I appreciate my daughters Princess and Joyness for being so patient and kind during this research work.

May the Almighty God abundantly bless all who supported me in the course of this research work.

ABSTRACT

The growing demand for long-term solutions to environmental pollution and energy concerns has sparked interest in photocatalysts that work efficiently in visible light. In particular, TiO_2 and ZrO_2 photocatalysts have shown great potential in photocatalytic degradation and disinfection applications. However, traditional TiO_2 and ZrO_2 photocatalysts feature metastable phases that are better photocatalysts, large bandgaps, low solar energy utilization, and rapid charge carrier recombination, limiting their usefulness. This study addresses these limitations by investigating Ca-Mg codoping as a defect engineering strategy for improving the photocatalytic performance of TiO_2 and ZrO_2. The primary objectives were to determine the phase stability of Ca-Mg codoped TiO_2 and ZrO_2 polymorphs using Density Functional Theory (DFT), to evaluate the effects of oxygen vacancies on their electronic structures, to establish optimal dopant concentrations for visible light activation, to green synthesize and characterize the predicted visible-active materials, to assess photocatalytic activity via Rhodamine B degradation under visible light and to evaluate antibacterial performance against *E. coli* and *S. aureus*. In this study, a combined ab initio and experimental approach was undertaken. Density Functional Theory (DFT) method was used to simulate the codoped polymorphs at different doping levels. Optimal codoped systems found suitable for visible light photocatalysis were green synthesized and characterized using XRD, ICP-MS and UV-VIS spectroscopy. The photocatalytic properties of the synthesized materials were evaluated by degradation of Rhodamine B (RhB) under visible light and the disinfection capability was tested against *Escherichia coli* and *Staphylococcus aureus* bacteria strains. The results yielded reasonable agreement between experimental and theoretical results, as well as a better understanding of the system. DFT results showed that Ca-Mg codoping stabilizes the anatase phase in TiO_2 by increasing the c/a ratio and induces tetragonalization in monoclinic ZrO_2 through lattice distortions and oxygen vacancy formation. Defective oxygen vacancy Localized mid-gap states were discovered in Ca-Mg codoped TiO_2 and ZrO_2 systems. These states served as trapping sites for the photogenerated charge carriers and significantly decreased the energy band, improving visible light absorption. Experimentally, the green synthesized codoped materials revealed smaller crystallite sizes (5.567 nm for TiO_2 and 8.647 nm for ZrO_2) and narrower bandgaps (1.92 eV and 2.4 eV, for TiO_2 and ZrO_2 respectively). Codoped TiO_2 degraded 99.3% of Rhodamine B in 120 minutes and completely inactivated *S. aureus* under visible light in 60 minutes. RhB degradation % for 5 cycles of codoped TiO_2 and ZrO_2 nanoparticles have remarkable stability and reusability, which is the key reason for their widespread use in photocatalytic degradation of dyes. Based on these findings, Ca-Mg codoping is recommended as an economical, non-toxic and effective strategy for tuning the structural and electronic properties of TiO_2 and ZrO_2 to enhance visible-light photocatalysis. Future work should focus on advancing the green synthesis technique and testing against a larger spectrum of contaminants and microbial strains to further establish its environmental application.

TABLE OF CONTENTS

LIST OF TABLES

LIST OF FIGURES

SYMBOLS AND ABBREVIATIONS

BFGS	Broyden–Fletcher–Goldfarb–Shanno
c-ZrO_2	Cubic ZrO_2
CDE	Conduction Band Edge
DFT	Density Functional Theory
DOS	Density of States
eV	Electron Volts
GA	Gradient Approximation
GGA	Generalised Gradient Approximation
ICP-MS	Inductively Coupled Plasma-Mass Spectrometry
K-S	Kohn Sham
LDA	Local Density Approximation
NCs	Nanocomposites
MP	Monkhorst Pack
m-ZrO_2	Monoclinic ZrO_2
NPs	Nanoparticles
PBE	Perdew Burke Ernzerhof
PDOS	Projected Density of States
QE	Quantum ESPRESSO
RhB	Rhodamine Blue
ROS	Reactive Oxygen Species
TDOS	Total Density of States
t-ZrO_2	Tetragonal ZrO
USPPs	Ultrasoft pseudopotentials
UV	Ultra Violet
UV-Vis	Ultraviolet-Visible
VBE	Valence Band Edge
VBM	Valence Band Maximum
VBs	Valence Bands
VESTA	Visualization for Electronic Structure Analysis
XRD	X-ray Diffraction

CHAPTER ONE
INTRODUCTION

1.1 Background Information

Nanoscale materials such as metal oxide nanoparticles (NPs) have attracted considerable attention in the recent years. One of their significant applications is in photocatalytic degradation and disinfection (Ayanwale & Reyes, 2019). Nanoparticle-based photocatalysts are promising, owing to their superb degrading and disinfection capabilities, environment friendliness, non-toxicity and biocompatibility (Mukherjee *et al*., 2020).

Transition metal oxides TiO_2 and ZrO_2 have demonstrated strong disinfection and degradation properties against a wide variety of pathogens and organic pollutants respectively (Chelliah *et al.,* 2023 ; Yasin *et al*., 2018), and hence are widely utilized in sewage treatment, food packaging, antimicrobial coatings, self-cleaning, and germ killing in operating rooms and other areas (Verma *et al*., 2022 ; Sagadevan *et al*., 2022). They are being targeted to be used in the degradation of major industrial pollutants such as methyl violet, methyl red, methylene blue (MB), Congo red, and Rhodamine Blue (RhB), which are widely used as key components in colour-related industries, such as paint, textile, leather, and printing, through photocatalytic methods. In addition, their use in the disinfection of pathogenic microbes, such as *E. coli* and *S. aureus*, which cause various health issues such as cholera, typhoid, inflammatory bowel disease, severe acute respiratory syndrome, among others continues to be explored (Balali *et al*., 2020). These diseases continue to be a leading cause of death to millions of people globally (Tropea, 2022).

Despite their novel properties and wide range of applications, the large band gaps of TiO_2 (3.2 eV) and ZrO_2 (5.2 eV) and the quick recombination of photogenerated charge carriers limit their photocatalytic applications (Jassal *et al*., 2022 ; Tijani *et al*., 2022).To reduce the band gaps and the quick charge recombination, techniques such as metal doping, non-metal doping and coupling with metal oxides have been employed with increasing success (Yadav *et al*., 2020).

In spite of the enormous success realized in the visible region response of photocatalysis by single dopants, there are a number of drawbacks that accompany single doping (Li *et al*., 2020 ; Sun *et al*., 2020).The first is the incomparable ionic radius and/or charge between the host ions and the dopant ions, hence dopant incorporation into TiO_2 usually results in a large increase in the system's energy (Chen *et al*., 2010). The high energy and existence of defects results in thermal and photochemical instability of monodoped TiO_2 (Ken *et al.*, 2007). It is also difficult to obtain the photocatalysts with high doping level through monodoping (Cao, 2016). Impurity bands formed above valence band in the single doped TiO_2 with anion dopant can lower the oxidation ability of the photogenerated hole, compared to that of the pure TiO_2, as a result, many organic pollutants and pathogens are not oxidized under visible light irradiation (Ken *et al*., 2007).

The quest for novel materials with increased photocatalytic activity, disinfection and degradation performance in the visible region is an important and ongoing research issue. The codoping of transition metal oxides provides a promising approach to extend the photo-response of the oxides to the more abundant visible region (Kumar *et al*., 2020). Codoping usually, increases the doping concentration of the photoactive dopants, passivates the impurity bands, enhances charge compensation between the dopants, depresses the bulk defects, enhances the reduction and oxidation power and mobility of the photogenerated carriers (Sun *et al*., 2020). For instance, in codoped TiO_2 the synergistic effect of two dopants has been demonstrated to form a photocatalyst with higher visible light absorption compared to monodoped TiO_2 (Mergenbayeva *et al*., 2022).

Some of the consequences of codoping are the engineering of the polymorphic phases and oxygen vacancies in the nanoparticle transition metal photocatalysts. The formation of oxygen vacancies within the crystal structure of materials, results in interesting changes in the electronic and optical properties of the doped system. An optimal concentration of oxygen vacancies can optimize the charge separation of photogenerated charge carriers, resulting in maximal photocatalytic performance enhancement (Wang *et al*., 2023). For instance, it has been repeatedly reported that oxygen vacancies can extend the TiO_2 absorption band to the visible light region

increase the carrier concentration and promote the transfer of photo induced charge (Liu *et al*., 2022).

Purposeful introduction of oxygen vacancies by doping metal oxides with lower valence cations than parent cations, improves the photocatalytic efficacy of the oxides (Takata & Domen, 2009). The incorporation of Ca^{2+} ions in the TiO_2 lattice structure by Bian *et al*., (2023) resulted in the loss of oxygen and creation of oxygen vacancies, boosting the photocatalytic hydrogen evolution. Fe doping significantly increased the photocatalytic capabilities of anatase TiO_2 due to formation of oxygen vacancies (Gharagozlou & Bayati, 2014). Sn doped ZrO_2-based catalysts rich in oxygen vacancies directly catalysed the synthesis of dimethyl carbonate from methanol and CO_2 (Song *et al*., 2021). An ab-initio study by De Souza & Appel, (2021) revealed that oxygen vacancies on Ca doped ZrO_2 surface greatly enhanced the CO_2 activation on the zirconia surface.

Phase transitions have also been induced through doping, with the desirable consequence of stabilizing higher temperature phases that possess superior photocatalytic properties due to factors such as a smaller particle size (Tijani *et al*., (2022). This has implications from an application point of view such as reduction of fracture that arises from applications that involve thermal cycling. Also, the impurity defects in the lattice lead to reduction of agglomeration resulting in nanoparticles of a smaller size (Rajesh *et al*., 2020; Fedorov & Yarotskaya, 2021).

Doping studies have generally been undertaken from both first principle and experimental studies. Experimentally, various chemical and physical approaches have been used successfully to produce nanoparticles, but they are often expensive and may involve the use of hazardous chemicals (Sagadevan *et al*., 2022). On the other hand, the biological approach is promising to be environmentally safe, cost-effective, dependable, convenient, and easy way to synthesize nanoparticles (Al-Zaqri *et al*., 2021).

Biologically produced nanoparticles have numerous uses in pollutant clean up, as well as antifungal, antibacterial, catalytic, and photochemical activities (Verma *et al*., 2022),

with green synthesized nanoparticles being reported to show improved photocatalytic performance (Ansari *et al*., 2022) and to produce good results as antimicrobial humidity sensors compared to those synthesised using physical or chemical methods (Jassal *et al*., 2022). For instance, TiO_2 nanoparticles successfully fabricated employing the chemical as well as the green synthesis method reported more excellent photocatalytic efficiency for biosynthesized TiO_2 nanoparticles compared to chemically fabricated TiO_2 nanoparticles (Aravind *et al*., 2021).

First principle techniques are increasingly being coupled with experimental work to leverage on their prediction power, to guide experimental work, leading to atomic scale understanding of system properties and advantages such as doping level determination. Density Functional Theory (DFT) method is a first principles technique that has an overwhelming advantage stemming from its numerical scaling properties. (Bartkowiak *et al.,* 2021; Alotaibi *et al*., 2020). For instance, a study on Au-doped TiO_2 have yielded reasonable agreement between experimental and theoretical results, as well as a better understanding of the system (Kanoun *et al*., 2024).

In this study, a combined first principles and experimental approach was undertaken. Ca and Mg dopants were used in both titania and zirconia. They are isoelectronic, being members of the same group in the periodic table. The combined action of charge transfer occasioned by the divalent cations substituting Ti^{4+} and Zr^{4+} and the different ionic radii contributed to phase stabilization and oxygen vacancy occurrence, resulting in more efficient photocatalysts that are also non-toxic. The suitable doping levels for the Ca-Mg codoped TiO_2 and ZrO_2 systems with suitable electronic structures for visible light applications were determined using the Density Functional Theory (DFT) method (Hussain *et al*., 2019). These were then green synthesized and characterized, with a specific focus on visible light photocatalysis via Ca-Mg codoping of TiO_2 and ZrO_2 oxides. Non-toxic, cost-effective, and efficient materials with potential to make good use of the sun's plentiful energy came to light.

1.2 Statement of the Problem

The use of NPs such as TiO_2 and ZrO_2 to provide environmentally friendly solutions in the energy and environmental conservation sectors continues to be explored due to their

potential to utilise renewable energy sources such as sunlight and to be synthesized using green synthesis methods. In particular, they have potential to be utilised in photocatalytic degradation and disinfection applications such as dye pigments removal and killing of bacterial strains such as, S. *aureus* and E. *coli* respectively, the latter being extremely dangerous pathogens that cause a variety of illnesses. They are however associated with drawbacks such as a wide energy band gap, charge recombination and metastable phases being better photocatalysts. There is therefore continued research efforts directed towards overcoming these drawbacks and searching for more efficient, environment friendly and cost effective photocatalysts using techniques such as doping, with codoping offering more promising results in photocatalytic applications. In this study, a combined first principles and experimental approach was undertaken. The suitable doping levels of the Ca-Mg codoped TiO_2 and ZrO_2 systems with suitable electronic structures for visible light photocatalytic activity were determined using the Density Functional Theory (DFT) method. These were then green synthesized and characterized. Non-toxic, cost-effective, and solar energy efficient materials came to light. Considering the harmful effects of dyes and pathogenic microbes, the photocatalytic degradation and disinfection activities of the DFT predicted and green synthesized Ca-Mg codoped TiO_2 and ZrO_2 NPs were studied. This contributed to revealing new visible light active materials that are suitable in addressing major issues confronting our society today of energy, detrimental health, economic, and environmental effects of pathogenic microbes and organic pollutants.

1.3 Objectives of the Study

1.3.1 General Objective

To simulate and green synthesize Ca-Mg codoped TiO_2 and ZrO_2 polymorphs for photocatalytic degradation and disinfection applications.

1.3.2 Specific Objectives

The specific objectives that directed the study include: -

i. To determine the phase stability of Ca-Mg codoped TiO_2 and ZrO_2 polymorphs using DFT.
ii. To determine the effect of oxygen vacancies on the electronic structure of Ca-Mg codoped TiO_2 and ZrO_2 polymorphs using DFT.

iii. To determine the optimal dopant concentration for experimental synthesis of visible light active Ca-Mg doped TiO_2 and ZrO_2 photocatalysts.

iv. To green synthesize and characterize the Ca-Mg codoped TiO_2 and ZrO_2 polymorphs predicted to have a visible region active band gap.

v. To determine the photocatalytic activity of the synthesized materials by degradation of Rhodamine B using visible light.

vi. To determine the disinfection activity of the synthesized materials by deactivation of *E. coli* and *S. aureus.*

1.4 Research Questions

The following research questions guided this study;

i. How does Ca-Mg codoping in titanium oxide and zirconium oxide affect the phase stability of the polymorphs?

ii. What is the effect of generation of oxygen vacancies on the electronic structure of Ca-Mg codoped titanium oxide and zirconium oxide?

iii. What is the optimal dopant concentration for experimental synthesis of visible light active Ca-Mg doped TiO_2 and ZrO_2 photocatalysts?

iv. What is the composition, structural, and electronic properties of the green synthesized Ca-Mg codoped titanium and zirconium oxides?

v. What is the optimum photocatalytic activity of the synthesized materials in degrading Rhodamine B using visible light?

vi. What is the optimum disinfection activity of the synthesized materials in deactivation of *E. coli* and *S. aureus?*

1.5 Significance of the Study

The study contributed knowledge of optimal structures, band gaps, Total Density of States (TDOS) and Projected Density of States (PDOS) of Ca-Mg codoped TiO_2 and ZrO_2. The knowledge of Ca-Mg codoped TiO_2 and ZrO_2 was beneficial to industries that endeavour to synthesize efficient photocatalysts and disinfectants that can be easily used by the community, industries, and hospitals for the degradation of organic pollutants and disinfection of surfaces and other microbe-prone areas. In addition, the prediction and synthesis of novel and more efficient photocatalysts immensely contributed to improvement of human health globally by contributing to the eradication

of the harmful effects caused by organic pollutants and pathogenic microbes, using renewable solar energy. Moreover, since the photocatalysts were green synthesized it additionally helped in environmental conservation. The study therefore contributed towards advancement in research as outlined in the economic and social pillars of Kenya vision 2030 and directly supports environmental conservation and Sustainable Development Goals (SDGs) 3 and 7 on good health & wellbeing, and affordable & clean energy respectively.

CHAPTER TWO
LITERATURE REVIEW

2.1 Overview

Over the years, extensive research on the electronic and structural properties of NPs has been conducted, both from first principles and by experimentation. An extensive variety of these will be outlined in this chapter under specific sections. For example, DFT calculations were done to theoretically interpret the experimental structures produced as well as to model the Cu doped TiO_2 structures found in the experiments (Navas *et al*., 2014). Zr^{4+} Doped TiO_2 nanoparticles were fabricated and used in solar cells that are sensitive to dyes (DSSCs) photoanodes. Density functional theory (DFT) with Hubbard correction was used to conduct extensive theoretical calculations in order to investigate the role of the Zr^{4+} ions in TiO_2 structures and to explain their effect on the electronic characteristics of anodes (Bartkowiak *et al.*, 2021).

2.2 Phase Stability and Structural Properties

Earlier research reports show that adding dopant ions to TiO_2 and ZrO_2 photocatalysts resulted into phase stabilization and improvement of photocatalytic performance. The anatase to rutile phase transition in pure titanium dioxide typically takes place between 600°C and 700°C. This temperature can be changed using a number of techniques, such as changing the precursor or doping the TiO_2 sample with a dopant or modifier (Hanaor & Sorrell, 2011). The anatase phase can be considerably stabilized by certain dopants. The anatase-to-rutile transition is delayed by Nb□O□-doping; for TiO_2 (Tobaldi *et al*., 2016). Since anatase typically has higher photocatalytic activity than rutile, this stabilization of the anatase phase is frequently preferred. Changes in surface energy, nucleation barriers, and activation energies for phase transformation are some of the intricate mechanisms behind these phase stability shifts. Compared to rutile, which has a band gap of around 3.0 eV, anatase has a bigger band gap of about 3.2 eV and a greater surface energy, making it widely acknowledged as the most photocatalytically active phase (Hanaor & Sorrell, 2011; Rajaraman *et al*., 2023). On the other hand, anatase is thermodynamically metastable and easily changes into the thermodynamically stable rutile phase when heated, usually between 450 and 850°C, depending on the purity, particle size, and synthesis circumstances. Since the conversion to rutile frequently results in decreased photocatalytic activity and other functional characteristics, this

phase transfer poses a serious problem for applications that need high-temperature processing or operation. As a result, methods for controlled doping to stabilize certain TiO_2 phases, especially anatase, at high temperatures have emerged as a key area of study.

Anatase is metastable but can be kinetically stabilized at lower temperatures, whereas rutile is the thermodynamically stable phase of TiO_2 at all temperatures and pressures under ambient circumstances (Hanaor & Sorrell, 2011). Because of kinetic considerations, reduced surface energy at tiny particle sizes, and the impact of synthesis circumstances, anatase often appears as the initial product phase during synthesis, even though rutile has better thermodynamic stability. Under typical circumstances, the phase transition from anatase to rutile is irreversible and occurs by a nucleation and growth mechanism that entails a substantial atomic rearrangement and a volume loss of around 8–10%. Numerous parameters, such as particle size, morphology, crystallite size distribution, impurity presence, surface area, and the synthesis process used, have a significant impact on the transformation temperature and kinetics. Due to variations in surface energy between the two phases, theoretical and experimental research has demonstrated that anatase becomes energetically more stable than rutile when particle sizes drop below a critical threshold, usually reported in the range of 6.9-22.7 nm (Rajaraman *et al*., 2023). In order to preserve the anatase structure in nanocrystalline materials, this size-dependent phase stability has been widely used. Additionally, research has shown that certain crystallographic interfaces specifically, the {112} twin boundaries in anatase are primarily where rutile nucleation takes place. These interfaces are advantageous nucleation sites for the phase transition (Rajaraman *et al*., 2023).

Cu doped TiO_2 systems investigated by Colón *et al*., (2006) revealed the stability of anatase TiO_2 phase and improvement of its photocatalytic performance. DFT calculations using all-electron atomic orbitals on the rutile and anatase's relative stability polymorphs of TiO_2 revealed that cationic dopants are most stable in Ti substitutional lattice positions (Hanaor *et al*., 2012). It seems that the anatase to rutile phase transition is hindered in these systems because all dopants were shown to significantly stabilise anatase relative to the rutile phase, with the studied dopants being ranked F > Si > Fe > Al in terms of anatase stabilisation strength. Setiawati & Kawano,

(2008) investigated stabilization of anatase TiO_2 nanoparticles using rare earth (RE) metal dopants Eu and Sm. With increasing doping concentrations, the transition to the rutile phase was suppressed and the anatase phase was stable, according to the powder XRD spectra. The structural studies indicate that the stability of the anatase phase has been significantly impacted by the RE ions. Shukla & Angappane, (2022) revealed that slanted TiO_2 nanorods produced on Si substrates via glancing angle deposition and electron beam evaporation exhibited stability of the TiO_2 anatase until 800 °C. The phase information obtained through Raman spectroscopy and XRD pattern revealed that the TiO_2 anatase is stable even at 800 °C.

Dominguez *et al*., 2016 showed that doping TiO_2 with Sm^{3+} was discovered to be effective even at temperatures as high as 1000 °C to stabilize the anatase phase. TiO_2:Sm^{3+} powder grew crystallinity relatively slowly, measuring 5 nm at 200 °C and 29 nm at 800 °C. Under all operating circumstances, it was found that the particles are composed of nano-sized crystals. Patra *et al*., (2015) discovered that anatase TiO_2 was stable even when the crystalline size was decreased to 4 nm. At this size, the surface contributes significantly to the volume, making the material resistant to temperature-induced particle coarsening. This causes a significant delay in the crystalline phase change from anatase TiO_2 to rutile TiO_2, up to 1000 °C in air. Ionic size differences play an important role in the degree of lattice distortion. The interplanar distance decreased when Se was substituted for Ti and N for O in the TiO_2 crystal lattice because the ionic radius of Se was smaller (64.0 pm) than that of the Ti^{4+} ion (74.5 pm) and the ionic radius of the N^{3-} ion was higher (14.6 pm) than that of the O^{2-} ion (14.0 pm) (Gurkan *et al*., 2017). According to structural analysis, variations in atomic radii caused the lattice constants of doped TiO_2 to increase, as computational studies have confirmed (Adawiya *et al*., 2025). Anisotropic lattice changes, in which the a and c parameters of the anatase or rutile structure change by varying amounts, are frequently the consequence of these competing effects from various dopants.

Compared to single-doping situations, the structural effects of concurrently introducing two dopants into the TiO_2 lattice are more complicated. Due to electronegativities, ionic radius differences, and the introduction of impurity states, the addition of foreign elements causes lattice distortions and band gap changes (Gupta *et al*., 2020).

According to Gurkan *et al*., (2017), the addition of dopants distorts the crystal structure when there is a slight shift in the peak position that corresponds to the (101) plane of anatase to a higher angle. The host and dopant atoms different ionic sizes are essentially responsible for this structural distortion. According to recent research, the rutile phase content rises in doped samples, reaching 20 ± 2.1% for Al and S codoped samples, while the anatase phase predominates in pure TiO_2 (100%) nanoparticles (Abd-Elnaiem *et al*., 2025). Grain morphology and crystallite size are significantly impacted by codoping. Since doping can result in the formation of new defects and disorder in the particles, peak broadening with increasing dopant content indicates a reduction in crystallite size and higher disorder or defectiveness of the crystallites (Gurkan *et al*., 2017). Several codoping systems have consistently shown this phenomenon. For example, Mo–N codoped TiO_2 showed a crystallite size of 18.14 nm (Sonkusare *et al*., 2024), whereas after doping with different dopants, the crystallite size and optical band gap decreased from 8 to 6 nm and 3.10 to 2.79 eV, respectively (Yuvakkumar *et al*., 2020). The decrease in crystallite size is typically ascribed to dopants, which segregate to grain boundaries and raise the interfacial energy needed for grain coalescence during sintering, thereby inhibiting grain growth. However, the type of dopant used can affect the precise effects. The crystallite size decreased from 53 to 16 nm and 24 nm, respectively, when Mg and Sn metals were added to the TiO_2 film; on the other hand, the crystallite size increased to 72 nm when Ni metals were added to the TiO_2 film (Ponnusamy *et al*., 2023). This illustrates how dopant selection has a significant impact on the evolution of grain structure.

Despite its theoretical appeal, charge-balanced codoping poses real-world difficulties. Understanding the true structural and electronic configurations that arise from codoping attempts is significantly impacted by this discovery, which calls into question previous theories regarding compensated codoping. Although Nb and Ta have both been demonstrated to dope into TiO_2 with ease and to achieve success in N-doped TiO_2, their combination does not result in the charge-balanced state that is predicted by theory (Long & English, 2019). This finding's practical ramifications indicate that rather than depending only on nominal charge balance calculations, researchers should carefully examine the actual defect structures that form. Additionally, excessive doping causes thermal instability and crystal defects (such as oxygen vacancies, titanium vacancies,

and interstitial titanium), which can impair photocatalytic performance (Chen *et al*., 2016). The synthesis technique used for codoping influence the structural properties that are produced. Phase formation, defect populations, and dopant distribution are all impacted by the different kinetic constraints and thermodynamic conditions imposed by different preparation methods. Materials produced using lower temperatures are frequently farther from thermodynamic equilibrium and have more uniform dopant distribution, but they may also contain higher concentrations of undesirable defects. Better crystallinity and lower defect densities might be possible with high-temperature techniques, but there is a chance of phase separation, dopant segregation, or dopant loss due to volatilization. Initially, P-doping results in a red shift and broadening of Raman bands, correlating with reduced crystallite size and enhanced conductivity; however, upon cycling, a lithiation-triggered effect emerges, characterized by a blue shift in the bands (Belekoukia *et al*., 2024). This demonstrates that post-synthesis treatments can significantly alter the structural properties of codoped materials.

Codoping is accompanied by morphological changes and surface reconstruction. TiO_2 doping results in crystallite agglomeration; this tendency is ascribed to the fact that impurity doping creates new defects and dislocations in the crystal lattice (Gurkan *et al*., 2017). According to observations made using scanning electron microscopy, codoped TiO_2 frequently consists of agglomerated particles with noticeably larger aggregate sizes than undoped material. This can change the surface area and accessibility of the active site, which can impact photocatalytic performance. Using a variety of atomic, nanoscale, and microstructural methods, dopant ions can significantly affect the anatase to rutile phase change. Lattice distortion and strain generation, changes in oxygen vacancy concentrations, modifications to surface and grain boundary energies, kinetic inhibition of atomic diffusion processes, and the formation of secondary phases or solid solutions are the main ways that dopants impact phase stability. A dopant's particular impact is mostly determined by its ionic radius in relation to the host Ti^{4+} (0.605 Å) or O^{2-} (1.40 Å) ions, as well as by its valence state, concentration, and whether it occupies interstitial or substitutional lattice sites.By establishing energy barriers for the coordinated atomic movements necessary for phase transformation, lattice constraint and mechanical stress may lead to kinetic stabilization of the anatase phase in the formation of interstitial solid solutions, where dopant species

occupy interstitial sites rather than replacing host atoms (Hanaor & Sorrell, 2011). By introducing dopants that cause a large amount of lattice strain because of size mismatch, it is possible to effectively pin grain boundaries and interfaces, preventing rutile domain nucleation and growth. Furthermore, dopants have the ability to segregate to grain surfaces and boundaries, altering interfacial energies and establishing kinetic or thermodynamic obstacles to rutile nucleation.

The complex and occasionally contradictory behaviors that have been revealed by thorough reviews examining the effects of various dopants on the anatase to rutile transformation are a reflection of the complex nature of dopant-structure-property relationships and the strong dependence on synthesis conditions, dopant concentration, and thermal treatment parameters (Hanaor & Sorrell, 2011; Nair *et al*., 2016). A basic understanding of these principles is necessary for the logical design of doped TiO_2 materials with regulated phase stability. One of the most studied methods for maintaining the photocatalytically active anatase phase at high temperatures and altering the anatase to rutile transition temperature is metal doping. Depending on their ionic properties and concentrations, various metal dopants have wildly disparate impacts on phase stability. According to systematic investigations, metal dopants can either enhance or accelerate the phase change (e.g., Fe, Cu, Mn, Co, Ni) or retard it (e.g., Nb, Ta, W, Zr, Si, Al). One of the best methods for maintaining the anatase phase at high temperatures is niobium doping. Studies have shown that even at synthesis temperatures as high as 850°C, niobium-doped TiO_2 significantly suppresses anatase to rutile phase change, despite the projected use at high temperatures above 600°C (Leong *et al*., 2015).

Nb^{5+} higher ionic radius (0.64 Å) than Ti^{4+} creates lattice strain and distortion, which prevents the coordinated atomic rearrangements required for phase change. This is the stabilizing mechanism. Furthermore, niobium's higher valence state limits the oxygen diffusion that promotes transformation by lowering the concentration of oxygen vacancies. According to the previously described size-dependent thermodynamic principles, niobium-doped TiO_2 has also been shown to exhibit grain growth retardation, with lower crystallite sizes leading to improved phase stability. At higher temperatures, tantalum doping has shown comparable efficacy in maintaining anatase

content. Crucially, research has shown that tantalum doping maintained the anatase content of TiO2 at annealing temperatures of 850°C, enabling the maintenance of anatase stability at standard ceramic processing temperatures (Smith *et al*., 2009). In addition to altering the electrical structure and raising electron concentration, the replacement of Ta^{5+} ions for Ti^{4+} ions also created lattice strain, which kinetically prevents phase change. Both electrical effects and the mechanical restrictions imposed by the bigger Ta^{5+} ion have been credited with tantalum's efficacy as a phase stabilizer.

Iron doping offers a more complicated situation in which the synthesis circumstances and dopant concentration have a significant impact on the phase transition effect. Research on the anatase crystalline phase to rutile TiO_2 transition of iron-doped TiO_2 nanoparticles showed that the anatase to rutile transformation was promoted when the Fe^{2+} dopant concentration was increased to 9.29 atomic percent (Manurung *et al*., 2020).

Fe^{3+} nanoparticles to redshift and the Raman modes to shift and widen. The creation of oxygen vacancies brought about by the replacement of Fe^{3+} for Ti^{4+} has been ascribed to the transformation-promoting impact. This process improves oxygen transport and reduces activation barriers for the structural rearrangement. However, iron can also have stabilizing effects through grain boundary pinning processes at lower concentrations or under particular synthesis circumstances. Controlled iron addition during titanium tetrachloride hydrolysis affected the transformation temperature and the shape of the emerging rutile phase, according to research on the impact of iron ions on anatase-rutile transition in mica-titania pigments (Roselló *et al*., 2012). In order to have a better knowledge of the microscopic intricacies of the anatase to rutile transition, manganese doping has been studied. Research on Mn-doped TiO_2 systems at dopant concentrations of 1, 5, and 10 atomic percent employing electron, X-ray, and gamma-ray spectroscopic probes showed intricate structural changes during phase transformation (Panda *et al*., 2018). Together with other methods, time differential perturbed angular correlation spectroscopy shed light on local structural alterations and the transformation's progression, showing that manganese occupies several different lattice sites and affects transformation kinetics in a concentration-dependent way.

Charge-compensated codoping techniques have become very potent methods for attaining greater phase stability while concurrently customizing electrical and optical features, even if single-element doping may successfully alter phase transformation behavior. In order to preserve overall charge neutrality and have a synergistic effect on crystal structure and transformation kinetics, two dopant species with complementary electronic characteristics—typically one donor and one acceptor—are introduced using the codoping idea. One well-known instance of charge-compensated codoping for anatase stabilization is gallium-vanadium codoping. Numerous charge-compensated Ga-V codoped TiO_2 samples with the composition $Ti(1-x)(Ga_{0.5}V_{0.5})xO_2$ that were created using modified sol-gel techniques have been shown to display exceptional phase stability (Bharati *et al*., 2019; Bharati *et al*., 2018). The anatase phase stabilizes in codoped samples up to around 650°C, according to X-ray diffraction research, while pure TiO_2 experiences a phase transition between 450 and 500 °C, signifying a notable improvement in thermal stability over 150 °C. Codoping causes the particle size to decrease in the anatase phase, which improves stability through size-dependent thermodynamic effects, according to high-resolution transmission electron microscopy. Ga-V inclusion in the lattice causes increased strain, which in turn generates energy barriers for the atomic rearrangements necessary for transformation.

Ga^{3+} (0.62 Å ionic radius) and V^{5+} (0.54 Å ionic radius) dopants have complimentary functions in Ga-V codoped systems, which results in synergistic effects. In order to preserve charge neutrality while optimizing lattice distortion, gallium replacement for titanium produces oxygen vacancies because of its lower valence state, whereas vanadium substitution lowers the concentration of oxygen vacancies because of its higher valence state. According to studies, this co-doping approach allows for both remarkable phase stability and bandgap tuning into the visible light range, which makes these materials very appealing for high-temperature photocatalytic applications (Bharati *et al*., 2019). Although they frequently have a distinct focus on modifying electrical properties as opposed to enhancing phase stability directly, other charge-compensated co-doping combinations have also shown the capacity to stabilize phases. The general idea behind successful codoping techniques is to choose dopant pairs that produce complementary lattice distortions, keep acceptable oxygen vacancy concentrations that strike a balance between lattice stability and diffusion kinetics, and

produce enough mechanical constraints to kinetically inhibit transformation while avoiding excessive defect concentrations that might jeopardize crystallinity or produce alternative phase unstable states.Because of brookite's distinct structural and electrical characteristics, brookite phase stabilization is an emerging field of study, whereas the majority of research on TiO_2 phase stabilization has been on maintaining anatase structure. of the three main TiO_2 polymorphs, brookite is the least common and most metastable; when heated, it usually changes into either rutile or anatase. Nonetheless, brookite's stabilization is academically and technologically significant due to its intriguing photocatalytic qualities and intermediate traits between rutile and anatase.

According to theoretical simulations employing density functional tight-binding techniques, under some circumstances, the brookite phase may be energetically advantageous at the nanoscale in comparison to anatase and rutile (Qiu *et al*., 2020). These results imply that brookite stabilization may be possible by deliberate manipulation of particle size and surface chemistry. Hydrothermal treatment at high temperatures with suitable reactants has been used in experimental methods to create phase-pure brookite nanoparticles. Phase-pure rutile and brookite nanoparticles were produced using hydrochloric acid at varying concentrations (Buonsanti *et al*., 2008). It is anticipated that brookite will change into either rutile or anatase during heat treatment since studies on heterophase TiO_2 systems including brookite have shown that brookite is metastable in comparison to rutile and anatase (Rajaraman *et al*., 2017). Nonetheless, kinetic stabilization can increase brookite stability under photocatalysis-relevant operating conditions by controlling surface energy, particle shape, and interface structure. Through interfacial energy considerations, studies on anatase/brookite and rutile/brookite heterophase junctions have demonstrated that phase barriers can actually stabilize minority phases, including brookite.

Compared to anatase stabilization, doping tactics especially tailored for brookite stabilization are still largely unexplored, which presents a research opportunity. Given brookite's distinctive crystal structure, which includes an orthorhombic unit cell and a unique Ti-O coordination, dopants with certain sizes and electrical properties may preferentially stabilize this phase. The best dopant combinations for brookite phase control may be found by methodical research that combines computational predictions

with experimental confirmation. In addition to stabilizing single phases, heterophase TiO_2 systems with regulated anatase, rutile, and/or brookite mixtures are increasingly being recognized for their ability to perform better photocatalytically than single-phase materials because of improved charge carrier separation at phase boundaries. By spatially separating photogenerated electrons and holes, heterophase junctions can efficiently promote electron transport from one phase to another, improving photocatalytic performance and lowering recombination (Rajaraman *et al*., 2023; Nair *et al*., 2023).

The commercial Degussa P25 catalyst, which contains roughly 75–80% anatase and 20–25% rutile, is an example of a biphase polymorph TiO_2 system. Other systems that have been reported include anatase/brookite, rutile/brookite, and anatase/TiO_2(B), where TiO_2(B) is the monoclinic bronze structure (Nair *et al*., 2023). Investigations have also been conducted on triphase systems that comprise all three primary polymorphs, with the phase composition regulated by synthesis conditions and thermal treatment procedures. By selectively preventing the transformation of particular phases or encouraging the creation of minority phases, doping can be extremely important in stabilizing desired phase ratios in heterophase systems. Controlled heterophase materials are useful, as evidenced by the commercial success of Degussa P25, which has a particular ratio of anatase TiO_2 and rutile TiO_2 crystalline phases. According to research, the improved performance of P25 results from effective electron transfer across phase boundaries from anatase TiO_2 to rutile TiO_2, which prolongs the lifetime of photo generated charges and produces effective charge separation. Analytical studies of the impact of the anatase/rutile ratio on photocatalytic efficacy have identified ideal compositions that strike a compromise between the properties of light absorption, charge production, and charge separation.

The impact of dopants on individual phase stabilities, the impact on interfacial structure and electronic band alignment at phase boundaries, and the possibility of preferential segregation of dopants to interfaces versus bulk phases are some of the variables that must be taken into account when developing doping strategies for heterophase systems. Dopants frequently preferentially accumulate at phase boundaries, where they can significantly alter interfacial structural and electronic features. Strategic doping can

improve charge separation efficiency while preserving advantageous phase compositions for solar water splitting applications, according to research on doped anatase/rutile heterojunctions in TiO_2 nanotubes (Rajaraman *et al*., 2017). The work underlined that maximizing heterophase photocatalyst design requires an understanding of the interactions among doping, phase composition, and interfacial events. Recent study has shown that, under some circumstances, it is possible to reverse the transformation from rutile to anatase, opening up new possibilities for phase control, even though the vast majority of research focuses on the anatase to rutile transformation and methods to suppress it. Sequential treatment with ammonia and oxygen atmospheres has been used to achieve high-temperature solid-state rutile-to-anatase phase change in TiO_2 (Samin *et al*., 2022). In order to create a high temperature pathway that converts rutile TiO_2 to the anatase phase through grain fracture and nitrogen doping, this work took advantage of the property that the stability of TiO_2 polymorphs depends on particle size and doping level.

Nitrogen incorporation during ammonia treatment is the process of reverse transformation, causing considerable lattice strain and encouraging the breakup of larger rutile grains into smaller crystallites. Surface energy studies show that anatase becomes thermodynamically beneficial in comparison to rutile at tiny enough sizes. Excess nitrogen is eliminated by further oxygen treatment, which also permits the anatase phase to crystallize. This finding shows that phase stability may be regulated by carefully introducing defects and controlling the size of crystallites, rather than being a one-way thermodynamic trend. Reverse phase transformation has important ramifications for the synthesis of materials since it implies that materials containing rutile or even pure rutile may be transformed into compositions high in anatase without the need for total dissolution and resynthesis. This strategy might make it possible to phase engineer current materials or open up new processing avenues for the production of phase-controlled TiO_2. To increase phase control capabilities, more research examining the extent and constraints of reverse transformation under different doping situations will be beneficial.

Both the initial phase composition and the following phase stability after heat treatment are significantly influenced by the method used in fabricating titanium (iv) oxide

nanoparticles. Materials with different microstructures, crystallite sizes, morphologies, and defect structures that impact phase behavior are produced by a variety of synthesis methods like hydrothermal synthesis, solgel, solvothermal processes, mist chemical vapour deposition, co-precipitation, and solid-state reactions.One of the most preferred ways of fabricating doped TiO_2 is sol-gel synthesis, usually produces the anatase phase at comparatively low temperatures (300–500 °C) with precise control over dopant uniformity and inclusion. Phase stability and selectivity can also be influenced by altered sol-gel procedures that include certain chelating agents, pH regulation, or aging conditions. Modified sol-gel synthesis allows for homogeneous dopant distribution, which is necessary to achieve maximum phase stabilization effects, according to research on charge-compensated Ga-V co-doped TiO_2 (Bharati *et al*., 2019).

For phase-selective synthesis, hydrothermal and solvothermal techniques done in enclosed vessels at elevated temperatures and autogenous pressure offer special possibilities. Brookite, anatase or rutile phases can be formed preferentially by adjusting the temperature, pressure, mineralizer (such as HCl, NaOH, or acetic acid), and solvent. Research on the manufacture of pure TiO_2 nanoparticles showed that acetic acid mineralizer promotes anatase formation, whereas hydrochloric acid at varying doses yields phase-pure rutile and brookite (Buonsanti *et al*., 2008). Dopants can be added to hydrothermal synthesis to improve stability of the target phase and further shift phase selectivity. A particularly promising method for creating stable anatase TiO_2 thin films at high temperatures is mist chemical vapour deposition. Films of pristine anatase TiO_2 were successfully created by research employing mist CVD, and they were stable up to 1000 °C. No anatase to rutile change was seen until 1100 °C, at which point only partial transformation took place (Rajaraman *et al*., 2020). A sheet-like grain structure that prevents rutile nucleation and the small crystallite size maintained during film formation were credited with the remarkable thermal stability. The amazing stabilization made possible by morphological control in vapour deposition procedures was demonstrated by the steady rise in crystallite size that was observed after post-annealing treatment in an oxygen atmosphere at 600–1100 °C while maintaining the anatase phase.

To correlate structure with functional attributes and comprehend how doping affects TiO_2 phase stability, precise characterization of phase composition, phase purity, and transformation behavior is crucial. To achieve thorough phase analysis, several complementary approaches are usually used. The principal method for identifying and quantifying phases is still X-ray diffraction; with Rietveld refinement, phase fractions in multiphase materials can be determined with an accuracy of typically 2–5%. When surface-sensitive analysis is needed for thin film materials, grazing incidence X-ray diffraction is especially useful. Compared to XRD, Raman spectroscopy offers complementing phase identification with lower detection limits for minority phases and a stronger sensitivity to local structure. Even in complicated combinations, unambiguous phase identification is made possible by the unique Raman active modes of rutile (143, 447, 612 cm^{-1}), anatase (145, 197, 399, 513, 519, and 639 cm^{-1}), and brookite (128, 153, 194, 247, 322, 366, 395, 460, 502, 545, 584, and 636 cm^{-1}). Temperature-dependent Raman spectroscopy has been used in phase transition studies in doped TiO2 to monitor transformation kinetics and pinpoint intermediate states.

Quantitative evaluation of how dopants alter transformation thermodynamics and kinetics is made possible by the information on transformation temperatures and enthalpies provided by thermogravimetric technique and differential scanning calorimetry method. For undoped TiO_2, the anatase-to-rutile transformation exothermic signal usually manifests between 450 and 850 °C, with dopant effects reflected in shifts in peak temperature and variations in transformation enthalpy. In situ high-temperature XRD during thermal treatment allows for the real-time monitoring of doping-related phase evolution, grain growth, and crystallographic alterations. Direct observation of phase distributions, grain sizes, phase borders, and crystallographic orientations at nanoscale resolution is made possible by the combination of chosen area electron diffraction and HRTEM. HRTEM has been used in studies of dopant effects on phase stability to show how dopants affect the nucleation of rutile domains at particular crystallographic interfaces, limit grain development, and affect grain boundary structure (Bharati *et al*., 2018). By revealing the distribution of dopants at grain boundaries and phase interfaces, energy-dispersive X-ray spectroscopy mapping in scanning TEM mode can shed light on segregation events.

Strategic doping of TiO_2 to create phase-stabilized TiO_2 directly meets the needs of many technological applications where thermal stability is essential. Anatase stabilization is crucial for sustaining activity in photocatalytic self-cleaning coatings for outdoor surfaces, automotive applications, and building materials because these coatings must tolerate high temperatures during processing (ceramic firing, paint curing) and during operation under solar irradiation (Rajaraman *et al*., 2020). In order to attain sufficient sensitivity and response kinetics, TiO_2-based gas sensors frequently function at high temperatures (300–500 °C), necessitating phase-stable materials that sustain constant sensing characteristics over prolonged use. Phase-stable anatase that maintains appropriate electrical characteristics is being developed because perovskite solar cells and dye-sensitized solar cells and with TiO_2 electron transport layers need to withstand processing temperatures of about 500 °C required for contact firing or sintering of metallic components. Although anatase's higher photocatalytic efficacy is advantageous for photocatalytic water splitting systems used to produce hydrogen, these systems may encounter high operating or illumination temperatures, especially in concentrated sun applications. Strong catalysts that retain phase composition and activity under extreme heat conditions are necessary for high-temperature photocatalysis applications in chemical synthesis or industrial-scale pollutant destruction.

Standard ceramic firing temperatures (800–1200 °C) significantly surpass typical anatase stability limitations, despite the fact that the commercial ceramic tile industry offers a sizable market for self-cleaning and antimicrobial TiO_2 coatings. Functional TiO_2 coatings can be integrated into ceramic manufacturing processes without the need for post-firing application, which increases costs and decreases durability, thanks to the development of anatase-stabilized compositions through doping strategies like strategic co-doping or mist CVD (Rajaraman *et al*., 2020). Because of its special ionic conductivity characteristics, zirconia (ZrO_2) has become an essential component of solid oxide fuel cells (SofCs), oxygen sensors, and catalytic applications (Badwal, 2001; Fergus, 2006). Since oxygen vacancies are the main mechanism for oxygen ion transport, creating and managing them in ZrO_2 is essential to improving its performance (Kharton *et al*., 2004; Steele, 2000). The potential of codoping techniques to synergistically improve oxygen vacancy formation and ionic conductivity beyond what

single dopants can accomplish has drawn a lot of attention, despite the fact that single-doping procedures have been well investigated (Arachi *et al*., 1999; Omar et al., 2008). The main source of oxygen vacancies in ZrO_2 is the substitution of lower-valence cations for Zr^{4+} ions (Kilner, 2000). In order to preserve electro neutrality when Zr^{4+} is replaced with a trivalent or divalent cation, charge compensation necessitates the creation of oxygen vacancies. Kröger-Vink notation can be used to express the general defect equation for trivalent dopant incorporation: $M_2O_3 \rightarrow 2M'z^R + V\bullet\bullet_o + 3O_{xo}$, where $M'z^R$ is the dopant cation on a Zr site with effective negative charge and $V\bullet\bullet_o$ indicates an oxygen vacancy with two positive charges (Kröger & Vink, 1956). The stoichiometry for divalent dopants is different, requiring one oxygen vacancy per dopant cation instead of two (Yamamoto, 2000).

In order to stabilize the cubic fluorite structure and create oxygen vacancies, traditional single-doping techniques have used alkaline earth metals (Ca, Mg) and rare earth elements (Y, Sc, Gd, Sm) (Minh, 1993; Singhal, 2000). With an ionic conductivity of roughly 0.1 S/cm at 1000 °C, yttria-stabilized zirconia (YSZ), which contains 8–10 mol% Y_2O_3, continues to be the standard material (Etsell & Flengas, 1970; Mogensen *et al*., 2000). Because of the closer ionic radius match between Sc^{3+} (0.87 Å) and Zr^{4+} (0.84 Å), which reduces lattice distortion and increases oxygen mobility, Scandia-stabilized zirconia (ScSZ) exhibits even higher conductivity (Badwal *et al*., 2000; Haile et al.,2001). Single-doping tactics do have some inherent drawbacks, though. Defect association and ordering processes take place at high dopant concentrations required for maximal oxygen vacancy production (Catlow, 1997; Strickler & Carlson, 1965). In order to efficiently lower the concentration of mobile charge carriers, oxygen vacancies frequently form defect clusters with dopant cations that become trapped and immobile (Yamamura *et al*., 2003). At dopant concentrations higher than the ideal level, this causes conductivity to plateau or even decline (Dent Glasser *et al*., 1962).

To get over the drawbacks of single doping, codoping techniques use two distinct dopants at the same time (Hong *et al*., 1998; Zha *et al*., 2003). There are multiple mechanisms in the underlying reasoning. First, codoping can minimize lattice strain and related defect entrapment by optimizing the size disparity between host and dopant cations (Bishop *et al*., 2009). Second, the long-range ordering of defect clusters may be

upset by the presence of two distinct dopant species, resulting in larger concentrations of mobile oxygen vacancies (Lee *et al*., 2005; Politova & Irvine, 2004). Third, the oxygen vacancy formation energy and migration barriers may be changed by the synergistic electrical effects of several dopants (andersson *et al*., 2006). There has been much research done on the combination of two rare earth dopants. One of the most researched combinations is the Y-Sc codoped system, in which a more heterogeneous cation distribution is produced by the bigger Y^{3+} ions (1.02 Å) and smaller Sc^{3+} ions (Haering *et al*., 2005; Spirin *et al*., 2012). According to research, the best compositions usually have 8–11 mol% total dopant concentration, and the highest conductivity is obtained with Y: Sc ratios between 1:1 and 1:2 (Yarmolenko *et al*., 2009). The reason is that Y^{3+} breaks Sc-vacancy clustering, which would otherwise trap mobile defects, while Sc^{3+} provides strong intrinsic mobility because of the small size mismatch with Zr^{4+} (Lei & Zhu, 2007; Yamaji *et al*., 2009).

Because of its optimized crystal structure, ScSZ has 1.5–3 times the ionic conductivity of YSZ (Omar *et al*., 2009; Ramesh *et al*., 2023). Long-term operation of ScSZ, however, causes phase instability problems that result in the production of β-phase precipitates that impair performance (Ruh *et al*., 1977). According to Nomura *et al*. (2000), codoping with yttria preserves improved conductivity while stabilizing the cubic phase. Excellent phase stability and ionic conductivity of 1.02×10^{-1} S/cm at 800°C with an activation energy of 0.578 eV have been demonstrated in recent investigations on Yb-Sc codoped zirconia (Zhang *et al*., 2025). Due to the intermediate ionic radius of Gd^{3+} (1.053 Å) in relation to Y^{3+}, Gd-Y codoped zirconia has shown increased conductivity when compared to YSZ alone (Norby & Larring, 2000; Tao & Irvine, 2004). Gd appears to lower the activation energy for vacancy migration by altering the local coordination environment surrounding oxygen vacancies. Codoping produces a more disordered oxygen sublattice, which is correlated with better ionic transport, according to studies employing neutron diffraction (Hayashi *et al*., 2005). Trivalent and divalent dopants together have special benefits in terms of vacancy formation efficiency (Dutta *et al*., 1992). According to Ca-Y codoped systems, the divalent nature of calcium creates one oxygen vacancy per Ca^{2+} ion (as opposed to one vacancy per two M^{3+} ions), which could raise the concentration of all vacancies (Lee *et al*., 2002; Stefanik & Tuller, 2001). The ideal Ca:Y ratio needs to be carefully

managed, though, because too much CaO might cause phase segregation or the development of secondary $CaZrO_3$ phases, which impair ionic conductivity (Mori *et al*., 1994).Divalent cations such as Ca^{2+} efficiently generate oxygen vacancies for charge compensation, as shown by DFT investigations on Ca-doped ZrO2 (Molinari *et al*., 2012). The significance of oxygen vacancies in surface reactions was highlighted by the discovery that the presence of Ca dopants increased catalytic activity in CO_2 -related activities (Shi *et al*., 2021).

According to Kendall *et al*., (1996), Mg-Sc codoping has shown promise as a system, especially for SofC applications involving intermediate temperatures. Significant lattice deformation is introduced by the extremely tiny Mg^{2+} ionic radius (0.72 Å); yet, when paired with Sc^{3+} , large vacancy concentrations are achieved while maintaining overall structural stability (Yamamoto *et al*., 1995). According to density functional theory (DFT) computational investigations, stable defect complexes with migration barriers ranging from 0.96 to 1.32 eV occur when Mg-Sc codoping lowers the oxygen vacancy formation energy (Romanov, 2025). Codoping with both acceptor dopants (M^{3+} or M^{2+}) and isovalent or donor dopants is a new tactic (Fu & Chen, 2010). Ce-Y codoped zirconia is an example of this strategy, in which Ce^{4+} alters the electronic structure and oxygen vacancy migration paths rather than producing oxygen vacancies directly (Inaba & Tagawa, 1996). Ce makes the system more reducible, which makes it easier for more oxygen vacancies to form in the reducing atmospheres that are typical in SofC operation (Mogensen *et al*., 1994). Research on NbO_5 codoping with YO_3 in tetragonal zirconia has revealed that niobium incorporation influences phase stability and oxygen vacancy annihilation (Kim *et al*., 1998). The study discovered that as the amount of NbO_5 grew, fracture toughness rose but ionic conductivity fell, suggesting intricate relationships between defect chemistry and mechanical characteristics (Nettleship & Stevens, 1987).

Codoping effects have been understood at the molecular level thanks to first-principles simulations (Bogicevic *et al*., 2001; Nolan *et al*., 2005). Codoping regularly modifies the migratory energy (E□) and oxygen vacancy formation energy (E^f) in non-additive ways, according to DFT investigations (Dwivedi & Cormack, 1990; Pornprasertsuk *et al*., 2005). Research on oxygen point defects in cubic ZrO_2 showed that oxygen

vacancies exist in neutral and +2 charge states under various equilibrium conditions (Foster *et al*., 2001). According to DFT, the activation energy for ion conductivity is roughly 0.87 eV, which is consistent with experimental results (Stapper *et al*., 1999). For instance, in Y-Sc codoped ZrO_2, the local lattice distortion is increased when Y is close to a Sc-vacancy pair. This, in turn, paradoxically, lowers the energy barrier for vacancy hopping by generating a more diffuse potential energy landscape. Research on oxygen-vacancy pairs in YSZ has demonstrated that ionic conductivity is significantly influenced by the relative abundance of oxygen vacancies in yttrium-containing environments, with a larger likelihood of O^{2-} -vacancy pairs leading to more hopping transitions (Jiang *et al*., 2009).

Codoping broadens the variety of oxygen vacancy hopping pathways, according to molecular dynamics simulations (Schelling *et al*., 2001). Vapours move preferentially along certain crystallographic orientations that correspond to dopant ordering in single-doped systems. By upsetting this ordering, codoping efficiently lowers the activation energy for long-range oxygen transport and permits three-dimensional vacancy percolation at lower temperatures (Pornprasertsuk *et al*., 2005). Complex characterisation is necessary to comprehend the formation of oxygen vacancies in codoped systems (Arunkumar *et al*., 2017). Via distinctive peak shifts and the emergence of vacancy-related defect modes, X-ray photoelectron spectroscopy (XPS) and Raman spectroscopy offer direct proof of oxygen vacancy concentration (Kim *et al*., 2012). The principal technique for measuring the impact of oxygen vacancies on ionic conductivity and distinguishing between bulk, grain boundary, and electrode contributions is still impedance spectroscopy (Bauerle, 1969).

Vacancy-type defects and their clustering behavior can be directly detected using sophisticated techniques like positron annihilation spectroscopy (PAS) (Ishibashi *et al*., 2007). At comparable total vacancy concentrations, codoped systems show smaller defect cluster sizes than single-doped materials, according to studies employing PAS. In YSZ, the distribution of oxygen vacancies across individual grain boundaries can now be directly measured thanks to atomic-resolution scanning transmission electron microscopy (STEM) combined with energy-dispersive X-ray spectroscopy (An *et al*., 2013). These investigations demonstrated that the macroscopic ionic transport

parameters are governed by complicated chemical inhomogeneity at crystalline surfaces. Important details on oxygen site occupancy and the local structure surrounding dopant cations are revealed by neutron powder diffraction, which also reveals minute distortions that affect vacancy mobility (Argyriou, 1994). Ionic conduction in $Y_2\ O_3$ -doped zirconia is regulated by oxygen vacancy mobility and vacancy-dopant association processes, as shown by internal friction measurements in conjunction with electrical conductivity and tracer diffusion tests (Weller *et al*., 2004).

Oxygen vacancy distribution and material performance are strongly influenced by the codoped ZrO_2 synthesis process (Shukla & Seal, 2005). At high temperatures (>1400 °C), conventional solid-state reactions frequently result in non-uniform vacancy distribution and dopant segregation (Yashima *et al*., 1993). Atomic-level dopant mixing is made possible by solution-based techniques such as sol-gel, coprecipitation, and hydrothermal synthesis, which result in more homogenous materials with better-distributed oxygen vacancies (Djurado & Labeau, 1998; Shukla *et al*., 2002). According to Patil *et al*., (2002), combustion synthesis has become a quick technique for creating nanocrystalline codoped zirconia with a large surface area and lots of surface oxygen vacancies. Although stabilizing these surface vacancies may be necessary to avoid coarsening during high-temperature operation, they are especially crucial for catalytic applications. In order to create scandia-stabilized zirconia layers on tubular substrates at low temperatures, chemical vapour deposition (CVD) techniques have been developed. These techniques offer benefits for the production of SofC components (Tietz *et al*., 2000). The development of functional grading that maximizes oxygen vacancy concentration across device architectures is made possible by thin film deposition techniques like atomic layer deposition (ALD) and pulsed laser deposition (PLD), which provide exact control over dopant concentration gradients (García-Barriocanal *et al*., 2008; Shim *et al*., 2007). Codoped ZrO_2 optimization requires striking a balance between several conflicting factors (Wachsman & Lee, 2011). Increasing the concentration of total dopants promotes the production of oxygen vacancies, but it also causes a rise in defect association and lattice distortion (OR *et al*., 2006). Similar to single-doped systems, the majority of codoping studies find that the ideal total dopant as been shown to exhibit enhanced oxygen diffusivity at surfaces; the maximum ionic conductivities have been reported for Y_2O_3 values of 7–10 mol%

(Mondal *et al*., 1999). This implies that in order to further improve oxygen vacancy mobility, codoping techniques can be supplemented by grain boundary engineering and nanostructuring.

Although the main application for codoped ZrO_2 research is SofC electrolytes, these materials' oxygen vacancies allow for additional functionalities (Wachsman & Lee, 2011). Surface oxygen vacancies act as active sites for water-gas shift reactions, CO oxidation, and methane reforming in catalysis (Montini *et al*., 2016; Trovarelli, 1996). The function of oxygen vacancies in CO_2 methanation over zirconia has been clarified by mechanistic DFT and microkinetic investigations, which have also shed light on reaction pathways and energy constraints (Wang *et al*., 2019). For catalytic applications, codoping techniques that optimize surface vacancy concentration while preserving bulk structural stability are especially beneficial. Improved CO_2 activation has been seen on surfaces with designed oxygen vacancies in Ca-doped ZrO_2 studies (Shi *et al*., 2021). The crucial role that oxygen vacancy effects play in the adsorption and dissociation of CO_2 molecules was demonstrated by DFT studies of these effects on monoclinic ZrO_2 surfaces (Zhao & Cheng, 2017).

The oxygen vacancy concentration gradients that form across ZrO_2 under oxygen chemical potential variations are exploited by oxygen sensors (Park *et al*., 2003). Improved response times and sensitivity are made possible by codoped materials with larger baseline vacancy concentrations and quicker vacancy equilibration kinetics. Codoping, which introduces phonon scattering centers while preserving mechanical integrity, lowers thermal conductivity in thermal barrier coatings by carefully creating oxygen vacancies (Clarke & Levi, 2003). Even with great advancements, there are still a number of difficulties in comprehending and managing the formation of oxygen vacancies in codoped ZrO_2 (Wachsman & Lee, 2011). Given that dopant segregation, grain expansion, and defect reorganization can take place over thousands of hours, more research is necessary to determine the long-term stability of codoped systems under operating conditions (Matsui *et al*., 2007; Simwonis *et al*., 1999). An essential area of research is comprehending the kinetics of these processes and creating methods to inhibit them. It is still unclear how grain boundaries function in codoped systems (Guo & Waser, 2006). Recent research indicates that properly designed grain boundaries in

codoped materials may actually improve conductivity by supplying quick diffusion pathways or by gettering impurities that would otherwise block bulk vacancies, despite the fact that grain boundaries typically obstruct oxygen transport (An *et al*., 2013; García-Barriocanal *et al*., 2008). More performance gains might be possible by creating synthesis and processing techniques that regulate the chemistry and structure of grain boundaries. To speed up the discovery of codoped materials, multiscale modeling techniques that connect atomistic DFT computations with mesoscale microstructure evolution and macroscale device performance are required (Chen & Aidun, 2010). Predicting the best dopant combinations from high-throughput computational screening using machine learning techniques shows promise (Sendek *et al*., 2017). The potential of these methods is demonstrated by recent developments in machine learning-based oxygen vacancy formation energy prediction on DFT datasets (Toyao *et al*., 2018).

Research on comprehending the charge state distribution of oxygen vacancies under various operating situations is still ongoing (Kofstad, 1972). Depending on the Fermi level and oxygen chemical potential, ZrO_2 oxygen vacancies can exist in a variety of charge states, according to computational simulations (Foster *et al*., 2001). The optimization of codoped materials for particular applications is further complicated by this intricacy. One effective method for increasing the formation of oxygen vacancies and ionic conductivity in ZrO_2 is codoping (Omar *et al*., 2008; Wachsman & Lee, 2011). Researchers have developed conductivities that surpass those of conventional single-doped materials by mixing dopants with complementary features, whether in terms of ionic radius, valence state, or electronic structure (Arachi *et al*., 1999; Ramesh *et al*., 2023). Reducing vacancy formation energy, upsetting defect ordering, and optimizing lattice strain distributions are the basic methods (andersson *et al*., 2006).

To comprehend vacancy production and evolution under realistic operating conditions, future developments will probably come from combining advanced synthesis techniques, operando characterization techniques, and computational materials design (Chen & Aidun, 2010; Shao & Haile, 2004). Next generation energy conversion and storage technologies will be made possible by the capacity to accurately control oxygen vacancy concentration, distribution, and mobility as the field advances toward the rational design of codoped systems (Jacobson, 2010; Steele & Heinzel, 2001). Ce doped

ZrO_2 exhibits a substantial increase in surface area and absorption of visible light, although crystallite size decreases as cerium concentration rises. According to the study, Ce doping stabilizes the monoclinic zirconia phase and surface area even after calcination at 600 ^oC (Aman *et al*., 2012). The structural properties of pristine zirconium (iv) oxide and zirconium (iv) oxide doped with Yttria were examined with an X-ray diffractometer device. The Yttria-doped ZrO_2 had a mixture of tetragonal and monoclinic phases, whereas the pure was monoclinic, demonstrating phase transition with doping. These findings showed that doping ZrO_2 with yttrium can produce a high-temperature phase at normal temperature (Kumar *et al*., 2021). A computational as well as experimental study was conducted on a Sc_2O_3-Y_2O_3-ZrO_2 nanocomposite synthesized using the co-precipitation technique to assess the results of dopants on the stability of monoclinic zirconia. Results demonstrate that after heat treatment, no monoclinic phase occurred, and the precursor materials were changed from amorphous to a substantial amount of tetragonal and a few cubic phases. The samples with pH10 and calcination temperature of 1000 °C demonstrated highest stabilization results, the most even grain formation, the greatest crystallinity, the most uniform morphology, the largest tetragonal phase quantity of 89.2%, and a stabilization efficiency of 94.58% (Zhou *et al*., 2024). Gong *et al*., (2024) studied the phase stability of SiO_2 and Y_2O_3 codoped ZrO_2 nanopowders with different amounts of Y_2O_3 and SiO_2 produced by co-precipitation. After repeated calcination at 1300 °C, all produced nanopowder samples exhibited a tetragonal phase.

The phase stability of produced Scandia, zirconia, and ytterbia crystals after prolonged high-temperature heat treatment was examined by Borik *et al*., (2021) The outcomes show that stabilizing ZrO_2 with1 mol.% Yb_2O_3 and 9 mol.% Sc_2O_3 yields uniform, transparent crystals with a tetragonal crystal composition and exceptional phase stability. Cao *et al*., (2022) investigated how high-temperature heat treatment affected the phase stability and change inY_2O_3 and Yb_2O_3 codoped ZrO_2 samples. The results show that the tetragonal phase of Yb_2O_3 and Y_2O_3 codoped zirconia material remains stable following heat treatment at 1300 °C for various amounts of time. Additionally, the inclusion of Yb^{3+} causes O-O coupling, which improves the crystal structure stability via raising the number of oxygen vacancies around the substituted ions. Codoping also results into phase stabilization and enhancement of photocatalytic

efficacy of titanium (iv) oxide by Mattsson *et al*., (2013) found that Y and Zr codoped anatase titanium dioxide nanoparticles produced by homogeneous hydrolysis with urea as a reducing agent had higher phase stability. Analysis of the produced material revealed that Zr^{4+} and Y ions replaced Ti $^{4+}$ in the TiO_2 anatase nanostructures up to an adequate sum doping levels around 13 weight percentage. The dual doped nanomaterials exhibited greater phase stability than pristine anatase TiO_2 particles. The efficiency of Ag-Cu codoped photocatalysts TiO_2 was investigated by Behnajady & Eskandarloo (2013). The anatase phase's stability was enhanced by codoping of copper and silver into anatase TiO_2 lattice. Khatun *et al*., (2020) investigated the effects of Ga and V codoping on the optical and crystalline characteristics of titania. The study's findings demonstrated that on codoping the anatase phase remained stable, the sample's band gap reduced, and the photocatalytic capabilities increased. Chen *et al*., (2007) investigated the stability of codoped transparent TiO_2 thin films in the anatase TiO_2 phase. The outcomes reveal that $Nb_{0.06}Sn_xTi_{0.94-x}O_2$ thin films can maintain a stable anatase TiO_2 phase when the Sn dopant level (x) is less than 0.3.

Previous DFT studies show that doping and codoping of TiO_2 and ZrO_2 polymorphs resulted into increase in lattice parameters and volume distortions. First principle study was used to examine the effect of single and codoped (Ni, Se, and B) anatase TiO_2 on its structural properties. Volume distortions were detected after the introduction of impurities into the anatase lattice. The inclusion of an impurity expanded the lattice parameters of the relaxed structures in all of the systems (Ibrahim *et al*., 2020). A DFT analysis on S-N interstitial and substitutional codoped rutile TiO_2 was carried out using hybrid density functional calculation. The lattice distortion was induced by the dopants, leading to the dipole moment change and the production of a local electric field (Chen *et al*., 2018). Heffner *et al*., (2022) examined the properties of boron-doped and carbon-boron-codoped TiO_2.The acquired data revealed that boron substitution into O sites causes it to migrate towards interstitial sites in both mono and codoping, hence resulting in significant geometrical distortion in contrast to pure TiO_2. Sasani *et al*., (2016) examined the effects of adding magnesium and niobium atoms on the TiO_2 anatase's surface structural characteristics using DFT. Because of its larger ionic radius, Mg^{2+} (0.072 nm) in contrast to Ti^{4+} (0.0605 nm), doping Mg into TiO_2 resulted in lattice enlargement. Using first principles calculations, Zhang *et al*., (2014) calculated the

structural parameters of cubic ZrO_2 structures that were undoped, C-doped, and F, C-codoped. The equilibrium structural parameters of C-doped cubic ZrO_2 were 0.55% greater than cubic ZrO_2, which could be explained by the larger radius and lower electronegativity of C atoms relative to O atoms. The lattice parameter for F, C-codoped cubic ZrO_2 remained largely unaltered when compared to the C-doped system.

2.3 Electronic Properties and Effect of Oxygen Vacancies

Recent theoretical studies have shown that codoping not only dramatically reduce titanium (iv) oxide energy band gap, but also effectively counteracts the occurrence of recombination centers. To reveal the electrical structure, Slimani *et al*., (2023) Calculated TDOS for pristine titanium (iv) oxide and Ce-Sm codoped titanium (iv) oxide. Ce and Sm dopant atoms introduced additional states at the Fermi energy level, modifying the electronic properties of Ce-Sm codoped titanium (iv) oxide and significantly lowering the energy band gap of pristine titanium (iv) oxide from 3.19 to 2.13 eV. Ibrahim *et al*., (2020) conducted a hybrid DFT investigation on (Ni, Se, and B) single and codoped anatase TiO_2 oxides under visible light. For all single and codoped materials, the computed DOS revealed additional states in the forbidden gap due to the addition of the doping agent into the lattice. The decrease in band gaps resulted in the observed red shift.

Khan *et al.,* (2019) used DFT based calculations to study defects on introduction of indium and nitrogen dopants in the network of TiO_2 . Indium doping produced the In 5p states in the band structure, which were associated with the oxygen *2p* levels. Above the valence band maximum, N-doped TiO_2 developed solitary N *2p* states. Codoping using indium and nitrogen lowered TiO_2's energy band gap and pushed the absorption edge towards the visible region. By successfully incorporating Ca^{2+} dopant ions into the Ti^{4+} lattice, oxygen vacancies were formed, altering the electronic properties through the introduction of dopant-induced states that efficiently trapped electrons and accelerated charge transfer, thereby improving the photocatalytic production of hydrogen. Lattice strain was caused by the added oxygen vacancies interfering with the lattice spacing (Bian *et al*., 2023).

Codoping TiO_2 with S and I caused lattice distortion and resulted in a decrease in optical the band gap. The charge density of the TiO_2 system redistributed with the S and I atom codoping. New chemical bonds were formed by an electron cloud overlap between the S & I atom and the surrounding O atoms. These findings suggested that S-O and I-O bonding narrows the band gap, which consequently contributes to anatase TiO_2 enhanced visible light absorption Lin *et al*., (2013) . Using first principles Fang *et al*., (2019) studied doped and codoped TiO_2 oxides. The hole effective mass increases after La substitute for Ti in La-TiO_2 and La-C codoped TiO_2 due to its lower oxidation state than Ti^{4+}. C dopant produces C 2p states near the TiO_2's VBE and the CBE shift towards the low energy range to lower the bandgap. Because of the synergistic impact of La and C codoping, the bandgap of codoped TiO_2 is narrower than in La-TiO_2 and the carrier concentration is larger than in C-TiO_2.

Titanium (iv) oxide potential for photo electrochemical water splitting, titanium dioxide (TiO2) has become a prototypical light induced catalyst due to its remarkable chemical stability, non-toxicity, natural abundance, and potent oxidizing ability. The primary drawback of pristine TiO2, however, is its broad band gap of roughly 3.0 - 3.2 eV, which limits photocatalytic activity to the absorption of UV light, which comprises around 5 percentage of the solar radiation (Perumal *et al*., 2019; Suryawanshi *et al*., 2023). Furthermore, photogenerated electron-hole pairs have a high rate of recombination, which severely reduces quantum efficiency and restricts useful applications. Defect disorder has a significant impact on TiO_2's characteristics; oxygen vacancies are notable defects that have been thoroughly investigated for their functions in altering electronic structure and improving photocatalytic performance (Suryawanshi *et al*., 2023). In order to create next-generation semiconducting nanomaterials with improved charge carrier dynamics and increased absorption of visible light, defective TiO_2 materials especially those with created flaws through intentional codoping have attracted a lot of attention. One of the most important and extensively researched defects in TiO_2 and other metal oxides is oxygen vacancies (V_O), which have a big impact on photocatalytic activity and electronic structure alteration. In addition to affecting the electrical structure, charge transport, surface characteristics, and other photocatalytic features of TiO_2-based materials, these intrinsic defects may serve as

both active sites and adsorption centers during heterogeneous catalysis (Suryawanshi *et al*., 2023).

By changing the rate at which electron-hole pairs recombine during photocatalytic processes, oxygen vacancies have been shown to be essential in semiconductor photocatalysis. This allows for the modification of chemical reactions that rely on charge transfer from either electrons or holes. The reactivity and surface adsorption of important adsorbates like water and molecular oxygen on TiO_2 surfaces are greatly impacted by the extra electrons connected to oxygen vacancy states, as demonstrated by both theoretical predictions and experimental results (Suryawanshi *et al*., 2023). Utilizing these special qualities in photocatalytic applications now requires the controlled production of oxygen vacancy-incorporating TiO_2.According to research on rutile TiO2 nanomaterials with tunable oxygen vacancy contents between 0 and 2.18%, controlled defect engineering can be used to systematically lower the band gap of the resulting materials (Wang *et al*., 2023). The production of these materials using in situ solid state chemical reduction techniques has shown color changes from white to black TiO2, which are correlated with higher vacancy concentrations and improved absorption properties of visible light. Chen *et al*., (2011) showed in their ground breaking study of black hydrogenated TiO_2 nanocrystals that hydrogen treatment produces materials with significantly increased solar absorption by generating disorder in the top layer while preserving crystalline cores.

Black TiO_2 nanoparticles produced by reduction/crystallization procedures have band gaps as low as 1.85 eV, which is in good agreement with visible light absorption, according to additional research by Naldoni *et al*., (2012). Their thorough investigation showed that the distinct type and spatial distribution of defects control the electrical structure of black TiO_2, with surface disorder being a key factor in band gap narrowing. According to recent research, rutile TiO_2's band gap may be efficiently narrowed by oxygen vacancies created by carbon doping and heat treatment in carbon powder. This improves the material's visible light sensitivity and increases the photocatalytic destruction of organic pollutants (Li *et al*., 2023). Research on heterophase junction TiO_2 has demonstrated that thermal annealing in inert atmospheres can be used to strategically create both interfacial and surface oxygen vacancies. These various

vacancy types have synergistic effects on the production of photocatalytic reactive oxygen species and overall catalytic performance (Dong *et al*., 2020). Since Liu *et al*., (2019) shown through quantum dynamics simulations that ground state multiplicity, defect levels, and formation energies substantially depend on vacancy position, the location of oxygen vacancies has become a crucial parameter. Their research demonstrated that whereas subsurface vacancies had more advantageous charge carrier dynamics, nanoparticles lacking partially coordinated surface oxygen exhibited rapid recombination.

Oxygen vacancies and their relationship to electrical structure and nanomagnetism are important for applications in diluted magnetic semiconductors, according to recent research on single-atom Co/TiO_2 nanostructures (Li *et al*., 2023). Modulated electronic structures and surface oxygen vacancies simultaneously promote the activation of surface-adsorbed intermediates and facilitate the separation of photogenerated charges, ultimately boosting photocatalytic activity for applications like carbon dioxide photo reduction, according to research on the engineering of stable nanoparticles and oxygen vacancies on defective TiO_2 through strong electronic metal-support interactions (Wang *et al*., 2020).The electronic structural changes in TiO_2 brought about by codoping and defect engineering have been greatly aided by density functional theory (DFT) computations. The band structure changes, density of states distributions, formation energies, and charge transfer mechanisms that control photocatalytic action may all be thoroughly examined thanks to these computational research. Dopant replacement at oxygen atom sites can efficiently push the absorption edge toward visible light wavelengths, according to recent DFT investigations on fluorine, nitrogen, chlorine, and sulfur-doped rutile TiO_2 by Manzoor *et al*., (2025). The band gap of 3.03 eV, which was calculated for pure rutile TiO_2, is in great agreement with experimental results, confirming the accuracy of computational methods for forecasting changes in electronic structure.

Codoping produces more advantageous electronic structures than single-element doping, according to thorough DFT studies on nitrogen and metal codoped TiO_2 systems. Charge transfer between implanted nitrogen atoms, adsorbed gold atoms, and oxygen vacancies is observed in work by Ortega Hernández et al., (2011) on nitrogen

and gold codoping of the anatase TiO_2 (101) surface. The formation of vacancies on nitrogen-modified and gold-supported anatase surfaces facilitates the migration of substitutional nitrogen impurities from bulk to surface sites. These results demonstrate the intricate interactions between various defect types and how they together affect electrical structure and photocatalytic processes.

Carbon-doped TiO_2 nanocomposites have demonstrated impressive band gap reductions in studies using DFT calculations; the systems' band gaps are significantly smaller than those of pure TiO_2. Dopant incorporation at oxygen sites has been shown repeatedly to produce localized states within the band gap by density of states analysis, which facilitates electron excitation pathways that extend photo response into the visible light area (Song *et al*., 2021). Carbon doping of TiO_2 bronze structures is advantageous in both titanium-rich and oxygen-rich synthetic conditions, according to DFT+U calculations. The band gap is reduced mainly when carbon dopants take the place of oxygen atoms, which causes spectral shifts toward the infrared spectrum. Using a combination of DFT and experimental methods, Graciani *et al*., (2021) study on hydrogen, fluorine, and chlorine doped and codoped TiO_2 showed that hydrogen incorporates in interstitial sites, but fluorine and chlorine can insert as both interstitial and oxygen substitutional defects. Through complementary electronic structural alterations, codoping techniques can produce greater performance, according to their work on the synergy of dopants in TiO_2. In-situ X-ray photoelectron spectroscopy revealed enhanced CO_2 activation through enrichment of photogenerated electrons, and recent DFT calculations on nitrogen-doped TiO_2 for enhanced CO_2 photocatalytic reduction confirmed that nitrogen doping can reduce the band gap and decrease the gibbs free energy of CO_2 reduction reactions (Li *et al*., 2025).

In comparison to single-element doping techniques, the strategic use of codoping approaches has become a potent mechanism for engineering flaws and altering the electronic structure of TiO_2 with higher performance. Codoping makes it possible to introduce several defect types at once, which can work together to improve charge carrier dynamics and optimize electronic band structures. Particularly a lot of research has been done on nitrogen and metal codoping, showing that the valence and conduction bands of TiO_2 undergo complimentary alterations when nitrogen and

transition metals are mixed. The simultaneous introduction of donor and acceptor dopants in compensated codoping techniques has demonstrated remarkable potential for charge neutrality and band gap narrowing. Compensated codoping systems, including carbon-molybdenum pairs, have been studied using first-principles hybrid density functional theory calculations with the HSE06 functional, showing successful band gap reduction using this method (Long & English, 2009). However, thorough studies by Deák *et al*., (2019) using hybrid DFT questioned the accepted notion of "passivated codoping," showing that complex defect chemistry and preferential defect formation energetics may make charge-neutral compensated codoping in TiO_2 impractical in some cases. Compared to single-doped systems, defect chemistry in codoped TiO_2 becomes significantly more complex. In the TiO_2 band gap, transition metals like Cu and rare-earth metals like La cause lattice deformation and the creation of oxygen vacancies, creating an impurity state that narrows the band gap and enhances visible light absorption (Gupta *et al*., 2020). The formation of oxygen vacancies in the TiO_2 lattice induces the creation of unpaired electrons or Ti^{3+} centers, confirming that these defects act as electron donors (Díaz-Reyes *et al*., 2023).

It has been demonstrated that nitrogen doping significantly affects the formation of oxygen vacancies. As a result, N-doping into TiO_2 produced surface oxygen vacancies in addition to improving absorption of visible light (Serpone, 2006). By manipulating the concentration of oxygen vacancies, the reduced band gap effectively enhances the visible light response of TiO_2 coatings, which in turn increases the visible light-driven photocatalytic activity (Li *et al*., 2023). Depending on the particular dopant chemistry, dopant ions penetrate the anatase lattice during substitutional solid solution production and affect the amount of oxygen vacancies, either favoring or hindering the transition to rutile (Hanaor & Sorrell, 2011). By acting as electron donors and lowering oxygen vacancy concentrations, dopants with valence states higher than Ti^{4+} (such as Nb^{5+}, Ta^{5+}, or W^{6+}) often slow down the phase shift by reducing the mobility of oxygen ions needed for the structural rearrangement. On the other hand, dopants with lower valence states (such Fe^{3+}, Al^{3+}, or Cr^{3+}) produce oxygen vacancies for charge compensation. Depending on concentration and the ratio of improved diffusion to lattice stabilizing effects, this can either speed up or slow down transformation. Different structural features can result from the combination of donor and acceptor

dopants, which can produce charge compensation mechanisms that either raise or lower the concentration of native point defects. Codoping increases the concentration of oxygen vacancies in the TiO_2 lattice, as evidenced by Raman spectroscopy studies that reveal shifting in Raman spectra is due to defect structures within the material, specifically oxygen vacancies, rather than grain size effects (Gurkan *et al*., 2017).

Band gap energies significantly lower than those of pristine TiO_2 have been discovered in studies on transition metal-doped TiO_2 utilizing iron, cadmium, and cobalt, indicating the usefulness of metal doping for electronic structure engineering (Katal *et al*., 2016). These changes allow optical and electrical characteristics to be fine-tuned for specific uses. Synergistic effects between multiple dopants, such as Ti^{3+} and Fe^{3+}, can dramatically decrease the bandgap and lead to efficient photocatalytic performance in the visible light range, according to work by Khan *et al*., (2016) on the implications of doping on photocatalytic capabilities. Zhang *et al*., (2018) work on nitrogen and fluorine codoped colloidal TiO_2 nanoparticles showed that it is possible to achieve tunable doping levels between 1 and 7 atomic percent, with the degree of codoping being adjusted by systematically varying the amounts of precursors and reaction periods.

These codoped materials enable effective visible light induced photocatalysis because of their substantial red shifts in the band edge that extend into the visible range. While retaining structural features necessary for photocatalytic activity, the energy gap of such nitrogen-fluorine codoped systems was lowered to as low as 2.34 eV as opposed to 3.26 eV for pure anatase TiO_2. With the reduction potential of conduction band electrons positively altered to diminish undesired oxygen reduction while promoting target reduction events, their work highlighted the synergistic interactions between nitrogen and fluorine that tune band topologies. It is crucial to comprehend these structural alterations since they have a direct bearing on the optical and electrical characteristics that control photocatalytic activity. Band structure is impacted by lattice distortions, midgap states are produced by defects, and the material's basic electronic properties are determined by phase composition. Band gap engineering has found success with codoping techniques. According to Long *et a*l., (2012), the computed results show that dual doping TiO_2 with C and W greatly reduces the band gap which is effective in

degradation of organic dyes. Additionally, it was shown that band gap tuning of the TiO_2 system is feasible as the crystallite size decreased with increasing Au concentration and the band gap decreased from 3.09 to 2.78 eV through Au substitution into the TiO_2 lattice (Rajaitha *et al*., 2024).

According to analysis, substitutional doping raises the quantity of electron transfers and surface oxygen vacancies; however, the impurity level produced in some codoped systems can hinder charge separation, resulting in activity that is even lower than that of unmodified materials (Rajaitha *et al*., 2024).The difficulty in studying codoped TiO_2 is in maximizing structural characteristics to accomplish the intended electronic changes while preserving structural integrity and steering clear of undesirable characteristics like undesired secondary phases or high defect concentrations. These structural changes often interact in a complex way to produce the synergistic effects seen in many codoping systems, where the total effect is greater than the sum of the individual dopant contributions. Effective codoping techniques must take into account phase stability effects, charge compensation mechanisms, ionic size compatibility, and synthesis conditions in order to produce materials with improved functional qualities and structural stability.

The structural characteristics and electronic structures of anatase, brookite, and rutile phase TiO_2 nanoparticles have been studied recently theoretically using density functional tight-binding (DFTB) calculations. The results show that, in some circumstances, the brookite phase is energetically more advantageous at the nanoscale than the anatase and rutile phases (Qiu *et al*., 2020). These simulations showed that oxygen atoms preferentially live on the surface of nanoparticles, whereas titanium atoms preferred to cluster near their center. The band gap also showed a temperature dependency that was consistent with the experimental evidence that was available. Gaining an understanding of these basic kinetic and thermodynamic concepts lays the groundwork for creating efficient doping schemes that control phase stability

Shaikh *et al*., (2024) study on nitrogen and sulfur codoped TiO_2 nanoparticles used both experimental characterisation and DFT simulations to shed light on defect engineering techniques. Their research showed that dual non-metal doping produces a number of

defect states in the band gap, which together improve the efficiency of charge carrier separation and visible light absorption. Since each dopant contributes unique electronic states that widen the total photo response spectrum, the synergistic effects were ascribed to complimentary alterations of the valence band structure. The most practical method for expanding TiO_2 photoactivity into the visible light spectrum is band gap engineering through the formation of intermediate states, according to thorough evaluations of metal-doped, non-metal-doped, and codoped TiO_2 systems (Perumal *et al*., 2019). Since too deep trap states can act as recombination centers instead of aiding in charge separation, the location and distribution of these intermediate levels are crucial in determining the overall photocatalytic efficiency. To maximize the improvement of photocatalytic activity, optimal defect engineering necessitates a careful balancing act between defect concentration, spatial distribution, and energetic placement. Electrochemical impedance spectroscopy in conjunction with UV-visible and electron paramagnetic resonance spectroscopies has been used in studies of tungsten and nitrogen codoped TiO_2 to investigate charge carrier dynamics and band structure. Codoping alters the distribution of density of states as well as the kinetics of charge carrier production, separation, and transfer processes, according to these thorough characterization techniques (Khan *et al*., 2016). The effective band gap is reduced and visible light photoexcitation is made possible by the addition of tungsten, which produces deep donor levels below the conduction band, and nitrogen, which produces acceptor levels above the valence band.

Various structural configurations that result in charge carrier separation, charge transfer, and extension of light absorption into the visible range exhibit varying degrees of photocatalytic enhancement, according to research on silver-doped and decorated TiO_2 nanocomposites that has investigated the relationship between photocatalytic efficiency and charge carrier separation mechanisms (Kaur & Singh, 2007). While substitutional doping produces scattered defect sites throughout the material that can act as charge carrier traps dispersed throughout the photocatalyst volume, noble metal surface decoration can produce Schottky barriers that promote electron transfer from TiO_2 to metal nanoparticles. Defect engineering can produce materials that absorb the entire visible light spectrum with optical band gaps ranging from roughly 1.9 eV at the surface to 3.2 eV in the core material. This is due to introduced defect concentration

gradients, according to research on reduced TiO_2 materials, including the extensively researched black TiO_2 (Naldoni *et al*., 2012; Chen *et al*., 2011). While preserving core regions with the essential electrical characteristics for charge carrier separation and transport, these gradient architectures allow for effective light harvesting. By offering intrinsic active sites for proton reduction and water oxidation processes, defect-engineered TiO_2-based cocatalyst-free hydrogen production systems have shown that suitable defect engineering can do away with the necessity for costly noble metal cocatalysts.

A thorough review of defective TiO_2 containing oxygen vacancies was given by Pan *et al*., (2013), who emphasized the need of controlled synthesis and knowledge of defect characteristics in maximizing photocatalytic applications. Their research shown that oxygen vacancies can provide active sites for catalytic reactions, improve charge carrier dynamics, and increase light absorption all at once. However, large vacancy concentrations can result in charge carrier recombination centers, which reduce overall performance. Since the pioneering work of Asahi *et al*., (2001) showed that nitrogen doping can lower the band gap for photoexcitation, allowing absorption of visible light from the solar irradiance spectrum and leading to significantly improved photocatalytic performance, it has attracted extraordinary attention as a defect engineering technique. Using variable-temperature synchrotron X-ray powder diffraction, Suter *et al*., (2021) conducted thorough structural analyses that demonstrated close connections between subsurface oxygen vacancies, nitrogen doping concentrations, and photocatalytic performance in rutile, anatase, and mixed-phase TiO_2 systems. These investigations revealed that highly doped anatase displays peculiar anisotropic thermal expansion behavior, which is indicative of the production of oxygen vacancies and the incorporation of nitrogen. This information is vital for understanding the links between structure and activity.

A new cubic titanium oxynitride phase appears for highly nitrogen-doped anatase materials, according to advanced characterization. This phase offers basic explanations for the observed shifts in absorption wavelength that allow for superior photocatalysis when exposed to visible light (Suter *et al*., 2021). High-level nitrogen doping causes a crucial structural change in the creation of this titanium oxynitride phase, with the cubic

structure displaying lattice characteristics halfway between those of titanium(II) oxide and titanium nitride end-members. Through extensive diffraction research, the existence of this phase has been conclusively determined, clearing up long-standing uncertainties about the structural effects of nitrogen incorporation.

Numerous studies have examined the electronic components influencing nitrogen-doped TiO_2's photocatalytic activity, and it has been generally agreed that nitrogen doping solves the slow response to visible light and ineffective separation of photo induced electron-hole pairs that essentially impair the performance of pristine TiO_2 (Zhu *et al*., 2021). According to theoretical work by Di Valentin *et al*., (2004), nitrogen-doped TiO_2 shows enhanced visible light harvesting capabilities through changes in the electronic band structure, with nitrogen atoms replacing oxygen to create localized states about 0.1-0.7 eV above the valence band maximum. These states allow lower energy photons that correspond to visible light wavelengths to excite electrons from the valence band through intermediate levels into the conduction band. Zhu *et al*., (2021) conducted thorough reviews on visible light responsive nitrogen-doped TiO_2 photocatalysis, synthesizing results from multiple studies to demonstrate that nitrogen incorporation produces a number of advantageous modifications, such as improved charge carrier mobility, surface area enhancement, band gap narrowing, and oxygen vacancy generation. Under visible and solar light irradiation settings, the synergistic combination of these effects produces photocatalysts with significantly increased activity for pollutant degradation, water splitting, and antimicrobial applications. New information on nitrogen-doped TiO_2 synthesis and characterisation was recently revealed by Gutiérrez-Moreno *et al*., (2025), who discovered that bandgap values drop with nitrogen doping, enabling stimulation with visible light below 403 nm.

Defect-mediated electronic structure modifications have been directly demonstrated by characterization studies using electron paramagnetic resonance measurements, which have validated the formation of defects like interstitial ions and vacancies with unpaired electrons during nitrogen doping processes (Batzill *et al*., 2006). Ihara *et al*., (2003) study established the significance of oxygen vacancies in facilitating improved photocatalytic performance by showing that visible light active TiO_2 may be achieved by combining an oxygen-deficient structure with nitrogen doping. In addition to the

well researched nitrogen-metal codoping systems, a number of anion-cation codoping combinations have shown remarkable potential for electronic structure change and defect engineering. Studies on fluorine and calcium codoped TiO_2 have shown a number of beneficial synergistic effects, such as increased surface acidity, oxygen vacancy formation, and active site growth, as well as the formation of an impurity energy state located about 2.0 eV below the TiO_2 conduction band (Li *et al*., 2014). This intermediate state preserves favorable energetics for photocatalytic redox processes while extending the photo response into the visible light area by efficiently shortening the electron excitation path and lowering the energy needed for photoexcitation.

Complex interactions between the cationic calcium dopant, which occupies titanium sites and alters the crystal field environment, and the anionic fluorine dopant, which replaces oxygen and produces local electronic perturbations, are the mechanisms behind the improved performance of fluorine-calcium codoped systems. These adjustments' complimentary qualities produce a synergistic effect in which the total impact surpasses the sum of the contributions of the individual dopants. While calcium doping modifies the energetic location of defect states and improves the stability of the changed electronic structure, fluorine inclusion has been demonstrated to increase the concentration of oxygen vacancies through charge compensation mechanisms. Research on boron-doped TiO_2 for improved Z-scheme anatase/rutile heterojunction photocatalysts showed that adjusting the amount of boron dopant can effectively modify the band structure and oxygen-vacancy content (Zhang *et al*., 2023). The study highlighted that band gap engineering mediated by oxygen vacancies by boron doping produces synergistic effects in heterophase junction systems, with both defect and interfacial properties enhancing photocatalytic performance. Using DFT calculations, recent studies by Manzoor *et al*., (2025) showed that different dopants provide unique alterations to the electronic structure and optical absorption properties. These studies carefully investigated a variety of dopants, including fluorine and chlorine.

By adjusting the electronic structure and surface chemistry, suitable codoping techniques can optimize materials for particular applications, as shown by research on copper and phosphorus codoped TiO_2 for hydrogen synthesis from seawater (Lin *et al*.,

2024). In these systems, transition metal and non-metal dopants combine to produce materials with improved charge carrier separation, increased absorption of visible light, and advantageous surface characteristics for water splitting processes. Likewise, studies on iron and nickel codoped TiO_2 made by alcohol-thermal techniques have demonstrated encouraging uses in hydrogen evolution through water splitting when exposed to visible light. The particular metal combination chosen was chosen to maximize both light absorption and proton reduction catalytic activity (Waghchaure *et al.*, 2024).

Although later research has shown that achieving true passivation is more difficult than first suggested, Gai *et al*., (2009) work on passivated codoping showed through first principles calculations that charge compensated donor-acceptor pairs can successfully narrow the TiO_2 band gap while maintaining charge neutrality. Research on different metal and non-metal codoping combinations has repeatedly shown that choosing the right dopant pairs is essential for maximizing photocatalytic performance, with the types and concentrations of defects produced being determined by the dopants' combined chemical makeup, ionic radii, electronegativity, and oxidation states. Defects in codoped TiO_2 materials must be accurately characterized and quantified in order to comprehend structure-property correlations and direct future material optimization. To investigate various aspects of defect structure, a variety of complementary characterization techniques have been used, such as X-ray diffraction for phase identification and changes in lattice parameters, X-ray photoelectron spectroscopy for chemical state determination and surface composition analysis, electron paramagnetic resonance for the detection of unpaired electrons and paramagnetic defects, optical spectroscopy for the identification of defect states and band gaps, and charge carrier dynamics and interface properties.

By identifying temperature-dependent lattice distortions linked to oxygen vacancies and facilitating the identification of secondary phases like titanium oxynitride that form during high-temperature nitrogen doping processes, XRD investigations have proven especially useful for examining the relationship between oxygen vacancy imperfections and nitrogen dopant impurities in titanium (iv) oxide catalyst (Suter *et al*., 2021). According to these investigations, the degree and directionality of changes in the lattice

parameter correlate with photocatalytic activity, and anatase phase materials show anisotropic thermal expansion behavior that can act as a fingerprint for subsurface oxygen vacancy concentrations. variations in surface species, such as Ti^{3+} , Ti^{4+} , oxygen ions, oxygen vacancies, and hydroxyl groups, were discovered through their study utilizing X-ray photoelectron spectroscopy. Moderate doping promoted the creation of charge trap centers while preventing charge recombination centers. Recent studies on the dual roles of oxygen vacancies in TiO_2/Bi_2O_3 composites by Luo *et al*., (2025) used a combination of experimental and DFT methods to show that a controlled distribution of oxygen vacancies improves persulfate activation and carrier separation for advanced oxidation processes.

Total oxygen vacancies characterize total defect concentrations regardless of depth distribution (Henderson, 2011). Analyses have revealed that very large bulk vacancy concentrations extend beyond the surface region of the anatase (101) surface, which is proportionately most active for photocatalysis. First-principles DFT studies analyzing the formation energies of several oxygen vacancy sites have confirmed these results.
Direct viewing of surface flaws in photocatalytically active anatase facets has been made possible by advanced transmission electron microscopy techniques, including as scanning transmission electron microscopy and high-resolution imaging. In their thorough analysis of oxygen vacancies, Katal *et al*., (2023) highlighted that by introducing controlled concentrations of oxygen vacancies, strategic defect engineering using electron beam irradiation and other techniques can greatly increase catalytic activity, electron transport efficiency, and stability. This result highlights how crucial it is to describe flaws across the material's volume rather than just its surface characteristics.

Defect engineering using codoping aims to significantly improve photocatalytic performance for a range of uses, including as CO_2 reduction, water splitting for H_2 gas release, pollutant degradation, and antimicrobial disinfection. Several investigations have shown that under visible and solar light irradiation circumstances, carefully designed flaws in codoped TiO_2 materials can provide photocatalytic activity that are orders of magnitude higher than those of pure TiO_2. The increases in light absorption, charge carrier separation, surface reactivity, and stability under operating

circumstances all work together to improve performance. Clear links between defect engineering techniques and photocatalytic performance metrics have been established by thorough reviews that look at codoped TiO_2 photocatalysts dye mineralization. These reviews have synthesized findings from hundreds of studies (Schneider *et al*., 2014). According to these analyses, the best results are usually obtained with moderate dopant concentrations, which minimize the negative impacts of excessive doping that can result in recombination centers while maximizing the positive effects on light absorption and charge separation. The most promising methods for attaining improved photocatalysis are metal-nonmetal codoping and TiO_2 nanostructured hybrids, according to work by Perumal *et al*., (2019).

Defect engineering is a crucial materials level strategy that needs to be combined with suitable reactor design, operating condition optimization, and system integration in order to achieve practical implementation, according to studies on material creation and reactor designing for titanium (iv) oxide catalysis in carbon dioxide reduction (Li *et al*., 2016). The thermodynamics and kinetics of carbon dioxide activation and reduction are directly impacted by the electronic structure changes brought about by codoping. Properly positioned intermediate energy levels enable the multi-electron transfer processes necessary for converting carbon dioxide into useful fuels and chemicals. Fundamental mechanisms by which defect engineering improves performance have been clarified by research on charge carrier dynamics and optical characteristics in titanium (iv) oxide and titanium (iv) oxide based heterojunction photocatalysts (Schneider *et al.,* 2014). Defect engineered TiO_2-based photocatalysis systems have shown promise in tackling important ecological transition issues.

Excellent photocatalytic performance and optical limiting applications were demonstrated in recent work by Shaikh *et al*., (2024) on nitrogen-sulfur codoped TiO_2. The combination of experimental results and DFT insights confirmed that defect engineering produces advantageous electronic structures for a variety of functional applications. According to research by Katal *et al*., (2024) on strategic defect engineering using electron beam irradiation, the controlled introduction of oxygen vacancies improves photocatalytic pathways for the mineralization of multicomponent

volatile organic pollutants, illustrating the usefulness of defect engineering in environmental remediation.

A band gap narrowing was seen in TiO_2 doped with sulfur (S) generated by oxidative annealing of titanium disulphide (TiS_2). When annealed at 600 °C, TiS_2 converted into Anatase TiO_2, with the S atoms occupying O-atom locations in TiO_2 to form the Ti-S bond, as seen in X-ray diffraction. TiO_2's absorption edge was moved to a lower energy area after sulfur doping. This was explained theoretically using ab-initio band calculations to be as a result of hybridization of the S *3p* states with the valence band (Umebayashi *et al*., 2002). In a different research work, Cravanzola *et al.*, (2017), Sulphur doped TiO_2 samples were generated by H_2S treatment at 623 K. Sulphur doping caused a red shift in the absorption edge of Sulphur doped TiO_2. This was explained as a result of Sulphur doping, which introduced extra extrinsic electronic levels. TiO_2's optical characteristics were improved by shifting its absorption edge to the visible light region. First principles calculations were used to obtain an appropriate doping model for rutile titanium Dioxide, through evaluating optical absorption spectra, density of states, geometrical parameters, dielectric functions, and electron densities for pristine, Rutile Titanium dioxide can be doped with carbon, Cr, or a combination of the two. In Ti-rich environments, carbon-doped structures are more stable, while Cr-doped and (Cr, C) codoped systems are more stable in O-rich situations. Co-doping with (Cr, C) results in higher energy absorption for incoming photons, as indicated by the imaginary component of the dielectric function. Furthermore, due to the big decrease in the direct bandgap, the red shift of the absorption edge in codoped systems is substantially larger than in Cr/C mono doped structures. The estimated absorption peaks reveal that rutile titanium dioxide with (Cr, C) codoping has greater photocatalytic performance in visible region (Chen *et al*., 2017).

Wu *et al*., (2014), used ab initio calculations density functional theory with Hubbard U (8.47 eV) on-site correction to investigate the photocatalytic processes of nitrogen doped anatase titanium dioxide. Using visible region, the charge density and electronic structural features of titania supercells with interstitial nitrogen, substitutional nitrogen, or oxygen deficiencies were evaluated to better understand the causes. According to the calculations, a large band gap reduction can only occur when substantial nitrogen

dopants are used. The photocatalytic degradation under visible illumination with little nitrogen doping is based on N-isolated dopant levels. The electronic structure of 2 x 2 x1 rutile supercell doped with double nitrogen was studied using first principles calculations. Exchange and correlation potential was treated using generalised gradient approximation where Plane wave ultra-soft pseudopotential method was used. Using the Monkhorst pack technique, a 2x2x7 K-grid was selected, and the cutoff energy was set at 300 eV. Analysis was done on how the three doping positions affected the band structure. When rutile was doped with N atoms, the band gap narrowed due to impurity states in the band gap, as seen by the band structure calculation. The optimized lattice parameters for undoped rutile are a = b = 4.594 Å. and c= 2.959 Å (Zeng *et al*., 2010).

Plane waves were expanded using a 30 Ry kinetic energy cut off, whereas charge density was expanded using a 16 times greater cut off. Monkhorst – Pack sampling and a 2 x 2 x 1 grid of k - points were used to sample the irreducible Brillouin zone. The bulk structure of anatase TiO_2 was first optimized, yielding lattice parameters a = 3.816 Å, c = 9.513 Å, which matched experimentally observed values. The band gap was filled with an empty *2p* states of N atom when nitrogen dopant was added on the (001) surface, which is consistent with other nitrogen doping studies made. It was discovered that interstitial and substitutional nitrogen implantation differed in some ways. Deposited metals contributed mostly in the band gap energy range, either at the top of the valence band or, in some instances, at the bottom of the conduction band, with their electronic states. P - type impurity states were mostly towards the valence band top, whereas n - type impurity states were on the conduction band edge (Batalovic *et al*., 2020)

Metal ions have also been employed to dope TiO_2 systems, with interesting results on the band gap. Doping TiO_2 with Mg via the sol-gel process resulted in a reduction in the energy band gap of TiO_2, making it more efficient in the utilization of visible light, and the material acquired the property of ferromagnetism at room temperature (Prudhvi & Bhaskar, 2017). Prabu and Anbarasan, (2014) prepared and characterized Ag, Mg and Bi doped TiO_2 nanoparticles for photovoltaic application using an acid modified sol-gel technique. The UV-visible and photo luminesce data revealed that the absorption edge shifted towards the visible light area, making the red shift more evident.

Nguyen *et al*., (2014) used DFT to investigate the effects of metallic X dopants (X = Mg, Ca, Zn, W, Al, Nb, and Be) on the electronic structure of Anatase TiO_2. The dopants introduced electronic structure alterations improving the photovoltaic characteristics of the X doped TiO_2 based dye sensitized solar cell (DSSC) and hence determining the photoelectric efficiency of the device. The implications of dopant ions on M-doped TiO_2 nanoparticles (M = Cu, Zn) produced by the sol–gel approach revealed that the doping ions enhanced the absorption edge wavelength by decreasing the bandgap energy of TiO_2 nanoparticles. In general, doped TiO_2 nanoparticles outperformed undoped TiO_2 nanoparticles in terms of photocatalytic activity. The photocatalytic activity of Cu doped TiO_2 nanoparticles was the best (Khairy & Zakaria, 2014).

Transition metals and lanthanides elements have also been used as TiO_2 doping ions with direct effects on its band gap. Rh dopants introduced states at the valence band minima and an intermediate band on rutile, causing a red shift in its optical absorption edge, as indicated by ab initio calculations and experimental observations. Codoping with Nb leads decreased the band gap by 0.5eV accompanied by elimination of band gap states, making the Rh, Nb codoped TiO_2 a more efficient and stable photo catalyst (Ghuman*et al.,* 2013). DFT calculations on Lanthanide optical absorption coefficient revealed that Lanthanide dopants extends TiO_2 optical absorption to the visible light range (Mulwa *et al.*, 2016). The X-ray diffraction patterns of undoped and Pd doped TiO_2 showed no significant effect on the particles sizes and there was no new crystalline phase formed (Ahmed *et al*., 2013). Also, the photocatalytic process of the Pr doped TiO_2 synthesized through sol gel method was found to be more than that of pure TiO_2 (Joanna *et al*., 2016).

Mohamed & Ulrich, (2020) studied the optical and electronic characteristics of transition metal doped TiO_2 nanotubes for photocatalytic and spintronic and applications using hybrid density functional theory. The TiO_2 nanotubes (TNTs) were doped through substitution of titanium ion with a transition metal ion to enhance their photocatalytic activity. These photocatalysts would also find application in clean fuel production. The Vienna ab initio simulation tool was used to do all of the calculations, which used plane-wave pseudopotentials. Yu *et al.*, (2012) DFT computations were

utilized to investigate the electrical and optical characteristics of Mo-doped titanium dioxide with imperfections. In both anatase and rutile forms, oxygen vacancies or interstitial Mo dopant atoms is explored systematically because imperfections are generally distributed in undoped or doped titanium dioxide. The magnetic moment and spin polarization of Mo-doped Titanium dioxide will be reduced by oxygen vacancies associated with the Mo dopant atoms or interstitial Mo. Furthermore, oxygen deficit had a detrimental effect on Mo-doped titanium dioxide photocatalytic performance.

Zhang *et al.,* (2015) prepared N and Ca co-doped TiO_2 sheets, and found out by X- ray photoelectron spectroscopy and X- ray diffraction that N and Ca codoped TiO_2 has higher crystallinity than N- doped TiO_2, as well as that N and Ca atoms were successfully codoped into TiO_2 as interstitial N and interstitial Ca or an O–Ti–N structure, respectively resulting in increased separation ability of photo- induced holes and electrons as well as the photocatalytic effect of TiO_2. Using density functional theory calculations, Xie *et al*., (2018) studied the electronic and optical properties of the rare earth metal doped anatase. For pristine anatase, the optimal lattice constants were a = b = 3.776 Å and c = 9.486 Å The 2*p* orbitals of O atom dominate the valence bands of pristine anatase with a little contribution from the 3*d* levels of Ti atom. The Ti 3*d* levels dominate the conduction bands, with a little influence from the O 2*p* levels. The introduction of dopant ions into the crystalline compound causes structural deformation as well as changes to titanium (iv) oxide electronic properties, such is the introduction of impurity levels into the band gap and changes in the valence and conduction band edges. Variations in electrical properties significantly affect the photocatalytic activity of Titanium dioxide. Because of its tiny band gap and high optical absorbance, titanium dioxide doped with Ce or Pr is the more preferred photocatalyst.

Khan *et al.,* (2018) analyzed the electronic properties and optical characteristics of titanium dioxide doped with indium. Because of the high formation energy of the indium interstitial defects in the host lattice, substitutional locations were the most likely location for indium dopant. The excitation wavelength of titanium dioxide was pushed towards visible range when Ti was replaced by an in dopant atom in the pristine anatase titanium dioxide. By producing in 5*p* levels, indium doping modified the band

structure of titanium dioxide. indium doping changed titanium dioxide's band structure by generating *5p* levels. The band gap has decreased as a consequence of the efficient coupling of the in *5p* states with the O *2p* orbitals. Raising the optical absorbance was increased by increasing the dopant concentration in titanium dioxide. Indium doped titanium dioxide model was created by compensating the charge imbalance using oxygen vacancies. The absorption edge of titanium dioxide was extended to the blue area and the band gap was widened owing to the creation of oxygen vacancies. The ideal concentration of dopant in titanium dioxide for the best band structure for photo-electrochemical applications and a consistent geometrical arrangement throughout the simulated systems was 2.08 percent.

Jin-Gang *et al*., (2015) used ab initio calculations with the screened hybrid functional Heyd-Scuseria-Ernzerhof 06 (HSE06) and generalized gradient approximation functional Perdew-BurkeErnzerhof (PBE) to examine the optical characteristics, formation energies, and electronic structures for alkaline earth metal doped Anatase TiO_2. The results indicated that the replacement of a lattice Ti atom with an alkaline earth metal dopant atom has higher energy under O-rich growth conditions than those of Ti - rich cases. In addition, the analysis of the band structures suggested that, alkaline earth metal dopants moved the valence bands to higher energy. The impurity states of the dopant ions of Ba, Ca, and Sr, are quite higher than the top of valence bands while Mg and Be dopants resulted into spin polarized dopant states near Fermi levels. Alkaline earth metal dopants introduce inter band states which make the TiO_2 more efficient in solar cell application. More significantly, because the absorbance edge shifts to a longer wavelength, alkaline earth metal-doped TiO_2 exhibits increased absorbance in the visible light area. In the visible light spectrum, the Ba, Sr, and Ca dopants exhibit superior absorption compared to the Mg and Be dopants while Mg and Be doping increased the absorbance of TiO_2 in the IR region more than Ba, Sr and Ca doping.

According to first principles calculations, the electronic interaction of Pt and N in TiO_2 enhances the mobility of current carriers, boosting photocatalytic activity (Kim *et al*., 2014). The properties of Co-N codoped TiO_2 were examined using DFT calculations. Due to the band gap narrowing and the insertion of impurity bands between valence bands (VBs) and conduction bands (CBs), the Co-N codoped system's light absorption

capability increased noticeably(Zhao *et al*., 2017). First principles calculations reveal that charge compensation does occur in the (Ta^{5+} , Ga^{3+} /In^{3+}) and (Mo^{6+} , Zn^{2+} /Cd^{2+}) codoped TiO_2, and with respect to cation single doped TiO_2, the bandgap is greatly reduced and the mid-gap states are passivated (Long & English, 2011).

Copper doped anatase titanium (iv) oxide, which only has one oxygen vacancy for compensation, and a reduced crystal structure with two oxygen vacancies, was examined by Mathew *et al*.,2018. The findings indicated that, in the ground state system, the Cu^{2+} ion's empty third state is located above the titanium (iv) oxide host's conduction band minimum (CBM), indicating that the dopant doesn't affect the size of the band gap. But after the second oxygen vacancy forms, states appear in the band gap. These states are produced by decreased Cu^{+} and Ti^{3+} ions, which have the potential to serve as recombination sites and lower photocatalytic activity. The reduced system also exhibits copper-derived states at the valence band edge, which narrows the band gap and extends the VBM to higher energies. In virgin titanium (iv) oxide, the Ti *3d* dominated conduction band area and the traditional O *2p* dominated valance band region. The DOS and PDOS of Mg-Nb codoped TiO_2 indicates that there is no contribution to the band edges due to the Mg while *d*-orbital of Nb contributes to the conduction band edge (Sasani *et al*., 2016).

Anatase TiO_2 nanoparticles' structure, stoichiometry, and photocatalytic activity were examined in relation to Fe doping by (Gharagozlou & Bayati, 2014). Fe doping was found to significantly increase the photocatalytic capacities of anatase TiO_2 by creating oxygen vacancies and Ti^{3+} defects. Realpe Jimenez *et al*., 2021, observed that codoping TiO_2 with Fe and N dual dopants improved morphological and optical properties. When compared to the outcomes of doping with a single element, this is explained by the low rate of charge carrier recombination and the large visible photocatalytic yield brought about by the codopant elements' synergistic impact. For example, in Fe-N codoped titanium (iv) oxide, the N atom's ionic radius is roughly equal to the O atom in the titanium (iv) oxide lattice structure, causing the N *2p* orbital to combine with the O *2p* states, changing the valence band's electrical structure and facilitating the easy migration of charge carriers. As a result, using both a metal and a non-metal as codoping materials can effectively modify TiO_2 for visible light sensitivity. According to Sarano

et al., (2021), doping TiO_2 with iron increases absorption in the visible light spectrum. Both visible and ultraviolet light are absorbed by the Fe doped titanium (iv) oxide samples. Increased absorption in the visible light range was observed in the diffuse reflectance spectra of all Fe doped titanium dioxide nanostructures. This increase was further evidenced by an increase in the molar Fe: Ti relationship, which is brought on by the electron transition from the O *2p* states in the valence band (VB) to the conduction band (CB), which is made up of Fe *3d* orbitals and results in a notable drop in the band gap energy of titanium (iv) oxide. Therefore, by injecting impurity or defect energy level through crystal lattice flaws and inducing local states below the conduction band edge, doping Fe^{3+} causes this redshift and narrows the band gap. Doping titanium (iv) oxide with Fe $^{3+}$ ions adds more energy levels of Fe^{3+} or Fe^{4+} ions to the titanium (iv) oxide band gap, but it does not alter the location of the titanium (iv) oxide valence band edge. DRS tests were performed to assess the calcium doped titanium (iv) oxide photocatalysts energy structure and optical characteristics. CaTi0 and CaTi5 had absorption edges of roughly 395 nm and 420 nm, respectively. As a result, pristine titanium (iv) oxide photocatalyst primarily absorbs UV radiation. Additionally, the inclusion of calcium dopants shifted the absorption edge of pure titanium (iv) oxide to the visible light spectrum. The observed shift probably improves the photocatalytic efficiency of calcium-doped titanium (iv) oxide under visible light. For the calcium doped titanium (iv) oxide photocatalysts, the band gap energy (Eg) could be estimated by plotting (αhv) (1/2) against photon energy (hv). The energy band gaps of CaTi0 and CaTi5 are 3.1 eV and 2.9 eV, respectively. In accordance with the adsorption edge trend, the calcium doped titanium (iv) oxide photocatalyst energy band gap decreased, which may be the cause of the elevated photocatalytic activity under artificial sunlight illumination(Sajjadi & Hosseinzadeh, 2025).

Ren *et al*., (2020) looked into how titanium (iv) oxide NPs could be modified for visible light photocatalysis by codoping with Er and Ce. The findings demonstrated that efficient electron and hole separations are not possible when the concentration of the Er and Ce dopants is less than the ideal level. Catalytic efficiency is decreased when the dopant ratio exceeds the ideal concentration because this results in a higher surface barrier and narrower space charge regions. Furthermore, compared to the undoped titanium (iv) oxide photocatalyst, the absorption edge of all codoped materials shows a

noticeable red shift, indicating that the band gap of the codoped photocatalyst has considerably shrunk. This is connected to the Ce^{2+} ions' partially occupied *4f* and *5d* orbitals. The characteristic electron orbitals can lower the rate of electron recombination and reduce the band energy gap by providing new energy levels. Photocatalytic activity would rise as a result.

Realpe Jimenez *et al*., (2021) investigated the optical properties of diffuse reflectance for both pure TiO_2 and TiO_2 codoped with Fe and N in the 200–800 nm wavelength range. At wavelengths shorter than 400 nm, unmodified TiO_2 displayed a wide absorbance band, indicating that its photoactivity is limited to the UV region of the spectrum. However, the absorption band shifts toward wavelengths longer than 400 nm for codoped materials, and this shift is bigger when the concentration of Fe^{3+} rises while N stays the same. Consequently, lower energy photons can be used to stimulate the modified samples' valence band. Conversely, absorbance falls as N concentration rises while Fe remains constant. According to the DFT research, the solitary vacancy that Cu creates in the Cu^{2+} (CuO) state only occurs on the surface and has very little effect on altering the material's band gap in terms of moles. However, the Cu dopant (Cu^{+} state) creates a dual vacancy that modifies the material's band gap and adds several trap sites in between. The overall band gap energy is decreased even though the trap locations might serve as recombination hotspots. Cu's coexistence in the +1(Cu_2O) and +2 (CuO) oxidation states was demonstrated by XPS analysis, and Cu^{+} is the main species in the sample that is inevitably responsible for the sample's obvious variations in optical properties (Mathew *et al*., 2018).

By creating a highly hydrophilic and distributed Zn-TiO_2/reduced graphene oxide (rGO) (HTGZ) nano-system with remarkable visible light catalytic activity, Lu *et al*., (2023) aimed to overcome the drawbacks of titanium dioxide NPs. A faster photodynamic reaction results from the HTGZ's improved synthesis of reactive oxygen species, quick electron transfer, and lowered energy barrier. On the one hand, the carbonaceous species on the surface of HTGZ became sensitized to visible light irradiation. It led to the electrons moving to titanium (iv) oxide's conduction band.

Zn^{2+} ion doping adds additional defects and impurity energy levels. More charge carriers could be produced by increased optical absorption because of a narrower band

gap. However, in order to achieve more efficient division of photogenerated Pairs of electron-holes and limit their recombination, rGO can function as an acceptor in electron transfer, receiving photogenerated electrons on titanium (iv) oxide photocatalyst. Together, these elements increase the yields of reactive oxygen species and support HTGZ's photodynamic potential in visible light.

Ab initio studies on ZrO_2 electronic structures also revealed a considerable reduction of bandgap on adding dopants (Khattab *et al*., 2021). First principle computations were used to investigate the doping effect of sulphur substitution on zirconium dioxide ZrO_2. The study shows that the existence of an impurity state of sulfur *3p* on the up spin of the valence band causes sulphur doping to dramatically decrease the band gap of doped ZrO_2 (Idrissi *et al*., 2021a).The Hubbard technique (DFT + U) was used to examine how doping with Nb and W affected the electrical and optical properties of pure ZrO_2. The bandgap edges shifted and the Fermi level reallocated when dopant atoms were added to the pure crystal structure. The band gap decreased from 5.79 to 0.89 eV for Nb-ZrO2 and to 1.33 eV for W-ZrO2 as a result of the Valence Band Maximum (VBM) migrating northward (Khattab *et al*., 2021).

A ZrO_2 supercell with 96 atoms (Zr = 32 and O = 64) was examined using DFT and the Vienna ab-initio simulation software (VASP). The impact of varying amounts of Al and Cu doping components (1.05%, 2.10%, and 3.15%) on the charge transport behaviour was studied. According to the DOS calculations, increasing the concentration of substitutionally doped Cu atoms increases the number of localized impurity states, which lowers the energy band gap and hence boosts ZrO_2 conductivity (Hussain *et al*., 2019). Zhang *et al*., (2014) examined the electronic properties of cubic ZrO_2 doped with C and F, C-codoped utilizing DFT-based first principles calculations. The valence band's breadth is widened by the impurity bands at its uppermost end, and C doping results in an apparent lowering of the band gap. It was shown that the photoluminescence intensity improved in Mg-doped nanocrystalline ZrO_2 thin films. The primary cause of this was the creation of oxygen vacancies (Salari & Ghodsi, 2017a; Salari & Ghodsi, 2017b). The research that was conducted by (Kenzhina *et al*., 2025) revealed that the substitution of Zr^{4+} ions (0.84 Å) with Y^{3+} (0.90 Å) led to an increase in oxygen vacancies. The creation of more oxygen vacancies in the lattice

caused the crystal structure to stabilize, resulting in the formation of the tetragonal phase t-Zr(Y)O_2.

Zirconia stabilization at high temperatures was noted in a theoretical research that employed yttrium as a dopant in a (2 x 2 x 1) c-ZrO2 supercell. Additionally demonstrated were the creation of oxygen vacancies and the synergistic effects of yttrium doping (Gul *et al*., 2017). The creation of oxygen vacancies on the surface of zirconia (111) was carefully investigated utilising periodic DFT methods. It was shown that oxygen vacancies can significantly affect the surface characteristics of zirconia. According to theoretical models, adding calcium significantly sped up the process of removing a surface oxygen atom and creating a vacancy, which required a significant amount of energy (De Souza & Appel, 2021).

Lattice oxygen vacancies and the evolution of energy levels in the Mo-TiO_2 framework were examined using DFT calculations. The most stable location for the formation of an oxygen vacancy was an equatorial Mo-dopant site. According to the findings, Mo-TiO_2 is an ideal choice for the manufacture of indoor construction materials with light active antimicrobial properties (Kumaravel *et al*., 2020). Electronic characteristics of codoped F-Zr anatase analysed using GGA + U calculations revealed that in TiO_2 photocatalysts. Both the F dopant and the oxygen vacancy generated Ti^{3+} gap states. The impact of oxygen vacancies showed that enhancing photocatalytic efficiency requires the interaction of dopants and oxygen vacancies (Long & English, 2010). UV-visible investigations showed that 1% Ni doping increased the optical band gap, but as the Ni dopant concentration increased to 3-5%, the bandgap narrowed due to the formation of oxygen vacancies and interstitial sites between the valence and conduction bands (Kumar *et al*., 2020). Chiara *et al*., (2014) studied Cerium doped ZrO_2, and found it to be a photocatalyst active in the visible light region. The charge carriers produced by photo induced photolysis were confirmed by ab initio studies to be as a result of availability of empty *4f* Ce states at the midgap in the solid, which acts as intermediate states in the double excitation mechanism. The solid was classified as a third generation photoactive material. Idrissi *et al*., (2020) used the density functional theory calculations under Quantum Espresso software to analyse the doping effect of sulfur substituting on the zirconium (iv) oxide. The sulfur doping concentrations employed

were: 5%, 9%, 14%, and 18%. These concentrations were below the percolation threshold. The effect of S - doping on pure zirconium (IV) oxide was studied using the gradient generalized approximation GGA. The substitutional S-impurity added to the zirconium (iv) oxide changed the doped material electronic structure, according to the findings of the ab initio density functional theory investigation. Garcial *et al*., (2006) calculated the optimal structure for m-ZrO_2, the optimized lattice parameters are for monoclinic crystal structure are a = 5.12 Å, b = 5.16 Å, c = 5.33 Å, and □ = 99.6. The band gap of monoclinic zirconia without on-site Coulomb interactions is 3.60 eV, which is substantially smaller than the observed result (5.8 eV). By including the Coulomb interactions of *4d* states on Zr atoms and *2p* states on O atoms, we can reproduce the reported band gap value.

Terki *et al*., (2006) used density functional theory to look into the electronic and structural features of ZrO_2 crystalline forms. The Kohn – Sham equations were solved using the (FP-LAPW) method. GGA approach was used to treat the exchange and correlation coefficients. The transition forces as well as the ground state parameters such as bulk modulus, lattice constants, and phase transformation stability were estimated. The optimal structures of monoclinic Zirconia are a = 5.15 Å, b = 5.21 Å, and c = 5.31 Å. The findings were in excellent accordance with previously published theoretical and experimental findings. On the basis of charge density estimates, the effect of deformation on crystalline structure was also investigated. Both the total and partial densities of states that enable the disclosure of orbital mixing features, were also provided. The results of PDOS and TDOS demonstrate that 2*p* orbitals of O atom dominate the top valence band, with energies ranging from 5 to 0 eV. Because of the hybridization with the O atom's 2p orbitals, it also has a minor amount of Zr-d orbitals. A portion of the Zr-d valence band is occupied, implying a partial Zr–O covalent connection, as shown by PDOS analysis of the Zr atom. The empty conduction band, which is comprised of Zr-d states, is isolated from the valence band by an energy gap. The band gap's width is determined by the energy of these levels. Calculations show that the band gap of monoclinic zirconia is 3.61 eV.

Using density functional theory (DFT), Luo *et al*., (2015) investigated the structures and catalytic activity of CO molecules on monoclinic ZrO_2 (111) (M = Ce, Ca, and Pr)

surfaces. The pseudo potential plane-wave CASTEP code was employed to do all of the calculations related to density functional theory. Perdew-Burke-Ernzerhof's (PBE) generalized gradient approach (GGA) was utilized to define exchange-correlation potential. All of our calculations employed a 300 eV cutoff energy. For the monoclinic ZrO_2 (111) surface, a Gaussian smearing of 0.01 eV was utilized. In all calculations, the Monk – horst - K-point mesh pack for the Brillouin zone sampling with a 3 x 3 x 1 mesh was employed. The 1.0×10^{-6} eV/atom energy of convergence criterion was adopted. The energy, force, and displacement convergence criterion for ideal geometry were 2.0×10^{-5} eV,5.0×10^{-2} eV and 2.0×10^{-3} respectively. The resulting lattice parameters from theoretical computations were as follows:$\beta = 90.23^0$,a = 5.1454 Å, b = 5.2075 Å, and c = 5.3107 Å. This was consistent with prior experimental and theoretical lattice constants. The band gap determined by first principle calculations was 4.021 eV, which was consistent with experimental findings. The Zr valence band edge on Pr-doped monoclinic ZrO_2 (111) surface shifts toward lower energy compared to undoped monoclinic ZrO_2 (111) surface when the density of states (DOS) of Zr site is analyzed. The catalytic behaviour of doped monoclinic ZrO_2 (111) surfaces toward CO oxidation has been studied, and it has been discovered that Pr doping significantly increased catalytic activity. Results from the density of states also reveal that the energy of carbon monoxide on Pr-doped monoclinic ZrO_2 (111) surface is the lowest.

Seema & Kumar (2015) examined the magnetic and electronic characteristics of undoped and doped monoclinic zirconium (iv) oxide (ZrO_2). All DFT computations were performed using the Perdew-Burke-Ernzerhof exchange-correlation potential-based Generalized Gradient Approximation (GGA). The computations only took into account the valence electrons, whereas the core electrons were characterized using norm-conserving pseudo-potentials built using the Troullier-Martins parameterization. The linear combination of orbitals wave functions was used to enlarge the valence wave functions. The conjugate gradient approach was used to perform geometric relaxations. To achieve well converged findings, the energy shift value of 0.001 Ry was chosen. All atomic sites were modified during the computations until the atomic forces were below 0.0016 Ry/Bohr. The finite real space grid for numerical integrals was defined using 250 Ry of energy. With corresponding concentrations ranging from 3.125 to 25%, substitutional doping of transition metals V, Cr, Mn, and Fe in zirconium (iv) oxide

was studied. All atomic sites and crystal structures were loosened following doping until the atomic forces were less than 0.0016 Ry/Bohr. Variations of the sides a, b, c, and angle beta (β) were used to compute the lattice constants, as well as the relaxation of inner atomic locations around the experimental value of the system parameters. The estimated lattice constants of pure Zirconium (IV) Oxide are $\beta = 99.37^{0}$, a = 5.164 Å, b = 5.239 Å, and c = 5.342 Å, which correspond well with previously published experimental and theoretical values. The conduction mechanism was largely dominated by *p* orbitals of O atom, as shown by the DOS plot. The valence band of zirconium (iv) oxide had few *d* orbitals of Zr, whereas the conduction band was mostly made up of the *d* orbitals of Zr atom. The calculated band gap of 3.60 eV for pure monoclinic zirconium (iv) oxide is in agreement with earlier theoretical findings. However, the experimental value was more than the calculated band gap energy. When transition metals were added, the *d* orbitals were introduced into the host material's band gap.

Pure and doped DOS curves reveal that the Zr and O atom levels for doped systems moved towards the Fermi level. The PDOS plot clearly shows that the transition O *2p* states and metal d states play a major role in the transition. metals dopant-induced impurity states (Seema & Kumar 2015). Cheng *et al.*, (2020) used a combination of utilizing both density functional theory and experimentation, the effects of adding iron dopant in the crystalline materials and electronic properties of zirconium (iv) oxide. Iron dopants caused the formation of tetragonal form of zirconium (iv) oxide and induced defect levels in the bandgap of iron doped zirconium (iv) oxide. The impurity states enhanced the light optical absorption of zirconium (iv) oxide to the area that is visible because of the coherence interaction between the electrons in the Fe 3*d* states and zirconium (iv) oxide pure electronic states. Iron doping narrowed the bandgap of the pure zirconium (iv) oxide, while maintaining a strongly negative conduction band potential. Since titanium dioxide (TiO_2) has so many uses in environmental remediation, photovoltaics, photocatalysis, and sensing technologies, it has become one of the most researched semiconductor materials. The chemistry of the material's defects has a major impact on its performance; one important defect type that considerably alters the material's electrical, optical, and catalytic capabilities is oxygen vacancies (V_0) (Pan *et al.*, 2023). Although pure TiO_2 has outstanding chemical stability and photocatalytic activity, its practical uses under solar irradiation are limited

by its broad band gap, which restricts light absorption to the ultraviolet range (around 3.2 eV for anatase) (Ni *et al*., 2007).

Point defects known as oxygen vacancies are created when oxygen atoms are extracted from the crystal lattice, leaving behind areas that are rich in electrons. These flaws are crucial in defining the optoelectronic characteristics of TiO_2 (Chen *et al*., 2013). Several techniques, such as high-temperature calcination, ion implantation, chemical doping, and plasma treatment, can be used to create oxygen vacancies. Oxygen vacancies have been shown to produce localised electronic states in the TiO2 bandgap, which usually occur below the conduction band minimum. These mid-gap states can have a major impact on charge carrier dynamics and act as centres for electron trapping (Henderson, 2011). As a result of the reduction of Ti^{4+} ions to preserve local charge balance, Ti^{3+} species are frequently formed in conjunction with oxygen vacancies (Chen *et al*., 2016). Oxygen vacancies in TiO_2 materials have been found and measured using a variety of analytical methods. Ti^{3+} states and oxygen deprivation are frequently detected using X-ray photoelectron spectroscopy (XPS) (Chen *et al.*, 2016). Unpaired electrons linked to oxygen vacancy sites can be directly detected by electron paramagnetic resonance (EPR) spectroscopy; these signals usually appear at g = 2.003-2.004 (Wang *et al*., 2023). Lattice parameter changes linked to the generation and distribution of oxygen vacancies can be detected by X-ray diffraction (XRD) investigations, especially variable temperature experiments (Rehman *et al*., 2021). When Ca^{2+} ions are added to the TiO2 lattice, the material defect chemistry is radically changed. Structural distortions and the need for charge correction result when Ca^{2+} (ionic radius ~1.00 Å) replaces Ti^{4+} (ionic radius ~0.61 Å) because to the size mismatch and charge discrepancy (Kumar *et al*., 2024).

According to the defect equilibrium, oxygen vacancies must arise in order to preserve electrical neutrality: When Ti^{4+} is substituted, $2Ca^{2+} \rightarrow V_0^{2+} + 2e^-$ Recent studies have validated this process experimentally. According to research, even in oxidizing settings, oxygen vacancy generation is naturally driven by the lower oxidation state of Ca^{2+} relative to Ti^{2+} (Wang *et al*., 2023). By varying the calcium doping level and synthesis conditions, these oxygen vacancies' concentration and distribution can be regulated. Ca-doped TiO_2 compounds frequently have unique morphological

characteristics. Ca-doped TiO_2 nano-sized polygon plates were synthesized recently by Wang *et al*., (2023), where the addition of Ca^{2+} ions affects crystal growth kinetics and produces distinct platelet morphologies. More active spots for photocatalytic reactions can be revealed and specific surface area can be increased by these morphological modifications. Comprehensive crystallographic studies have established the alterations in lattice parameters brought about by calcium doping and the resulting generation of oxygen vacancies (Kumar *et al*., 2024). Signals at g = 2.004, which are indicative of oxygen vacancy sites and Ti deficit in Ca-doped systems, have been detected using EPR spectroscopy (Wang *et al*., 2023). These spectroscopic fingerprints offer concrete proof of the doped materials' flaws.

The electronic band structure of Ca-doped TiO_2 is significantly altered by oxygen vacancies. These defects can function as intermediary levels between the valence and conduction bands by producing localized electronic states (Chen *et al*., 2013). This engineering of the band structure has a number of significant effects. The material can absorb visible light by successfully narrowing the optical bandgap by the creation of mid-gap states (Pan *et al*., 2023). This phenomenon expands TiO_2 photo sensitivity outside of the ultraviolet spectrum, which is essential for effective solar energy use. A wider spectrum of light absorption is enhanced by oxygen vacancies (Chen *et al*., 2016). New optical transitions brought about by the defect states raise absorption coefficients, especially in the visible light spectrum (400–700 nm). In charge carrier dynamics, oxygen vacancies have two functions. On the one hand, they may serve as recombination centers by capturing photogenerated electrons. However, by lowering the resistance during electron migration through the lattice, these imperfections can promote electron transport (Wang *et al*., 2023).

According to studies, charge transport resistance is decreased by carefully regulated oxygen vacancy concentrations, increasing total photocatalytic efficiency. Strategic oxygen vacancy creation can improve the Photogenerated electron-hole pair separation efficiency (Ahmad *et al*., 2023). These imperfections enhance the lifetime and availability of charge carriers for surface reactions by preventing fast recombination and serving as electron reservoirs and extra channels for charge migration. The creation of Ti^{3+} species is inextricably tied to the existence of oxygen vacancies (Chen *et al*.,

2016). These reduced titanium sites can take part in surface processes and act as electron donors. As a measure of the concentration of defects in the material, the Ti^{3+} concentration corresponds with the oxygen vacancy density. Photocatalytic water splitting for hydrogen production is one of the most promising uses of Ca-doped TiO_2 with oxygen vacancies. According to recent studies, the presence of oxygen vacancies significantly accelerates the evolution of hydrogen (Ahmad *et al*., 2023; Zhang *et al*., 2023). Oxygen vacancies efficiently absorb photogenerated electrons in Ca-doped TiO_2 systems and enable them to combine with water's H^+ ions to produce H_2 (Wang et al., 2023). By successfully creating oxygen vacancies in manufactured samples by replacing Ti^{4+} sites with Ca^{2+}, the photocatalytic hydrogen evolution reaction is directly aided.

According to Wang *et al*., (2023), Ca-doped TiO_2 with regulated oxygen vacancies can produce hydrogen at substantially higher rates than pure TiO_2. The combination of oxygen vacancy defects and the nanoscale polygon plate shape produces a synergistic effect that optimizes photocatalytic effectiveness. Together, the improved charge separation and increased light absorption increase the activity of hydrogen creation. One of the basic drawbacks of pure TiO_2 is its incapacity to efficiently use visible light, which is addressed by the introduction of oxygen vacancies through calcium doping (Asahi *et al*., 2001). The practical utility of TiO_2-based photocatalysts is greatly increased by the defect-induced band structure alterations that allow photocatalytic activity under visible light irradiation. But studies have also shown that there is a complicated link between photocatalytic activity and oxygen vacancy concentration (Chen *et al*., 2013). Excessive concentrations of defects can reduce ultraviolet-light responsive performance by producing too many recombination centers, even while oxygen vacancies can increase visible light-responsive photocatalytic activity. This result emphasizes how crucial it is to attain the ideal oxygen vacancy concentrations for certain uses.

Several synthesizing techniques have been used to generate Ca-doped TiO_2 with regulated levels of oxygen vacancies. Ca-doped TiO_2 can be created using sol-gel processes and thermal treatment using calcium precursors such calcium chloride ($CaCl_2$) or calcium nitrate (Zhang *et al*., 2023). The ultimate oxygen vacancy

concentration is strongly influenced by the environment and calcination temperature. Ca-doped TiO_2 nanostructures with regulated morphologies and defect densities can be synthesized using hydrothermal techniques (Wang *et al*., 2023). The oxygen vacancy concentration can be tuned by varying the reaction temperature, pH, and precursor ratios. In order to add oxygen vacancies to TiO_2 materials while preserving structural control, sophisticated wet-chemistry techniques have been devised (Pan et al., 2023). These techniques frequently entail the application of particular reducing agents during synthesis or reduction processes. In addition to direct synthesis, oxygen vacancy concentrations can be further altered by post-treatment techniques. Oxygen vacancy densities can be raised or lowered by high-temperature calcination in reducing, inert, or oxidizing atmospheres (Behara et al., 2023).

Defect concentrations are generally increased by annealing in hydrogen atmospheres or vacuum. Chen *et al*., (2016) showed that air plasma treatment increases the production of Ti^{3+} states and oxygen vacancies in TiO_2 thin films. This approach provides a quick and manageable way to engineer defects without substantially changing the bulk structure. There are various forms of TiO_2, but the most prevalent ones are rutile and anatase. Phase-to-phase variations in oxygen vacancy formation and consequences can be substantial (Henderson, 2011). Because of its higher photocatalytic capabilities, anatase TiO_2 has been the main target of calcium doping experiments. According to research, anatase Ca-doped TiO_2 with oxygen vacancies undergoes more advantageous band structure alterations than the rutile phase (Ni *et al*., 2007). The density and distribution of oxygen vacancies are significantly influenced by the calcium dopant concentration. Research has determined the ideal doping concentrations to optimize advantageous benefits and minimize harmful recombination processes (Wang *et al*., 2023). Phase segregation, the development of secondary phases (like $CaTiO_3$), or high defect concentrations that function more as recombination centers than as advantageous electron traps can all result from excessive calcium doping.

Recent studies have highlighted the synergistic interactions between several elements, such as Morphology and Defects. Wang *et al*., (2023) showed that the combination of oxygen vacancies and controlled morphologies (like nano-sized polygon plates) results in increased surface areas and better light absorption at the same time. Some crystal

facets have stronger catalytic activity and are more likely to create oxygen vacancies (Henderson, 2011). To optimize performance, one can take advantage of the preferential exposure of particular facets in Ca-doped TiO_2. Studies have demonstrated that, in contrast to single-element doping, the combination of calcium with other dopants (such as carbon, nitrogen, or other metals) can produce complex defect structures with better characteristics (Asahi *et al*., 2001; Chen *et al*., 2013). Long-term stability is a major issue with Ca-doped TiO_2 containing oxygen vacancies. Performance can deteriorate over time when ambient oxygen or water molecules gradually fill oxygen gaps (Pan *et al*., 2023). Behara *et al*., (2023) investigated methods to improve thermal stability, such as stabilizing the damaged structure by combining dopants like lanthanum with calcium. It is still difficult to strike the ideal balance between improved charge transport and oxygen vacancy induced charge trapping. Excessive flaws can become harmful recombination centers, whereas moderate oxygen vacancy concentrations enhance charge separation and transport (Chen *et al.,* 2013). Although technically challenging, precise control over defect density and distribution is crucial. It could be challenging to scale up several laboratory-size production techniques for Ca-doped TiO_2 with regulated oxygen vacancies for industrial use. For commercial application, it is necessary to overcome the practical hurdles of ensuring reproducible defect concentrations throughout large batches (Zhang *et al.*, 2023).

According to Chen *et al*., (2016), elements such as Fe and Co introduce extra electronic states from their d-orbitals in addition to oxygen vacancies. In contrast to alkaline earth metal doping with calcium, these may introduce more recombination centers even if they can improve absorption of visible light. The capacity of lanthanum and other rare earth metals to create oxygen vacancies while enhancing thermal stability has been investigated (Behara *et al*., 2023). But compared to calcium, these substances are less common and more costly. According to Wang *et al.*, (2023), calcium has a number of benefits, such as low cost, high abundance, low toxicity, and efficient oxygen vacancy creation without the introduction of complicated electronic states that can encourage undesired recombination. Two common methods for activating TiO_2 with visible light are nitrogen and carbon doping (Asahi *et al*., 2001). By adding dopant states above the valence band, these methods usually lower the bandgap. Although they work well, they also encourage the production of oxygen vacancies, and the interaction between

nitrogen doping and oxygen vacancies has been thoroughly investigated. A complementary strategy that mainly concentrates on oxygen vacancy engineering via charge compensation mechanisms is provided by calcium doping.

To comprehend oxygen vacancy behaviour under operating settings, future studies should use sophisticated in-situ and operando characterisation techniques (Rehman *et al.*, 2021). The kinetics of charge carrier entrapment and release at oxygen vacancy sites during photocatalytic processes may be revealed by time resolved spectroscopy techniques. Deeper understanding of the energetics of oxygen vacancy production, migration, and interaction with charge carriers in Ca-doped TiO_2 can be obtained using density functional theory (DFT) investigations and first-principles calculations (Kumar *et al.*, 2024). By forecasting ideal doping concentrations and synthesis conditions, computational research could direct experimental efforts. An important future path is the development of energy-efficient and environmentally friendly synthesis techniques for Ca-doped TiO_2 with regulated oxygen vacancies (Zhang *et al.*, 2023). Priority should be given to green chemistry techniques, lower temperature synthesis pathways, and less usage of dangerous chemicals.

2.4 Green Synthesis and Characterization

2.4.1 Green Synthesis Method

One innovative and incredibly effective way to produce NPs is through the green synthesis process.It is a current research focus that is very promising, simple, affordable and eco-friendly in contrast to other existing methods (Al-Zaqri *et al*., 2021). Previous research work reveals TiO_2 and ZrO_2 nanoparticles have successfully been green synthesized and used in various applications.

In green synthesis, cellular extracts of plants possess different phytochemicals serving as agents that reduce, stabilize, and cap (Coronell *et al*., 2022), which prevent agglomeration during the synthesis process, contributing to the correct size and shape of the nanoparticles (Santiago *et al*., 2023). Rao *et al.*, (2015) synthesized TiO_2 nanoparticles utilizing orange fruit peel extract. In the creation of TiO_2 nanoparticles, the polyols and phenolics in the orange peel extract served as reducing agents, and citric acid served as a stabilizer. Balashanmugam *et al*., (2014) biosynthesized silver

nanoparticles derived from orange peel extract. water-soluble organics found in orange peel components mostly reduced silver ions to nano-sized Ag particles. Due to non-toxicity and non-volatility, the aqueous biological extract is a suitable media for the nanoparticles' production (Sethy *et al*., 2020). The green technique is therefore a novel way of synthesising nanoparticles as it enhances environmental sustainability (Aslam *et al*., 2021).

Amanulla & Sundaram, (2019) successfully fabricated TiO_2 nanoparticles made using extract from orange peel. Green TiO_2 has been shown in antibacterial investigations to be more effective than chemically produced TiO_2 NPs against strains of both gram-positive and gram-negative bacteria. Orange peel contains soluble sugars and insoluble polysaccharides, Polyphenols operate as reducing agents, while carboxylic groups, amino acids, and citric acid stabilize the mixture (Torrado *et al*., 2011). Thus, orange peel extract is suitable for synthesis of more efficient photocatalytic degradation and disinfecting nanomaterials. TiO_2 NPs have been manufactured effectively utilizing environmentally friendly technologies. For instance, Ansari *et al*., (2022) Green generated TiO_2 NPs were evaluated for their photocatalytic and in vitro antibacterial properties using leaf extract from Acorus calamus. The green chemistry approach was used to successfully synthesis Fe-TiO_2 nanoparticles for possible use in the photocatalytic treatment of wastewater using an aqueous extract of lemongrass (Cymbopogon citratus) made by soxhlet extraction and doped with wet impregnation (Solano *et al*., 2019). Biosynthesized TiO_2 NPs using *Caricaceae* (Papaya) shell extracts were evaluated for antifungal applications (Saka e*t al*., (2022). Singh *et al*., (2022) effectively produced TiO_2 nanoparticles with extract from citrus lemons as a bio-capping agent to enhance dye-sensitized solar cells performance. TiO_2 nanoparticles made of *Cucurbita pepo* seeds extract and titanium trichloride ($TiCl_3$) solution were synthesized and characterized by Abisharani *et al*., (2019). Green TiO_2 nanoparticles made from Syzygium cumini extract were used to remove lead (Pb) from explosive industrial effluent catalytically. (Sethy *et al*., 2020). Ahmad *et al*., (2022) synthesized *Ocimum sanctum* leaf extract-mediated TiO_2 NPs and tested their wound healing ability in streptozotocin (STZ)-induced diabetic lesions in Wistar rats. Bhullar *et al.,* (2021) synthesized green TiO_2 NPs for medicinal purposes utilizing extracts of clove (Syzygium aromaticum), coriander (Coriandrum sativum), and black pepper

(Piper nigrum). Shanavas *et al*., (2020) created TiO_2 NPs with leaf extract from Phyllanthus niruri and examined their morphological, structural, and optical properties. Nanoparticles of titanium dioxide made with leaf extract from Cymbopogon Citratus and doped by silver photodeposition were used to test photocatalytic acetaminophen degradation (Coronell *et al*., 2022).

Shimi *et al*., (2022) effectively synthesized the green TiO_2 photocatalyst from *mulberry* plant extract for potential antibacterial activity and photocatalytic dye removal. Green production and antibacterial effectiveness of titanium dioxide nanoparticles was achieved by the use of *Luffa acutangula* leaf extract (Anbumani *et al*., 2022).Green synthesized TiO_2 NPs using extract from jasmine flowers as a stabilizing and reducing agent were characterized and their antimicrobial and photocatalytic capability evaluated (Aravind *et al*., 2021).TiO_2 nanoparticles are made in an environmentally friendly manner by replacing organic solvents with an aqueous extract solution of lemongrass leaves, which acts as a stabilizing and reducing agent. To alter the electromagnetic spectrum absorption range, the nanoparticles were codoped with N–Fe (Realpe Jimenez *et al*., 2021). The strongest optical absorption band at 350 nm was visible in the capture spectra of TiO_2 nanoparticles that were bio-synthesised using extracts from Carica papaya shells. The absorption peaks obtained were identical to those reported in previous investigations. With decreasing nanoparticle sizes, edges often shifted to higher energies or inferior wavelengths, according to the absorption. In order to create metallic nanoparticles and stabilize the environment, the phenolic groups inhibited agglomerations. This supports the idea that biological molecules have two functions in the creation and stabilization of TiO_2 nanoparticles in an aqueous medium (Saka *et al*., 2022).

A solution of zirconium oxychloride octahydrate and a green tea leaf extract were combined to create spherical zirconia nanoparticles, which were then heated to 90 °C, dried at 120 °C, and calcined for four hours at 550 °C. The photocatalytic and antimicrobial properties of the produced zirconia nanomaterials against five distinct pathogenic bacteria were tested (Kumari *et al*., 2023). In a different investigation, the antibacterial properties of *Thespesia populnea* extract coated nano zirconium on cotton gauze fabrics were investigated by Whangchai *et al*., (2023). Chau *et a*l., (2023)

produced zirconia nanoparticles using the aqueous leaf extract of *Laurus nobilis* (bay leaf) and tested the green synthesized nanoparticles for potential antibacterial efficiency against gram positive and gram negative bacteria. *Tinospora cordifolia* leaf extract was applied to synthesize ZrO_2 nanoparticles. The bio-based ZrO_2 nanoparticles were used as antibacterial and antifungal agents (Joshi *et al*., 2021). Annu *et al*., (2020), green synthesized ZrO_2 NPs using *Moringa oleifera* leaves for antioxidant and antibacterial evaluation. Chelliah *et al*., (2023), biosynthesized ZrO_2 NPs from a 0.1 M $Zr(NO_3)_4$ metal nitrate solution mixed with ten millilitres of *Murraya koenigii* plant extract. The biosynthesized ZrO_2 NPs were evaluated for bacterial deactivation of *E. coli*. Zirconium nanoparticles were biosynthesised using *Phyllanthus niruri* extract, and their photocatalytic color degradation action, antimicrobial capacity and bioremediation process efficacy investigated (Yuan *et al*., 2022). For adsorptive degradation of methylene blue, zirconium oxide dye nanoparticles were produced making use of the pericarp extract of *Sapindus mukorossi* (Alagarsamy *et al.*, 2022). Goyal *et al.,* (2021) successfully synthesized monoclinic zirconia Nanoparticles for antibacterial applications via green synthesis analysis from methanolic extract of *Helianthus annuus*(sunflower)seeds. Tijani *et al*.,(2022)fabricated carbon-sulphur codoped ZrO_2 nanocomposites from *Plumeria acuminate* aqueous leaves extract, polyvinylpyrrolidone, zirconia salt precursor, and sodium hydrosulphide, and the photocatalytic, electrochemical, antibacterial and antioxidant properties of the biosynthesized nanocomposite was investigated.

Zirconium oxide nanoparticles made from the leaf extract of Annona reticulata (AR-ZrO_2 NPs) were investigated for photocatalytic degradation of antibacterial activity and Malachite Green (MG)(Selvam *et al*., 2023). Chau *et al*., 2022 fabricated Zirconium nanoparticles made using pomegranate peel extract and an analysis of their antioxidant and antibacterial properties. Methyl orange and picloram photocatalytic degradation was evaluated using the vanadium oxide zirconium oxide nanocomposite (V_2O_5 /ZrO_2) made by a green technique utilizing *Daphne alpine* (*D. alpine*) leaves extract (Rasheed *et al*., 2020). In another study, green synthesized zirconia nanoparticles utilizing ginger, garlic, and zirconium nitride extract were evaluated for prospective dental implant applications (Chowdhury *et al*., 2023).To create Zirconium (iv) oxide NPs, Murraya koenigii leaf bio-extracts were utilized. Zirconium (iv) oxide NPs showed

improved optical, and crystalline capabilities due to its broad bandgap (4.7 eV), the spherical form, and a monoclinic structure. When compared to alternative ways, green synthesis of nanoparticles has been shown to be a highly regarded production strategy. The generation of nanoparticles was significantly influenced by the plant extract. Among the various functions of Murraya koenigii leaf extract are the bio-reduction, stability, and bio-capping of zirconium (iv) oxide NPs. Green-encapsulated Zirconium (iv) oxide NPs were created by the synergistic interactions of strontium source materials and Murraya koenigii (Chelliah *et al*., 2023).

Saka *et al*., (2022) prepared carica papaya shells by peeling and washing them. They were broken into small pieces and dehydrated at 50 °C. 20 grams of dry carica papaya shells were heated in deionized water for 30 minutes. Impurities were removed from the extract by filtering it using Whatman paper. In order to create titanium (iv) oxide nanoparticles, 15 milliliters of the extract were added dropwise to 65 milliliters of 0.2 M titanium isopropoxide (99.98%) dissolved in distilled water, and the mixture was magnetically agitated for five hours at 85 degrees Celsius while keeping the pH at 11. In order to eliminate contaminants, ten milligrams of CS leaves were first gathered and cleaned with distilled water to get rid of impurities. The leaves were cut into little pieces after being left to air dry. They were then immersed in 100 milliliters of deionized water and heated to 60°C for an hour. For fifteen minutes, the leaf extract a light brown solution was centrifuged at 4000 rpm. After being separated, the upper clear portion was utilized in the synthesis. The green solgel method of creating calcium doped TiO_2 photocatalysts started with the addition of a suitable quantity of titanium precursor, which was then agitated in 50 millilitres of ethanol for one hour and at 25 degrees Celsius. After two hours of stirring, 10 millilitres of the leaf's extract were introduced dropwise to a homogeneous titanium precursor solution. The use of deionized water dissolved a suitable quantity of calcium nitrate tetrahydrate, which was then added to the mixture. Five more millilitres of the leaf extract were then gradually introduced to the mixture. After two additional hours of stirring, the resultant solution was allowed to cool to 25 °C. For fifteen minutes, the fluid was centrifuged at 4000 rpm. The solid product at the bottom of the centrifuge was cleaned twice with deionized water, dried for 12 hours at 110 °C, and then calcined for 5 hours at 600 °C. The resulting powders were photocatalysts made of Ca-doped TiO_2.

In order to synthesize zirconium (iv) oxide nanoparticles, ten millilitres of *W. tinctoria* extracts of leaves were introduced dropwise to ten millilitres of 0.1 M aqueous $ZrOCl_2 \cdot 8H_2O$ solution while being vigorously stirred for three to four hours at 75 °C. To get rid of impurities, the aforementioned sample was centrifuged for five to seven minutes at 5000 rpm and then rinsed with deionized water. The manufactured sample was dried in an oven at 70°C .Following drying, the sample's value was determined at 800°C in a muffle furnace to produce powder zirconium (iv) oxide nanoparticles (Al-Zaqri *et al*., 2021). Murraya koenigii leaves that were fresh and green were obtained and washed with deionised water. After being cleaned, the leaves were steeped in deionised water and crushed with a mortar. The dark green extract was filtered through white cotton cloth, and the resulting solution was diluted in 100 millilitres of deionised water. Ten milliliters of the Murraya koenigii bio extract were mixed with 0.1 molar zirconium nitrate aqueous solution using a magnetic stirrer to create green manufactured zirconium (iv) oxide NPs in 60 minutes. A milky white solution is produced when the extract of Murraya koenigii reacts with the metal nitrate solution. The atomic layer nuclei of ZrO2 NPs are delivered by the white-coloured solutions. After treating the white ZrO2 NPs with repeated centrifugation at 10,000 rpm for 15 minutes, the precipitate was rinsed with double-distilled water. Ultimately, the white powder of zircon dioxide NPs was produced by drying the collected white precipitate for one hour at 100 degrees Celsius (Chelliah *et al.*,2023).

With ecologically friendly techniques that make use of plant extracts, microbes, or natural reducing agents, green synthesis of nanomaterials has become a viable substitute for traditional chemical processes (Hussain *et al*., 2016). Because of its remarkable photocatalytic, antibacterial, and electrochemical qualities, titanium dioxide (TiO_2) nanoparticles have garnered a lot of interest among nanomaterials (Anucha *et al.,* 2022). However, pristine TiO_2 has shortcomings such as strong electron-hole recombination rates and a broad bandgap (~3.2 eV) that limits photo absorption to the UV spectrum (Etacheri et al., 2015). By altering the electrical structure, reducing the bandgap, and improving visible light absorption, doping TiO_2 with different metal and non-metal ions has demonstrated efficacy in getting around these restrictions (Ansari *et al*., 2016).

Doped TiO_2 has been successfully synthesised environmentally using a variety of plant resources in recent investigations. Croton macrostachyus leaf extract was used by Tasisa *et al*., (2025) to synthesise strontium-doped TiO_2 nanoparticles. The extract's polyphenolic chemicals acted as reducing agents for titanium isopropoxide (TTIP) and facilitated the incorporation of strontium. The FTIR analysis revealed that hydroxyl groups (O-H stretching at 3427 cm^{-1}) from polyphenols played a crucial reducing role, with characteristic peaks shifting to lower frequencies upon TiO_2 formation. Titanium isopropoxide (TTIP) is the most commonly used titanium precursor due to its reactivity with aqueous plant extracts. According to Tasisa *et al*. (2025), dopant precursors are chosen for their compatibility and solubility in the green synthesis medium. Calcination at 400-500 °C is commonly employed to enhance crystallinity, remove organic residues, and activate dopant incorporation into the TiO_2 lattice (Dubey et al., 2021).

By altering the electronic structure, adding intermediate energy levels to the bandgap, and increasing the absorption capacity of visible light, strategic doping with metal and non-metal ions has demonstrated remarkable efficacy in resolving these basic constraints (Ansari *et al*., 2016). A paradigm shift towards the production of sustainable nanomaterials is represented by the combination of systematic doping techniques and green synthesis procedures, which combine improved functional performance with environmental stewardship. According to Hussain *et al*., (2016), green synthesis makes use of natural components, especially plant extracts that are high in phytochemicals. These compounds have multiple uses as reducing agents, capping agents, and morphology-directing agents. These bioactive substances provide surface functionalisation that regulates particle size, shape, and aggregation behaviour while also aiding in the reduction of metal precursors. In the generation of nanomaterials, the idea of "green synthesis" embodies the concepts of resource efficiency, environmental benignity, and sustainability. Green synthesis uses the natural chemical complexity of biological systems to form nanoparticles in mild conditions, as opposed to traditional chemical synthesis methods that usually use toxic reducing agents like sodium borohydride, hydrazine hydrate, or dimethylformamide, as well as stabilisers like polyvinylpyrrolidone or cetyltrimethylammonium bromide (Bhuiyan *et al*., 2020). Because of their availability, accessibility, chemical diversity, and the amount of

traditional knowledge about their properties, plant extracts are the most extensively studied class of biological resources for green synthesis. Multiple phytochemical constituents of plant extracts, especially phenolic compounds like tannins and terpenoids, allow them to chelate metal ions and aid in their reduction to the metallic or oxide state (Hussain *et al*., 2016).

Plant extracts are the most researched class of biological resources for green synthesis due to their accessibility, availability, chemical variety, and the amount of conventional knowledge about their qualities. Phytochemical elements in plant extracts, particularly phenolic compounds like flavonoids, tannins, and terpenoids, contain several hydroxyl and carbonyl functional groups that enable them to chelate metal ions and facilitate their reduction to the metallic or oxide state (Hussain *et al*., 2016). Most studies use relatively mild settings between 60 and 100 °C during the initial reaction phase, making temperature a critical element in green synthesis techniques. While preventing the breakdown of thermally sensitive substances that aid in capping and stabilisation, these moderate temperatures are adequate to trigger the reducing potential of phytochemicals. The removal of organic residues, improvement of crystallinity, and encouragement of dopant incorporation into the TiO_2 lattice through solid state diffusion are some of the benefits of post-treatment by calcination at temperatures usually between 400 and 600 °C after the initial synthesis (Dubey *et al*., 2021).Another important factor is the calcination atmosphere; air calcination produces well-oxidized TiO_2, but inert or reducing atmospheres might produce more oxygen vacancies and Ti^{2+} species that alter electrical characteristics.

Metal ions are reduced to their lower oxidation states or elemental forms during the reduction process, which usually entails the transfer of electrons from phenolic hydroxyl groups to metal ions, creating quinone structures in the organic molecules. Concurrently, the remaining functional groups in the phytochemicals adsorb onto the surfaces of the developing nanoparticles, resulting in steric and electrostatic stabilisation that permits control over particle size and shape and inhibits unchecked aggregation (Titasa *et al*., 2025). Because the dopant precursor needs to be added either during the formation process or through post-synthetic modification, the synthesis of doped TiO_2 using green approaches adds another level of complexity. By adding

strontium nitrate to the titanium precursor solution prior to adding the plant extract, Tasisa et al., (2025) showed that strontium doping could be accomplished, enabling simultaneous reduction and doping. The creation of oxygen vacancies is necessary to preserve electrical neutrality due to the charge imbalance caused by the lower valence state of Sr^{2+} compared to Ti^{4+}. This occurrence has a substantial impact on the material's optical and electronic properties.

Similar strategies have been effectively used for various dopants, such as calcium, zinc, and transition metals; dopant distribution and incorporation efficiency are mostly determined by the dopant precursor selection and compatibility with the chemistry of the plant extract. Methods of Green Synthesis Because the synthesis of nanomaterials has an impact on the environment, scientists are working to create environmentally benign substitutes for traditional chemical processes. Green synthesis techniques do not use hazardous solvents or high temperature treatments since they use biological materials including plant extracts, microbes, and biopolymers as reducing and capping agents (Asrani *et al*., 2022). Because of its affordability, ease of use, and biocompatibility, plant-mediated synthesis has become increasingly popular (Kumar et *al*., 2024). Flavonoids, terpenoids, polyphenols, and quercetin are among the phytochemicals found in plant extracts that play a number of vital roles in the green synthesis process. Through surface functionalisation, these bioactive substances avoid agglomeration, regulate particle size and shape, and act as reducing agents (Siregar *et al*., 2024). By choosing the right botanical sources, researchers may fine-tune the synthesis process because different plant species produce extracts with different contents. Plant extracts contain phytochemicals such as flavonoids, terpenoids, polyphenols, and quercetin, which are essential for the green synthesis process. These bioactive compounds work as reducing agents, prevent agglomeration, and control particle size and shape by surface functionalisation (Siregar *et al.,* 2024). Because different plant species yield extracts with different contents, researchers can fine-tune the synthesis process by selecting the appropriate botanical sources.

The effects of varying calcination temperatures (400, 500, and 600 °C) on the characteristics and photocatalytic efficacy of the resultant TiO_2 nanoparticles for organic dye removal were investigated using *Inula Viscosa* aqueous extract for one-pot

green synthesis (Elmakki et al., 2024). Further highlighting how organic components and secondary metabolites in plant extracts aid in the reduction of metal ions and stabilisation of nanoparticles was the research of red spinach leaf extract (*Amaranthus Tricolour L.)* (Siregar *et al*., 2024). Another possible environmentally friendly method is microbial synthesis, in which bacteria, fungi, or algae operate as biological factories to produce nanoparticles. The efficiency of microbial-mediated production of TiO_2 nanoparticles has been emphasised in recent thorough studies, underscoring its significance in antibacterial and wastewater treatment applications (Kumar *et al*., 2023). These microbes generate enzymes that aid in metal ion reduction and nanoparticle stabilisation, and they have built in metal resistance mechanisms. There are now more options for creating environmentally friendly photocatalysts with improved qualities because to the combination of green synthesis concepts and doping techniques. Studies on TiO_2 and Ag-doped TiO_2 nanoparticles made with plant extracts showed that green synthesis techniques can create materials with superior antibacterial and photocatalytic capabilities while utilising fewer hazardous substances (Malik *et al*., 2024). The study underlined that one of the most straightforward, economical, and environmentally advantageous methods for producing metal nanoparticles is green synthesis based on plant extract.

The photocatalytic efficacy of the synthesised TiO_2 for water remediation applications was successfully enhanced by silver nanoparticles, as shown by the green synthesis of TiO_2/Ag nanoparticles using *Thymus vulgaris* leaf extract. Numerous water pollutants were successfully photo degraded in the study, and zebrafish embryo toxicity tests verified the synthetic materials' biocompatibility (andrade *et al*., 2023). This study emphasises how green synthesis techniques can lead to both improved photocatalytic activity and decreased toxicity. The efficient doping of TiO_2 with magnesium using eco-friendly procedures was proven by the green synthesis of Mg-TiO_2 nanoparticles using titanium tetrachloride and peepal *(Ficus religiosa)* leaf extract. The efficiency of the resultant photocatalysts in breaking down organic dyes confirmed the feasibility of using green synthesis to create doped TiO_2 materials (Ghazi *et al*., 2020). More recently, co-doping techniques in conjunction with green synthesis have been investigated. The potential of codoping to improve photocatalytic water splitting applications has been shown by work on copper and phosphorus codoped TiO_2 for hydrogen synthesis from

seawater (Lin *et al*., 2024). Furthermore, studies on sulfur-nitrogen codoped TiO_2 nanoparticles made with root extract from *Dactylorhiza hatagirea* revealed increased photocatalytic activity, proving that plant extracts can act as reducing agents and nitrogen sources for metal dopants.

The green synthesis of codoped TiO_2 still faces a number of obstacles despite tremendous advancements. Reproducibility issues arise from the natural variability in plant extract composition, which depends on factors such as growing conditions, harvest time, and extraction methods. Standardization of green synthesis protocols requires careful characterization of plant extracts and correlation of specific phytochemical components with resulting nanoparticle properties (Aslam *et al*., 2024). Since most studies are conducted at laboratory scale, with batch sizes usually restricted to grams, further research is needed to determine whether green synthesis processes are scalable. To evaluate commercial viability, economic assessments contrasting green synthesis with traditional techniques are required. Practical implementation also requires thorough research on the long-term stability and recyclability of green-synthesized photocatalysts under actual operating conditions. Future studies should concentrate on broadening the scope of codopant combinations investigated using green synthesis, with a special emphasis on ternary and quaternary doping schemes. Recent work on predicting band gaps of doped TiO_2 from structural and morphological factors suggests that machine learning approaches could speed up optimisation by predicting optimal synthesis parameters based on desired properties (Li *et al*., 2020). New levels of photocatalytic efficiency may be possible by investigating synergies between codoped TiO_2 that has been green synthesized and other materials in composite or heterojunction topologies.

High thermal stability, chemical inertness, mechanical strength, and biocompatibility are just a few of the remarkable qualities of zirconium dioxide (ZrO_2), also referred to as zirconia, a technologically significant ceramic material (Chevalier *et al.*, 2009). Conventional production techniques for ZrO_2 nanoparticles usually entail energy-intensive procedures that produce hazardous waste, high temperatures, and toxic reagents (Shukla & Seal, 2005). Green synthesis techniques, which use biological resources like plant extracts, microorganisms, and biopolymers to create ZrO_2

nanoparticles with regulated morphology and improved properties, have become environmentally friendly substitutes in recent years (Iravani, 2011; Singh *et al*., 2016). Sol-gel, hydrothermal, precipitation, and thermal decomposition procedures are examples of conventional synthesis methods for ZrO_2. Although these techniques provide good control over crystallinity and particle size, they frequently involve organic solvents, hazardous precursors, high temperatures (over 400 °C), and hazardous by products (Kumari *et al*., 2015). For example, the sol-gel process usually employs zirconium alkoxides and necessitates high temperature calcination to produce crystalline ZrO_2 (Deshmukh & Lavand, 2012). A paradigm shift toward the manufacture of sustainable nanomaterials is represented by green synthesis. This method uses biologically derived natural reducing and capping agents, works at lower temperatures, produces less toxic waste, and uses less energy (Dauthal & Mukhopadhyay, 2016). According to Mittal *et al*., (2013), the biological molecules serve as stabilizing agents to regulate particle growth and avoid agglomeration as well as reducing agents to change metal ions into their oxide forms. Because there are so many phytochemicals that aid in the creation of nanoparticles, plant-based green synthesis has attracted a lot of interest. As reducing and stabilizing agents, a variety of plant extracts that comprise proteins, phenolic compounds, alkaloids, terpenoids, and flavonoids are used (Makarov *et al*., 2014; Ahmed *et al*., 2016).

ZrO_2 production using various plant materials has been successfully proven in a number of research. ZrO*2* nanoparticles with diameters ranging from 20 to 100 nm have been created using leaf extracts from *Aloe vera, Hibiscus rosa-sinensis, Nyctanthes arbor-tristis,* and *Catharanthus roseus* (Balaji *et al*., 2017; Ramesh *et al*., 2015). When calcined at comparatively lower temperatures (300–500 °C) than with traditional procedures, the phytochemicals in these extracts work in tandem with zirconium ions to promote the formation of crystalline ZrO_2 (Darroudi *et al*., 2014). The fabrication of ZrO_2 nanoparticles using *Aloe barbadensis miller* leaf extract was reported by Suresh et al., (2018). They showed that proteins and polysaccharides stabilize the nanoparticles and stop them from aggregating. These biomolecules' hydroxyl and carboxyl groups interact with Zr^{4+} ions to produce regulated nucleation and growth. Citrus fruit extracts, which are high in vitamin C and organic acids, were also used by Vijayakumar *et al*.,

(2015) and demonstrated efficacy in lowering metal precursors and generating homogenous nanoparticles.

Using leaf extract from Elaeagnus angustifolia, Nagajyothi *et al*., (2020) created ZrO_2 nanoparticles and shown exceptional antibacterial efficacy against both gram-positive and gram-negative bacteria. Cost-effectiveness, scalability, and the creation of nanoparticles with increased biological activity are benefits of plant extract-mediated synthesis (Thakkar *et al*., 2010). According to studies, ZrO_2 nanoparticles made using plant extracts have better antibacterial and photocatalytic qualities than those made with traditional techniques. This is probably because the particle surface still contains bioactive substances (Nethravathi *et al*., 2015).

Another environmentally friendly method for producing ZrO_2 is by microorganisms, such as bacteria, fungus, and actinomycetes. These organisms generate metabolites and extracellular or intracellular enzymes that mediate the creation of nanoparticles and decrease metal ions (Hulkoti & Taranath, 2014; Ovais *et al*., 2018). The enormous yield of proteins and enzymes has made fungal-mediated synthesis particularly promising. Reductases and other proteins secreted by fungi like Aspergillus niger and Fusarium oxysporum aid in the creation of metal oxide nanoparticles (Bhainsa & D'Souza, 2006; Durán *et al*., 2005). Because it streamlines subsequent purifying procedures, the extracellular synthesis pathway is very beneficial (Gahlawat & Choudhury, 2019). Usually, bacterial production uses both external and intracellular processes. On their cell walls or inside cellular compartments, where enzymatic reduction takes place, some bacteria build up metal ions (Klaus *et al*., 1999). Following cell lysis, the resultant nanoparticles can be extracted or discharged into the culture medium. Although bacterial synthesis allows for the adjustment of culture conditions to alter particle characteristics, the procedure may necessitate longer incubation periods than plant extract approaches (Mohanpuria *et al*., 2008). In green ZrO_2 synthesis, natural biopolymers such gelatin, cellulose, chitosan, and starch have been used as stabilizing and templating agents. According to Dhand *et al*., (2016), these polymers offer a three-dimensional network that regulates particle nucleation and development, producing a consistent size distribution and particular morphologies. In starch-assisted synthesis, zirconium precursors are combined with starch solutions and then heated.

Mesoporous ZrO_2 structures with large surface areas are created as a result of the starch molecules' dual roles as reducing agents and templates (Jain *et al*., 2015). Pal & Giri (2020) showed that ZrO_2 nanoparticles with increased photocatalytic activity for dye degradation are produced by starch-mediated synthesis. A cationic polymer made from chitin, chitosan provides hydroxyl and amino functional groups that stabilize the developing nanoparticles and chelate zirconium ions (Viswanathan *et al*., 2016). ZrO_2 nanoparticles with improved biocompatibility have been created using this method, which qualifies them for use in biomedical applications (Saravanan *et al*., 2011). Chitosan-ZrO_2 nanocomposites were effectively produced by Depan *et al*., (2011), exhibiting enhanced mechanical characteristics and antibacterial activity. The most prevalent crystalline phases seen in green-synthesised ZrO_2 nanoparticles are monoclinic and tetragonal. Synthesis variables like calcination temperature, pH, and the type of biological agents employed all affect the crystalline phase (Garvie, 1965; Ramesh *et al*., 2015). While TEM shows particle morphologies ranging from spherical to rod-like structures, XRD tests verify the development of crystalline ZrO_2 (Balaji *et al.,* 2017). The existence of organic functional groups on the surface of the nanoparticle is demonstrated by FTIR analysis, which also shows the adsorption of biomolecules that support biological and stability perfomance (Suresh *et al*., 2018; Vijayakumar *et al.,* 2015). Depending on the synthesis conditions and the biological agent used, the particle size typically varies between 10 and 100 nm (Darroudi et al., 2014).

Because biological molecules have a templating impact, green synthesised ZrO_2 nanoparticles frequently exhibit increased surface area and porosity when compared to conventionally manufactured materials (Nethravathi *et al*., 2015). According to Dhand *et al.,* (2016), these structural characteristics help applications like medication delivery and catalysis function better. The unique properties of green synthesized ZrO_2 nanoparticles have led to diverse applications across multiple fields. Because ZrO_2 is biocompatible, it can be used in biomedical applications such as scaffolds for tissue engineering, drug delivery, and dentistry materials (Chevalier *et al*., 2009; Saravanan *et al*., 2011). By minimizing hazardous chemical residues, green synthesis improves biocompatibility (Depan *et al*., 2011). According to cytotoxicity experiments, green-synthesised ZrO_2 nanoparticles selectively kill cancer cells while doing little harm to

healthy cell types (Vijayakumar *et al*., 2015). Because of their electronic and stability characteristics, ZrO_2 nanoparticles have been used in chemical and biosensors (Faia & Furtado, 2013). Through surface-bound biological molecules that can improve sensing selectivity, green synthesis offers extra functionality (Viswanathan *et al*., 2016). Notwithstanding the benefits, there are a number of obstacles to green ZrO_2 synthesis. Standardization of extraction and synthesis procedures is necessary since variations in the composition of plant extracts can result in irregular nanoparticle characteristics (Makarov *et al*., 2014). More basic research is required to fully understand the precise mechanisms by which biological agents promote ZrO_2 production (Mittal *et al*., 2013). The transition from laboratory to industrial production presents both financial and technological difficulties. Although small-scale synthesis is well established, process parameter modification and perhaps the creation of continuous flow systems are necessary to ensure quality control and repeatability at higher sizes (Dauthal & Mukhopadhyay, 2016). Furthermore, industrial adoption may be constrained by the comparatively lengthy synthesis periods and lower yields in comparison to conventional approaches (Ovais *et al.,* 2018).

Future studies should concentrate on clarifying the molecular processes of bio-mediated synthesis, locating and isolating particular bioactive substances that cause the formation of nanoparticles, and creating hybrid strategies that combine the advantages of chemical and biological techniques (Singh *et al*., 2016). Reaction kinetics and yields may be enhanced by process intensification techniques like green synthesis aided by microwave or ultrasound (Ahmed *et al.,* 2016). Furthermore, the usefulness of green synthesized ZrO_2 will be increased by investigating new biological sources and refining synthesis conditions for particular uses (Gahlawat & Choudhury, 2019).

2.4.2 Characterization of Nanoparticles

Nanoparticles can be characterized using different techniques to determine their size, size distribution, shape, surface area, porosity, aggregation, zeta potential, crystallinity and electronic properties (Mourdikoudis *et al.,* 2018a). Several studies report on characterization of transition metal oxide nanoparticles. In an experimental study, Ahmad *et al*., (2022) analysed green synthesized TiO_2 NPs. The first sign that TiO_2 NPs were being biosynthesised was a steep peak at 235 and 320 nm in the UV-visible

spectrum. The crystallinity of TiO_2 NPs in the anatase polymorph was discovered by XRD investigation. Microscopic examination indicated that TiO_2 NPs were polygonal and round in form, having diameters between 75 and 123 nm.

In another study, Green synthesized TiO_2 nanoparticles were characterized by Anbumani *et al*., (2022). The results showed crystalline structure and hexagonally shaped nanoparticles, with size ranging from 10 –59 nm. Ruíz-Santoyo *et al*., (2021) examined the TiO_2 anatase phase that had been slightly changed by the insertion of Zr^{4+} ions into its structure using XRD analyses. The UV-Vis measurements revealed that doped zirconium introduces new energy levels in the TiO_2 structure. Kunnamareddy *et al.,* (2021) synthesized pristine, Ni-doped, S-doped, and Ni-S codoped TiO_2 nanoparticles. The bandgap energy for pristine to codoped TiO_2 nanoparticles was reduced from 3.08 eV to 2.87 eV determined using UV spectroscopy. Alotaibi *et al*., (2021) characterized Zn-N codoped TiO_2. When Zn was added, the TiO_2 lattice expanded slightly, rising from 136.21 $Å^3$ in the undoped TiO_2 sample to 137.03 $Å^3$ in the 1.0% Zn, N: TiO_2 sample. This is due to the addition of Zn^{2+} ions, which are larger than the Ti^{4+} ions that they are expected to replace. The bandgap of the undoped TiO_2 was 3.3 eV, which remained constant after N doping, as expected with interstitial doping. The optical bandgap was slightly reduced when N: TiO_2 was doped with Zn. Thambiliyagodage & Usgodaarachchi, (2021) created N, Fe, and Cu codoped TiO_2 nanoparticles.TiO_2 nanoparticles in the anatase phase were detected by XRD analysis.

The analyses revealed that doping with N, Fe, and Cu had no effect on the crystal structure. Mai *et al*., (2021) investigated Co-Fe codoped TiO_2 nanomaterials. The synthesised materials' XRD patterns showed that monocrystalline TiO_2 developed in the anatase phase in every sample. Kunnamareddy *et al*., (2018) successfully synthesized nanoparticles of undoped TiO_2, Ag-TiO_2, S-TiO_2, and Ag-S codoped TiO_2. The clean anatase phase of the nanoparticles was confirmed by the X-ray diffraction study. When compared to other synthesized nanoparticles, the Ag-S codoped nanoparticle's average crystallite size shrank. The size of the crystallite was lowered from 19 to 11 nm. The energy gap was discovered to be reduced using the UV-vis diffuse reflectance spectrum from from 3.08 to 2.89 eV for undoped and codoped TiO_2 respectively.

X-ray diffraction patterns from papaya shell extracts revealed peaks at 2θ = 12.8, 18.2, 20.0, 28.3, 32.9, 35.3, 36.6, 40.2, 49.7, 58.3, 64.6, and 70.5, the individual diffraction peaks correlated with the (100), (002), (101), (102), (102), (110), (111), (102), (111), (101), and (111) crystal planes, respectively. All of the deflection peaks were precisely correlated with the hexagonal phases of TiO_2's rutile and anatase. Strong X-ray diffraction peaks concealed the high degree of crystallization of the nanoparticles (Saka *et al.,* 2022). F- doped Titanium dioxide developed was smaller in size than pristine TiO_2 and had a tetragonal crystalline structure. SEM images confirmed the nanoflakes-like structure of pristine and F- doped Titanium dioxide. When compared to undoped Titanium dioxide, F- doped Titanium dioxide has a lower band gap, higher strain, and higher dislocation density. In comparison to undoped Titanium dioxide, it also has a higher photocatalytic performance (Umadevi *et al*.,2014). Realpe Jimenez *et al*., (2021) discovered that the nanoparticles' size for Fe-N codoped TiO_2 is between 37 nm and 58 nm, which is less than the 70 nm particle size of pure titanium (iv) oxide nanoparticles. The reduction in particle size suggests that the codoping altered the lattice structure of titanium (iv) oxide in contrast to the nondoped sample, given the restricted growth of the particle size, which can be connected to the incorporation of Fe^{3+} ions in the crystal structure of TiO2 due to the differences in the atomic radius of Fe^{3+} and $Ti^{4+.}$

ZrO_2-NPs studied using XRD revealed the average crystallite size of synthesized particles to be 9.15 nm and the ZrO_2-NPs had spherical shapes and had an average size of 17 nm (Al-Zaqri *et al.*, 2021). The sol-gel process was used to create powders of pure and Ni doped ZrO_2 (0%, 1%, 3%, and 5%). XRD measurements revealed that the size of crystallites varied from 11 to 22 nm as doping increased. Doufar *et al*., (2020) investigated the structural and photochemical characteristics of Fe-doped ZrO_2. For low Fe-content, XRD investigation revealed the development of the tetragonal $Zr_{(1-x)}\ Fe_{\ x}\ O_{(2-x/2)}$ solid solution, while for higher Fe-content, the existence of hematite -Fe_2O_3 was found. The produced powders have specific surface areas ranging from 25.25 to 31.88 $m^2\ g^{-1}$. The optical bandgap increased as the Fe content decreased from 1.77 to 2.15 eV.

The sol-gel approach was used in this study to fabricate calcium doped titanium (iv) oxide photocatalysts with different concentrations of calcium (0, 3, and 5 weight percent) using Cannabis Sativa leaves. The photocatalysts' physicochemical characteristics were then evaluated using XRD, EDAX, FESEM, BET, TEM, and DRS analysis. Prominent peaks were generated at 25.33, 36.01, 37.90, 48.06, 53.96, 55.06, 62.70, 69.01, 70.41, and 75.32° in the XRD patterns of the calcium doped titanium (iv) oxide photocatalysts made using the green solgel method. These planes correspond to (101), (103), (004), (200), (105), (211), (204), (116), (220), and (215) respectively. The generated structure was attributed to the anatase phase of titanium (iv) oxide by comparing the provided peaks with the literature. There were no CaO peaks in the patterns that were generated when the patterns of pristine titanium (iv) oxide nanoparticles and calcium doped ones were compared. As a result, the titanium (iv) oxide crystal lattice fully incorporated Ca^{2+} dopant ions. The existence of calcium ions was verified by EDAX analysis. In general, the peaks were broader and their intensity decreased as the calcium dopant loadings increased. Consequently, the uniform dispersion was improved and the crystal size was decreased for the calcium doped photocatalyst (Sajjadi & Hosseinzadeh, 2025).

Characterization of Fe-TiO_2 was investigated using Raman spectroscopy, XRD, XPS and AFM. According to the results of Raman spectroscopy and XRD, TiO_2 crystalline phase was anatase, and the films' crystallite sizes ranged from 19.24 nm to 22.24 nm. According to XPS data, iron was present in iron-doped films of titanium dioxide as Fe^{3+} ions (Meng *et al*.,2019). MgO doped titanium (iv) oxide nanocrystals (NCs) were successfully formed using an easy wet-chemical process, according to Kaviyarasu *et al*., (2013). When MgO dopant is added, the XRD results reveal a little reduction in the crystalline size of titanium (iv) oxide nanomaterials. According to UV-Vis spectral study, the absorption edge redshifted when MgO was added to titanium (iv) oxide material. Photoluminescence (PL) and micro-Raman scattering approaches were used to determine the optical energy bandgap and molecular vibrational analysis of the doped nanomaterial, respectively. The substitution has significantly decreased the particle size of TiO_2 nanocrystals, according to HR-TEM examination.

All of the codoped titanium (iv) oxide nanoparticles are mixed crystals, as indicated by the XRD spectra of the Ce-Er codoped materials. The ratio of rutile decreases as the temperature for annealing rises, suggesting that the addition of Ce is delaying the transition of the crystal structure. The creation of Ti – O – Er or Ti – O – Ce bonds may be connected to the inhibition caused by both dopants. The addition of Ce clearly improves the responsiveness to visible light irradiation, according to UV-vis spectra. 0.2 mol% and 0.5 mol% Er Ce out of all the samples, titanium (iv) oxide shows the greatest absorption of visible light (Ren *et al*., 2020). Kunnamareddy *et al*., 2021 studied sol-gel prepared nickel (Ni) and sulfur (S) codoped titanium (iv) oxide photocatalysts. To explore the crystal structure, phase shifts, particle size, and bandgap energy of these samples, the as-prepared catalyst was characterized using X-ray diffraction (XRD) and UV-Vis diffuse reflectance spectra (DRS). The XRD diffraction pattern suggested that the particles were in the anatase phase, and the codoped titanium (iv) oxide nanoparticles were smaller than the pure and doped particles. The bandgap energy fell from 3.08 eV to 2.87 eV when pure TiO_2 nanoparticles were codoped, indicating that the localized and band electrons in codoped titanium dioxide interacted. The Debye-Scherrer formula (D, λ, k, β) was used to estimate the crystallite size. The computed sample values for the crystallite sizes of pure Ni/TiO_2, S/TiO_2, and Ni-S/TiO_2 were 19 nm, 13 nm, 15 nm, and 9 nm, respectively. Furthermore, as the dopant concentration rose, the crystallite's size shrank, which may be explained by peak expansion caused by dopant-induced flaws in the doped titanium (iv) oxide nanoparticles. There were no distinct Ni/NiO peak observed, which can be because to the extremely low metal content or the efficient dispersion of metal particles on titanium (iv) oxide. The stability and reusability of the Ni-S codoped TiO_2 nanoparticle were confirmed by the recycling experiment. Moreover, Ni-S/TiO_2 nanoparticles could be recycled four times without clearly losing their reactivity when exposed to visible light.

Cu and Mg codoped titanium (iv) oxide nanoparticles were produced using the Sol gel method by (Sandhya & Babu, 2018), and characterized by FE-SEM, XRD, FT-IR, HR-TEM and EDX,. The anatase phase of titanium (iv) oxide is present, in reference to X-ray diffraction studies of the Co-Mg codoped titanium (iv) oxide. FE-SEM pictures of the Co-Mg codoped titanium (iv) oxide sample reveal their reduced size and shape in comparison to pure titanium (iv) oxide nanoparticles. Several methods,

including EDAX, SEM, and HR-TEM, were used to get the elemental data and particle distribution in the samples. EDAX verified the elemental data for oxygen, magnesium, cobalt, and titanium. According to TEM pictures, the size is about 10 nm, confirming that the dopants Co and Mg cause the nanoparticles to shrink in size.

According to X-ray diffraction (XRD) research done by Laghrib *et al*., (2025) only the anatase phase was visible at annealing temperatures more than 400 °C, but the rutile phase predominated in both media when the temperature rose up to 700 °C. The material's photocatalytic effectiveness was impacted by the size of the crystallites increasing with temperature. Characteristic TiO_2 chemical linkages were confirmed by Fourier-transform infrared (FTIR) spectroscopy, however some of them vanished at higher temperatures. UV-Vis diffuse reflectance spectroscopy (DRS) exhibited a reduction in bandgap energy from 3.33 to 3.29 eV in acidic media and 3.17 to 3.13 eV in neutral medium with increasing temperature. SEM also revealed the creation of spherical TiO_2 nanoparticles. The bandgap values for samples sintered at 500, 700, and 900 °C were determined to be 3.3 eV, 3.2 eV, and 3.1 eV, respectively. The formation of new energy states in the TiO_2 forbidden band, which promotes photo generation, is responsible for the drop in bandgap energies at higher temperatures, which is compatible with the bigger grain sizes shown in XRD and SEM images. The certain surface area and light scattering characteristics of the nanomaterials are impacted by the bigger crystal sizes that result from higher annealing temperatures. Thus, structural alterations such as decreased interatomic spacing and thermal stresses, which have a major impact on bandgap energies, are reflected in the lowered bandgap energy.

Zirconium (iv) oxide Nanoparticles crystal structure is monoclinic, with a crystallite dimension of 24 nm, according to an XRD investigation. The spherical shape of zirconium (iv) oxide NPs is confirmed by TEM and FESEM morphology pictures, and their surface distributions reveal less agglomerations. The Zirconium (iv) oxide NPs displayed a broad bandgap and strong optical absorption in the UV. This suggests surface oxygen vacancies and charge carriers. FTIR and EDX spectroscopy were utilized to identify the presence of Zr and O atoms, as well as their O=Zr=O connections. XPS examination was utilized to determine the plant molecules' interface,

binding energy, bonding, and presence on the surface of zirconium dioxide NPs. Using plant molecules to form metal-oxygen connections, zirconium metals were able to attract and combine lattice oxygen. Zirconium (iv) oxide NPs were created when 69% zirconium was drawn to oxygen (27%). Because of the presence of Zr4+ and O2− and the spherical shape formed by the lattice oxygen and zirconium metal harmful chemicals were hindered from spreading (Chelliah *et al*.,2023).

The hydrothermal method was used to generate zirconium dioxide nanomaterials and Ag - doped ZrO_2 nanocomposite in a short amount of time, under mild temperatures, and without the use of any chemicals. The materials were described using Scanning Electron Microscopy (SEM), Raman, Fourier transform infrared (FTIR), diffuse reflectance spectroscopy (DRS), photoluminescence (PL), X-ray diffraction (XRD), and transmission electron microscopy (TEM). The zirconium (iv) oxide nanoparticles and Ag doped zirconium (iv) oxide nanomaterials generated at 200 °C were largely composed of cubic Ag nanomaterials and the tetragonal crystal phase, according to X-ray diffraction features. By using diffuse reflectance spectroscopy and the Ag plasmon band, the existence of Ag nanoparticles was verified. TEM and HRTEM verified that the Ag nanoparticles were within the 40 – 50 nm range and the zirconium (iv) oxide particles were smaller than 10 nm. Furthermore, zirconium (iv) nanoparticles were applied on top of Ag nanoparticles. According to the PL results, Ag doped ZrO_2 nanomaterials showed less intensity emission, which suggested that the charge separation efficiency had improved. Ag doped zirconium (iv) oxide nanoparticles retained their tetragonal structure, although the relative intensities of all Raman peaks fell. The FT-IR spectra of zirconium (iv) oxide nanoparticles and silver doped ZrO_2 nano samples revealed the presence of functional groups on their surfaces after hydrothermal processing. Both samples exhibit broad absorption bands between 3000 and 3600 cm^{-1}, as well as a unique band at 1634 cm^{-1}. These bands represent the bending and stretching vibration modes of the -OH bond induced by hydroxyl groups or absorbed water molecules on the nanomaterial surfaces. Furthermore, the metal and oxygen link (Zr–O) was located between 800 and 400 cm^{-1}, and peroxide cluster bands were seen at about 1000 cm^{-1}. Furthermore, when quantities of Ag were introduced, these bands did not exhibit any discernible shifts in spectra when the amount of Ag is added (Nova *et al*., 2021).

For antibacterial purposes, Yuan *et al*., (2010) synthesized a variety of titanium (iv) oxide nanoparticles using $Ti(OBu)_4$. Titanium dioxide nanoparticles were created through hydrolysis of ammonia and silver nitrate. Transmission electron microscopy (TEM), Fourier transform infrared spectroscopy (FTIR), X-ray diffraction measurements (XRD), and UV-Vis diffuse reflectance spectroscopy (UV-Vis-DRs) were used to assess the crystalline structure, interfacial structure, particle size, and UV-visible light response of the prepared materials. According to the XRD measurements, every sample underwent three hours of anatase structure calcination at 450 °C. The diffraction peak widened due to the silver doping. The titanium dioxide, N - doped titanium oxide, and 1% silver-nitrogen codoped TiO_2 nanomaterials were all round in shape in form and evenly dispersed, with mean sizes of 19.8 nm, 39.2 nm, and 20.7 nm, respectively, according to the TEM data. The size of the nanoparticles rose with nitrogen doping, whereas the dimension of the titanium dioxide particles reduced with increasing silver doping. According to the FTIR, N and Ag codoping of TiO_2 displayed the distinctive absorption band of NH_4^+ and Ag and seemed to have considerable absorption by the -OH group. The UV-Vis-DRs showed a clear augmentation of the absorption spectrum response (between 400 nm and 700 nm) and a red shift in the intake range of silver-nitrogen dual doped titanium dioxide.

Photocatalytic efficiency of titanium (iv) oxide based catalysts doped with 1 percent La in Ultraviolet radiation caused decomposition of two β-blockers – metoprolol tartrate (MET) and propranolol hydrochloride (PRO) were investigated by Armakovic *et al*., (2019). Sol–gel photocatalysts were created and then calcined at temperatures ranging from 450 to 750 degrees Celsius. BET, SEM, XRPD, and Raman scattering tests demonstrated a Significant impact of calcination temperature on the compositional, structural, and morphological properties of the generated catalysts. Photocatalytic activity was better in doped photocatalysts calcined at 450 – 650 °C, with a dominating anatase phase. The mesoporous structure developed, revealed a greater photocatalytic activity than much less porous samples calcined at 700 – 750 degrees Celsius, with sodium hexatitanate as the dominating phase.

Visible light (VL) sensitive mesoporous Sulfated rare earth ions Nd (3+), La (3+), Y (3+) infused titanium dioxide @ fumed SiO_2 catalysts produced by sol-gel technique with P123 (EO20PO70EO20) as a template were investigated by Zhan *et al*., (2013). The final samples (TG-DTA) were characterized using N2 adsorption-desorption measurements (BET), X-ray diffraction (XRD), X-ray photoelectron spectroscopy (XPS), electron microscopy (TEM), UV-vis diffuse reflectance spectroscopy, thermal analyses, Fourier transform infrared spectroscopy (FTIR), and photoluminescence (PL) spectra. In addition to showing increased pore volumes and surface areas, rare earth metal-doped samples also showed that they prevented titanium dioxide from transitioning from anatase to rutile form. Titanium (iv) oxide nanoparticles were created using a sol gel approach, and zirconium (IV) oxide nanoparticles were created using a sonochemical process. Characterization of zirconium (iv) oxide and titanium (iv) oxide particles was carried out using FTIR, XRD, UV-VIS spectroscopy, EDX, SEM, and TEM. The size of both types of particles was around 50 nm. The tetragonal anatase phase of titanium (iv) oxide particles and tetragonal polymorph of nano porous zirconium (iv) oxide particles were used. Using nanoparticle suspensions in a THF medium, these particles were applied to polypropylene and polyethylene. The decomposition of the polymers was investigated using SEM and FTIR to examine both morphological and chemical changes (Nisansala *et al*.,2017).

Gan *et al.*, (2017) synthesized Bi-S-titanium dioxide composites for decomposition of industrial dinitrotoluene solutions under ultraviolet rays The mesoporous Bi-S-titanium dioxide was found to be a highly crystalline anatase titanium dioxide with good thermal stability, a greator surface area of 75-120 m^2/g, and big mesopores of 10-20 nm. The results also demonstrated that S and Bi species existed in the mesoporous. Titanium dioxide in S^{6+}, S, S^{2-} and Bi^{4+}, forms, allowing the mesoporous Bi-S-Titanium dioxide to exhibit high absorbance in the UV area before shifting to the visible light zone. Under ultraviolet light for 5 hours, nearly 92.3 percent of an industrial aqueous dinitrotoluene (DNT) solution could be decomposed by 1.5 percent Bi-S-titanium dioxide. Its mesoporous characteristics and catalytic properties were discovered to be influenced by Bi ion dopant concentration and the range of calcination temperature. Using the microwave-assisted sol-gel process and chemical reduction procedures, Chiang *et al*., (2014) produced Cu doped titanium dioxide nanorods with

improved UV and visible light response for bisphenol A decomposition in the presence of ultraviolet and visible light. After Cu^{2+} dopants were chemically reduced by $NaBH_4$, Cu nanoparticles measuring 4.5 ± 0.1 nm were well deposited onto the surface of titanium dioxide nanorods, according to electron microscopic analysis. Cu particles on the Cu doped titanium dioxide nanorods were primarily a mixture of Cu_2O and CuO, based on the results of X-ray photoelectron spectroscopy and X-ray diffractometry under visible and ultraviolet light stimulation.

ZrO_2 NPs for two molar ratios (0.5 M and 1 M) were created using the solgel technique. The morphology and crystallinity of the manufactured samples were verified by X-ray diffraction (XRD), which also showed that the zirconium dioxide produced was crystalline. The FESEM study revealed that the nanoparticles were smaller than 20 nm, had a spherical shape, and were extremely consistent in size. Reactive oxygen species production in zirconium dioxide is confirmed by the FTIR. The solgel method successfully created zirconium dioxide nanoparticles in two molar ratios (0.5 M and 1 M). The XRD pattern displays zirconium (iv) oxide cubic crystalline phases; the average crystal size for (0.5 M) is 12.71 nm, whereas for (1 M), it is 15.91 nm. However, FESEM examination reveals that the majority of particles are uniformly distributed in a spherical shape, with an average size of between 14.26 and 12.71 nm (Thamir *et al*., 2021).

ZrO_2 NPs and Ag-ZrO_2 samples were characterized. Raman spectroscopy and XRD analyses confirmed the tetragonal crystalline phase of ZrO_2 NPs and Ag-ZrO_2 NPs. Analysis of the ZrO_2 NPs' optical, structural, and morphological characteristics showed that they had a monoclinic structure and a crystallite size of 24 nm. XRD analysis verified that the nanoparticles were spherical. FTIR spectroscopy was used to classify the presence of Zr and O elements and their O = Zr = O bonds(Chelliah *et al*., 2023)**.** Zirconium (iv) oxide nanoparticles were green synthesized using leaf extract from Wrightia tinctoria. to evaluate its potent antibacterial and photocatalytic qualities. Zirconium (iv) oxide nanoparticles were investigated using XRD, SEM, UV-visible, and PL. The tetragonal crystal structure of the zirconium (iv) oxide nanomaterials, with an average crystallite size of 9.15 nm, was confirmed by X-ray diffraction analysis. In their UV–visible spectra, the green produced zirconium (iv) oxide nanoparticles

displayed a strong absorption at 374 nm. The green synthesized ZrO_2 nanoparticles had an estimated bandgap of 3.78 eV, which is lower energy than that of the bulk ZrO_2 (5.00 eV). Because zirconia nanoparticles have a large surface area, they could have more surface defects (Al-Zaqri *et al*., 2021).

Using the sol-gel approach, Ahmed & Ali, (2021) successfully produced zirconium oxide nanoparticles in two molar ratios (0.5 M and 1 M). The XRD pattern showed ZrO_2 crystals with average diameters of 12.71 nm for (0.5 M) and 15.91 nm for (1 M). SEM examination showed that the bulk of the particles had a uniform distribution and a spherical shape, with an average size of the particle between 12.71 nm and 14.26 nm. The FT-IR spectra of ZrO_2 NPs showed several peaks for the significant functional groups O-H stretch or the N-H, stretching vibrations C = C in ketene, and C-H bend of unsubstituted alkane. Goudarzi *et al*., (2020) produced and characterised Fe doped ZrO_2. According to the XRD data, the average size of the crystallite produced sample was 12 ± 1 nm. Elemental analysis revealed that the primary constituents in the composite were iron, oxygen, and zirconium, confirming the successful manufacture of ZrO_2/Fe_3O_4 nanocomposite. Codoped Er^{3+}/Yb^{3+} ZrO_2 nanoparticles were fabricated and studied. According to X-ray powder diffraction and high-resolution transmission electron microscopy, well crystallized monoclinic nanoparticles with sizes ranging from 20 to 30 nm for pure ZrO_2 and 30 to 40 nm for doped ZrO_2 were produced (Paramonova *et al*., 2019). C-S codoped ZrO_2 nanocomposites were fabricated and characterised by Tijani *et al.,* (2022). The presence of spherical and irregular hexagonal forms was shown by SEM investigation. ZrO_2 nanoparticles and C-S codoped ZrO_2 were found to have band gap values of 5.2 eV and 3.4 eV, respectively. The XRD pattern that was examined by Tijani *et al*., (2022) revealed formation of crystalline tetragonal and a mixture of tetragonal and orthorhombic phases for ZrO_2 and C-S codoped ZrO_2 nanocomposite with an average size of 20.03 nm and 12.40 nm respectively.

Using a hydrothermal process, Halder *et al*., (2024) produced Te^{4+} and Er^{3+} doped zirconium (iv) oxide catalysts and examined how well they degraded pathogens and Congo red (CR) when exposed to visible light. Impurity-free monoclinic and tetragonal mixed phases are confirmed by Raman spectroscopy and XRD. Doping induced

defects, reduced crystalline size, resulted in a large surface area and reduced the bandgap (2.95 eV), photoluminescence inhibition, and interface polarization all help the EZO compound achieve incredible photocatalytic effectiveness, which is confirmed by LC-MS, phototoxicity evaluation, and photo electrochemical analysis. Ashis, (2009), used co-precipitation method to synthesize Silica-doped ZrO_2 with 5,10,15,20 MOL %. X-ray diffraction analysis indicated a change of monoclinic phase of ZrO_2 to a tetragonal phase in presence of Silica at higher temperatures. Zirconia system obtained had higher surface temperature stability and a large surface area, which showed great adsorption and catalytic behaviours.

2.5 Photocatalytic Activity

Photocatalysis is a phenomenon, in which an electron-hole pair is generated by a semiconducting material on exposure to light of sufficient energy. Generation of Reactive Oxygen Species (ROS) such as superoxide radical ($\cdot O^{2-}$), and hydroxyl radical ($\cdot OH$) in presence of light causing the photocatalyst to be a degradation and disinfection agent. Researchers have demonstrated that adding cation dopants to the transition metal oxides' lattice structure creates oxygen vacancies, increasing the photocatalysts' photocatalytic efficiency. The degradation of Rhodamine Blue (RhB) dye by photocatalysis was investigated using Green Synthesis of TiO_2 nanoparticles. After 120 minutes of irradiation, it was discovered that the degradation efficiency of RhB dye was greater for biosynthesized TiO_2 nanoparticles (96.59%) and pure TiO_2 nanoparticles (78.90%) (Ansari *et al*., 2022).

Zirconium (iv) oxide NPs were successfully green synthesized by (Al-Zaqri *et al*., 2021) using leaf extract from *W. tinctoria* as a stabilizing agent. Using biosynthesized zirconium (iv) oxide nanomaterials, the organic dye Reactive Yellow (RY 160) was photocatalytically degraded when exposed to sunlight. Within 120 minutes, 94% of the RY 160 dye was broken down by the green synthesized zirconium (iv) oxide nanomaterials. The capacity of a green synthesized zirconium (iv) oxide sample to photocatalyze the degradation of RY160 dye under sun radiation was investigated. The absorbance spectra of the RY160 dye were taken at various times while synthetic zirconia nanoparticles were present. The degradation of RY160 dye was measured using absorbance at 452 nm. Green-synthesised zirconium (iv) oxide nanoparticles

showed more than 94% dye catalytic activity against RY160 dye. This demonstrated that the photocatalytic activity of nanocatalysts is influenced by the size and shape of the nanoparticles as well as the processes of energy transfer, consumption, and the creation of photogenerated carriers. Thus, it was evident from the study results that zirconium (iv) oxide nanomaterials made with leaf extract from *W. tinctoria* exhibited superior photocatalytic activity against the dye RY160.

Safeen *et al*., (2023) examined the use of cobalt-doped TiO_2 produced by the co-precipitation technique for the photocatalytic degradation of methylene blue (MB). In contrast to pure TiO2, which only deteriorated 14%, and rutile titanium dioxide nanoparticles (62%), the cobalt doped anatase TiO_2 photocatalyst showed the highest methylene blue degradation rate of 93% in 90 minutes, according to the data (Gorgani & Kaleji, 2020) used Nb/Ag codoped titanium dioxide nanoparticles at different mol% to study the photocatalytic degradation of methylene blue. When compared to pure titanium dioxide nanoparticles, the results demonstrated that the codoped samples had the highest photocatalytic activity. 95.60% photocatalytic activity was achieved with the optimal molar concentration of Nb (0.5 mol%) and Ag (1 mol%) dopant ions. The creation of a magnetic zirconium oxide composite served as a catalyst for the reduction of methylene blue. Methylene blue was used to test the generated nanocomposites. According to the reported results, ZrO_2/Fe_3O_4 nanocomposites with a mass ratio of 5:2 showed remarkable catalytic activity and reusability (Goudarzi *et al.,* 2020).

Study of monodoped ZrO_2 reveal a better photocatalytic performance than pure ZrO_2. Analysis of the degradation of the RhB dye was used to examine the photocatalytic activity of ZrO_2 NPs and Ag-ZrO_2 nanocomposites (NCs). Ag-ZrO_2 NCs were found to have greater photocatalytic activity than pure ZrO_2 NPs under 467 nm irradiation, destroying more than 98% of the original RhB dye concentration in only 60 minutes as opposed to 140 minutes for pure ZrO_2 NPs (Nova *et al.,* 2021). Kianfar *et al*., (2021) fabricated CuO-ZrO_2 nanocomposite which displayed a good photocatalytic performance. 1 mg of the photocatalyst removed 10 ppm of MB and RhB within 30 and 60 minutes, respectively. Keerthana *et al*., (2022) produced and investigated a Nd doped ZrO_2 sample. The photocatalytic activity was tested against the dyes MB and RhB, as well as the pollutant acetophenone. The dye sample with 2% Nd doped ZrO_2

photo catalyst demonstrated 90% efficiency in decreasing MB dye, 77% efficiency in lowering RhB dye, and 60% efficiency in degrading acetophenone dye. The dye sample systems exhibited pseudo first order kinetics. The optimal level of rare earth metal Nd doping on ZrO_2 demonstrated good photocatalytic performance against all three dyes.

Halder *et al.*, (2024) investigated the effectiveness of Te^{4+} and Er^{3+} codoped zirconium (iv) oxide nanoparticles in degrading pathogens and Congo red (CR) under visible light irradiation. Under ideal circumstances, EZO outperforms ZO (77%) and TZO (84%), achieving 99% congo red degradation in 100 min (TOC 79.9%). The impact of solution pH, dye concentrations, and catalyst dosages on EZO's photocatalytic performance is methodically evaluated. After four cycles, the scavenging experiment confirmed the exceptional stability of OH and highlighted its crucial role in congo red degradation with an efficiency of 96.4%. Magnetic zirconium oxide (ZrO_2/Fe_3O_4) nanocomposites were manufactured by Goudarzi *et al*., (2020) in a variety of mass ratios, including 1:1, 3:1, 5:2, and 7:2. The produced nanocomposites' catalytic activity was examined by dispersing 7 mg of magnetic ZrO_2 nanocomposites in 50 ml of methylene blue (MB) azo dye (10 ppm) and adding 50 mL of aqueous $NaBH_4$ solution (5.3×10^{-3} M). After stirring the solution at room temperature, a UV-Vis spectrophotometer was used to measure the amount of methylene blue contained in the solution at a wavelength of 665 nm (λ maximum). The blue MB solution turns into a totally colourless solution during this process. The ZrO_2/Fe_3O_4 nanocomposite with the greatest catalytic efficiency was found to have a weight ratio of 5:2. This catalytic behavior results from the ZrO_2/Fe_3O_4 nanocomposite's surface facilitating the electron move from BH_4 to the methylene blue dye during the reduction process.

Co-Fe codoped titanium (iv) oxide photocatalyst was evaluated on MB dye in visible light. The results revealed that MB degradation on TiO_2 samples doped with Co^{2+} and Fe^{3+} worked remarkably well when compared to undoped and Co^{2+} doped TiO_2 samples (Mai *et al*., 2021).Under the simulated sunshine illumination, the green-fabricated photocatalysts were used in the photocatalytic decomposition of Rhodamine B (RhB) and Methylene Blue (MB). Among the produced photocatalysts, the 5 weight percent calcium doped TiO_2 (CaTi5) photocatalyst showed outstanding characteristics, including a decreased energy band gap, a greater surface area, and uniform dispersion

and particle size. CaTi5 showed the maximum dye degradation according to the superior characterizations. Following 240 minutes of simulated sunlight illumination, the CaTi5's MB and RhB degradation were 85% and 90%, respectively. Furthermore, the degradation of photocatalytic dyes followed the pseudo first-order reaction kinetics.

Furthermore, the highest level of degradation was seen at a catalyst concentration of 100 ppm, out of all CaTi5 concentrations tested (50, 75, 100, 125, and 150 ppm). Thus, CaTi5 has the potential to act as a photocatalyst for the degradation of MB and RhB in aqueous solution induced by solar light. RhB and MB were photocatalytically degraded at 79% and 72%, respectively, using pure titanium (iv) oxide. The improved properties of CaTi5, including its higher surface area, smaller particle size and uniform dispersion, higher ability to produce surface free radicals (OH), and lower energy band gap, were attributed to its superior efficiency. Although the results showed that higher calcium ions concentrations resulted in better catalytic characteristics and increased photocatalytic activity, it appears that adding more than 5 weight percent of Ca may have some disadvantages. Additional calcium addition may result in agglomeration, pore blockage, reduced surface area, uneven dispersion, and ultimately limited photocatalytic activity. Therefore, it appears that the pure titanium (iv) oxide should only have a smaller amount of calcium dopant added to it (less than or equivalent to 5 weight percent) (Sajjadi & Hosseinzadeh, 2025). Doping with Ca ion incorporated into the lattice or positioned on an interstitial lattice site of anatase titanium dioxide induced changes in the structure. The stretching vibrational peaks around 1630 cm^{-1} are contributed to the red shift of the -OH bond caused by raising the doped calcium quantity and thiophene adsorption capability, according to the Infrared. Furthermore, as compared to pristine titanium dioxide, the Ca-TiO_2 nanoparticles have outstanding photocatalytic activity when exposed to thiophene (Liu *et al*., 2014).

To track degradation, the absorbance of the dye by ZrO_2 nanomaterials and silver doped ZrO_2 nanomaterials suspension was measured; the intensity of the dye's maximum absorbance at 554 nm gradually decreased over time, indicating that ZrO_2 nanoparticles and silver doped ZrO_2 nanomaterials photocatalytically degraded the dye. Furthermore, the RhB dye changed very little under irradiation, even after 140 minutes of exposure, when ZrO_2 nanoparticles and Ag-doped zirconium (iv) oxide nanomaterials were not

present. Under 467 nm irradiation, Ag-doped ZrO_2 nanomaterials demonstrated higher photocatalytic activity than pure ZrO_2 nanoparticles, breaking down over 98% of the initial RhB dye concentration in 60 minutes, whereas pristine ZrO_2 particle's photocatalytic activity took place 140 minutes later. Ag doped ZrO_2 nanomaterials produced less excitons, which was linked to the improvement in photocatalytic process (Nova *et al*., 2021). The degradation of methylene blue at 664 nm was used to determine the photocatalytic activity of the ZrO_2 nanoparticles. When the ZrO_2 photocatalyst is present, the absorption of the methylene blue dye solution decreases as the simulated visible light irradiation time increases. Sources of visible light are plentiful, have a wide absorption range, and don't require a lot of energy. Since there is very little electron excitation under light irradiation, the dye degradation rate without nanoparticles is 8%. The dye bonding was lessened by the surface electron migration. When nanoparticles are present during excitation, the active sites are significantly higher than in nanoparticle samples that are not exposed to light (Chelliah *et al*., 2023).

Shao *et al*., (2014) created a zirconia – titania composite to degrade MB under UV. For ultra violet analysis the suspension was stirred magnetically while withdrawing some sample and centrifuging it. The photocatalytic work of the samples was examined by adding an equal amount of methyl blue solution and photocatalyst to the glass reactor and then stirring for 30 min in darkness. An experiment involving irradiation of methyl blue solution without the photocatalyst was carried out to act as a control for the experiment. Comparisons of the activities of the samples toward decolourization of methylene blue the composite was more efficient than pristine TiO_2. Shikha & Ritu, (2013) prepared undoped and iron doped zirconium (iv) oxide photocatalysts using sol-gel method. The photocatalytic breakdown of malachite green by undoped and iron doped semiconductor zirconium (iv) oxide and the progress of the reaction was studied using spectrophotometer at 616 nm. The impact of several operational factors on the rate of degradation was noted, including pH, dye concentration, semiconductor quantity, and light intensity. Fe- doped ZrO_2 was more efficient in degradation of malachite green compared to pure ZrO_2. Moon *et al*., (1997) fabricated Zirconium - silicon (Zr/Si) binary oxides catalysts having different Zr contents was made from mixtures of tetraethyl orthosilicate (TEOS) and zirconium oxychloride in ethanol. The quenching of the photoluminescence by the added butene molecules showed that the higher

photocatalytic action of the zirconium-silicon binary oxides having a low Zr content is linked to the catalytic activity of the charge-transfer excited state of the zirconium oxide species.

Kambur *et al*. (2012) used a solid state procedure to make TiO_2 – ZrO_2 binary oxide photocatalysts. The photocatalytic effectiveness of the combination was influenced by the interaction between ZrO_2 and TiO_2. In the photo degradation under ultra violet irradiation, the 50 percent TiO_2 – ZrO_2 photocatalyst had much better photocatalytic efficiency than undoped titanium (iv) oxide and the conventional degussa TiO_2 P-25. When a smaller amount of ZrO_2 (10–50 wt percent) was loaded to TiO_2, the binary oxide catalysts' catalytic activity steadily rose with an increase in the amount of ZrO_2 loading; however, beyond 50 wt percent, the reactivity decreased. The photocatalytic degradation activity was highest at 50 wt% ZrO_2 – TiO_2. The phenol photo degradation rate was highest in the 50 wt% TiO2 sample. Zhou *et al*., (2012) examined the photocatalytic action of meso-tetraphenylporphyrins adsorbed on TiO_2 (degussa P25) surfaces with various metal centers (Co, Fe, Cu, and Mn). The catalysts for the degradation studies were made as follows: TiO_2 (P25, 2 g) was added to a solution of metalloporphyrins (12 mol) diluted in CH_2Cl_2 (30 mL). The suspension was then magnetically swirled for 10 hours at room temperature. The catalyst was obtained by extracting the solvent under vacuum and drying it for 12 hours at 60 degrees Celsius. Co P-TiO_2, FeP-TiO_2, CuP-TiO_2, and MnP-TiO_2 were used as photocatalysts, respectively. Photocatalysts were evaluated on their ability to degrade methyl orange in aqueous solution. The photo catalysis studies were conducted in a batch reactor using a 500 W high-pressure mercury lamp positioned 10 cm away. A circulating water jacket kept the batch reactor cool at approximately 25 degrees Celsius. A 400 nm wavelength cut-off filter was used during visible light irradiation. A magnetic bar was used to agitate the reaction mixture, which contained methyl orange aqueous solution (20 mg L^{-1}, 150 mL) and catalyst (0.04 g). The mixture was infused with molecular oxygen.
Before irradiation, the mixture was maintained in the darkness for thirty minutes to check that the maximum utilisation had been achieved. The sample was collected from the suspension every 30 minutes throughout the irradiation to determine the absorption variation of methyl orange after visible light or UV illumination. Photocatalyst was separated by centrifugation, and the remaining methyl orange content in the solution

was determined by measuring the clear solution's light absorption at a wavelength of 464 nm. A Shimadzu UV-2450 UV-Vis spectrophotometer was used to collect UV-Vis spectra. Finally, meso-tetraphenyl metalloporphyrins (Fe, Co, Mn, & Cu) adsorbed on TiO_2 (degussa P25) catalysts were effective in degrading methyl orange aqueous solution when directed to UV radiation. Under visible light or UV exposure, the Copper porphyrin-sensitized TiO_2 catalyst (CuP-TiO_2) demonstrated the best action for photo degradation of methyl orange. Copper ion has a higher positive charge than methyl orange ion, as evident from density functional theory calculations methyl orange ion is more easily utilized by CuP-TiO_2 (Zhou *et al*.,2012).

Abdi *et al*., (2019) developed a porous TiO_2/ZrO_2 photocatalyst based on UiO-66 and titanium (iv) oxide hybrids. The solvothermal approach was used to make UiO-66 nanoparticles, which were then used as a photocatalytic support to grow titanium (iv) oxide particles on their surface. Under light emitting diode (LED) visible light, the produced Titania/Mof nanocomposite was calcined to yield porous TiO_2/ZrO_2 photocatalyst for decomposition of organic contaminants from coloured effluents. The results revealed that the new TiO_2/ZrO_2 increased Rhodamine B (RhB) photocatalytic degradation ability when compared to a mixture of previous UiO-66 and TiO_2, and that it influenced photocatalytic performance by increasing photon adsorption in the visible range and boosting charge transport and separation. The dynamics of colour removal followed a first-order kinetic model. Furthermore, even after four recycling cycles, the regenerated nanocomposite maintained its high stability and photocatalytic degradation ability by 90 percent.

Photocatalytic efficiency of polyethylene and polypropylene was examined by Nisansala *et al*., (2017). Zirconium (iv) oxide nanoparticles and titanium (iv) oxide nanoparticles were examined for their impact on photocatalytic activity. A solar simulator was used to optimize the concentration and exposure time under laboratory circumstances. Both polypropylene and polyethylene were treated in a solar simulator and under sun light conditions. At 95 percent confidence levels, there was a substantial difference in plastic degradation between the two treatment conditions, with zirconium (iv) Oxide nanoparticle suspension treated polypropylene and polyethylene showing more degradation than nano titanium (iv) Oxide particle suspension treated samples.

Rare earth doped samples shown a considerable improvement in photocatalytic performance, and their experimental methyl orange (MO) degradation rates were higher than those of the undoped samples. The maximum photocatalytic efficiency was found in the Nd-doped sample, and the best dosage was 0.25 mol percent, which led to methyl orange degradation rates of 99.8 percent and 90.05 percent after Ultraviolet illumination for 60 minutes and visible light exposure (>400 nm) for 40 hours, respectively. Strong visible light absorption, higher specific area, better crystallinity, and the catalyst's ability to successfully separate photogenerated electron-hole pairs could all lead to improved photocatalytic performance (Zhan *et al*., 2013).

Under UV irradiation, the Cu-doped titanium dioxide nanorods showed greater photocatalytic efficiency in the photodegradation of bisphenol A. The pseudo-first-order rate constant (kobs) for the photocatalytic degradation of bisphenol A by 7 weight percent Cu-doped titanium dioxide nanorods was 18.4 and 3.8 times higher than that of degussa P25 titanium dioxide and as-synthesised titanium dioxide nanorods, respectively. Furthermore, when compared to degussa P25 titanium dioxide, the kobs for bisphenol A photocatalytic degradation by 7 wt% Cu doped titanium dioxide nanorods improved by a factor of 5.8 when put in visible light illumination of about 460 nm. The findings of this work show that one dimensional Cu doped titanium dioxide nanorods can be used to photocatalytically degrade bisphenol A and other cosmetic and personal care items in conventional waste water treatment processes. (Chiang *et al*., 2014). In comparison to pure zirconium (iv) oxide, iron metal doping considerably improved photocatalytic performance, photo electrochemical characteristics and electron-hole pair separation efficiency. It was also discovered that 0.5 percent iron doped zirconium (iv) oxide had the best photocatalytic efficiency, degrading rhodamine B (RhB) by 96 percent in 150 minutes when directed to visible light. The process of photocatalytic decomposition of RhB over Iron doped zirconium (iv) oxide was explored in this study, as well as a viable technique for creating very negative conduction band potential of zirconium (iv) oxide via iron metal doping for long term environmental remediation (Cheng *et al*., 2020).

Sayama & Arakawa, (1993) studied catalytic reduction of water & catalytic decomposition of CO_2 over ZrO_2 photocatalyst. Some special characteristics of ZrO_2

semiconductor were discovered for the first time, it involved the photocatalytic reduction of water over ZrO_2 nanoparticles in the presence of ultraviolet light without any loaded metal. When Na_2CO_3 and $NaHCO_3$ were added the amount of H_2 and O_2 being produced increased. The green produced zirconium (iv) oxide NPs were tested against two distinct human-borne diseases and harmful dye pollutants. Zirconium (iv) oxide NPs demonstrated increased photocatalytic destruction of methylene blue dye pollutants when exposed to visible light. Zirconium (iv) oxide NPs' bacterial deactivations performed better against *E. coli*. The ZrO_2 Nanoparticles' reactive oxygen species production shown superior antibacterial activity. The findings suggest that ZrO_2 Nanoparticles could be used as a photocatalytic poisonous dye removal agent, pathogenic inhibitor, or treatment of wastewater. Furthermore, the green way of producing zirconium dioxide Nanoparticles is a more affirming approach than other accessible methods and is found to be an alternate successful technique for synthesizing of Nanoparticles (Chelliah *et al*., 2023).

Conventional methods for degrading organic pollutants and eliminating pathogenic bacteria, such as the use of chemicals, are prohibitively expensive and produce hazardous by- products that are harmful to human health. This necessitates the search for newer and more effective methods. The scientific explorations of nanoparticles for their novel photocatalytic and disinfection potencies presents a very promising approach in killing microbes and degrading organic pollutants. The working principle in most of these nanoparticles involves production of Reactive Oxygen Species (ROS) such as superoxide radical ($\cdot O^{2-}$), and hydroxyl radical ($\cdot OH$) in presence of light, that degrade organic pollutants and coupled with biochemical reactions, damage pathogens (Tijani *et al*., 2022). An alternative mode of action for killing microorganisms is the interaction of the metal oxide nanoparticles with the cell wall resulting into their deactivation (Sagadevan *et al*., 2022). Several ways are accessible for the extraction of dye compounds from surfaces, with photocatalysis being one of the most efficient, cost-effective and widely available technique to eradicate organic compounds with the help of visible light, a renewable energy source available all over the world (Keerthana *et al*., 2022). Dye contaminants affect the natural source of the water bodies, causing ecological domains to be disrupted. In addition, the discharge of dye effluents creates mutagenic and carcinogenic diseases.

Currently, nanoscale particles have been extensively applied to the development of novel disinfecting agents (Anbumani *et al*., 2022). Bacterial strains like, *S. aureus* and *E. coli* are extremely dangerous pathogens that cause a variety of illnesses at the intestinal and gastrointestinal sites. These harmful bacterial strains cause an annual rise in mortality rates throughout the world. Various studies reveal TiO_2 and ZrO_2 NPs synthesized through various methods exhibit excellent disinfection activity against a wide range of microbes.

2.6 Disinfection Activity

Bacterial cells are inactivated by first coming into touch with their cell walls through an oxidation process called lysis. The metabolism cell will then die, which also reduces the permeability of the cell. Additionally, damaged cell membranes can be reached by the synthesized nanoparticles, and direct attacks can hasten cell death. Furthermore, the nanoparticles have other benefits in the photocatalyst system, including photo stability, inert, and the capacity to completely mineralize organic pollutants (Quan *et al*., 2014).

Anbumani *et al*., (2022) evaluated the deactivation ability of the fabricated TiO_2 nanoparticles, the results showed high toxicity against various fungal strains. The mean of triplicates of obvious zone of inhibition (in millimetres) around each disc was estimated for each of the pathogens. A study by Mantravadi, (2017) evaluated the antibacterial action of pure titanium oxide nanoparticles (NPs) or those combined with silver (Ag) against Escherichia coli germs. After six hours of incubation in visible light the bacteria that were injected onto titanium (iv) oxide sample annealed at 200 °C exhibited a slower antibacterial degradation rate. After eight hours of incubation, there were no colony forming units left. After six hours of incubation, the samples treated with titanium (iv) oxide at 400 °C did not exhibit any growth. The incubation period for the total absence of colony forming units was correspondingly shortened in samples treated with titanium (iv) oxide containing silver impurities.

The antibacterial activities were assessed using gram positive cocci (S. *mutans*) and gram negative coliform bacteria (E. *coli*). First, following 15 minutes of exposure to visible light, the bacterial growth curve at an optical density of 600 nm was measured.

The outcomes demonstrated that both species of bacteria were significantly inhibited by the produced nanomaterials. The Colony Forming Unit (CFU) counts were used to determine the relative viability of the bacteria. S. *mutans* was successfully destroyed by 200 μg mL−1 HT with an antibacterial efficiency of 70.26%. The rate of HTG and HTGZ increased to 87.64% and 98.25%, respectively. The antibacterial rates for HT, HTG, and HTGZ against E. *coli* were 61.23%, 78.17%, and 99.15%, respectively. Furthermore, there was a concentration and time-dependent decrease in bacterial viability. HTGZ has more potent antibacterial activity against S. *mutans* than E. *coli*. This is most likely a result of the remarkable PDA resistance displayed by gram negative bacteria with thick outer membranes made of lipopolysaccharides and lipoproteins (Lu *et al*., 2023a).

The antibacterial activity test using Mn-N-TiO_2 composite coated wall paint to inhibit the S. aureus bacteria was evaluated by (Quan *et al*., 2014). Above the surface of the nutritional agar, a number of bacterial colonies developed. Furthermore, the total number of bacterial colonies was impacted by the difference in Mn-N-TiO_2 concentration. Data showed that in visible light, the 60% Mn-N-TiO_2 concentration of coated wall paint was more effective at inactivating *S. aureus* germs. This is because MnN-TiO_2 created an OH radical that may react with bacteria. Strong oxidative chemicals exploit photo generation processes on the titanium (iv) oxide surface to free radicles that damage cell walls and cell membranes. These species are composed of O_2^- and OH.

Alotaibi *et al*., (2021) synthesised Zinc-Nitrogen TiO_2 .Under both ultraviolet and fluorescent light conditions, the 1.0% Zn, N: TiO_2 film had the best antibacterial properties. By comparing the growth of the cultures under xenon lamp irradiation with the growth of the bacteria cultivated in titanium (iV) oxide film alone, the impact of the obtained Fe-doped titanium (iv) oxide films on the antibacterial actions of E. *coli* was ascertained. The findings demonstrated that, following a 3-hour photocatalytic reaction, 0.1% Fe doping of titanium (iv) oxide film outperformed the bare titanium (iv) oxide film, which exhibited only weak antibacterial activity, in inhibiting the formation of E. *Coli* colonies. Fe^{3+} ions make up the majority of the iron doped titanium (iv) oxide films. The bactericidal qualities of the iron doped titanium (iv) oxide films were inferior

to those of the bare titanium (iv) oxide films when the doping concentration exceeded 2.0 at%. Even in actual dye waste water, a low amount of iron dopant of less than 2.0 at% demonstrated outstanding antibacterial efficacy (Meng *et al*., 2019).

Previous research works show ZrO_2 NPs are efficient disinfectant agents. Chowdhury *et al*., (2023) produced ZrO_2 NPs from garlic, ginger, and zirconium, and they demonstrated significant antibacterial action against *S. aureus*. ZrO_2 NPs generated hydrothermally were employed as an antibacterial agent against Staphylococcus aureus at various dosages. (Ahmed & Ali, 2021). Zirconium (iv) oxide nanoparticles have demonstrated antibacterial actions against bacteria at concentrations comparable to those of traditional antibiotics. The produced zirconia nanoparticles showed inhibitory effect against gram negative *E. coli* bacteria by drawing in negatively charged bacteria and attacking the walls of the cell with positively charged zirconium ions.

According to the results, release of free radicles is accelerated by produced multifunctional zirconium (iv) oxide nanoparticles, which causes bacterial cells to be destroyed. Lipid peroxidation is one of the multiple effects that these highly reactive radicals have on the bacteria. As the concentration of zirconium (iv) oxide nanoparticles increases, bacteria die as a result of the cell wall collapsing. In general, it has been demonstrated that nanoparticles can enter bacteria because of their unique form. The diffusion of nanoparticles across the bacterial membrane is directly correlated with their size. Smaller nanoparticles are more likely to cause harm to bacterial membranes. Transporter proteins and ion channels have made it easier for nanoparticles to pass across the plasma membrane. The positive charge of zirconium ions causes cell death (Thamir *et al*., 2021).

The antibacterial *W. tinctoria's* aqueous leaf extract and biosynthesized zirconium oxide nanoparticles were tested against bacteria at different concentrations (2, 4, 6, 8, and 10 µl). As the sample concentration against the bacterial strain increases, so does the zone of inhibition. At 10 µg/ml, the aqueous leaf extract of *W. tinctoria* demonstrated the highest inhibitory zone against *P. aeruginosa* (9 mm ± 0.4) and B. subtilis (7 mm ± 0.3), *E. coli* (12 mm ± 0.2) and *S. aureus* (10 mm ± 0.1). The produced samples showed a higher disintegration rate for gram-negative bacteria compared to

gram-positive bacteria due to structural differences between the two types. The biogenic technique produces zirconium (iv) oxide samples with a large surface area and small particle size, resulting in excellent antibacterial actions. The enhanced antibacterial actions of the nanomaterials may be due to their tiny spherical shape and crystallite size. *W. tinctoria* leaf extract is also valuable for medical uses since it contains flavonoids, protein, tannins, alkaloids, animal acids, and carbohydrates, all of which may contribute to its antibacterial qualities (Al-Zaqri *et al*., 2021).

Doping zirconium with various metals, non-metals or by forming composites improved the antibacterial actions of ZrO_2 NPs significantly. Antibacterial effectiveness tests of ZrO_2 NPs and Ag-ZrO_2 NPs were carried out using *S. aureus* and *E. coli* as model species of gram negative and gram positive bacteria, respectively. Compared to ZrO_2 NPs, Ag-ZrO_2 NPs effectively inhibited the growth of bacterium cultures in more than 75% of the *E. coli* bacteria (Nova *et al.,* 2021). Using sol-gel process, Ayanwale *et al*., 2020 synthesized pure zirconium oxide, silver oxide, and ZrO_2-Ag_2O NPs and their antibacterial activity was examined. Compared to pure ZrO_2 and Ag_2O, ZrO_2-Ag_2O significantly increased the antibacterial actions against all of the tested microorganisms. Silver-doped zirconium (iv) oxide nanoparticles and zirconium (iv) oxide were tested for their antibacterial characteristics against strains of *S. Aureus* and *E. coli*.

First, the upcoming of bacteria was assessed both with and without ZrO_2 nanoparticles and Ag doped ZrO_2 for up to six hours. The growth of *E. coli* bacteria decreased as the quantity of ZrO_2 nanomaterials and Ag-doped ZrO_2 nanomaterials increased. In the presence of Ag-doped ZrO_2 samples, the growth inhibition of *E. coli* bacteria rose dramatically, resulting in approximately 77% inhibition of *E. coli* compared to 9% in the presence of zirconium (iv) oxide nanosamples. Nevertheless, *S. aureus* exhibited 76% and 70% elimination for zirconium (iv) oxide nanoparticles and Ag doped ZrO_2 nanomaterials, respectively. *E. coli* was efficiently suppressed when coupled to an Ag doped ZrO_2 sample, but *S. aureus* was inhibited by both zirconium (iv) oxide nanoparticles and Ag doped ZrO_2 nanomaterials. The differences in bacterial growth suppression seen can be attributed to the permeability, electrostatic attraction, and composition of gram positive and gram negative bacteria, respectively. Furthermore, silver nanoparticles (mean size 40–50 nm) have a hard time diffusing through the cell

membrane of gram positive bacteria because their cell membranes are made of a denser peptidoglycan layer attached to short peptides. The observed rise in antibacterial activity of silver-doped ZrO_2 nanomaterials, which are more effective against gram negative *E. Coli* bacteria than gram positive *S. aureus* bacteria, was caused by the synergistic interaction of the two constituents, silver nanoparticles and ZrO_2 nanomaterials. At very low dosages, the antibacterial efficacy against *S. aureus* is higher than in *E. coli*. The structure, makeup of the bacteria is linked to this unique behavior. Furthermore, the bacterial cells exposed to zirconium (iv) oxide nanoparticles and Ag-doped ZrO_2 nanoparticles showed obvious damage, according to the scanning (Nova *et al*., 2021).

The few studies done on antimicrobial effects of codoped ZrO_2 reveal that codoping considerably decreases the band gap and improves the antimicrobial efficacy of the photocatalyst. Tijani *et al*., 2022 determined how well a C-S codoped ZrO_2 nanoparticles performed well against gram positive (*Salmonella typhi* and *Pseudomonas aeruginosa)* and gram negative (*Escherichia coli*) bacteria. The nanomaterials' antibacterial activity against the chosen bacteria was in the following order: C-S codoped ZrO_2 > C-ZrO_2 > S-ZrO_2 > ZrO_2.

2.7 Theoretical Framework

2.7.1 Density Functional Theory (DFT)

Density Functional Theory is an approach for obtaining approximate solution to a system's many-body Schrödinger equation. In DFT, an interacting system of fermions is defined by its density rather than its many-body wave function. DFT begins with determining the wave function Ψ and the accompanying energy E(Ψ) and progresses to determining the electron density ρ and the corresponding energy E(ρ), from which all system parameters are determined. The electron density plays a key role in determining the ground state features of a system. The electronic, magnetic and structural characteristics of molecular materials, including defects, can be investigated using DFT computational codes (Jones, 2015)**.**

2.7.2 Hohenberg and Kohn (H-K) Theorems

DFT is guided by the Hohenberg and Kohn theorems, which state as follows: -

1st H-K Theorem – The ground state features of many electron systems are solely determined by the electron density ρ(r), as seen in equation 2.1

$$E = E_{(\rho)} \tag{2.1}$$

2nd H-K Theorem – The true ground state density for a system is one that minimises total energy using the functional E(ρ) (Aamir *et al*., 2022).

2.7.3 Kohn-Sham equation.

The Hohenberg and Kohn theorems show that if the electron density functional is known, the total energy of a system may be calculated. The electron density functional yields an effective one-electron Schrödinger equation, known as the Kohn-Sham equation, as shown in equation (2.2).

$$\left[-\frac{\hbar^2}{2m}\left(\frac{\partial^2}{\partial x_i^2}+\frac{\partial^2}{\partial y_i^2}+\frac{\partial^2}{\partial z_i^2}\right)+V_{H(r)}+V_{xc(r)}+V_r\right]\psi_i(r_i)=\epsilon_i\psi_i(r_i) \tag{2.2}$$

where, $V_{H(r)}$ is known as the Hartree potential, $V_{xc(r)}$ is the self-interaction correction in $V_{H(r)}$ and also includes the exchange and correlation contributions to the single electron equations. V_r is the coulomb attraction between the collection of atomic nuclei and the electron. While the single electron solution ψ_i of the Kohn Sham equation is not a quantity of physical interest, its modulus squared, $\psi^*(r_{1,\ldots..}r_N)\psi(r_1,\ldots.r_N)$ and the density of electrons, $\rho(r)=2\sum_i \psi^*{}_i(r)\psi_i(r)$, a function of 3 coordinates at a particular position in space, contains physically observable information. The total energy comprises the sum of single electron energies and the double counting corrections (Sahni, 2004).

2.7.4 Born- Oppenheimer Approximation.

The nuclei have much larger masses compared to electrons and therefore move at much slower speeds. Electrons can therefore be considered to be moving in the field of fixed nuclei. This is known as the Born-Oppenheimer approximation. In this approximation, the kinetic energy of the nuclei is taken to be zero and their potential energy is a constant. The Hamiltonian for the electrons is therefore given by equation (2.3)

$$H^{elec}=-\frac{\hbar^2}{2m}\sum_{i=1}^{N}\left(\frac{\partial^2}{\partial x_i^2}+\frac{\partial^2}{\partial y_i^2}+\frac{\partial^2}{\partial z_i^2}\right)+V_{ee}+V_{en} \tag{2.3}$$

where , $-\frac{\hbar^2}{2m}\sum_{i=1}^{N}\left(\frac{\partial^2}{\partial x_i^2}+\frac{\partial^2}{\partial y_i^2}+\frac{\partial^2}{\partial z_i^2}\right)$ represents the kinetic energy of the electrons , V_{ee} is the coulomb repulsion between electrons and $V_{en}$the coulomb attraction between the electrons and the nuclei (Jorge,1995;Claeys & Simoen, 2011).

2.7.5 Exchange Correlation Potential.

The exchange correlation potential shows the effect of the Pauli's principle and the coulomb potential beyond an electrostatic interaction of the electron. Pauli's exclusion principle does not allow two identical particles to lie in the same quantum state, since this gives rise to repulsion between electrons with parallel spins and is accounted for by the Hartree potential $V_{H(r)}$ in equation (2.2), which is the average repulsive potential experienced by the i^{th} electron due to the remaining N-1 electrons. Therefore, correlation interaction is as a result of Pauli's exchange interaction. There is also correlation motion between electrons of antiparallel spins which arise due to their mutual coulombic repulsion, hence the exchange part. Exchange correlation energy therefore results from Pauli's exchange interaction. The exchange correlation potential is approximated using approximation methods such as the Local Density Approximation (LDA) and Generalised Gradient Approximation (GGA). LDA assumes that the electron density is slowly varying and the inhomogeneous density of a solid or molecule can be calculated using the homogenous electron gas functional. Therefore, LDA substitutes the exchange correlation energy density of an inhomogeneous system by that of an electron gas evacuated at the local density. LDA can be modified by including the gradient of the density into the functional. When the gradient is included in the functional, the functional now belongs to a class of Gradient Approximation (GA) functionals, which take the density of the gradient into account (Perdew *et al.*,1996;Xinlei *et al.*, 1997).

2.7.6 Inductively Coupled Plasma Mass Spectroscopy (ICP-MS).

ICP-MS is a robust analytical method for determining the multi-element composition (qualitatively), concentration (quantitatively), and isotopic abundances of different matrices (Mazarakioti *et al.*, 2022). It is a powerful technique whose application in characterization of nanomaterials has been studied in the last decade (Meermann & Nischwitz, 2018). An ICP-MS instrument has six fundamental compartments, that is;

sample introduction system, an ion source (Inductively Coupled Plasma, ICP), the electrostatic lenses, an interface, a mass spectrometer and a detector (Ammann, 2007). ICP-MS instruments are designed to analyse liquids however, for solid samples, chemical digestion using strong acid(s) or alkali must be carried out. ICP-MS allows determination of elements with atomic mass ranging from 7 to 250, which encompasses Li to U elements in the periodic table (Wilschefski & Baxter, 2019). ICP-MS techniques introduce samples from a liquid via aspiration or pump into a nebulizer where an aerosol is produced that is injected into an argon plasma. In the plasma, the high temperatures cause the atoms in the sample to undergo ionization (Bulska & Wagner, 2016). The m/z of the ion allows for qualitative identification of the isotope or molecule, whilst the amplitude of the ion current is utilized to quantify the amount of the analyte in the original sample(Thomas, 2008).

2.7.7 Ultraviolet-Visible Spectroscopy (UV–VIS)

UV-visible spectroscopy is used to investigate the chemical characteristics of a material. It can be used to determine the physical and electrical structures of organic and inorganic substances. It can be used to determine concentrations and identify unknown compounds (Daniel & Astruc, 2004). When incident light comes into resonance with the conduction band electrons on the nanoparticle's surface, it causes distinct absorbance bands to appear in characteristic spectra. Metal and metal oxide nanoparticles are commonly characterized using wavelengths ranging from 200 to 700 nm (Patra & Baek, 2014).

2.7.8 X-Ray Diffraction (XRD)

XRD is used in the field of nanotechnology to characterize and acquire accurate information regarding the composition, crystal structure, and crystalline grain size of nanoparticles. The analyzed material is finely ground, homogenized, and average bulk composition is determined (Mourdikoudis *et al*., 2018b). From the XRD equipment, the peaks' position and intensity of a sample are compared with the patterns from various diffraction database references, which assists in quantifying the composition of nanoparticles (Raja *et al.*, 2022). The peaks of the XRD pattern play a key role in the identification of the phases as well as the properties of the nanoparticles. In this case, the width of the peak would reveal the average crystalline size of a nanoparticle where

sharp peaks indicate a large size of crystallites, whereas broad peaks indicate smaller crystallites (Biswas & Rangari, 2022).

CHAPTER THREE
MATERIALS AND METHODS

3.1 Research Site

The DFT calculations as implemented in the Quantum ESPRESSO code were executed at the Centre for High Performance Computing in South Africa (CHPC) through remote access. Synthesis of photocatalysts was carried out at the Physics laboratory, Chuka University. The composition and concentration of elements in the synthesised samples was determined at the Kenya Bureau of Standards (KEBS). The structural properties of the samples were done in Geology & Mines, Kenya and in Chuka University, Kenya. The electronic properties were determined at the Chuka University Chemistry laboratory, Kenya. The disinfection capability of the samples was carried out at the biology laboratory, Chuka University, Kenya. The photocatalytic efficacy of the synthesized materials will be evaluated at the chemistry laboratory, Chuka University, Kenya.

3.2 Research Design

The study adopted mixed research approach combining DFT simulations and experimental synthesis to evaluate the phase stability, effects of oxygen vacancy defects and photocatalytic properties of Ca-Mg codoped TiO_2 and ZrO_2 photocatalysts. DFT simulations were carried out using the Quantum ESPRESSO simulation software, focusing on structural optimization and electronic structure analysis. Experimentally, nanoparticles were fabricated through green synthesis technique, and XRD, ICP-MS, and UV-Vis spectroscopy were used for characterization. Rh B degradation in visible light conditions was used to examine its photocatalytic properties, while strains of the bacteria *S. aureus* and *E. coli* were used to assess antimicrobial efficacy. Results of theoretical and experimental methods were compared to validate material performance.

3.3 Materials

Fresh orange peels were obtained from oranges bought at Chuka market. Calcium nitrate ($Ca(NO_3)_2$), magnesium nitrate ($Mg(NO_3)_2$), zirconium oxychloride octahydrate ($ZrOCl_2 \cdot 8H_2O$, 95%), titanium oxysulfate ($TiOSO_4$), Rhodamine B ($C_{28}H_{31}ClN_2O_3$, 90%), deionised water, Phosphate Buffered Saline (PBS), Nutrient Broth and Nutrient Agar were purchased from Kobian (Kenya) Limited and used without any further

purification. Two bacteria cultures, *S. aureus* (ATCC 154008) and *E. coli* (ATCC 25922) were procured from Kenya Medical Research Institute (KEMRI).

3.4 Computational Details

First principle calculations using the density functional theory (DFT) method were carried out using the Open-Source Package for Research in Electronic Structure, Simulation, and Optimization (Quantum ESPRESSO), which uses plane wave basis sets and pseudopotentials. The electronic wave functions were expanded in plane waves up to a cutoff energy of 40 Ry, while the core-valence interaction was treated using ultrasoft pseudopotentials (USPPs). The exchange-correlation was treated using the generalised gradient approximation (GGA), employing the Perdew–Burke–Ernzerhof (PBE) exchange-correlation functional (PBE-GGA). Brookite has an orthorhombic structure with space group pbca (61) while rutile TiO_2 and anatase have tetragonal structures with space groups of I41/amd and P42/mnm with space group numbers 141 and 136, respectively. The P21/c space group, with space group number 14, describes the monoclinic zirconia (m-ZrO_2). The supercells were realized and the atomic locations were obtained using the Visualization for Electronic Structural Analysis (VESTA) visualization program. Then, 2 x 2 x 1 supercells with four units each for brookite and m-ZrO_2 and 2 × 2 × 2 supercells with eight units each for rutile and anatase were built. The number of atoms in each anatase and brookite supercell is 96, of which 32 are titanium and 64 are O, rutile supercell has 48 atoms, where 16 are Ti and 32 are O atoms and m-ZrO_2 supercell consists of 48 atoms, having the composition of 16 Zr and 32 O atoms. Ca-Mg codoped ZrO_2 and TiO_2 models were realized by cationic substitution of Ca & Mg atoms for Ti or Zr atoms. Hence, the obtained configuration is $Ti_{(32-x-y)}Mg_xCa_yO_{(64)}$ for anatase and brookite, $Ti_{(16-x-y)}Mg_xCa_yO_{(32)}$ for rutile and $Zr_{(16-x-y)}Mg_xCa_yO_{(32)}$ for m-ZrO_2. The process of optimizing the bulk structures began with experimental lattice values, and the Broyden–Fletcher–Goldfarb–Shanno (BFGS) quasi-newton method was used to relax the atomic locations of the supercells until the residual forces were less than 10^{-3} Ry/Bohr. The bulk structures were optimized following atomic substitution. For the undoped supercells the K-Point selection employed a Monkhorst–Pack (MP) sampling matrix consisting of (2 x 2 x 3) for m-ZrO_2, (3 x 3 x 5) for brookite, and (4 × 4 × 7) for rutile and anatase. The MP sampling array utilized for the codoped supercells were (2 x 2 x 3) for m-ZrO_2 and brookite TiO_2,

and (3 x 3 x 5) for rutile and anatase TiO_2 polymorphs. Self-consistent cycles and numerical techniques such Davidson iterative diagonalization algorithms were used to determine the electronic ground state energy and assess the Kohn–Sham equation solution. For the density of states calculation, the occupations within the irreducible Brillouin zone were calculated using the linear tetrahedron method with Blöechl's corrections, and the total energy was calculated using the Marzari–Vanderbilt smearing scheme with a Gaussian distribution of 0.05 Ry. The iterations ended at a convergence criterion of 10^{-8} eV. The maximum number of electronic and geometric iterations was set to 100. The relaxation was continued with updated atomic locations if the residual force threshold was not met. Calculations for optimization of structure and electronic properties were typically started from scratch.

3.5 Green Synthesis

3.5.1 Preparation of Orange Peel Extract

To acquire the extracts, the fresh orange fruit was repeatedly washed and peeled. The peels were dried for five hours at 80 °C in an oven until completely dehydrated, and then ground into powder. Add fifty grams of orange peel powder to 250 ml of deionized water, stir with a magnetic stirrer, and heat at 70°C for 2 hours. After cooling to ambient temperature for about 15 minutes, whatman filter paper was used to filter the mixture so as to eliminate any impurities. The colour of the filtrate was noted.

3.5.2 Green Synthesis of Ca-Mg Codoped ZrO_2 NPs

One-pot green synthesis method as per Tijani *et al*., (2022) was adopted for the preparation of Ca-Mg codoped nanoparticles. In this technique, calcium nitrate and magnesium nitrate in various atomic percentage (at%) dopant ratios of Ca:Mg, 6.25%:6.25%, 6.25%:12.5%, and 12.5%:12.5% (corresponding to weight percentage (wt%) of 3.4:3.1, 3.5:6.4, and 7.3:6.6, respectively) as predicted in the DFT simulations, were added to the mixture of 100 ml, 0.15 M zirconium oxychloride octahydrate ($ZrOCl_2 \cdot 8H_2O$) solution and 50 ml aqueous orange peel extract in a beaker and swirled for two hours at 500 rpm, observing the colour changes. Centrifugation was used to separate the nanoparticles for 15 minutes at 1000 revolutions per minute

The nanoparticles were then oven dried at 80 °C for 3 hours and calcined at 1200 °C in a furnace for 3 hours to produce Ca-Mg codoped ZrO_2 nanoparticles at different doping levels. The colour change of the calcined nanoparticles was noted.

3.5.3 Green Synthesis of Ca-Mg Codoped TiO_2 NPs

Ca-Mg codoped TiO_2 was prepared by adding calcium nitrate and magnesium nitrate with different at% dopant ratios of Ca: Mg, 3.125%:3.125%, 3.125%:6.25%, and 6.25%:6.25% (equivalent to wt% of 3.2:2.9, 3.2:5.8 and 6.4:5.8) as predicted in the DFT simulations, was added to a mixture of 100 ml, 0.3 M titanium oxysulfate ($TiOSO_4$) and 50 ml aqueous orange peel extract in a beaker and stirred at 500 rpm for about 2 hours. The nanoparticles were separated by centrifugation at 1000 rpm for 15 minutes and oven dried at 80 °C for 3 hours and calcined at a temperature of 500 °C in a furnace for 3 hours to produce Ca-Mg codoped TiO_2 nanoparticles at different doping levels.

3.6. Sample Characterization

3.6.1. Analysis of Elements

The concentration of elements and composition in the synthesised samples was evaluated by inductively coupled plasma-mass spectrometry (ICP-MS). Samples were digested with a mixture of HNO_3 and H_2SO_4 acids in a microwave digester (Milestone Ethos X, Chuka University) and analyzed using an Agilent 7900 ICP-MS spectrometer (KEBS, Kenya) by the standard calibration method.

3.6.2. Structural Analysis

Powder X-ray diffraction was used to examine the materials' structural characteristics. The Bruker D8 powder diffractometer was used to obtain the patterns from the XRD (Geology & Mines, Kenya). The finely ground powder of the sample was transferred to the sample holder. The patterns were obtained using Cu-Kα X-ray radiation whose wavelength is 1.5418 Å, with a beam of 45kV voltage and a current of 40 milli amperes. Scans were performed in a continuous mode at a rate of 2 ^{o} per minute in the 2θ range of 0-90 ^{o}.

3.6.3 Electronic Properties

Optical properties for codoped TiO_2 and ZrO_2 were determined by use of UV visible absorbance spectroscopy with λ ranging from 200 to 800 nm. The UV-Vis spectra of the samples were analyzed utilizing a Shimadzu 1800 UV-Visible spectrophotometer (Chuka University, Kenya). Using the Tauc graphical approach, the band gaps of the fabricated samples were ascertained using the following equation;

$$(\alpha hv)^{1/n} = A\,(hv - Eg) \tag{3.1}$$

where n indicates the type of electronic transition interband, α is the absorption coefficient, hv is the photon energy, A is a constant and Eg is the band gap. The values of 1/2, 2, 3/2, and 3 for the variable n represent direct permitted, indirect permitted, direct forbidden, and indirect forbidden transitions, respectively(Realpe *et al*., 2021).

3.7 Evaluation of Photocatalytic Activity

The method according to El-Dossoki *et al*., (2021) was adopted with modifications when assessing the photocatalytic efficacy of the synthesized materials. First, pH, starting concentration of dye and adjustment of dosage were performed. In a typical experiment, 20 mg of Ca-Mg codoped TiO_2 or 50 mg of Ca-Mg codoped ZrO_2 photocatalyst sample was put into 50 millilitres of a 10 ppm Rh B dye solution at pH4 and stirred thoroughly using a magnetic stirrer. To achieve the adsorption-desorption equilibrium state, the mixture was then left in the dark for half an hour. After that, the resulting mixture was exposed to visible light of wavelength (400-700 nm) with continuous stirring for 2 hours a portion of the mixture of 5 millilitres was withdrawn at thirty minute intervals, centrifuged, and analyzed utilizing a UV-Vis spectrophotometer (Shimadzu 1800 UV-Vis spectrophotometer; Chuka University) at a wavelength of 554 nm. RhB concentration was determined using a linear regression equation obtained by plotting a calibration curve of RhB within a range of known concentrations. The photocatalytic efficacy of the synthesized samples was determined through the percentage of rhodamine B dye degradation as follows:

$$\text{Degradation percent} = \frac{Co - C}{C_0} \times 100\% \tag{3.2}$$

C_o represents the initial amount of rhodamine B dye, while C represents the remaining amount at a given period of measurement.

3.8 Evaluation of Disinfection Activity

The disinfection activity of the codoped ZrO_2 and TiO_2 NPs was evaluated using colony count method. The experiment was conducted against reference gram negative *E. coli* bacteria (ATCC 25922) and gram positive *S. aureus* (ATCC 154008). Samples and all of the equipment and media were previously sterilized before antibacterial evaluation. First, a few colonies from the pure bacterial cultures were put into 10 ml Nutrient Broth, which was then incubated overnight at 37 °C with shaking (180 rpm) to get log-phase growth. The bacteria concentration was adjusted to about 1×10^4 colony forming units/ml (CFUs/ml) using Phosphate Buffered Saline (PBS). The synthesized nanoparticles were dispersed in deionized water to obtain a desired dopant concentration. Ultra-sonication was performed for 30 minutes to ensure uniform dispersion and prevent agglomeration.1 ml of bacterial solution was combined with 1 ml of nanoparticles and shaken at 100 rpm. The mixture was then subjected to visible light of wavelength (400-700 nm) for the prescribed amount of time:0, 15, 30, 60, 90 and 120 minutes, with the same distance and intensity throughout the experiment. For negative control, samples of bacteria with no photocatalyst were exposed to visible light for equal amount of time. After each exposure time, 100 µl of the sample was obtained and serially diluted in sterile PBS (10^{-1} to 10^{-4}). Approximately 30 millilitres of nutrient agar was placed onto petri dishes and allowed to solidify. To determine the antibacterial rate, 100 µl of each dilution was equally spread on Nutrient Agar in petri dishes and incubated at 37 °C for 24 hours. Each test was performed in triplicates under the same set of conditions for reproducibility. The antibacterial rate of the synthesized samples was calculated by following formula:

$$R = \frac{(c - a)}{c} \times 100\%, \tag{3.3}$$

where '*R'* is the antibacterial rate, '*c'* is the average number of bacterial colony count on control samples (CFU/ml), and *a* is the average number of bacterial colonies on the test samples (CFU/ml) (Chelliah *et al.,* 2023; Tijani *et al*., 2022).

3.9 Ethical and Policy Issues

This work was done with permission from NACOSTI and in line with the principles and guidelines of Chuka University. Contributions from other sources were properly cited and referenced accordingly to avoid plagiarism even in the final report. The final findings were summarized and published as per the policies and regulations of Chuka University.

CHAPTER FOUR
RESULTS AND DISCUSSION

4.1 Introduction

This chapter presents an in-depth analysis of structural properties, phase changes, electronic properties, and impact of oxygen vacancies in Ca and Mg codoped TiO_2 and ZrO_2 phases using the Density Functional Theory (DFT) approach. In addition, the results of characterisation, photocatalytic degradation, and disinfection applications using the novel visible light materials identified in the First principles study are extensively explained.

4.2 Ca-Mg Codoped TiO_2 Polymorphs

In this sub-section, the DFT results of electronic and structural modification of TiO_2 polymorphs via Ca and Mg codoping are presented.

4.2.1 Structural Properties and Phase Stability

VESTA was utilized to generate (2 x 2 x 2) anatase TiO_2 and rutile TiO_2 supercells, as well as a (2 x 2 x 1) brookite TiO_2 supercell, with Ti atoms substituted by Ca and Mg atoms at varying ratio. Figure 4.1 illustrates supercells with 6.25 at% Ca and 6.25 at% Mg doping concentrations.

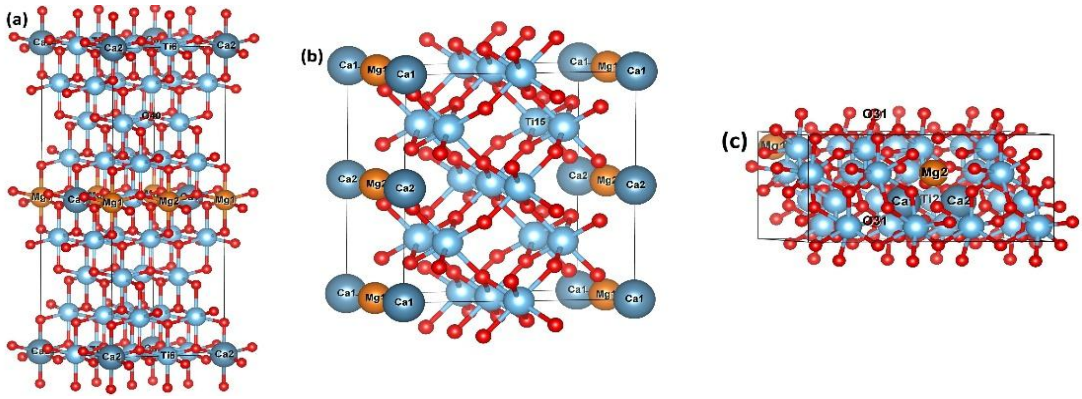

Figure 4.1: Mg - Ca (2 x 2 x 2) codoped supercells of a) anatase TiO_2, b) rutile TiO_2 and c) Mg - Ca (2 x 2 x 1) codoped brookite TiO_2 supercell. The blue and red balls represent titanium and oxygen atoms respectively

Experimental lattice constants were used to do structural optimization for the pristine systems. To begin with, the lattice parameter a was optimized at a constant c/a ratio. Next, the c/a ratio was optimized at the optimum lattice parameter a. After that, the b/a ratio for brookite was reduced to the optimal lattice parameter a and c/a ratio. At varying dopant concentrations, ranging from 3.125 at% to 6.25 at%, which correspond to one and two cationic substitutions within the supercells, respectively, optimization for the Ca-Mg codoped structures was subsequently performed for the three polymorphs. The optimization curves for the lattice constant a for anatase TiO_2 at various dopant concentrations are displayed in Figure 4.2. The configuration $Ti_{(29)}Mg_2Ca_1O_{(64)}$, which represents the substitution of two Mg atoms and one Ca atom in place of Ti atoms within the anatase titanium (iv) oxide lattice, exhibited the lowest total energy among the various dopant concentrations taken into consideration. In comparison to Ca-rich configurations, Mg-rich doped structures are generally more energetically stable due to their lower total energies.

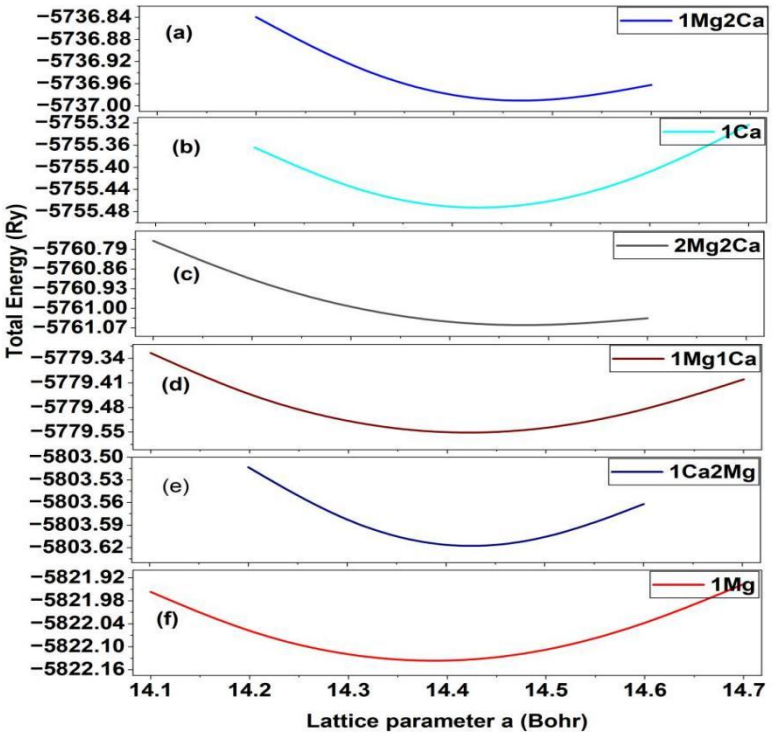

Figure 4.2: Structural optimization for doped anatase TiO_2 with dopant ratio of; a) 6.25 at% Ca + 3.125 at% Mg, b) 6.25 at% Ca + 6.25 at% Mg, c) 3.125 at% Ca, d) 3.125 at% Ca + 3.125 at% Mg, e) 3.125 at% Ca + 6.25 at% Mg and f) 3.125 at% Mg

The same process used for anatase optimization was used to obtain optimization curves for rutile and brookite. The tetragonal (2 x 2 x 2) supercell yielded the lattice parameters for anatase, which are a = b = 3.816 Å, c = 9.693 Å. The lattice parameters for rutile determined by this study are a = b = 4.625 Å, c = 2.989 Å, using the same supercell dimensions as for anatase. The orthorhombic (2 x 2 x 1) supercell was used to compute Brookite's lattice parameters, which are a = 9.184 Å, b = 5.507 Å, and c = 5.143 Å. As seen in Table 4.1, the calculated cell parameters are comparable to those from other DFT and experimental research in the literature.

Table 4.1: The lattice constants of anatase, rutile and brookite of various DFT and experimental studies from literature.

Polymorph	Method	a (Å)	b (Å)	c (Å)	Reference
Anatase	Theoretical studies	3.798	3.798	9.852	Ahmed *et al*., 2012
		3.692	3.692	9.471	Asahi *et al*., 2000
		3.823	3.823	9.612	Qiang & Hong-Hong, 2004
	Experimental studies	3.805	3.805	9.514	Sutrisino, 2012
		3.782	3.782	9.502	Long *et al*., 2010
		3.785	3.785	9.502	Burdett *et al*., 1987
Rutile	Theoretical studies	4.705	4.705	2.966	Khan *et al*., 2012
		4.705	4.705	2.966	Ahmed *et al*., 2012
		4.656	4.656	2.967	Yin *et al*., 2010
		4.630	4.630	2.957	Ma *et al*., 2009
		4.590	4.590	2.960	Ahmed *et al*., 2012; Thilagam *et al*., 2010
	Experimental studies	4.631	4.631	2.989	(Mu'izayanti & Sutrisno, 2018)
		4.587	4.587	2.955	(Conde-Gallardo & Olguin, 2008)
		4.580	4.580	2.950	(Burdett *et al*., 1987)
Brookite	Theoretical studies	9.170	5.442	5.131	Thilagam *et al*., 2010
		9.099	5.595	5.088	Samat *et al*., 2019
		9.263	5.507	5.177	Samat *et al*., 2019
	Experimental studies	9.160	5.436	5.135	Meagher & Lager, 1979

As indicated in Table 4.2, supercells with varying cell features were produced by cationic substitution of Ti with varying amounts of alkaline earth metal dopants, such

as magnesium and calcium. As far as we are aware, no prior findings are available for direct comparison; hence, these findings could be used as a guide for further research. However, for the singly doped systems, we used (2 x 2 x 1) supercells to obtain the following cell parameters: a = b = 3.840 Å , c = 9.988 Å (Mbae & Muthui, 2022), a = b = 4.736 Å , c = 3.221 Å (Mbae & Muthui, 2022), and a = 9.207 Å , b = 5.524 Å , c =5.156 Å (Mbae & Muthui, 2022), respectively. For Ca doped anatase, rutile, and brookite, the cell parameters obtained were a = b = 3.930 Å , c = 3.730 Å , a = 4.974 Å , c = 3.730 Å , and a = 9.247 Å , b = 5.548 Å , c = 5.179 Å respectively. By varying the dopant concentrations and positions within the TiO_2 lattice, the impact of Ca and Mg codoping on TiO_2 phases was investigated in greater detail. Table 4.2 compiles the optimal lattice parameters for the various codoped TiO_2 polymorph combinations.

Table 4.2: Lattice constants for anatase, Rutile and Brookite polymorphs of TiO_2 codoped with Mg and Ca

	2 x 2 x 2 Supercell		Conventional unit cell			
	(Bohr)	(Å)	a (Å)	b (Å)	c (Å)	c/a ratio
Anatase (pure) ($Ti_{(32)}O_{(64)}$)	14.423	7.632	3.816	3.816	9.693	2.540
Mg ($Ti_{(31)}MgO_{(64)}$)	14.385	7.612	3.806	3.806	9.698	2.548
Ca ($Ti_{(31)}CaO_{(64)}$)	14.427	7.634	3.817	3.817	9.730	2.549
CaCa ($Ti_{(30)}Ca_{(2)}O_{(64)}$)	14.463	7.654	3.827	3.827	9.778	2.555
MgCa ($Ti_{(30)}MgCaO_{(64)}$)	14.419	7.630	3.815	3.815	9.744	2.554
MgMgCa ($Ti_{(29)}Mg_{(2)}CaO_{(64)}$)	14.424	7.633	3.817	3.817	9.766	2.559
CaCaMg ($Ti_{(29)}MgCa_{(2)}O_{(64)}$)	14.464	7.654	3.827	3.827	9.809	2.563
MgMgCaCa ($Ti_{(28)}Mg_{(2)}Ca_{(2)}O_{(64)}$)	14.476	7.660	3.830	3.830	9.817	2.563
Rutile (pure) ($Ti_{(16)}O_{(32)}$	17.478	9.249	4.625	4.625	2.989	0.646
Mg ($Ti_{(15)}MgO_{(32)}$)	17.462	9.240	4.620	4.620	3.077	0.666
Ca ($Ti_{(15)}CaO_{(32)}$)	17.473	9.246	4.623	4.623	3.125	0.676
CaCa ($Ti_{(14)}Ca_{(2)}O_{(32)}$)	17.556	9.290	4.645	4.645	3.141	0.676
MgCa ($Ti_{(14)}MgCaO_{(32)}$)	17.465	9.242	4.621	4.621	3.039	0.658
MgMgCa ($Ti_{(13)}Mg_{(2)}CaO_{(32)}$)	17.578	9.302	4.651	4.651	3.110	0.669
CaCaMg ($Ti_{(13)}MgCa_{(2)}O_{(32)}$)	17.725	9.380	4.690	4.690	3.551	0.757
MgMgCaCa ($Ti_{(14)}Mg_{(2)}Ca_{(2)}O_{(32)}$)	17.657	9.343	4.672	4.672	3.153	0.675
	2 x 2 x 1 Supercell		Conventional unit cell			
	(Bohr)	(Å)	a (Å)	b (Å)	c (Å)	c/b ratio

Table 4.2 (Continued)

Brookite (pure)	34.710	18.368	9.184	5.507	5.143	0.934
Mg ($Ti_{(31)}MgO_{(64)}$)	34.830	18.431	9.216	5.474	5.161	0.943
Ca ($Ti_{(31)}CaO_{(64)}$)	34.970	18.505	9.253	5.524	5.181	0.938
MgCa ($Ti_{(30)}MgCaO_{(64)}$)	35.100	18.574	9.287	5.572	5.182	0.930
MgMgCa ($Ti_{(29)}Mg_{(2)}CaO_{(64)}$)	35.220	18.638	9.319	5.591	5.200	0.930
CaCaMg ($Ti_{(29)}MgCa_{(2)}O_{(64)}$)	34.817	18.424	9.212	5.582	5.251	0.940
MgMgCaCa ($Ti_{(28)}Mg_{(2)}Ca_{(2)}O_{(64)}$)	34.920	18.479	9.240	5.599	5.174	0.924

Volume distortions and variation in lattice parameters was observed on addition of Ca and Mg dopants into the TiO_2 polymorphs. The observed size fluctuation can be explained by the substitution of divalent cations for Ti^{4+} , which is predicted to result in atomic rearrangements as the atoms nearest the impurity strengthen their bond with the lattice (Khan & Han, 2023 ; Foo *et al*., 2021). It was more challenging to incorporate Ca^{2+} ions into the TiO_2 crystal lattice than Mg^{2+} ions due to the forces created in the crystal system during the cationic substitution. This is explained by the fact that Ca^{2+} ion has a larger ionic radius at 1.00 Å than Ti^{4+} ion, which is 0.605 Å, but Mg^{2+} ion has a relatively comparable ionic radius at 0.72 Å, which is larger than Ti^{4+} (Thongyong *et al*., 2023 ; Shannon, 1976). As shown in Table 4.2, the addition of these divalent cations has the noteworthy effect of stabilizing the tetragonal structure. In the doped rutile and anatase systems, the c/a ratio rises, but more so for Ca^{2+} doped structures than for Mg^{2+} doped ones. The addition of Yb^{3+}, which has a larger ionic radius of 0.89 Å, to the TiO_2 lattice was shown to stabilize the anatase phase in a similar way by lowering the lattice vibration frequency and red-shifting the Raman peak (Sun *et al*., 2020b). The synergistic effect of differing ionic radii and charge rearrangement of the codopants have a phase stabilizing effect while inducing the appropriate production of charge carriers which has been proven to boost the photocatalytic performance of TiO_2 polymorphs (Khatun *et al*., 2020).

Lattice constants of TiO_2 systems codoped with other elements are shown in Table 4.3.

Table 4.3: Lattice parameters for anatase TiO_2 codoped with other elements

Method	codoped samples	a (Å)	b (Å)	c (Å)	Reference
Theoretical studies	Sc- C codoped TiO_2	3.861	3.861	9.769	Xiong *et al*., 2020
	Fe-N codoped TiO_2	3.807	3.861	9.682	Gul *et al*., 2018
	Cu-S codoped TiO_2	3.858	3.858	9.897	Su *et al*., 2016
Experimental studies	N-F codoped TiO_2	3.789	3.789	9.512	Zhao *et al*., 2017
	Fe-N codoped TiO_2	3.792	3.792	9.535	Realpe Jimenez *et al*., 2021
	F-Cl codoped TiO_2	3.782	3.782	9.502	Fillipatos *et al*., 2019

The results show lattice distortions of the codoped TiO_2 samples on codoping, which is attributed to the mismatch in the ionic radius of the dopant ions and the host ion (Khan & Han, 2023).

4.2.2 Electronic modifications of the TiO_2 polymorphs

For the codoped polymorphs, the Projected Density of States (PDOS) and Total Density of States (TDOS) were computed. All of the codoped crystal systems showed changes in occupation close to the Fermi level, which is important for photo-driven technology. The TDOS of the codoped anatase TiO_2 crystal systems at various dopant levels is displayed in Figure 4.3. The valence band states intersected the Fermi level and the Fermi level moved to lower energies in all cases. At greater dopant concentrations, the formation of unoccupied states is more noticeable.

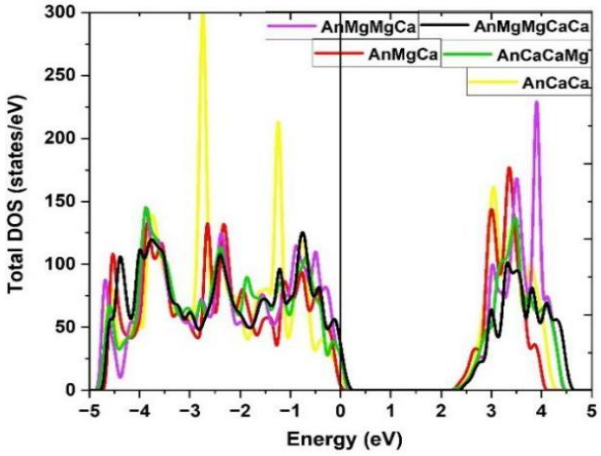

Figure 4.3: TDOS of Ca-Mg codoped anatase TiO_2 polymorph: 6.25 at% Ca + 3.125 at% Mg (AnCaCaMg), 6.25 at% Ca + 6.25 at% Mg (An MgMgCaCa), 3.125 at% Ca + 3.125 at% Mg (AnMgCa), 3.125 at% Ca + 6.25 at% Mg (AnMgMgCa) and 3.125 at% Mg + 6.25 at% Ca (AnCaCaMg)

The lowest energy Ca-Mg codoped anatase system among the various concentrations considered in this study has a concentration of 6.25 at% Mg + 3.125 at% Ca (An

Ca2Mg), i.e. ($Ti_{(29)}Mg_{(2)}CaO_{(64)}$), corresponding to two cationic substitutions with Mg and one cationic substitution with Ca within the (2 x 2 x 2) anatase supercell. The TDOS of this system is shown in Figure 4.4 together with the TDOS for pure anatase. The concentration of 6.25 at% Mg + 3.125 at% Ca (An Ca_2Mg), i.e. ($Ti_{(29)}Mg_{(2)}CaO_{(64)}$), is the lowest energy Ca-Mg codoped anatase TiO_2 system among the different concentrations taken into consideration in this study. This corresponds to two cationic substitutions with magnesium atoms and one cationic substitution with calcium atom within the (2 x 2 x 2) anatase TiO_2 supercell. The TDOS for the pristine anatase TiO_2 and the Ca - Mg codoped (6.25 at% Mg + 3.125 at% Ca) for this system is displayed in Figure 4.4.

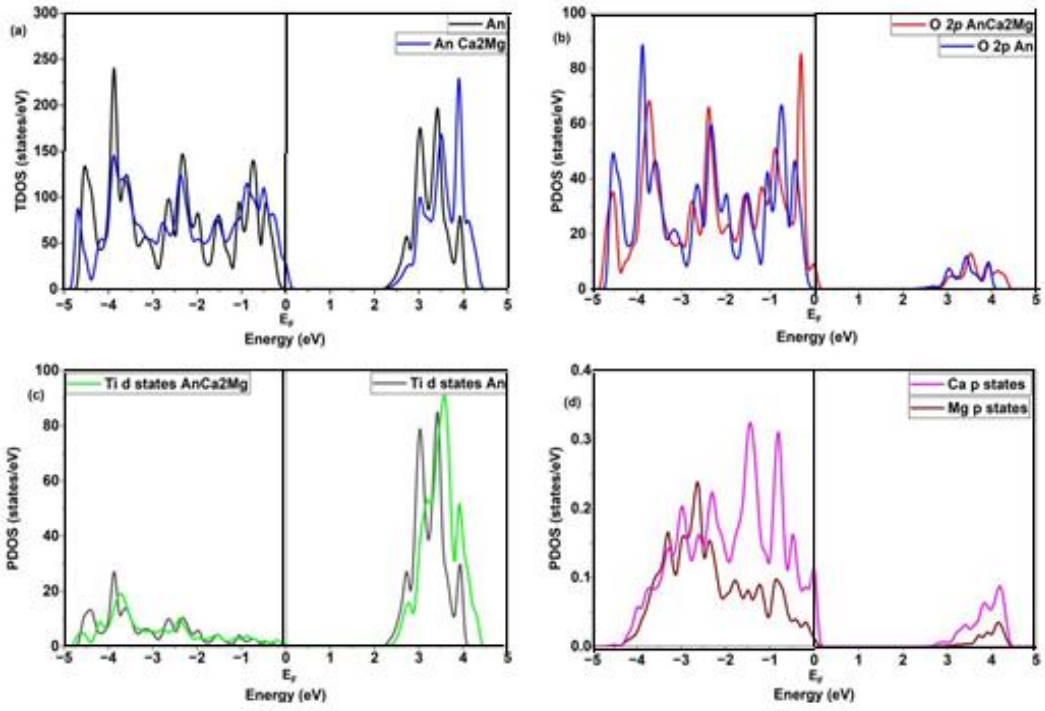

Figure 4.4: 6.25 at% Mg + 3.125 at% Ca codoped anatase TiO_2 (AnCa2Mg) and pristine anatase TiO_2 (a) TDOS, (b) Oxygen *2p* PDOS, (c) Titanium *3d* PDOS and (d) PDOS of Calcium and magnesium *p* states for 6.25 at% Mg + 3.125 at% Ca codoped anatase TiO_2.

Figure 4.4 (b) shows the Projected Density of States (PDOS) of the unoccupied states in the Ca-Mg codoped system, where the O *2p* states are detected slightly above the Fermi level of the Ca-Mg codoped system, as opposed to the pristine system depicted in the same figure. Figure 4.4 (c) shows that the empty states slightly above the Fermi level do not have Ti nature. The inclusion of the divalent impurity atoms in the TiO_2

lattice does not significantly alter the energy of the Ti states, with the exception of a slight shift toward higher energies. Figure 4.4 (d) illustrates the role of dopant impurity states. They are found to contribute near the Fermi level's edge of occupied states, in the same energy area as the O *2p* levels. The overlap causes hybridization of the dopant states with O *2p* and Ti *3d* levels occupying the same energy region, producing charge redistribution due to electron deficit and the formation of two holes per dopant ion, which is caused by the substitution of Ti^{4+} by divalent dopant cations.

The electronic structure modifications observed in rutile and brookite follow a similar trend to those observed in anatase. Figure 4.5 a – d shows the TDOS of pure rutile compared to that of Ca-Mg codoped rutile, as well as the orbital contribution of the individual atoms near the Fermi level.

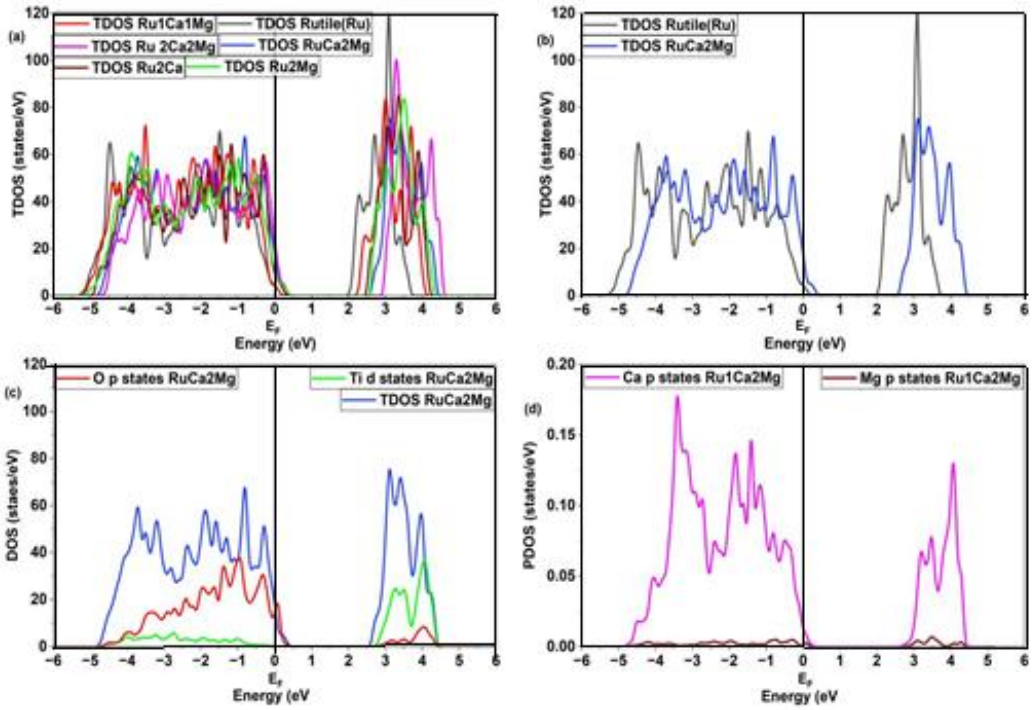

Figure 4.5: (a)TDOS pristine and Ca-Mg codoped rutile at varying dopant ratios, (b) TDOS of 3.125 at% Ca + 6.25 at% Mg codoped rutile (RuCa2Mg) and pure rutile, (c) TDOS, O 2*p* &Ti 3*d* PDOS for 3.125 at% Ca + 6.25 at% Mg codoped rutile and (d) PDOS of magnesium and calcium *p* states for 3.125 at% Ca + 6.25 at% Mg codoped rutile.

The TDOS of pristine brookite TiO_2 and Ca-Mg codoped brookite TiO_2 are displayed in Figure 4.6a–d, together with the orbital contributions of the constituent atoms. The occupied states close to the Fermi level in all titania Ca-Mg codoped systems are primarily ascribed to oxygen, magnesium, and calcium states, whereas the unoccupied

states are primarily of a Ti character. As seen with C-B codoping of TiO_2, the parent material's O orbitals and the added magnesium & calcium dopant valence band orbitals are mixed on or above the Fermi level (Glover *et al*., 2016).

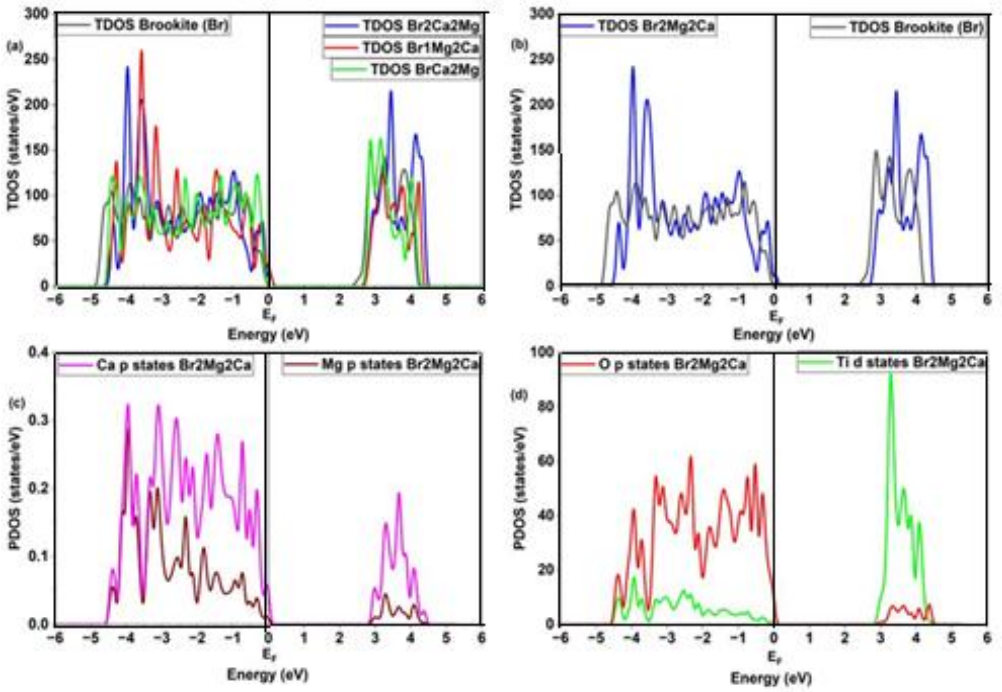

Figure 4.6: (a) TDOS of pristine and Ca-Mg codoped brookite TiO_2 at varying dopant concentrations, (b) TDOS 6.25 at% Ca + 6.25 at% Mg codoped brookite-$Ti_{(28)}Mg_{(2)}Ca_{(2)}O_{(64)}$ (Br2Mg2Ca) and pure brookite, (c) PDOS of Mg and Ca *p* states in 6.25 at% Ca + 6.25 at% Mg codoped brookite and (d) O 2*p* &Ti 3*d* PDOS in 6.25 at% Ca + 6.25 at% Mg codoped brookite.

The differences between the Valence Band Maximum (VBM) and Conduction Band Minimum (CBM) in pure brookite TiO_2 and 6.25 at% Mg + 6.25 at% Ca codoped brookite ($Ti_{(28)}Mg_{(2)}Ca_{(2)}O_{(64)}$) are depicted in the band structures in Figure 4.7. In contrast to pure brookite, the codoped system's valence band maximum intersects the Fermi level quite extensively and the conduction band shifts slightly to higher energies. The band structures in Figure 4.7 show the variations of the Valence Band Maximum (VBM) and the Conduction Band Minimum (CBM) in the case of pristine brookite and 6.25 at% Mg + 6.25 at% Ca codoped brookite ($Ti_{(28)}Mg_{(2)}Ca_{(2)}O_{(64)}$). The VBM of the codoped system intersects the Fermi level quite significantly compared to pristine brookite, while the conduction band shifts slightly to higher energies.

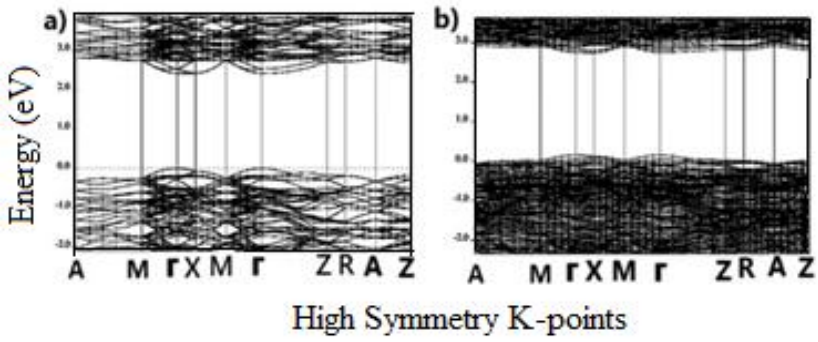

Figure 4.7: Band structures patterns for (a) pure brookite TiO_2 and (b) Ca-Mg codoped brookite TiO_2 ($Ti_{(28)}Mg_{(2)}Ca_{(2)}O_{(64)}$)

Due to the holes that the divalent cation dopants introduced into the systems, there are notable unoccupied O *2p* states located 0.1 eV above the Fermi level. More charge carriers are made available by the hybridized states of the codoped systems, which raise the valence band edge and increase the intersection of orbitals with the Fermi level, particularly at higher dopant concentrations. Numerous theoretical investigations, including the codoping of N-Si in a 48-atom anatase supercell, Cr-N in a 108-atom anatase supercell, and N-C in a 72-atom anatase supercell, have revealed similar findings. For codoped systems, the impurity bands have been linked to better visible light responsiveness (Sun *et al*., 2020b).

4.2.3 Electronic Structure modification by oxygen vacancies

Oxygen vacancies have been found to enhance the photocatalytic performance of titanium (iv) oxide phases by changing the crystal structure electronic properties (Bitsos *et al*., 2025). The influence of oxygen vacancy was investigated by removing an oxygen atom from pure anatase supercell. The results of oxygen vacancy (O_v) formation are examined by comparing the TDOS plots of pure anatase and oxygen deficient pure anatase, as shown in Figure 4.8

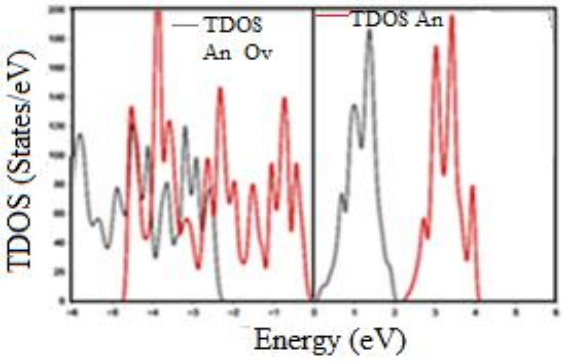

Figure 4.8: TDOS for pure anatase and Oxygen deficient pure anatase

Removing an oxygen atom resulted in the shifting of the valence band maxima to lower energies by about 2 eV. Localized donor states resulting from oxygen vacancies are formed below TiO_2 conduction band. These states are generated by electrons occupying Ti *3d* orbitals near the vacancy site (Alotaibi *et al*., 2023).For further understanding of the oxygen vacancy's impact on electronic modification for codoped anatase TiO_2, analysis of oxygen defective pure and codoped anatase TiO_2 TDOS are shown in Figure 4.9.

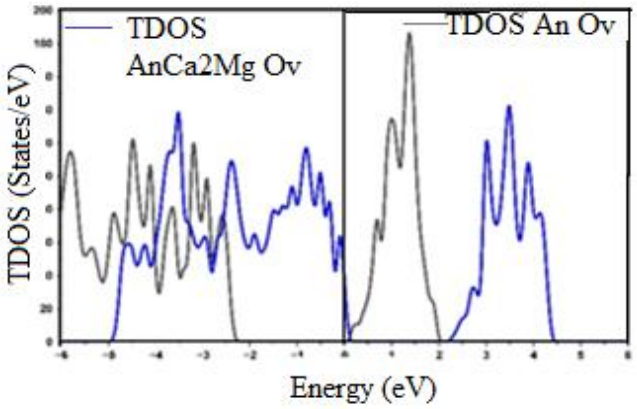

Figure 4.9: TDOS oxygen defective pure and Ca-Mg codoped anatase TiO_2

The findings of codoping anatase with Ca and Mg dopants demonstrate a notable valence band shift of Ca-Mg codoped anatase TiO_2 toward higher energies, resulting in band gap narrowing and increased energy absorption. Figure 4.10 show the formation of midgap states, which implies that band gap reduction comes from the synergetic effect of Ti^{3+} states, oxygen vacancy defect energy states, and Ca and Mg impurity states.

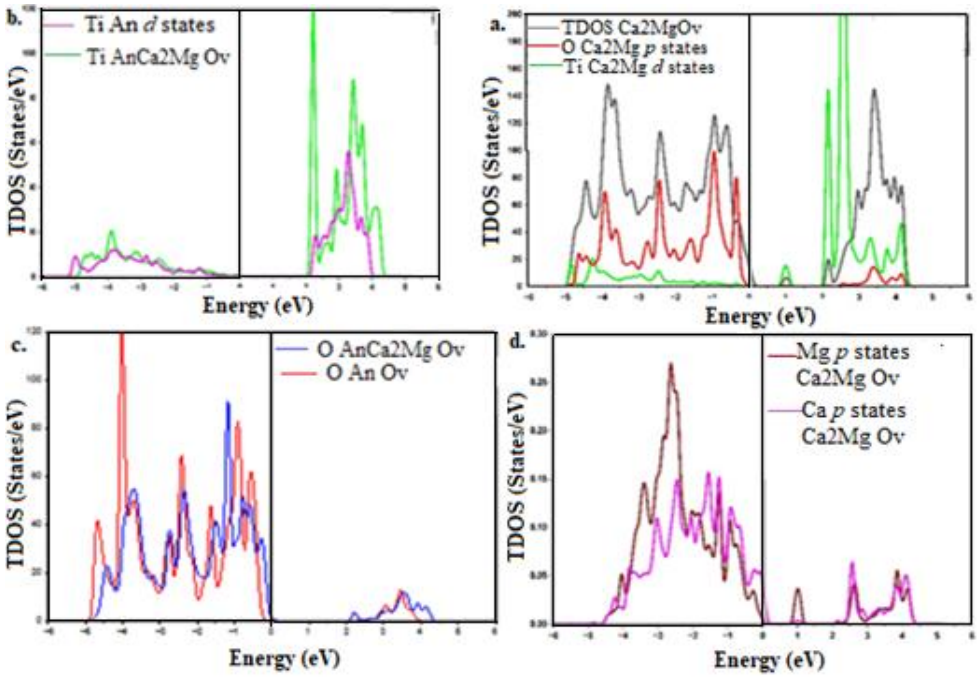

Figure 4.10: (a) TDOS and PDOS oxygen vacancy defective Ca-Mg codoped anatase TiO_2 (b) PDOS Ti states for pure and oxygen vacancy defective Ca-Mg codoped anatase (c) PDOS oxygen states for oxygen defective pure and codoped anatase (d) PDOS Mg and Ca states in Ca-Mg codoped anatase TiO_2.

Figure 4.10 a) shows the band gap of Ca-Mg codoped anatase narrows to roughly 1.7 eV, resulting in a red shift of the absorption edge. This is nearly identical to the experimental findings of this study, which indicated a red shift of Ca-Mg codoped anatase TiO_2 through reduction of bandgap to 1.92 eV. Furthermore, the produced midstates act as traps for photogenerated electron enhancing both charge separation and photocatalytic performance of Ca-Mg codoped anatase photocatalysts. The TDOS for oxygen deficient pure and Ca-Mg codoped rutile are as shown in Figure 4.11.

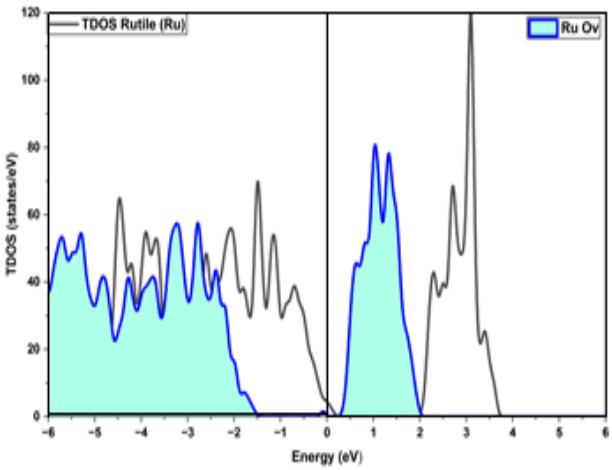

Figure 4.11: TDOS oxygen deficient pure rutile phase and Ca-Mg codoped rutile

The formation of oxygen vacancies in pure rutile TiO_2 resulted in the creation of donor states below the conduction band and a shift of the valence band maximum to lower energy. This is because oxygen vacancies cause the production of Ti^{3+} sites, which provide localized states in the bandgap that have been shown to enhance photocatalysis (Bitsos *et al*., 2025).

Electronic properties modification on removal of an oxygen atom in pure and codoped (2 x 2 x 1) brookite supercell was investigated by plotting TDOS of oxygen deficient pure brookite TiO_2 and Ca-Mg codoped TiO_2 are depicted in Figure 4.12.

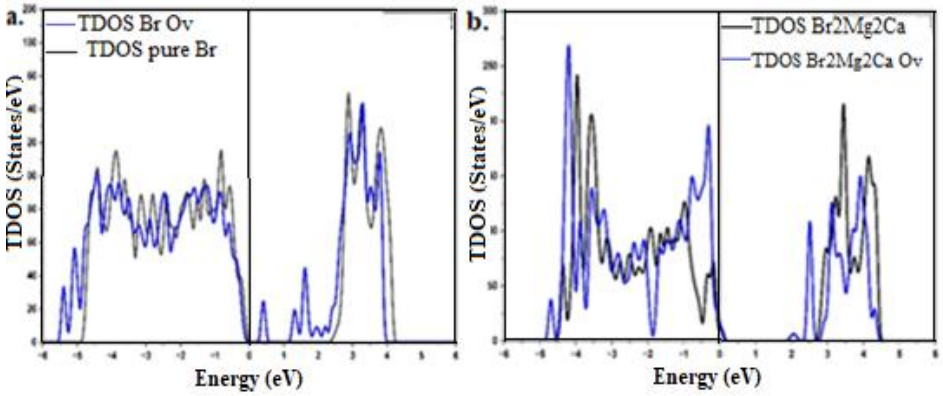

Figure 4.12: (a) TDOS of pure brookite and oxygen deficient pure brookite TiO_2 (b) TDOS of Ca-Mg codoped brookite and oxygen deficient Ca-Mg codoped brookite TiO_2

For the oxygen deficient pure brookite TiO_2 in Figure 4.12 (a), donor levels are formed within the band gap between 0-2 eV above the Fermi level, narrowing its width. These

donor states have been reported to act as trapping sites of photogenerated charge carriers and efficient in improving visible light absorption hence improving photocatalytic efficacy (Guan *et al.*, 2023).To understand the contribution of Ca and Mg impurity states the TDOS of oxygen deficient Ca-Mg codoped brookite TiO_2 and PDOS of Ca and Mg states are analysed as shown in Figure 4.13.

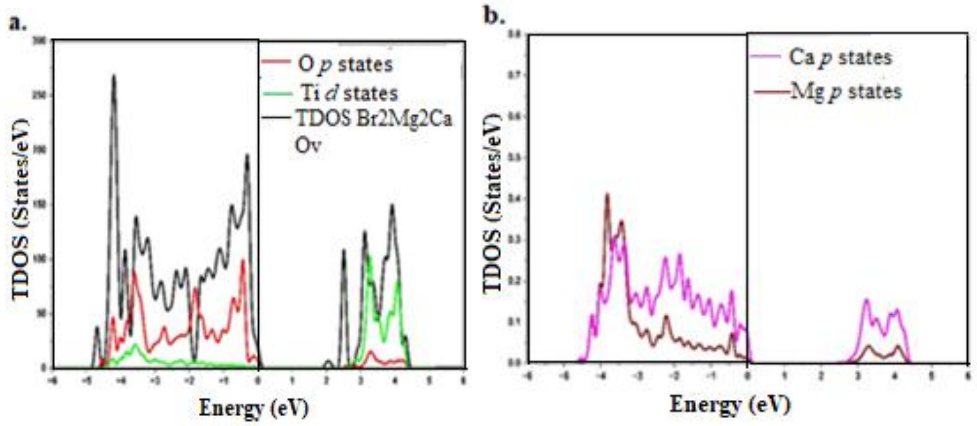

Figure 4.13: a) TDOS and PDOS of oxygen deficient Ca-Mg codoped brookite TiO_2 b) PDOS of Ca and Mg states in Ca-Mg codoped brookite.

As seen in Figure: 4.13 a) When brookite TiO_2 is codoped with Ca and Mg, the valence band maximum intersects the Fermi level, the midgap states increase near the conduction band minimum, and the Fermi level shifts to lower energies. Divalent Ca and Mg dopants substitute Ti^{4+} ions, resulting in charge compensation through formation of oxygen vacancies or Ti^{3+} centers. This boosts extra midgap states and narrows the bandgap. Furthermore, as is evident in Figure 4.13 b) the Ca and Mg impurity orbitals overlap with O *2p* and Ti *3d* contributing to the enlarging of midstates and raising the valence band maximum to higher energy.

4.3 Ca-Mg Codoped ZrO_2

The electronic and structural properties of monoclinic zirconium (iv) oxide (m-ZrO_2) codoped with alkaline earth metals (Mg and Ca) will be covered in this section. The electronic characteristics of tetragonal zirconium (iv) oxide (t-ZrO_2) will be examined so as to explain the observed modifications in electronic structure of codoped systems. We'll also discuss about how introduction of oxygen deficiency modify the electronic properties of the monodoped and codoped systems.

4.3.1 Structural Properties and Phase Stability

The ZrO_2 monoclinic phase which is the stable phase at ambient temperature is described by *P*21/*c* space group. Figure: 4.14 shows the supercell of Ca-Mg codoped (2 x 2 x 1) ZrO_2 obtained using VESTA visualization software whose parameters were used in this work in the DFT calculations.

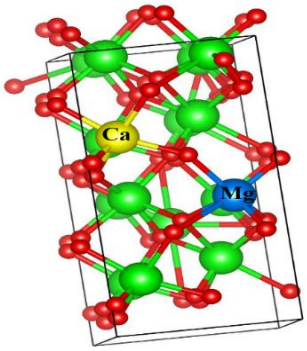

Figure 4.14: Ca-Mg codoped (2 x 2 x 1) ZrO_2 supercell. Atoms of oxygen and zirconium are represented by the red and green balls, respectively.

At varying dopant concentrations, from 6.25 at% to 12.5%, which correspond to one and two cationic substitutions within the supercells, respectively, optimization for Ca-Mg codoped ZrO_2 was subsequently conducted. The optimization curves for the lattice parameter a for the codoped supercells at various dopant concentrations are displayed in Figure 4.15.

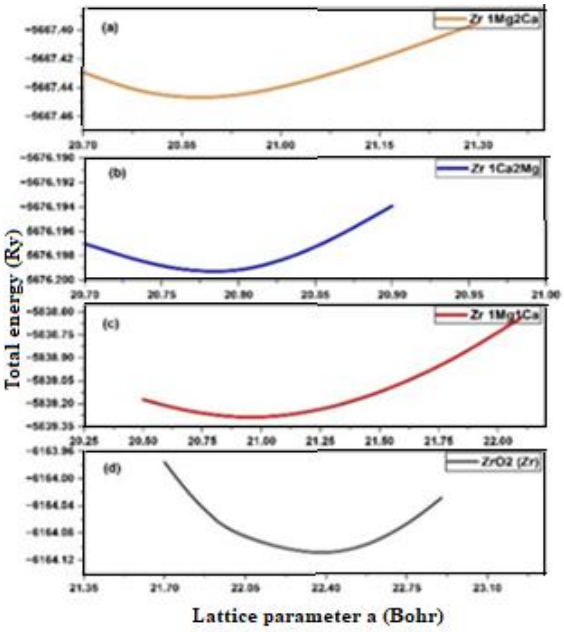

Figure 4.15: Structural Optimization for lattice parameter of Zr pristine and Ca-Mg codoped systems

Among various dopant ratios considered, the 6.25 at% Ca + 6.25 at% Mg codoped configuration, $Zr_{(14)}Mg_1Ca_1O_{(32)}$, matching the replacement of one Mg atom and one Ca atom in the place of Zr atoms in ZrO_2 lattice structure of the codoped system had the least total energy. Table 4.4 shows lattice parameters of a) (2 x 2 x 1) m-ZrO_2 supercells for pure & singly doped systems as obtained from our previous work (Mbae & Muthui, 2022), and the Ca-Mg codoped ZrO_2

Table 4.4: Lattice parameters pure, monodoped and codoped ZrO_2

	a (Å)	b(Å)	b/a	c (Å)
m-ZrO_2	11.853	10.972	0.926	5.369
6.25% Mg - ZrO_2	11.642	10.943	0.940	5.310
6.25% Ca - ZrO_2	11.589	11.009	0.950	5.296
6.25% Ca + 6.25% Mg - ZrO_2	10.400	9.900	0.952	4.905

The b/a ratio rises from 0.926 in m-ZrO_2 to 0.940, 0.950, and 0.952 in Mg doped, Ca doped, and Ca-Mg codoped ZrO_2, respectively, as a result of doping with Mg and Ca. It is clear that the addition of dopants tends to tetragonalize the monoclinic crystal structure as the b/a ratio approaches unity. A similar observation was made on yttrium doping of m - ZrO_2 where the lattice parameters changed from a = 10.1788 Å, b = 10.3742 Å to a = 10.2223 Å, b = 10.3765 Å with 3.23% Y doping and a = 10.2386 Å and b = 10.3711 Å for 6.67% Y doping, respectively (Gebresilassie, 2016). These findings provide an explanation for why Ca doping was previously thought to contribute to the ZrO_2 mesoporous structure's increased stability at high calcination temperatures for biological applications (Tana *et al*., 2020), and how solutes like MgO, CaO, and Y_2O_3 help to lower the temperature at which the tetragonal phase transforms into the cubic phase (Garcia *et al*., 2006).Codoping has also been found to considerably enhance the stability of monoclinic zirconium (iv) oxide crystal structure. Kumar *et al*., (2025) showed lattice distortion and transformation of the m- ZrO_2 crystalline phase to the tetragonal ZrO_2 phase on codoping m-ZrO_2 with roughly 6–15 mol% Gd_2O_3 and Y_2O_3. Khajavi *et al*., (2020) identified the phase transition as arising from the substitution of Zr^{4+} ions with ions of a lower or larger ionic radius, leading to the expansion or contraction of the lattice and the formation of oxygen vacancies. From this section it is evident that the Mg and Ca dopants distort the structure of the m-ZrO_2

by adjusting the b/a ratio of the cell and can be considered to be used as dopants for partially stabilizing the tetragonal phase at lower temperatures, where the tetragonal phase may co-exist with the monoclinic phase. The experimental observation of partially stabilized zirconia with a tetragonal phase along with the other two phases, which occurs when the stabilizer content is insufficient for the formation of the cubic phase, as reported for 2–5% of Yttria doping, may be explained by this result (Fedorov & Yarotskaya, 2021).

4.3.2 Electronic structure modifications of monodoped and codoped ZrO_2

Plotting the Total Density of States (TDOS) and Projected Density of States (PDOS) of m-ZrO_2 and t-ZrO_2 facilitated the study of their electronic properties, as seen in Figure 4.16.

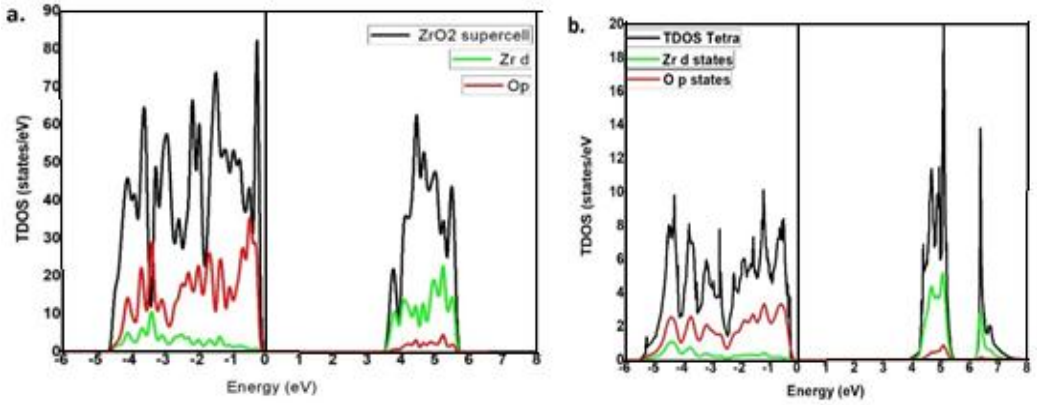

Figure 4.16: Total Density of States (TDOS) and Projected Density of States (PDOS) for: a) m-ZrO_2 and b) t-ZrO_2

It is evident that in both situations, the lowest energy unoccupied states are primarily of Zr *d* character, which is consistent with the finding by Milman *et al*., (2009), while the valence states next to the Fermi level are primarily composed of the O *2p* orbitals. The TDOS of t-ZrO_2, as shown in Figure 4.16b), increase less gradually, while the maximal valence band edge of the TDOS for the m-ZrO_2, which is located just below the Fermi level, increases smoothly. Li *et al.*, (2017) describes the tetragonal ZrO_2 and cubic ZrO_2 as having an enhanced stepping feature near the edge of the occupied states, just below the Fermi level. Another significant distinction is that the Zr *d* orbitals of t-ZrO_2 exhibit a split e_g - t_2g in the unoccupied states, while the Zr *d* orbitals of m-ZrO_2 do not. The symmetry of a cubic or tetragonal crystal structure is the source of this feature, according to crystal field theory. The unoccupied states, which

are mainly composed of Zr *d* orbitals in t-ZrO_2, show an e_g - t_2g splitting between doubly degenerate and triply degenerate orbitals made up of the higher energy, d_{xy}, d_{xz}, and d_{yz} orbitals, and the lower energy, dx^2-dy^2 and dz^2 orbitals, respectively. As per the explanation provided by Ricca *et al*., (2015), this feature is absent for m-ZrO_2 in Figure 4.16 a), where the Zr *d* orbitals are composed of a single band.

Figure 4.17 shows: a) TDOS and PDOS for magnesium doped monoclinic ZrO_2, b) PDOS for magnesium *p* states, c) TDOS and PDOS for Mg-Ca codoped ZrO_2 d) TDOS and PDOS for t-ZrO_2

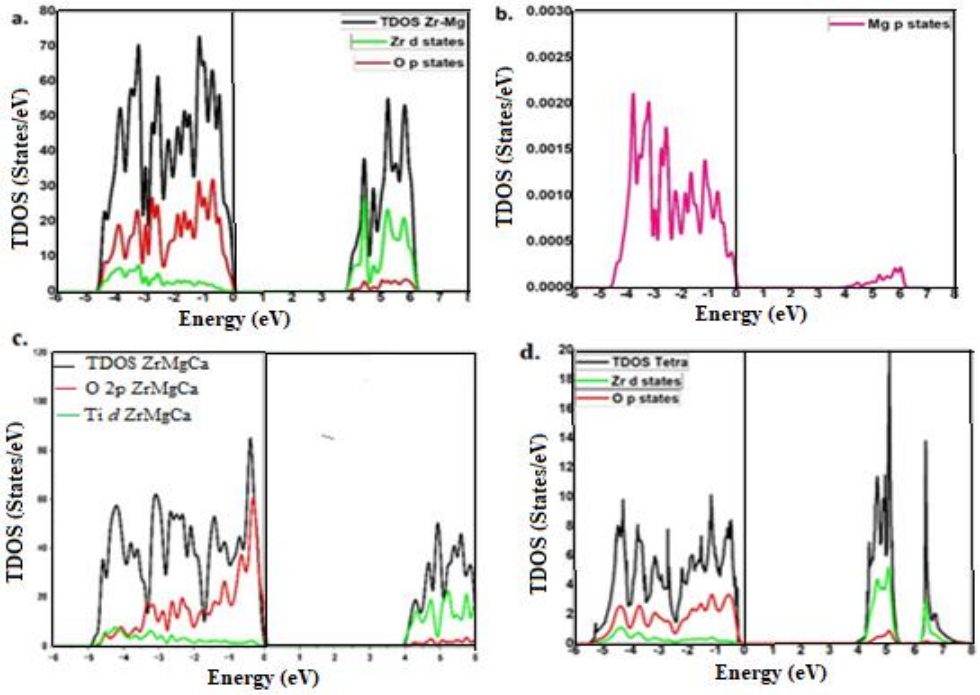

Figure 4.17: a) PDOS and TDOS for magnesium doped ZrO_2 b) PDOS for magnesium doped ZrO_2 c) PDOS and TDOS for Ca-Mg codoped ZrO_2 d) TDOS and PDOS for t-ZrO_2

Figure 4.17 (a) and (c) display the total density of states of magnesium doped zirconium (iv) oxide and Ca-Mg codoped ZrO_2. As can be observed, the Zr *d* states in the unoccupied levels begin to separate, and both share similarities with t-ZrO_2 at the border of the valence band states below the Fermi level. The occupation of magnesium *p* states in Figue 4.17 (b) illustrates the contribution of the dopant ion to the modification near the TDOS edge, just below the Fermi level. In addition to the zirconium 5*d* and oxygen 2*p* levels, the magnesium *p* states have similar energy ranges

and would be implicated in hybridization. Furthermore, a shift in the Fermi level nearer the edge of the valence states is seen. Given that a Zr^{4+} ion has been replaced by a dopant with the oxidation state +2, this could be explained via charge compensation (Mardare *et al*., 2024). Figure 4.18, which displays the band structures for monoclinic zirconium (iv) oxide and magnesium doped zirconium (iv) oxide, clearly shows how, in contrast to monoclinic ZrO_2, the Fermi level shifts in magnesium doped monoclinic ZrO_2 towards the valence band.

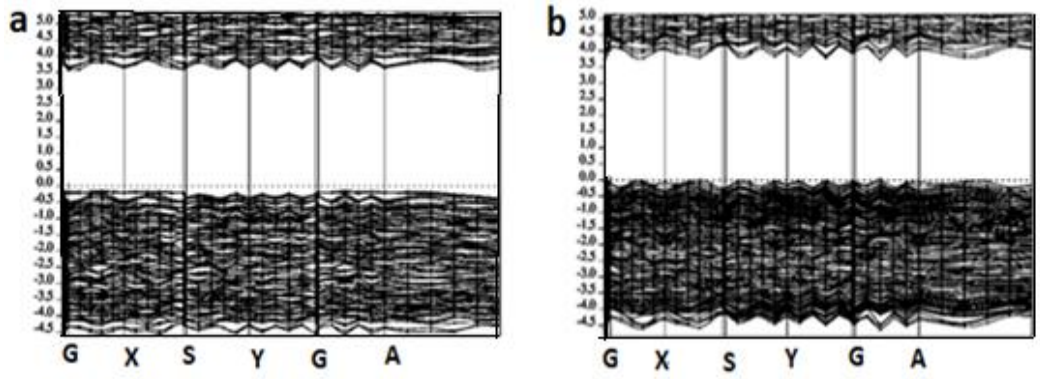

Figure 4.18: Band structure for a) monoclinic zirconium (iv) oxide and b) magnesium doped zirconium (iv) oxide

Given the variations in the b/a ratio with calcium doping, as shown in Table 4.3, it is not surprising that Figure 4.19 shows a significant feature at the border of the valence states below the Fermi level in the total density of states of Calcium doped zirconium (iv)oxide. As seen in Figure 4.19 (b), calcium dopant states occupied higher energies at the valence state border, slightly below the Fermi level.

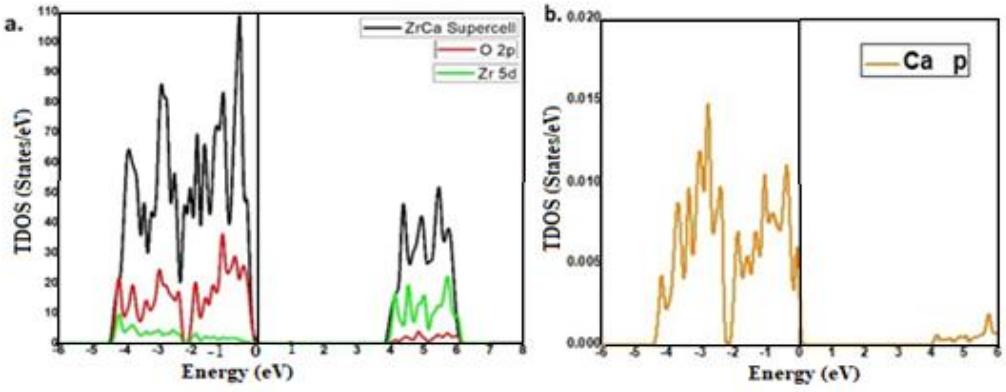

Figure 4.19: a) PDOS and TDOS of Ca-ZrO_2 b) PDOS of calcium states in Ca-ZrO_2

In contrast the m-ZrO_2 system (Figure 4.18 a), the Fermi energy shifts towards the valence band edge in the calcium-doped zirconium (iv) dioxide band structure, as shown in Figure 4.20.

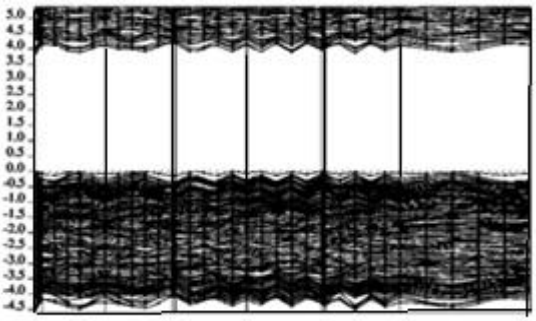

Figure 4.20: Band structure of ZrO_2 doped with calcium

Doping with Ca and Mg has so far been demonstrated to tetragonalize the crystal structure, move the Fermi level towards the valence band, and create dopant states at the edge of valence states below the Fermi level. Ca and Mg codoping had a considerable influence on the electronic modification of the monoclinic zirconium (iv) oxide crystal structure. Figure 4.21 shows the TDOS of pure and Mg-Ca codoped ZrO_2.

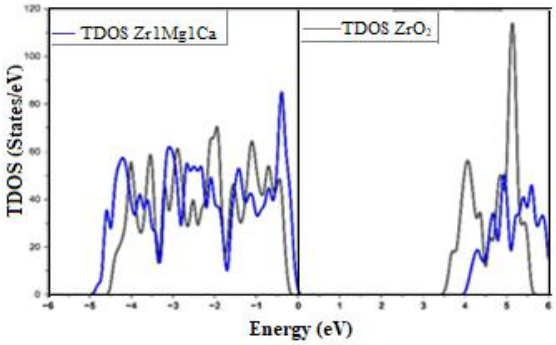

Figure 4.21: TDOS of pristine m-ZrO_2 and Ca-Mg codoped ZrO_2

Fermi level intersects the edge of the valence states in Ca-Mg codoped system.This suggests an increase in hole density near the valence band, which has been found to improve hole-driven oxidation processes (Guo *et al*., 2024). Holes being important oxidizing agents in photocatalysis, they help generate hydroxyl radicals (•OH), enhancing photocatalytic remediation of organic contaminants and disinfection (Al-Nuaim *et al*., 2023). Figure 4.22 illustrates the TDOS and PDOS of Ca-Mg codoped ZrO_2 systems.

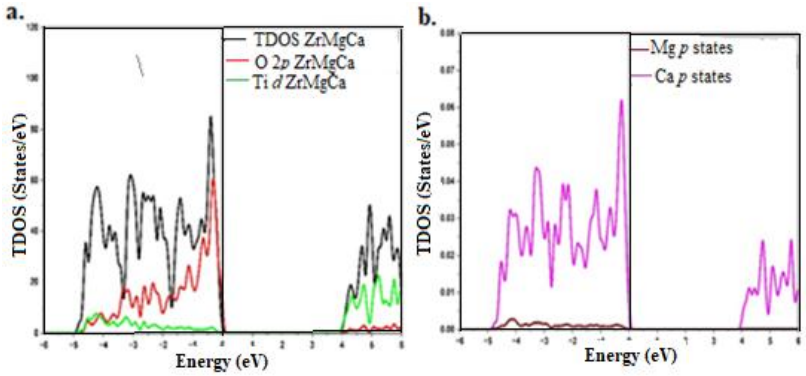

Figure 4.22: (a) TDOS Ca-Mg codoped ZrO_2 (b) PDOS Ca and Mg states in codoped ZrO_2

As demonstrated in Figure 4.22 (b), Ca valence bands lie close to the Fermi level and overlap with oxygen 2*p* orbitals, bringing the valence band edge maximum to higher energies. Figure 4.23 shows the effect of dopant amount on the electronic characteristics of Ca-Mg codoped ZrO_2 at various concentrations.

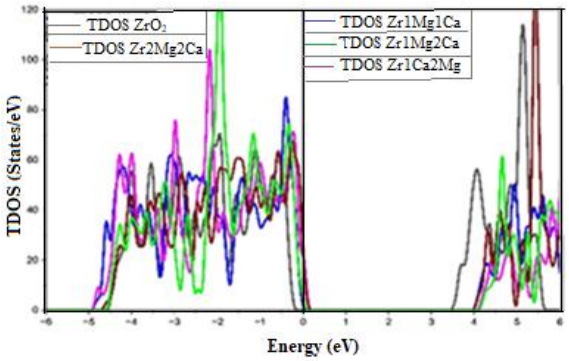

Figure 4.23: TDOS of Ca-Mg codoped ZrO_2 systems

As seen in Figure 4.23, increasing the Ca and Mg dopant concentration in codoped systems creates more defect states, which interact with the valence band edge states, resulting in a significant shift valence band maximum to higher energies. This phenomenon is induced by an increasing overlap between the dopant energy levels and the band edges, which changes the effective energy levels and modifies the semiconductor's electrical characteristics (Lyons *et al.*, 2024).

4.3.3 Electronic Structure Modification through Oxygen Vacancy Creation

The creation of oxygen vacancies during doping is investigated in order to learn more about the consequences of calcium and magnesium doping of monoclinic zirconium

(iv) oxide. Initially, the impact of an oxygen vacancy on m-ZrO_2's electronic structure was examined. Figure 4.24 displays the TDOS for both pristine and oxygen vacancy deficient m-ZrO_2.

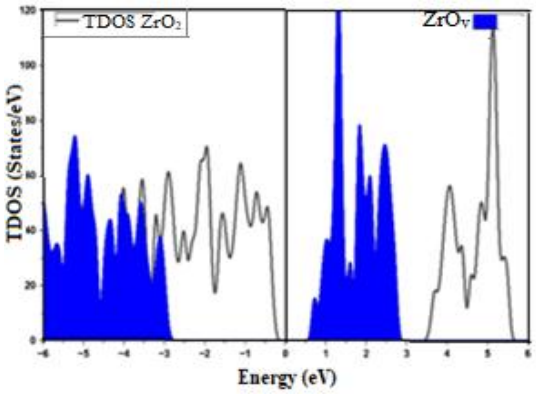

Figure 4.24: TDOS of pure m-ZrO_2 and oxygen vacancy defective pure m-ZrO_2

Figure 4.24 shows that introduction of an oxygen vacancy deficiency in pristine monoclinic zirconium (iv) oxide, results in the valence band maxima shifting towards lower energies by about 2 eV and the bandgap narrows from 3.75 to 3.25 eV. The lowering of the bandgap is due to emergence of defective states in the band gap as shown in Figure 4.25.

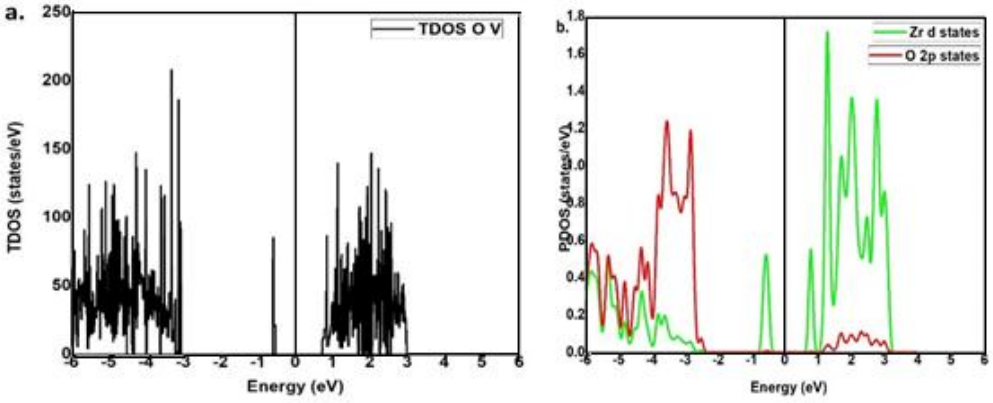

Figure 4.25: a) TDOS for oxygen vacancy defective M-ZrO_2 and b) oxygen 2*p* and Zr 4*d* PDOS for oxygen vacancy defective m-ZrO_2

As observed in Figure 4.25 (b), the Zr 4*d* orbitals are responsible for the defective energy state that appeared at roughly 0.8 eV below the Fermi level. An energy state located within the same energy region below the Fermi level emerges as a result of the oxygen vacancy leaving two surplus valence electrons that partially occupy the *d*

orbitals, as is the case for TiO_2, which is isoelectronic with ZrO_2 (Parrino *et al*., 2021; Vásquez *et al*., 2016).

The formation of oxygen unoccupied states at around 0.5 eV above the Fermi level in Mg-doped ZrO_2 is caused by an oxygen vacancy and is explained by charge compensation, as seen in Figure 4.26

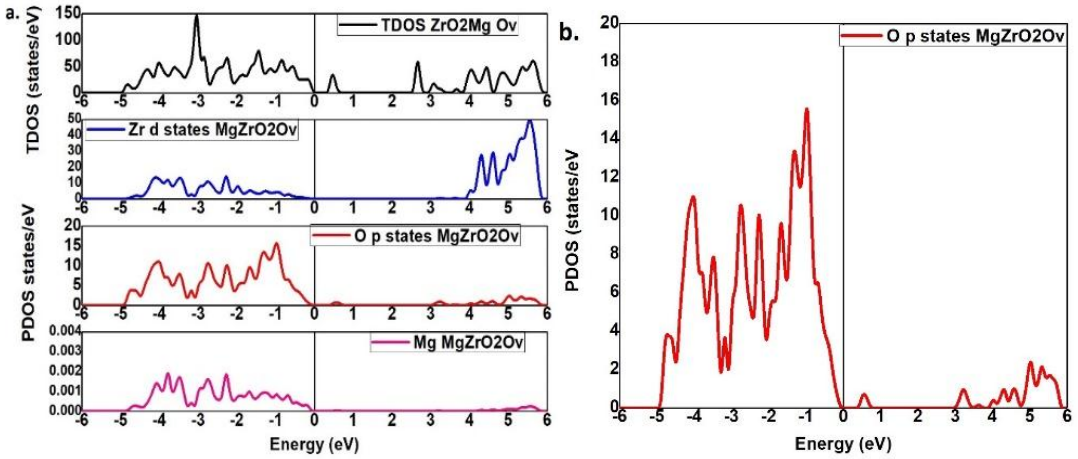

Figure 4.26: a) PDOS and TDOS for zirconium 4*d*, Oxygen 2*p* and magnesium 2*p* states for oxygen vacancy defective magnesium doped ZrO_2 and b) oxygen *2p* states in oxygen vacancy defective magnesium doped ZrO_2

The Fermi level is found in the narrow gap in between the O *2P* states. This could help explain the enhanced photo luminescence intensity that has been found experimentally as a result of Magnesium doping of ZrO_2, tetragonal phase stabilization, enhanced oxygen ion conduction, and use in resistive random access memory (RRAMs) (Bandara *et al*., 2017; Salari & Ghodsi, 2017c). This outcome supports the idea that the creation of oxygen vacancy deficiency in magnesium-doped ZrO_2 is responsible for the previously described experimental findings. Figure 4.27 illustrates the impact of an oxygen vacancy deficiency in Calcium doped zirconium (iv) oxide).

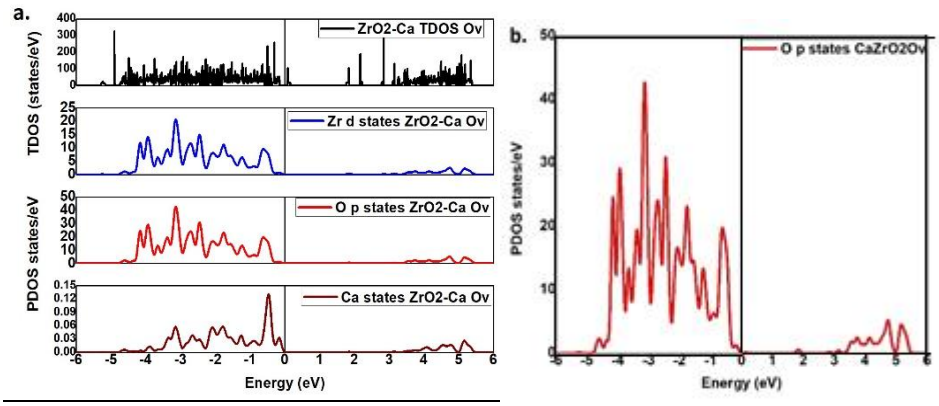

Figure 4.27: a) PDOS and TDOS for zirconium *4d*, oxygen *2p* and calcium 2*p* states for oxygen vacancy defective calcium doped ZrO_2 and (b) oxygen 2*p* states in oxygen vacancy defective calcium doped ZrO_2

Unlike Magnesium dopant impurity levels, calcium dopant impurity states exist in the higher levels of energy right below the Fermi level. The zirconium *4d* and oxygen *2p* states shift towards lower energy. consequently, the Fermi level lies inside the wider gap between the occupied and unoccupied oxygen *2p* levels, as seen in Figure 4.27(b). This would lead to a reduced O ion conduction as compared to the case of Mg doping (Funahashi *et al.*, 2016). Therefore, magnesium doping is preferred in applications that need ionic mobility, while calcium doping is better suited for tetragonal zirconium (iv) oxide stability. The ionic radius of the alkaline earth metal impurity seems to be crucial in the ensuing structural and electronic alterations, in addition to charge compensation effects.

Effect oxygen vacancies on a Ca-Mg codoped ZrO_2 electronic structure was further investigated using a TDOS for Ca-Mg codoped ZrO_2 and oxygen deficient Ca-Mg codoped ZrO_2 as shown in figure 4.28.

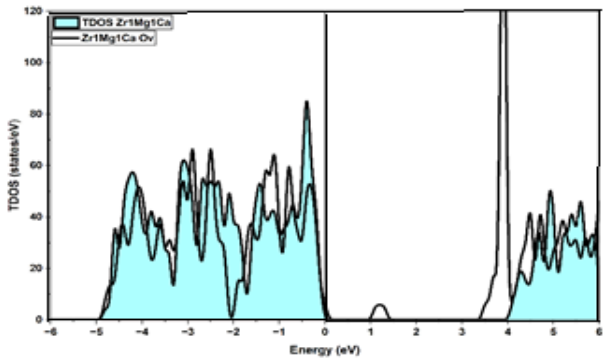

Figure 4.28: TDOS for Ca-Mg codoped ZrO_2 and oxygen deficient Ca-Mg codoped ZrO_2

It is evident that localized mid-gap states emerge at around 1 eV above the fermi energy and the conduction band minimum shifts to lower levels of energy by 0.6 eV. This results in reduction in the band gap energy from around 4 eV to approximately 3.2 eV, which is comparable with the experimental findings in this study, which reveal that Ca-Mg codoping resulted in a bandgap narrowing. The midgap states have been shown to act as traps for photogenerated charge carriers hence enhancing photocatalytic efficiency of Ca-Mg codoped ZrO_2 (Guan *et al.*, 2023).

4.4 Characterization

This part provides a thorough analysis of the outcomes of the characterization and applications of the green synthesized photocatalytic materials with the optimal Ca and Mg dopants as anticipated by DFT analysis.

4.4.1 Elemental Composition

The concentration of calcium and magnesium in codoped TiO_2 and ZrO_2 synthesized samples is given in Table 4.5.

Table 4.5: Concentration of calcium and magnesium in the synthesized samples

Samples (wt%)	Chemical analysis (wt%)	
	Ca	Mg
3.20% Ca + 2.90% Mg - TiO_2	3.07	2.88
3.20% Ca + 5.80% Mg - TiO_2	3.02	5.71
6.40% Ca + 5.80% Mg - TiO_2	4.31	5.73
3.40% Ca + 3.10% Mg - ZrO_2	3.12	3.02
3.50% Ca + 6.40% Mg - ZrO_2	3.23	6.32
7.30% Ca + 6.60% Mg - ZrO_2	5.62	6.46

The Inductively Coupled Plasma Mass Spectrometry (ICP-MS) analysis confirmed that Ca and Mg dopants were successfully incorporated into the codoped TiO_2 and ZrO_2 samples. The results reveal that for samples with high calcium dopant concentration, less calcium ions were incorporated into the codoped samples. For example, in codoped 6.40% Ca + 5.80% Mg-TiO_2, only 4.31% of Ca atoms were incorporated into the synthesized samples, whereas 5.73% of magnesium was successfully absorbed. This

disparity mainly occurs due to the difference in their ionic radius compared to the host Ti^{4+} ions, as Mg^{2+} (0.72 Å) is easier to substitute for Ti^{4+} (0.605 Å) due to their similar size compared to Ca^{2+} (1.00 Å), which is significantly bigger and harder to incorporate into the TiO_2 lattice (Thongyong *et al*., 2023). This is aligned with the theoretical findings in Figure 4.2, which show that magnesium rich doped anatase are more stable than Ca-rich structures and have lower total energies.

4.4.2 Structural Properties

Figure 4.29 (a) and (b) depicts the diffractogram for pristine titanium (iv) oxide and Ca-Mg codoped titanium (iv) oxide, with pure TiO_2 having strong diffraction peaks at 25.3 °, 37.8 °, 48.3 ° and 62.3 ° corresponding to the miller indices (101), (004), (200), and (204), respectively, and codoped TiO_2 having some of the conspicuous peaks at 25.44 ° (101), 29.4 ° (121), 31.38 ° (120), 42.72 ° (111), and 58.04 ° (211), indicating formation of anatase, rutile, and brookite mixed phases. The mixed phase TiO_2 photocatalyst combining rutile, anatase and brookite is considered as a superior photocatalyst than any of the single phase materials on their own, because the particular features of each contribute to the overall efficiency (Gong *et al*., 2025). The peaks with highest intensity appeared at 25.3 ° (101) and 25.44 ° (101) for pristine TiO_2 and Ca-Mg codoped TiO_2, respectively, showing that the dominant phase in both pristine TiO_2 and Ca-Mg codoped TiO_2 nanoparticles is the anatase phase.

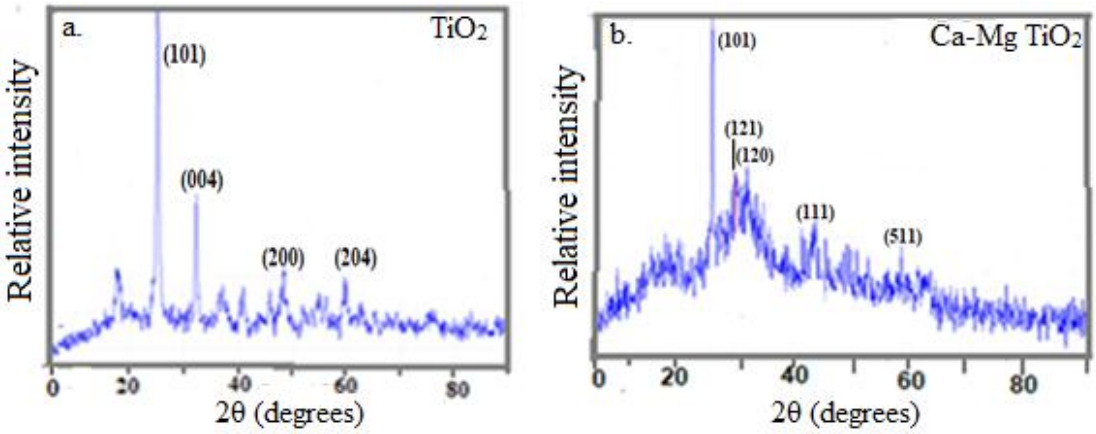

Figure 4.29: XRD diffraction patterns of: a) pristine TiO_2 and b) 3.125 at% Ca + 6.25 at% Mg - TiO_2

The XRD diffractograms of Ca doped ZrO_2, Mg doped ZrO_2 and Ca-Mg codoped ZrO_2 are shown in figure 4.30. Ca-Mg codoped ZrO_2 in figure 4.30 a), exhibited a tetragonal

phase with strong peaks at 30.28 º, 35.3 º, 50.4 º, 60.34 º, and 62.2 º corresponding to miller indices (101), (110), (112), (211), and (202) respectively. This is as expected from the theoretical findings obtained in this study, in which the b/a ratios increased with Ca and Mg doping indicating tetregonalization of the monoclinic ZrO_2 structure, which is the low temperature phase. A similar finding was obtained by Khajavi *et al*., (2020), indicating that Cerium-Yttrium codoping at low concentration stabilized tetragonal Zirconia at room temperature.

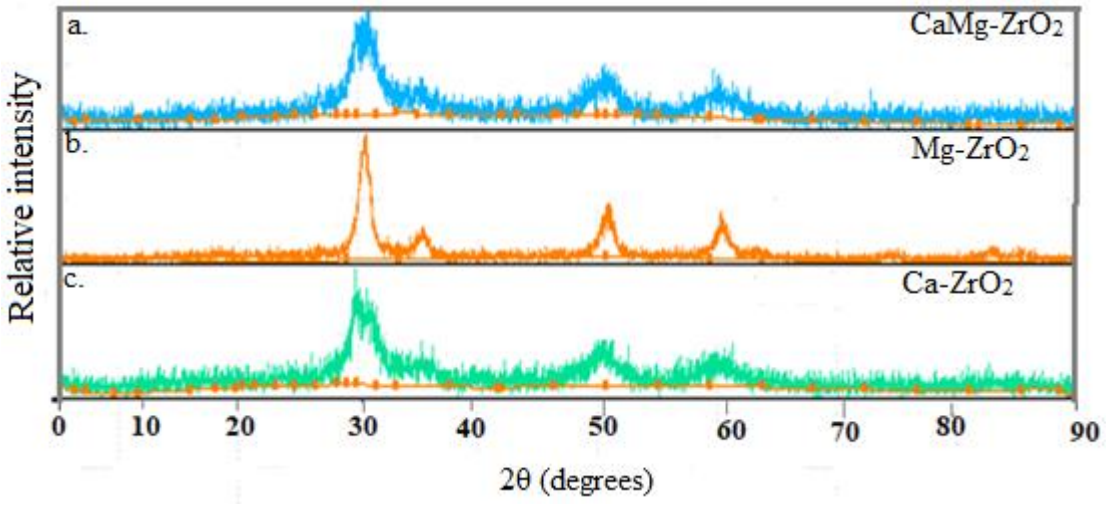

Figure 4.30: a) Diffractograms of a) 6.25 at% Ca + 6.25 at% Mg-ZrO_2, b) 6.25 at% Mg-ZrO_2, c) 6.25 at% Ca-ZrO_2

Introduction of the Ca and Mg dopant ions into the ZrO_2 lattice slightly affected the position and the width of the XRD peaks. Doping with Ca ions caused broadening of the XRD peaks showing reduction in crystalline size as well an induced microstrain as reported by Bashir *et al*., (2021), in a study where ZrO_2 films were doped with Zn. Doping with Mg^{2+} ion (0.72 Å) which is slightly smaller than Zr^{4+} ion (0.84 Å) caused a slight contraction of the lattice leading to a small decrease in interplanar spacing *d* by 0.0132 nm and therefore 2θ slightly shifted to a higher value. This is as expected for a contracted lattice (Limbu, 2022). In contrast, Ca^{2+} ion (1.00 Å) being larger than Zr^{4+} ion (0.84 Å) caused expansion of the lattice leading to a small increase of *d* by 0.0586 nm, hence shifting the peak to a lower 2θ value as per expectation for an expanded lattice (Zhang *et al*., 2025).

Table 4.6 summarizes the lattice constants and average crystallite size of synthesized TiO_2 and ZrO_2 nanoparticles. The crystallite size was calculated using the Scherer equation ($D = K\lambda / \beta\cos\theta$) (Mathumba *et al.*, 2024), where D is the average crystallite size (nm), K is the Scherer constant (0.94), λ is the x-ray wavelength ($CuK\alpha = 0.15406$ nm), β is the line broadening at FWHM in radians, and θ is the Bragg's angle in degrees. To compute lattice parameters from XRD data, d was first determined for each diffraction peak using Bragg's Law ($n\lambda = 2d\sin\theta$). The lattice parameters (a, b, and c) were then determined using the d values and the applicable lattice geometry equation as per relevant theory (Saowadee *et al*., 2017).

Table 4.6: Average Crystallite size and lattice parameters TiO_2 and ZrO_2 samples

Sample (at%)	Average crystallite size (nm)	lattice parameters (nm)		
		a	*b*	*c*
TiO_2	17.281	3.784	3.784	9.505
3.125% Mg - TiO_2	14.264	3.751	3.751	9.459
3.125% Ca -TiO_2	10.352	3.813	3.813	9.620
3.125% Ca + 6.25% Mg-TiO_2	8.647	3.926	3.926	9.760
ZrO_2	9.031	5.158	5.200	5.321
6.25% Mg - ZrO_2	8.732	3.579	3.579	5.062
6.25% Ca- ZrO_2	6.238	3.598	3.598	5.074
6.25% Ca + 6.25% Mg-ZrO_2	5.567	3.611	3.611	5.081

Undoped TiO_2 has an average crystallite size of 17.281 nm, which is comparable to the crystalline size of 17.300 nm obtained by Mobeen Amanulla & Sundaram, (2019b) when pure TiO_2 was synthesized using orange peel extract. Pure ZrO_2 has an average crystallite size of 9.031 nm, which is similar to crystalline size of 9.000 nm achieved by (Annu et al., 2020b) via the synthesis of ZrO_2 NPs using *Moringa Oleifera* leaves. The computed average particle size for 3.125% Ca + 6.25% Mg-TiO_2 and 6.25% Ca + 6.25% Mg-ZrO_2 codoped samples is 8.947 nm and 5.567 nm, respectively, which is significantly lower than pure or single doped samples. This is because presence of dopant atoms disturbs the usual crystal lattice, leading to smaller crystallites (Saoud *et al*., 2023). Impurity lattice defects caused by the introduction of dopants have been demonstrated to reduce agglomeration, resulting in nanoparticles of smaller size (Hassan & Jalil, 2022 ; Fedorov & Yarotskaya, 2021). Particle size has been shown to play a considerable effect in material attributes; for example, smaller particles have excellent performance in photocatalysis applications (Li *et al*., 2020). Pure ZrO_2 has lattice constants a = 5.158 Å, b = 5.200 Å and c = 5.321 Å, indicating a monoclinic

phase of ZrO_2, similar to what is observed by Ramos-Justicia *et al*., (2023), while Ca-Mg codoped ZrO_2 has lattice constants a = b = 3.587 Å and c = 5.081 Å ,corresponding to tetragonal phase of ZrO_2 .

4.4.3 Electronic Properties

Energy bandgap (Eg) was analysed by using data from UV-Vis spectroscopy technique. Equation 3.1 displays the Tauc formula used to compute the nanoparticles' optical band gap. Figure 4.32 shows the optical bandgaps for a) Pure TiO_2 b) 3.125 at% Mg-TiO_2 c) 3.125 at% Ca-TiO_2 d) 3.125 at% Ca + 6.25 at% Mg - TiO_2. As indicated in Figure 4.32 a), the optical energy band gap of pure TiO_2 is 3.20 eV, which is in good agreement with experimental values for anatase obtained by Soussi *et al*., (2021) and Etafa Tasisa *et al*., (2024). Upon doping with 3.125 at% calcium the band gap energy of the pristine TiO_2 decreased from 3.20 to 2.45 eV as shown in Figure 4.32 c). Mg dopant significantly lowered the pure titanium (iv) oxide band gap from 3.20 to 2.90 eV. This is attributed to Mg^{2+} substituting Ti^{4+} in the TiO_2 lattice structure hence creating new energy levels and decreasing the bandgap (Kayani *et al*., 2023).

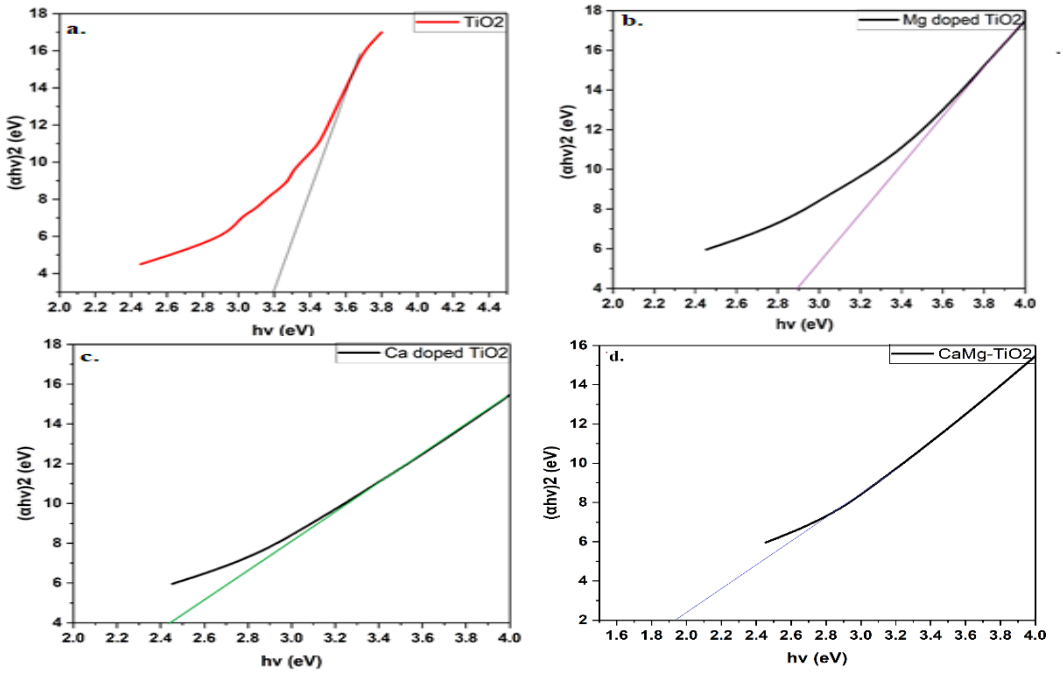

Figure 4.31: Band gaps of a) Pure TiO_2 b) 3.125 at% Mg-TiO_2 c) 3.125 at% Ca-TiO_2 d) 3.125 at% Ca + 6.25 at% Mg-TiO_2

Doping TiO_2 with calcium impurity introduces intermediate states in the bandgap, modifying its electronic structure and lowering the band gap energy, allowing for absorption in the visible region of the electromagnetic spectrum (Mondal *et al*., 2025). Furthermore, the drop in Ca doped TiO_2 bandgap is ascribed to oxygen vacancies created as Ca^{2+} ions enter the lattice, replacing Ti^{4+} ions. (Minchi *et al*., 2019). Calcium doping produces partial Ti^{3+} , which reduces the rate of charge carrier recombination and increases photocatalytic activity (Arshad *et al*., 2022). Figure 4.31 d) shows that the optical bandgap further decreases to 1.92 eV when TiO_2 is codoped with Ca and Mg dopants. The synergistic effect after the incorporation of both dopants is therefore expected to lead to a red shift of the absorption spectrum (Ibrahim *et al*., 2020 ; Chen *et al*., 2018). Codoping alkaline earth metal dopants, such as Ca and Mg, causes oxygen vacancies and lattice deformation, which narrows the TiO_2 band gap by introduced midgap states (Slimani *et al*., 2023 ; Klinbumrung *et al*., 2020 ; Salari & Ghodsi, 2017b).This is evident in theoretical study in Figure 4.10 a), which shows a considerable lowering of bandgap in oxygen defective Ca-Mg codoped anatase TiO_2 due to generation of impurity states in the bandgap.

Figure 4.32 a) - d) shows: Bandgaps of a) Pristine ZrO_2 b) 6.25 at% Mg - ZrO_2 c) 6.25 at% Ca -ZrO_2 and d) 6.25 at% Ca +6.25 at% Mg-ZrO_2.

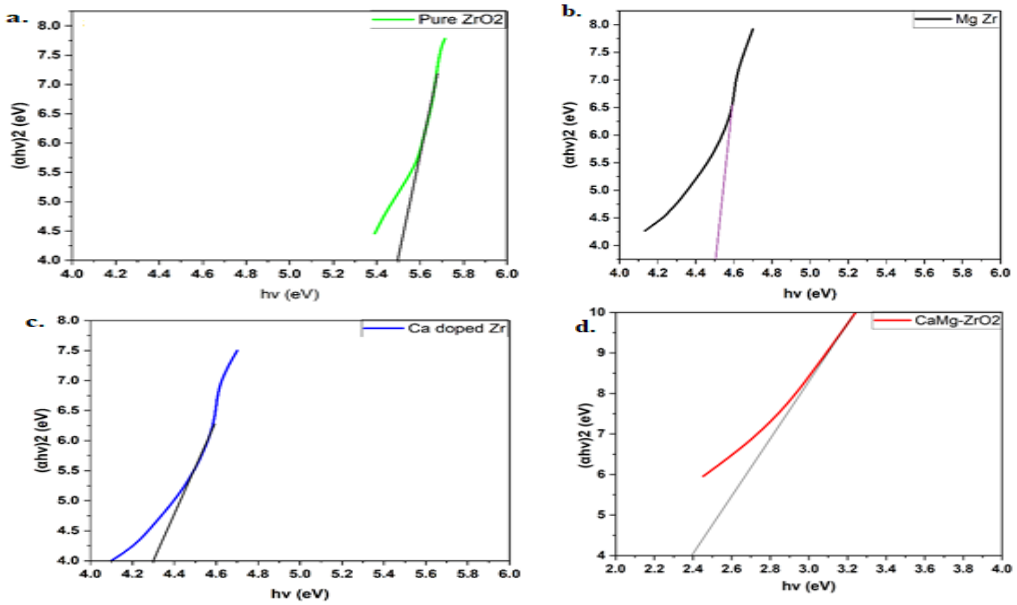

Figure 4.32: Bandgaps of a) Pure ZrO_2 b) 6.25 at% Mg-ZrO_2 c) 6.25 at% Ca-ZrO_2 and d) 6.25 at% Ca + 6.25 at% Mg-ZrO_2

Figure 4.32 a) clearly shows that pure ZrO_2 NPs have a wide band gap of 5.5 eV, which is in line with experimental value for undoped ZrO_2 obtained by Sharaf *et al*., (2024). The energy band gap lowers to 4.5eV and 4.3eV with the addition of 6.25% Mg and 6.25% Ca dopants, respectively. The shrinkage in the optical band gap of Ca or Mg doped ZrO_2 relative to pure ZrO_2 results from the creation of dopant impurity levels above the valence band edge, resulting in shifting valence band edge to higher energies (Mardare *et al*., 2024) .This is consistent with theoretical findings in this study as shown in Figure 4.19, where Ca dopant states resulted in shifting of the valence band edge of Ca doped ZrO_2. Additionally, the synergistic effect of Ca and Mg dopants results in further reduction of the bandgap to 2.4 eV as illustrated in Figure 4.32 d).

The Table 4.7 highlights the comparison bandgaps of the synthesised samples with other doped TiO_2 or ZrO_2 in literature.

Table 4.7: Optical band gaps of single and codoped TiO_2 and ZrO_2

Sample	Energy band gap (Eg)	Reference
Ca doped TiO_2	2.52 eV, 2.45 eV and 2.35 eV for 2%, 5% and 9% Ca-doped	Mondal *et al*., 2025
	3.10 eV for 2 wt% Ca dopant	Etafa Tasisa *et al.,* 2024
	2.986 eV for 3 at%	Liu *et al*., 2014
	2.45 eV 3.125 at% Ca	present work
Mg doped TiO_2	2.9 eV,2.72 eV and 2.6 eV for 0.5 ,1 and 2 mol% of Mg respectively.	Winda *et al*.,2023
	3.0955 eV for 0.8 wt%	Shivaraju *et al*., 2017
	2.92 eV for 0.2 mol%	Behnajady *et al*.,2011
	3.11 eV, 3.07eV and 2.97 eV, for 0.5, 1 and 2 mol % respectively	Klinbumrsung *et al*., 2020
	2.9 eV for 6.25 at% Mg	present work
Ca-Mg codoped TiO_2	1.92 eV for 3.125 at% Ca + 6.25 at% Mg-TiO_2	present work
Mg doped ZrO_2	5.72 eV,4.81 eV & 4.12 eV for 1,2 & 3 mol% respectively	Mardare *et al*., 2024
	3.83 eV for 15 at% MgO doped ZrO_2	Berar *et al*.,2020
	4.5 eV for 6.25 at% Mg ZrO_2	present work
Ca doped ZrO_2	4.3 eV for 6.25 at% Ca ZrO_2	present work
Ca-Mg codoped ZrO_2	2.4 eV for 6.25 at% Ca + 6.25 at% Mg-ZrO_2	present work

4.5 Photocalytic Activity Evaluation

4.5.1 Optimization of The Initial Concentration of the Dye

To evaluate the effect of the initial dye amount on rhodamine B dye degradation, a series of tests were analysed at different RhB concentrations (2, 4, 6, 10, 12, and 14 ppm) with a photocatalyst amount of 20 milligrams per litre. As seen in Figure 4.34, altering the solution's pH significantly affected the photodegradation efficiency. The results show that degradation efficiency of the codoped TiO_2 and ZrO_2 samples first rose with dye concentration up to a maximum of 10 ppm, after which it declined.

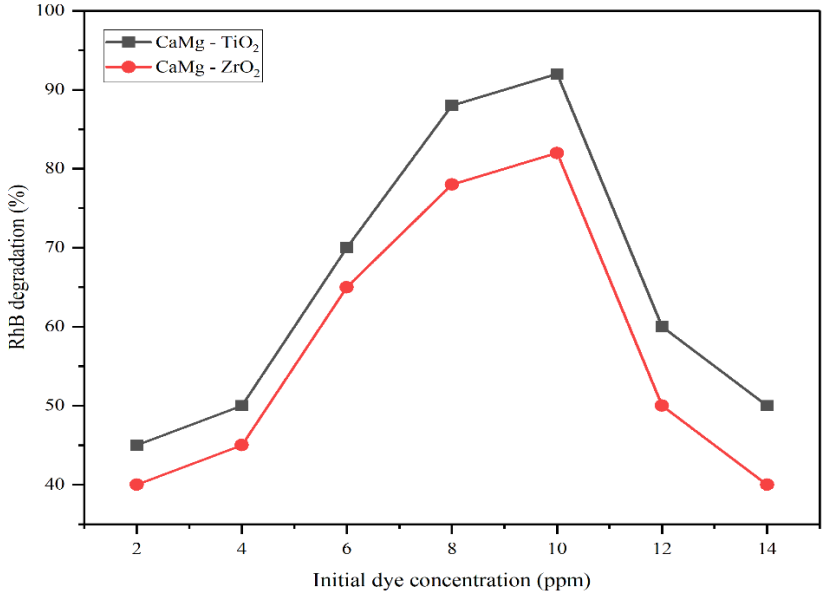

Figure 4.33: Effect of initial RhB dye concentration on its degradation efficiency.

As the initial RhB concentrations rise, the number of dye molecules in the solution increases, resulting in heightened competition for the available active sites on the photocatalyst surface, hence enhancing the degradation rate (El-Dossoki *et al*., 2021). The efficiency of dye degradation declines at concentrations exceeding the optimal level leading to a decrease in the generation of reactive species like hydroxyl radicals (Mugumo *et al*., 2023). In addition, a part of the light energy may be absorbed by the dye molecules instead of the photocatalyst, thereby lowering the efficacy of the catalytic activity (Groeneveld *et al*., 2023).

4.5.2 pH Optimization

To investigate the influence of pH on RhB degradation by codoped TiO_2 and ZrO_2 photocatalysts, 0.1M HCl and 0.1M NaOH were used to modify the RhB solution to

various pH values (2, 4, 7, 10, and 13). Varying of the solution pH had a substantial effect on photodegradation efficiency, as illustrated in Figure 4.34.

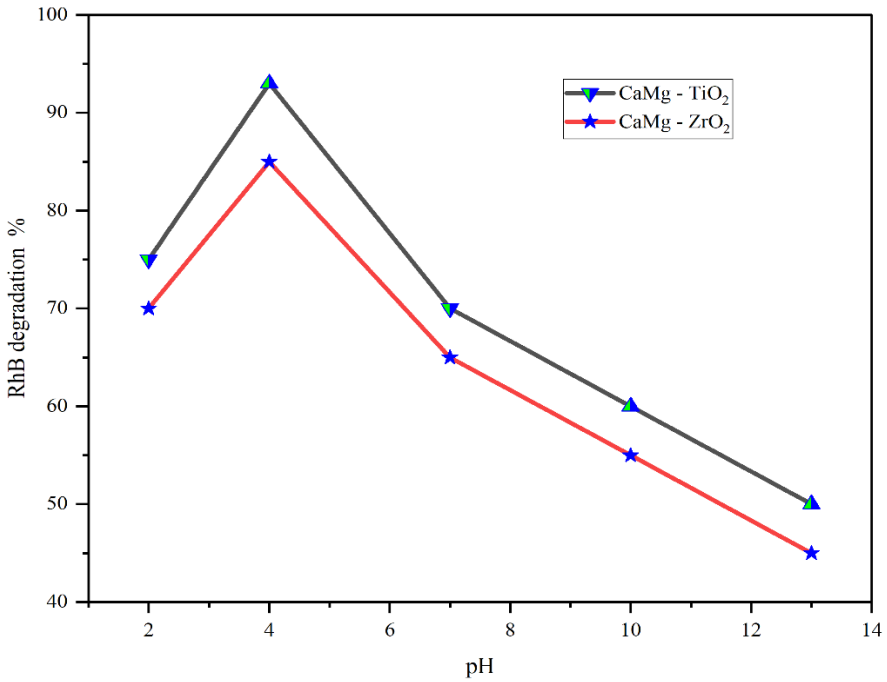

Figure 4.34: Effect of pH on degradation of RhB (20 mg for each photocatalyst, 10 ppm RhB).

The results show that RhB degrades more quickly in acidic environments than in neutral or alkaline ones, with pH4 achieving the highest degradation efficiency. Acidic conditions promote the adsorption of RhB molecules onto the surface of TiO_2 or ZrO_2 photocatalysts, which is a vital step in the degradation process (Chen *et al*., 2024) . At lower pH, TiO_2 surfaces are positively charged which attract the anionic RhB molecules, aiding their adsorption and degradation (Zhao *et al*., 2025; Ahmadpour *et al*., 2020). Furthermore, acid solution is excellent for minimizing agglomeration and the generation of reactive species, which lead to increased photocatalytic efficiency (El-Dossoki *et al*., 2021).

4.5.3 Photocatalyst Dosage Optimization

The effectiveness of the photocatalytic process is largely affected by the dosage of the catalyst. Figure 4.35 illustrates how varying catalyst loadings affect the photocatalytic efficacy of Ca-Mg codoped nanoparticles in the degradation of RhB dye.

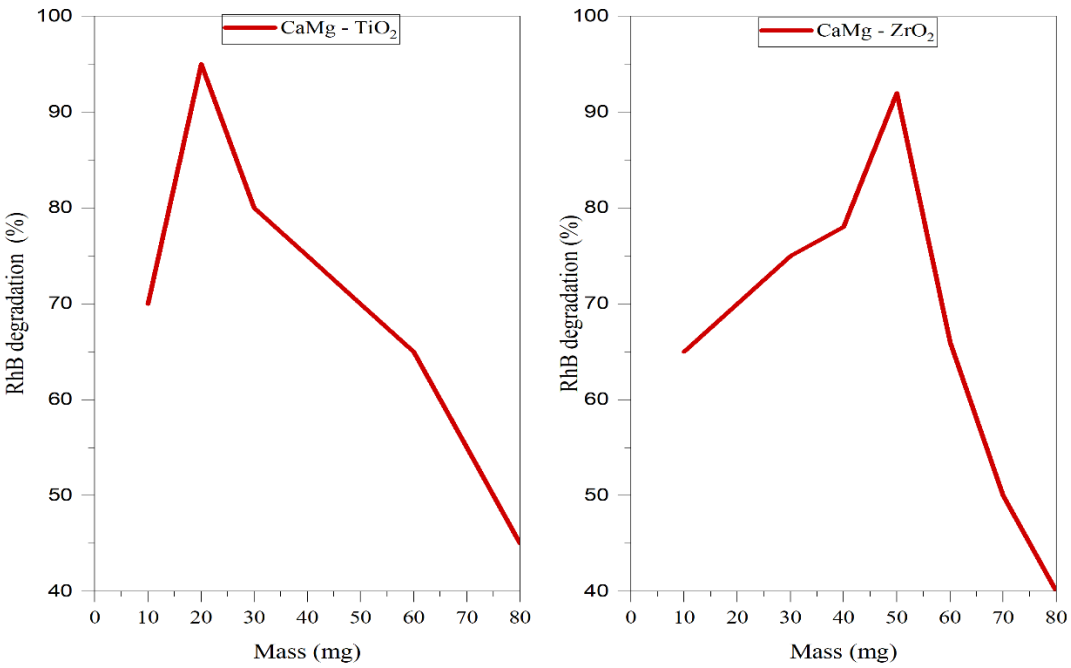

Figure 4.35: Effect of dosage on photocatalytic efficacy of: a) Ca-Mg codoped titania photocatalyst and b) Ca-Mg codoped zirconia photocatalyst. (RhB = 10 ppm, pH4)

The findings show that increasing catalyst loading significantly increases the photocatalytic effect of the photocatalyst. For Ca-Mg codoped TiO_2 and Ca-Mg codoped ZrO_2, the ideal catalyst loading was found to be 20 mg and 50 mg respectively, beyond which the rate of photodegradation decreased. The rise in efficiency with increased catalyst loading up to the optimal value can be attributed to the increased surface area and active sites, resulting in more free electrons available in the conveyance band and more hydroxyl radicals being produced (Arulkumar *et al*., 2023 ; Rahman & Kar, 2022). However, beyond the optimum value, the rate of RhB dye removal decreases due to photocatalyst particle agglomeration (Sajjadi & Hosseinzadeh, 2025; Moradi *et al*., 2020), which reduces the surface area available for the photocatalytic reaction, and may also prevent reactants from reaching active sites (Wang *et al.,* 2023). Higher dosages of some photocatalysts may cause deactivation or toxic consequences (Ling *et al*., 2025).

4.5.4 Photocatalytic Effect of the Monodoped and Codoped Photocatalysts

The photocatalytic degradation efficiencies of single and codoped nanoparticles were examined by loading 20 mg and 50 mg of TiO_2 and ZrO_2 photocatalysts, respectively, on a 10 ppm rhodamine B solution at pH4. To reach adsorption-desorption equilibrium

and ensure that the degradation of RhB was due to the photocatalytic reaction in the presence of the synthesized materials rather than adsorption, the reaction mixture was first shaken in the dark for 30 minutes. After two hours of exposure to visible light, its photocatalytic effectiveness was assessed. The outcomes of RhB photodegradation employing (a) TiO_2-based and (b) ZrO_2-based systems are displayed in Figure 4.36.

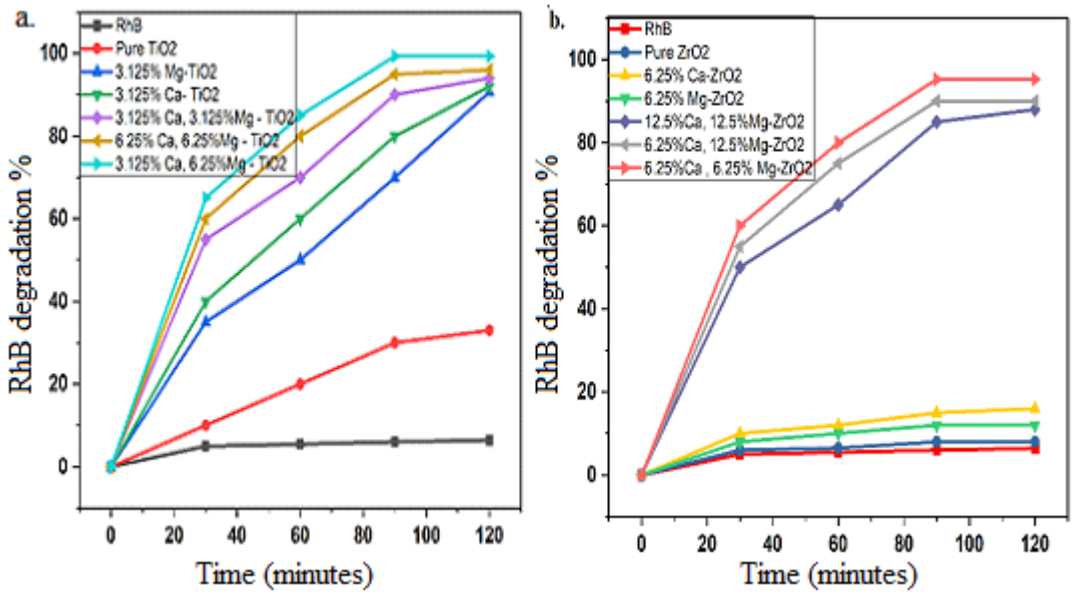

Figure 4.36: Photodegradation of RhB using: (a) TiO_2- based and (b) ZrO_2-based systems

For a comparison, control studies were conducted under the same conditions, with RhB exposed to visible light illumination without photocatalyst. Following 120 minutes of exposure to visible light without a photocatalyst, RhB degradation was minimal at 6.4%. Similarly, pure ZrO_2, Ca, or Mg doped ZrO_2 showed slight RhB degradation of 8%, 16%, and 12% in 120 minutes, respectively. This is attributed to their broad bandgaps that were unresponsive to visible light (Tekin *et al*., 2022).

The 3.125 at% Ca + 6.25 at% Mg codoped TiO_2 and 6.25 at% Ca + 6.25 at% Mg codoped ZrO_2 samples had photocatalytic degradation efficiencies of 99.3% and 95.28%, respectively, following a 120-minute exposure time. The disparity in the degradation rate clearly relates to the semiconductor features, such as TiO_2 narrower bandgap compared to ZrO_2 (Acosta-Silva *et al*., 2024) .In comparison to pristine, Ca, or Mg single doped nanoparticles, the results demonstrated that Ca-Mg codoped TiO_2 or ZrO_2 nanoparticles exhibited significantly higher photocatalytic activity. This is primarily due to the synergistic effect of the dopants (Ibrahim *et al*., 2020), as well as

the formation of surface defects like oxygen vacancies as a result of the insertion of Ca^{2+} and Mg^{2+} ions into the TiO_2 or ZrO_2 lattice (Minchi *et al*., 2019; An *et al*., 2022).As a result, the defects cause the formation of impurity energy states in the bandgap which act as trapping sites for both photogenerated charges, slowing the recombination process and lowering the bandgap energy (Mardare *et al*., 2024 ; Hadi, 2024; Thambiliyagodage & Usgodaarachchi, 2021).The photogenerated charge carriers combine with water to form highly reactive species such as ·OH radicals, which have a large oxidation potential for RhB breakdown (Kunnamareddy *et al*., 2021).

The RhB dye degradation percentage steadily increases with the concentration of co-dopants, with the maximum degradation efficiency recorded at 99.3% and 95.28% for 3.125 at% Ca + 6.25 at% Mg codoped TiO_2 and 6.25 at% Ca + 6.25 at% Mg codoped ZrO_2, respectively. With the rise in the amount of Ca dopants to 6.25%, the RhB dye degradation drops from 99.6% to 96%. Increased Ca dopant concentrations above the optimum value reduced the photocatalytic reduction rate of RhB. The negative effects on photocatalytic activity have been reported to arise from excessive dopant concentrations (Zare & Mehrabani-Zeinabad, 2022). In particular, excessive Ca doping reduces photocatalytic activity by creating too many surface oxygen vacancies on the ZrO_2 or TiO_2 surface, which causes electron traps and slows down the electron transfer process (Khan, 2025 ; Sultana *et al*., 2023). Furthermore, there may be a risk of lowering the amount of photoactive sites in the sample with too many dopants due to agglomeration (Zarzzeka *et al*., 2024). Table 4.8 highlights the codoped samples' optimal effect on RhB in comparison to other single and codoped samples.

Table 4.8: Summarizes the optimal effect of the codoped samples

Photocatalyst	RhB dye concentration	Catalyst Concentration	Irradiation time in minutes	% degradation	Reference
5 %wt Ca- TiO_2	5 ppm	100 ppm	240	90.00	(Sajjadi & Hosseinzadeh, 2025)
Ca(30%)/TiO_2/NH_2-MIL-125	5 ppm	0.2 g/L	120	82.70	(Ahmadpour *et al*., 2020)
3g Mg -TiO_2	0.01 ppm	30 mg	30	43.86	(Lv *et al*., 2019)
3.125% Mg- TiO_2	10 ppm	20 mg	120	90.61	present work
3.125% Ca -TiO_2	10 ppm	20 mg	120	92.00	present work
3.125% Ca + 3.125% Mg - TiO_2	10 ppm	20 mg	120	94.00	present work
6.25% Ca + 6.25% Mg - TiO_2	10 ppm	20 mg	120	96.00	present work
3.125% Ca +6.25% Mg -TiO_2	10 ppm	20 mg	120	99.30	present work
2 mol% Mg- ZrO_2	40 ppm	40 mg	60	90.20	(Renuka *et al*., 2016)
1 Wt% ZrO_2-TiO_2	30 ppm	30 mg	150	78.00	(Ruiz-Santoyo *et al*.,2021)
2% Nd - ZrO_2	0.1 M	100 mg	120	77.00	(Keerthana *et al*., 2022)
6.25% Mg- ZrO_2	10 ppm	50 mg	120	12.00	present work
6.25% Ca-ZrO_2	10 ppm	50 mg	120	16.00	present work
12.5% Ca + 12.5% Mg-ZrO_2	10 ppm	50 mg	120	88.00	present work
6.25% Ca + 12.5% Mg-ZrO_2	10 ppm	50 mg	120	90.00	present work
6.25% Ca + 6.25% Mg- ZrO_2	10 ppm	50 mg	120	95.28	present work

Table 4.8 shows that 3.125 at% Ca doped TiO_2 has a degradation rate of 92%, which is nearly identical to the 90% degradation rate recorded by Sajjadi & Hosseinzadeh, (2025), when TiO_2 was doped with 5 wt% Ca. Few research studies have been done to investigate the degrading of RhB utilizing Ca or Mg doped ZrO_2 nanoparticles under visible light radiation; our findings will serve as a reference for future research.

4.5.5 Photocatalytic Stability of the Codoped Samples

To investigate the reusability and photocatalytic stability of synthesized nanoparticles, samples of 3.125 at% Ca + 6.25 at% Mg-TiO_2 and 6.25 at% Ca + 6.25 at% Mg-ZrO_2 were utilized in repeated degradation studies of RhB dye under similar initial conditions. Figure 4.37 depicts the RhB degradation percentage over 5 cycles of TiO_2 and ZrO_2 codoped samples.

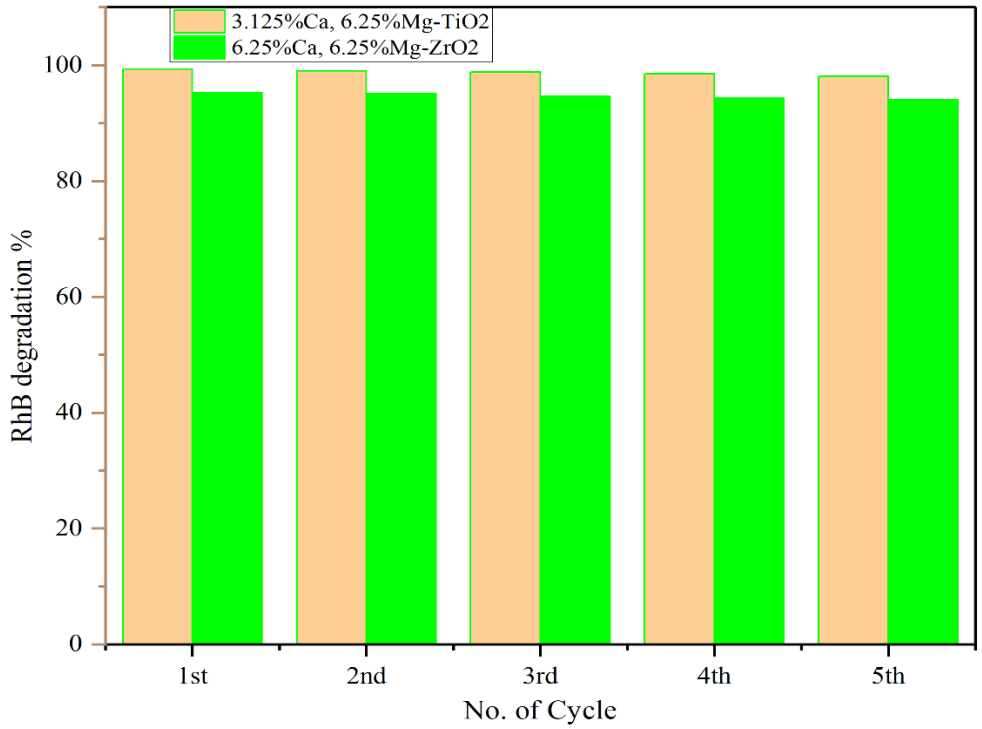

Figure 4.37: RhB degradation % for 5 cycles of the TiO_2 and ZrO_2 codoped samples.

The results in Figure 4.37 shows that the degradation rate for sequential 5 cycles is 99.3%, 99.0%, 98.8%, 98.5%, 98.1% and 95.28%, 95.1%, 94.6%, 94.3%, and 94% for TiO_2 and ZrO_2, respectively, which are comparable with the findings of Tumbelaka *et al.*, (2022), who found that green synthesized Fe_3O_4/TiO_2 nanoparticles could be recycled up to four times without a significant decrease of activity. These results confirm that the codoped TiO_2 and ZrO_2 nanoparticles have remarkable stability and reusability, which is the key reason for their widespread use in photocatalytic degradation of dyes.

4.5 Disinfection Activity Evaluation.

S. aureus and *E. coli* bacteria were used to test for antibacterial activity. Figure 4.38 summarizes the antibacterial rates of 3.125 at% Ca + 6.25 at% Mg-TiO_2 and 6.25 at% Ca + 6.25 at% Mg-ZrO_2 following 90 min of being exposed to visible light.

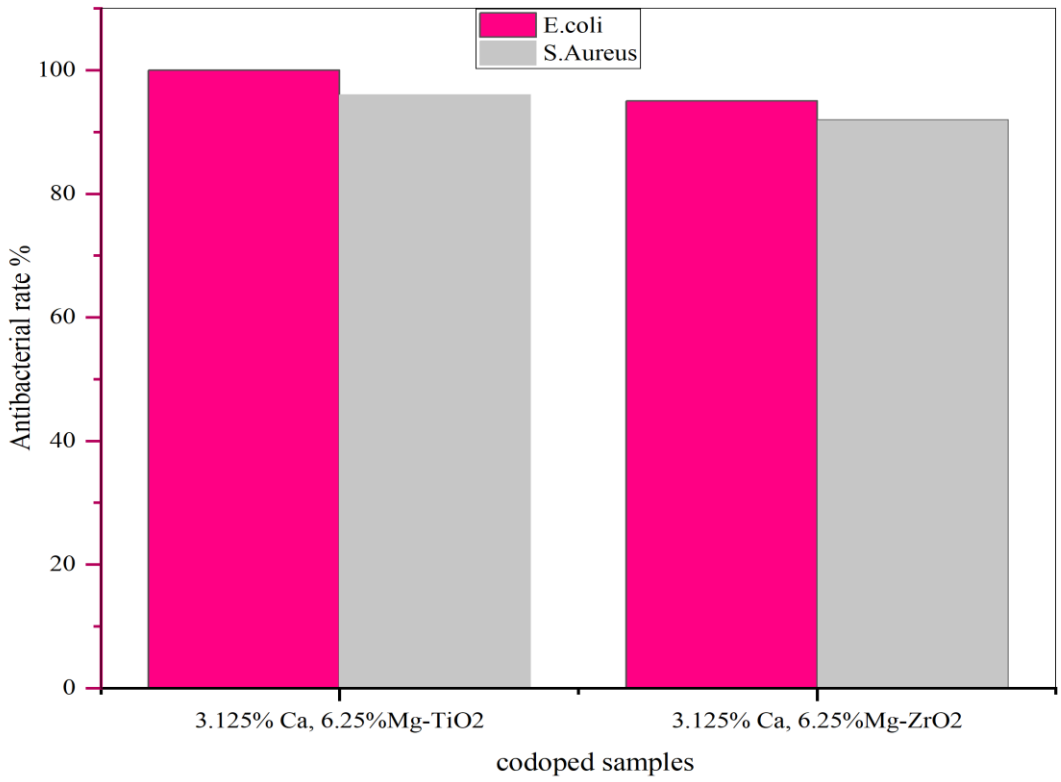

Figure 4.38: The antibacterial activity of codoped TiO_2 and ZrO_2 samples against *S. aureus* and *E. coli* following 90 minutes of being exposed to visible light

Figure 4.39 demonstrates that codoped TiO_2 has 100% antibacterial capability against *S. aureus* and 96.00% against *E. coli* bacteria, whereas codoped ZrO_2 has antibacterial rate of 95.19% against *S. aureus* and 92.30% against *E. coli* bacteria after 90 minutes of exposure to visible light. It is evident that the codoped nanoparticles exhibit higher antibacterial effects against *S. aureus* (gram positive bacteria) than *E. coli* (gram negative bacteria). This is mostly due to *S.aureus* bacteria's single peptidoglycan coating and reduced lipid content, which facilitate quicker penetration of antibacterial agents (Lu *et al*., 2023 ; Zaqri *et al*., 2021).Codoped TiO_2 photocatalyst was shown to have a greater antibacterial activity compared to codoped ZrO_2 samples against all bacteria strains owing to its smaller energy gap, which requires less energy to generate Reactive Oxygen Species (Abd *et al*., 2025). Antibacterial rate of different TiO_2 samples exposed to visible light for 90 minutes are indicated in Figure 4.39.

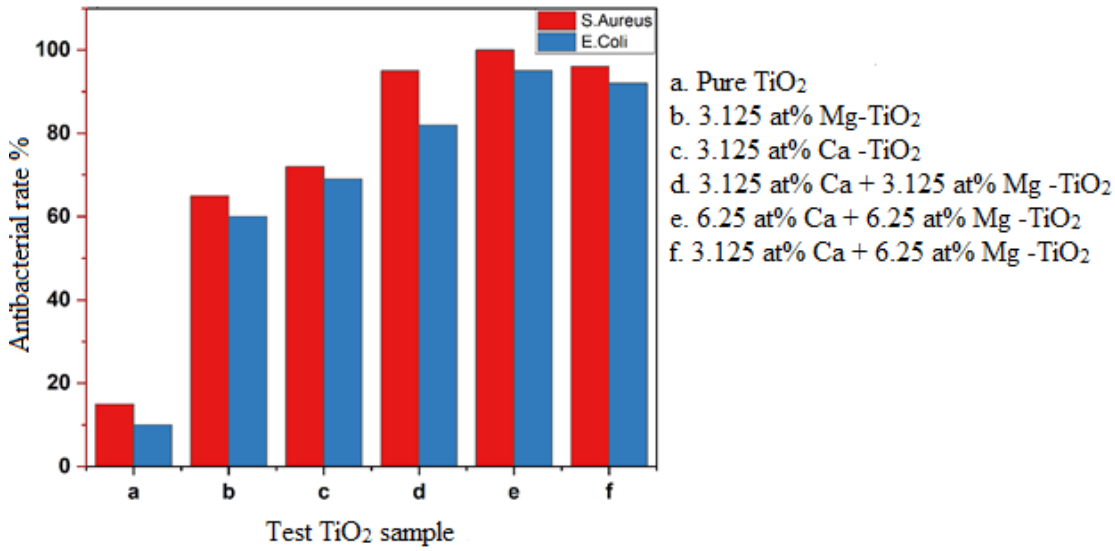

Figure 4.39: Antibacterial efficiency of TiO_2 samples after 90 minutes of exposure in visible light

As indicated in figure 4.39, the antibacterial activity for pure TiO_2, 3.125 at% Mg-TiO_2, 3.125 at% Ca-TiO_2, 3.125 at% Ca + 3.125 at% Mg - TiO_2, 6.25 at% Ca+ 6.25 at% Mg-TiO_2 and 3.125 at% Ca + 6.25 at% Mg-TiO_2 in *S. aureus* was found to be 15%, 65%, 72%, 95%, 96%, and 100% respectively, while in *E. coli* bacteria it was found to 10%, 59%, 69%, 82%, 92%, and 95% respectively. The codoped sample exhibited higher antibacterial activity than pristine or single doped samples. This is because codoping TiO_2 has been shown to cause significant decrease in the energy gap, allowing for visible light absorption and the formation of additional free radical species such as •OH and $\bullet O_2^-$ which attack cell walls and cell membranes in bacteria (Lu *et al*., 2023b). In addition, the impurity states such as those created by Ca and Mg dopants have been reported to prevent the recombination of photogenerated charge carriers, hence increasing antibacterial action (Ikram *et al*., 2021). The synergistic effect of the dual components results in remarkable visible light antibacterial performance.

TiO_2 samples exhibit stronger antibacterial efficiency than ZrO_2 samples. This is owing to the reduced energy gap, which takes less energy to generate Reactive Oxygen Species (Abd *et al*., 2025). Among all codoped samples, 3.125 at% Ca + 6.25 at% Mg-TiO_2 had the highest antibacterial efficacy in 90 minutes, with an antibacterial rate of 95% against E. coli and 100% against S. aureus.

Photographs of *S. aureus* and *E. coli* bacterial colonies taken after 120 minutes of being exposed to visible light are displayed in Figure 4.40.

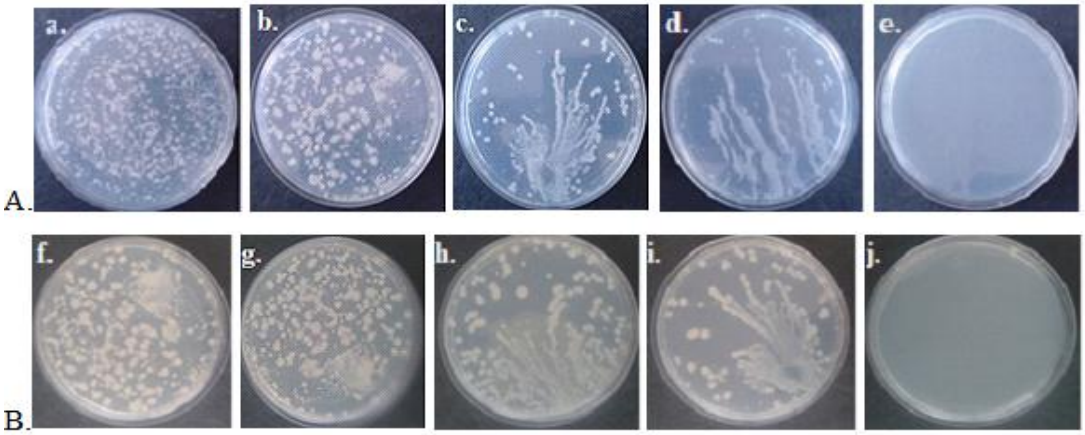

Figure 4.40: A. The formed viable colony units of *S. aureus* after 120 min., where a) Control sample (no photocatalyst), b) Pure TiO_2, c) 3.125 at% Ca + 3.125 at% Mg -TiO_2, d) 12.5 at% Ca + 12.5 at% Mg -TiO_2, e) 6.25 at% Ca + 6.25 at% Mg -TiO_2, and B. The formed viable colony units of *E. coli* after 120 min, where f) Control sample (no photocatalyst), g) Pure TiO_2, h) 12.5 at% Ca + 12.5 at% Mg -TiO_2, i) 6.25 at% Ca + 12.5 at% Mg -TiO_2, j) 3.125 at% Ca + 6.25 at% Mg-TiO_2.

Figure 4.40 shows that both control groups representing (a) *S. aureus* and (f) *E. coli*, without nano-TiO_2 photocatalyst, generated a considerable number of colonies when exposed to visible light. After 120 minutes of visible light irradiation, there are slightly less bacterial colonies on TiO_2 than in the control groups. This is because of its broad bandgap of around 3.20 eV, hence producing just a few oxidative species (Haque *et al*., 2024).The bacterial colonies on the codoped TiO_2 decreased rapidly due to the increased rate of nanoparticle killing caused by the significant reduction in band gap on codoping, which improved its visible light responsiveness (Ren *et al*., 2020). There are no bacterial colonies in Fig.(e) and (j), indicating that a codoped TiO_2 with an optimum dopant concentration of 3.125 at% Ca and 6.25 at% Mg exhibited a 100% antibacterial rate against *S. aureus* and *E. coli* bacteria after 120 minutes of exposure to visible light. This demonstrated that the green synthesized codoped nanomaterials produced in this work had outstanding antibacterial impact, providing an economical and environmentally friendly disinfection material.

CHAPTER FIVE

SUMMARY, CONCLUSION AND RECOMMENDATIONS

5.1 Summary

In this study, first principle techniques coupled with experimental work was done. The results yielded reasonable agreement between experimental and theoretical results, as well as a better understanding of the system. Phase stabilization of codoped ZrO_2 phases predicted through DFT was confirmed through XRD peaks which showed formation of tetragonal ZrO_2 phase at room temperature. DFT studies showed codoping of TiO_2 and ZrO_2 polymorphs resulted into increase in lattice parameters and volume distortions, which was agreeable with the XRD results. Narrowing of the energy band gap due to emergence of impurity levels above the valence band observed in DFT studies was verified by UV-Vis results which showed a significant reduction of bandgap on codoping. Codoped samples revealed better photocatalytic performance which could be explained by the decrease in the nanoparticle size as well as the modification of electronic properties and structural properties that enhance photocatalysis. The understanding of the improved photocatalytic capability of the codoped samples was enhanced through extensive theoretical calculations that were used to investigate the effect of Ca and Mg doping in ZrO_2 and TiO_2 structures showing their influence on the structural and electronic characteristics that promote better photocatalytic performance.

5.2 Conclusion

5.2.1 Structural Properties and Phase Stability

Generally, Mg-rich doped structures are more energetically stable than Ca-rich configurations because they have lower total energies. The optimal Ca and Mg concentrations for codoped TiO_2 polymorphs were found to be 6.25 at% Mg atoms and 3.125 at% Ca atoms, which is equivalent to the replacement of two Mg atoms and one Ca atom in place of Ti atoms, whereas the optimal dopant concentration for codoped ZrO_2 polymorphs was 6.25 at% Ca and 6.25 at% Mg, corresponding to the substitution of one Mg atom and one Ca atom in place of Zr atoms. The synergistic action of the Ca and Mg dopants resulted in the stability of superior photocatalytic phases. The stabilization effect was observed in TiO_2 tetragonal phases, where the c/a ratio increased in doped rutile and anatase TiO_2 systems, but more evident for Ca^{2+} doped systems than Mg^{2+} doped structures. The same stabilizing effect was observed in the

m-ZrO_2 phase, where adding of magnesium and calcium dopants resulted in increase of b/a ratio from 0.926 in m-ZrO_2 to 0.940, 0.950, and 0.952 in Mg doped, Ca doped, and Ca-Mg codoped m-ZrO_2, respectively. The b/a ratio gets closer to one due to addition of dopants impurities which tends to tetragonalize the monoclinic crystal structure.

5.2.2 Electronic Properties and Effect of Oxygen Vacancies

Significant alterations in the orbital contribution on and just above the Fermi level in the three titanium (iv) oxide polymorphs examined in this study are indicative of the synergistic Ca-Mg codoping effects of TiO_2. Other investigations have linked the observed shallow states above the Fermi level to the prevention of charge recombination effects, which is a significant disadvantage of TiO_2 polymorphs in photocatalysis (Guo *et al*., 2024). Introduction of an oxygen vacancy in Ca-Mg codoped TiO_2 polymorphs caused the valence band maximum to intersect the Fermi level and midgap states to emerge in the bandgap. This is because the divalent Ca and Mg dopants substituted Ti^{4+} ions, resulting in charge compensation through formation of oxygen vacancies or Ti^{3+} centers which boosted extra midgap states and narrowed the bandgap. Furthermore, the Ca and Mg impurity orbitals overlapped with titanium *3d* and oxygen *2p*, contributing to the enlarging of midstates and raising the valence band maximum to higher energy. For codoped ZrO_2, when Ca and Mg dopant states are introduced, the Fermi level moves towards the edge of the valence states; this effect has been noted in prior research using doping with main group elements like sulfur reported by Idrissi *et al*., (2021b). Furthermore, the Zr *4d* orbitals in the unoccupied states and on the valence band edge of Ca-Mg codoped m-ZrO_2 displayed the characteristics of t-ZrO_2 in its Density of States (DOS). Oxygen vacancy defective Ca-Mg codoped ZrO_2 revealed localized mid-gap states emerge at around 1eV above the Fermi energy and the conduction band minimum shifted to lower energies by 0.6 eV. This resulted in decrease of the band gap from around 4 eV to approximately 3.2 eV, which is comparable with the experimental findings in this study, which reveal that Ca-Mg codoping resulted in a bandgap narrowing. The midgap states have been shown to act as traps for photogenerated charge carriers hence enhancing photocatalytic efficiency of Ca-Mg codoped ZrO_2 (Guan *et al.*, 2023).

5.2.3 Characterization of the Synthesized Samples

The Inductively Coupled Plasma Mass Spectrometry (ICP-MS) analysis confirmed that the Ca and Mg dopants were successfully incorporated into the codoped TiO_2 and ZrO_2 samples. Ca-Mg codoped ZrO_2 exhibited a tetragonal phase with strong peaks at 30.28 ^{o}, 35.3 ^{o}, 50.4 ^{o}, 60.34 ^{o}, and 62.2 ^{o} corresponding to miller indices (101), (110), (112), (211), and (202) respectively. This is as expected from the theoretical results obtained in this study, in which the b/a ratios increased with Ca and Mg doping indicating tetregonalization of the monoclinic ZrO_2 structure, which is the low temperature phase. The computed average particle size from XRD results for 3.125 at% Ca + 6.25 at% Mg-TiO_2 and 6.25 at% Ca + 6.25 at% Mg-ZrO_2 codoped samples is 8.947 nm and 5.567 nm, respectively, which is significantly lower than pure or single doped samples. This is because presence of dopant atoms disturbs the usual crystal lattice, leading to smaller crystallites (Saoud *et al*., 2023). Impurity defects in the lattice caused by the introduction of dopants have been demonstrated to reduce agglomeration, resulting in nanoparticles of smaller size (Hassan & Jalil, 2022 ; Fedorov & Yarotskaya, 2021). The optical bandgaps of 3.125 at% Ca +6.25 at% Mg-TiO_2 and 6.25 at% Ca + 6.25 at% Mg-ZrO_2 were 1.92eV and 2.4eV respectively. Codoping alkaline earth metal dopants, such as Ca and Mg, causes oxygen vacancies and lattice deformation, which narrows the TiO_2 band gap by introduced extra states in the bandgap (Slimani *et al*., 2023 ; Klinbumrung *et al*., 2020).

5.2.4 Photocatalytic Activity Evaluation

The codoped 3.125 at% Ca + 6.25 at% Mg-TiO_2 and 6.25 at% Ca, 6.25 at% Mg-ZrO_2 samples had photocatalytic degradation efficiencies of 99.3% and 95.28%, respectively, following a 120-minute exposure time. The disparity in the degradation rate clearly relates to the semiconductor features, such as TiO_2 narrower bandgap compared to ZrO_2 (Acosta-Silva *et al*., 2024) .In comparison to pristine, Ca, or Mg single doped nanoparticles, the results demonstrated that Ca-Mg codoped TiO_2 or ZrO_2 nanoparticles exhibited significantly higher photocatalytic activity. This is primarily due to the synergistic effect of the dopants (Ibrahim *et al*., 2020), as well as the formation of surface defects like oxygen vacancies as a result of the insertion of Ca^{2+} and Mg^{2+} ions into the TiO_2 or ZrO_2 lattice (Minchi *et al*., 2019; An *et al*., 2022).As a result, the defects cause the formation of impurity energy states in the bandgap which

act as trapping sites for both photogenerated charges, slowing the recombination process and lowering the bandgap energy (Mardare *et al*., 2024 ; Hadi, 2024; Thambiliyagodage & Usgodaarachchi, 2021).The photogenerated charge carriers combine with water to form highly reactive species such as ·OH radicals, which have a large oxidation potential for RhB breakdown (Kunnamareddy *et al*., 2021).RhB degradation % for 5 cycles of the TiO_2 and ZrO_2 codoped samples was found to 99.3%, 99.0%, 98.8%, 98.5%, 98.1% and 95.28%, 95.1%, 94.6%, 94.3%, and 94% for codoped TiO_2 and ZrO_2 photocatalysts, respectively. These results confirm that the codoped TiO_2 and ZrO_2 nanoparticles have remarkable stability and reusability, which is the key reason for their widespread use in photocatalytic degradation of dyes.

5.2.5 Disinfection Activity Evaluation

The codoped samples exhibited higher antibacterial activity than pristine or single doped samples. The impurity states created by Ca and Mg dopants have been reported to prevent the recombination of photogenerated charge carriers, hence increasing antibacterial action (Ikram *et al*., 2021). Among all codoped samples, the 3.125 at% Ca + 6.25 at% Mg TiO_2 showed the best antibacterial efficacy in 90 minutes, where its antibacterial rate toward *E. coli* and *S. aureus* was 95% and 100 %, respectively. Codoped TiO_2 photocatalyst was shown to have a greater antibacterial activity compared to codoped ZrO_2 samples against all bacteria strains owing to its smaller energy gap, which requires less energy to generate Reactive Oxygen Species (Abd *et al*., 2025).

5.3 Recommendations

Future research can focus on atomistic modelling of Ca-Mg codoped TiO_2 and ZrO_2 surfaces to predict pollutant interactions with different surface terminations and identify favorable adsorption sites for photocatalytic degradation. These insights would help guide the design of more effective green photocatalysts.

REFERENCES

Aamir Iqbal, M., Ashraf, N., Shahid, W., Afzal, D., Idrees, F., & Ahmad, R. (2022). Fundamentals of Density Functional Theory: Recent Developments, Challenges and Future Horizons. In D. Glossman-Mitnik (Ed.), *Density Functional Theory Recent Advances, New Perspectives and Applications*. IntechOpen. https://doi.org/10.5772/intechopen.99019

Abd Elhamid Abo Salh, I., Add El-Salam, E., Ezzat, A., Aboshama, M., & Elhagali, A. (2025). Antimicrobial Effect of Three Different Nanoparticles-Modified 3D-Printed Denture Resin: An in Vitro Study. *Journal of International Society of Preventive and Community Dentistry*, *15*(1), 42–49. https://doi.org/10.4103/jispcd.jispcd 53 24

Abd-Elnaiem, A., Mostafa, M., Saber, O., Sadeq, M., & Abdel-Rahim, M. (2025). Phase transition and bandgap modulation in TiO_2 nanostructures for enhanced visible-light activity and environmental applications. *Scientific Reports*, *15*, Article 84316. https://doi.org/10.1038/s41598-025-07000-x

Abdi, J., Yahyanezhad, M., Sakhaie, S., Vossoughi, M., &, Alemzadeh, I. (2019). Synthesis of Porous TiO_2/ZrO_2 Photocatalyst Derived from Zirconium Metal Organic Framework for Degradation of Organic Pollutants Under Visible Light Irradiation. *Environmental Chemical Engineering.* (7)103096.

Abisharani, J., Devikala, S., Kumar, .R. Dinesh, Arthanareeswari, M., & Kamaraj, P. (2019). Green synthesis of TiO_2 Nanoparticles using Cucurbita pepo seeds extract. *2nd International Conference On Recent Advances in Material Chemistry, 14-16 February 2018*, *14*, 302–307. https://doi.org/10.1016/j.matpr.2019.04.151

Adawiya, J., Abbas, J., & Tawfeeq, A. (2025). Density Functional Theory Study of Chlorine, Fluorine, Nitrogen, and Sulfur doped rutile TiO_2 for photocatalytic application. *Scientific Reports*, *15*, Article 1139. https://doi.org/10.1038/s41598-024-84316-8

Ahmad, I., Zou, Y., Yan, J., Liu, Y., Shukrullah, S., Naz, M., Hussain, H., Khan, W., & Khalid, N. (2023). Hydrogen Production Using TiO_2-Based Photocatalysts: A Comprehensive Review. *ACS Omega*, 8(28), 25257-25287. https://doi.org/10.1021/acsomega.3c00963

Ahmad, M., Alasiri, A., Ahmad, J., Alqahtani, A., Abdullah, M., Abdel-Wahab, B. A., Pathak, K., Saikia, R., Das, A., Sarma, H., & Alzahrani, S. (2022). Green Synthesis of Titanium Dioxide Nanoparticles Using Ocimum sanctum Leaf Extract: In Vitro Characterization and Its Healing Efficacy in Diabetic Wounds. *Molecules*, *27*(22), 7712. https://doi.org/10.3390/molecules27227712

Ahmadpour, N., Sayadi, M., & Homaeigohar, S. (2020). A hierarchical Ca/TiO_2 /NH_2 -MIL-125 nanocomposite photocatalyst for solar visible light induced photodegradation of organic dye pollutants in water. *RSC Advances*, *10*(50), 29808–29820. https://doi.org/10.1039/D0RA05192F

Ahmed, A., Abdi, E., Mahmmould, S., Abdi, S., Mohamed, M., El-Sayed, B. & Fawzy, H. (2013). Characterization and Photocatalytic Efficiency of Palladium Doped-TiO_2 Nanoparticles. *Advances in Nanoparticles.*Vol.2 No.4, doi:10.4236/anp.2013.24051.

Ahmed, M., & Ali, M. M. (2021). Synthesis and Characterization of Zirconium Oxide Nanoparticles Via the Hydrothermal Method and Evaluation of their Antibacterial Activity. *Pharmacy and technology*, *14*(2), 938–942. https://doi.org/10.5958/0974-360X.2021.00167.0

Alagarsamy, A., Chandrasekaran, S., & Manikandan, A. (2022). Green synthesis and characterization studies of biogenic zirconium oxide (ZrO_2) nanoparticles for adsorptive removal of methylene blue dye. *Molecular Structure*, *1247*, 131275. https://doi.org/10.1016/j.molstruc.2021.131275

Al-Nuaim, M., Alwasiti, A., & Shnain, Z. (2023). The Photocatalytic Process in the Treatment of Polluted Water. *Journal of Chemical Papers*, *77*(2), 677–701. https://doi.org/10.1007/s11696-022-02468-7

Alotaibi, A., Promdet, P., Hwang, G., Li, J., Nair, S., Sathasivam, S., Kafizas, A., Carmalt, C., & Parkin, I. (2021). Zn and N Codoped TiO_2 Thin Films: Photocatalytic and Bactericidal Activity. *ACS Applied Materials & Interfaces*, *13*(8), 10480–10489. https://doi.org/10.1021/acsami.1c00304

Alotaibi, A., Williamson, B., Sathasivam, S., Kafizas, A., Alqahtani, M., Sotelo-Vazquez, C., Buckeridge, J., Wu, J., Nair, S., Scanlon, D., & Parkin, I. (2020). Enhanced Photocatalytic and Antibacterial Ability of Cu-Doped Anatase TiO_2 Thin Films: Theory and Experiment. *ACS Applied Materials & Interfaces*, *12*(13), 15348–15361. https://doi.org/10.1021/acsami.9b22056

Alotaibi, M., Wu, Q., & Lambert, C. (2023). Computational Studies of Ag5 Atomic Quantum Clusters Deposited on Anatase and Rutile TiO_2 Surfaces. *Applied Surface Science*, *613*, 156054. https://doi.org/10.1016/j.apsusc.2022.156054

Al-Zaqri, N., Muthuvel, A., Jothibas, M., Alsalme, A., Alharthi, F. A., & Mohana, V. (2021). Biosynthesis of Zirconium Oxide Nanoparticles Using Wrightia Tinctoria Leaf Extract: Characterization, Photocatalytic Degradation and Antibacterial Activities. *Inorganic Chemistry Communications*, *127*, 108507. https://doi.org/10.1016/j.inoche.2021.108507

Aman, N., Satapathy, P., Mishra, T., Mahato, M., & Das, N. (2012). Synthesis and Photocatalytic Activity of Mesoporous Cerium Doped TiO_2 as Visible Light Sensitive Photocatalyst. *Materials Research Bulletin*, *47*(2), 179–183. https://doi.org/10.1016/j.materresbull.2011.11.049

Ammann, A. (2007). Inductively coupled plasma mass spectrometry (ICP MS): A versatile tool. *Journal of Mass Spectrometry*, *42*(4), 419–427. https://doi.org/10.1002/jms.1206

An, J., Zhang, P., Ma, T., Liu, J., & He, Y. (2022). The Synthesis of Nanoscale Structure of Calcia-Stabilized Zirconia Electrolytes by Lamellar Liquid Crystal Template Method. *Materials Today Sustainability*, *18*, 100144. https://doi.org/10.1016/j.mtsust.2022.100144

Anbumani, D., Dhandapani, K. vizhi, Manoharan, J., Babujanarthanam, R., Bashir, A. K. H., Muthusamy, K., Alfarhan, A., & Kanimozhi, K. (2022). Green Synthesis and Antimicrobial Efficacy of Titanium Dioxide Nanoparticles Using Luffa Acutangula Leaf Extract. *Journal of King Saud University - Science*, *34*(3), 101896. https://doi.org/10.1016/j.jksus.2022.101896

andrade, (2023). Green Synthesis of Photocatalytic TiO_2/Ag Nanoparticles for an Efficient Water Remediation. *International Journal of Hydrogen Energy*, 48(84), 32604-32614.

Annu, A., Sivasankari, C., & Krupasankar, U. (2020a). Synthesis and Characterization of ZrO_2 Nanoparticle by Leaf Extract Bioreduction Process for Its Biological Studies. *Materials Today: Proceedings*, *33*, 5317–5323. https://doi.org/10.1016/j.matpr.2020.02.975

Annu, A., Sivasankari, C., & Krupasankar, U. (2020b). Synthesis and Characerization of ZrO_2 Nanoparticle by Leaf Extract Bioreduction Process for Its Biological Studies. *Materials Today: Proceedings*, *33*, 5317–5323. https://doi.org/10.1016/j.matpr.2020.02.975

Ansari, A., Siddiqui, V., Rehman, W., Akram, Md. K., Siddiqi, W., Alosaimi, M., Hussein, M., & Rafatullah, M. (2022). Green Synthesis of TiO_2 Nanoparticles Using Acorus calamus Leaf Extract and Evaluating Its Photocatalytic and In Vitro Antimicrobial Activity. *Catalysts*, *12*(2), 181. https://doi.org/10.3390/catal12020181

Aravind, M., Amalanathan, M., & Mary, M. (2021). Synthesis of TiO_2 Nanoparticles by Chemical and Green Synthesis Methods and Their Multifaceted Properties. *SN Applied Sciences*, *3*(4), 409. https://doi.org/10.1007/s42452-021-04281-5

Armakovic, S., Brojcin , M., Scepanovic. M., Golubovic, A., Babic, B., & Abramovic, F.(2019) Efficiency of La-Doped TiO_2 Calcined at Different Temperatures In Photocatalytic Degradation of B-Blockers. *Arabian Journal of Chemistry.* Volume 12, Issue 8, Pages 5355-5369

Arshad, Z., Shakir, S., Khoja, A., Javed, A., Anwar, M., Rehman, A., Javaid, R., Qazi, U., & Farrukh, S. (2022). Performance Analysis of Calcium-Doped Titania (TiO_2) as an Effective Electron Transport Layer (ETL) for Perovskite Solar Cells. *Energies*, *15*(4), 1408. https://doi.org/10.3390/en15041408

Asahi, R., Morikawa, T., Ohwaki, T., Aoki, K., & Taga, Y. (2001). Visible-light Photocatalysis in Nitrogen-doped Titanium Oxides. *Science*, 293(5528), 269-271. https://doi.org/10.1126/science.1061051

Asahi, R., Taga, Y., Mannstadt, W., & Freeman, A. (2000). Electronic and Optical Properties of Anatase \mathrmTiO$_2$. *Phys. Rev. B*, *61*(11), 7459–7465. https://doi.org/10.1103/PhysRevB.61.7459

Aslam, M., Abdullah, A., & Rafatullah, M. (2021). Recent Development in The Green Synthesis of Titanium Dioxide Nanoparticles using Plant-Based Biomolecules for Environmental and Antimicrobial Applications. *Journal of Industrial and Engineering Chemistry*, *98*, 1–16. https://doi.org/10.1016/j.jiec.2021.04.010

Balali, G., Yar, D., Dela, V., & Adjei-Kusi, P. (2020). Microbial Contamination, an Increasing Threat to the Consumption of Fresh Fruits and Vegetables in Today's World. *International Journal of Microbiology*, *2020*, 3029295. https://doi.org/10.1155/2020/3029295

Bandara, W., De Silva, R., De Silva, K., Dahanayake, D., Gunasekara, S., & Thanabalasingam, K. (2017). Is Nano ZrO_2 a Better Photocatalyst Than Nano TiO_2 for Degradation of plastics? *RSC Adv.*, *7*(73), 46155–46163. https://doi.org/10.1039/C7RA08324F

Bashir, A., Siddiqui, H., Naseem, S., & Bhatti, A. (2021). Ecofriendly Water-Based Solution Processing: Preliminary Studies of Zn-ZrO_2 Thin Films for Microelectronics Applications. *Coatings*, *11*(8), 901. https://doi.org/10.3390/coatings11080901

Batalovic, K., Radakovic, J., Bundaleski, N., Rakocevic, Z., Pasti, I., Skorodumova, N., & Range, C. (2020). Origin of Photocatalytic Activity Enhancement in Pd/Pt Deposited Anatase N- TiO_2 - Experimental Insights and Dft Study of (001) Surface. *Phys. Chem. Chem. Phys.* **(**22) Doi :10.1039/DOC3186K.18536-18547

Behara, D., Ummireddi, A., Aragonda, V., Pala, R., & Sivakumar, S. (2023). Experimental and Theoretical Study of Oxygen Vacancy Induced La-Doped Mesoporous TiO_2 for Enhanced Thermal Stability. *AIP Advances*, 13(5), 055107. https://doi.org/10.1063/5.0146008

Behnajady, M., & Eskandarloo, H. (2013). Characterization and Photocatalytic Activity of Ag–Cu/TiO ₂ Nanoparticles Prepared by Sol–gel Method. *Journal of Nanoscience and Nanotechnology*, *13*(1), 548–553. https://doi.org/10.1166/jnn.2013.6859

Belekoukia, M., Kaltzoglou, A., Lappas, A., & Antonopoulos, I. (2024). The Electrochemical and Structural Changes of Phosphorus-Doped TiO_2 Through in Situ Raman and in Situ X-ray diffraction analysis. *ACS Omega*, *9*(2), 2748–2759. https://doi.org/10.1021/acsomega.3c08122

Belošević-Čavor, J., Batalović, K., Koteski, V., Radaković, J., & Rangel, C. (2015). Enhancing Photocatalytic Properties of Rutile TiO_2 by Codoping With N and Metals – Ab Initio Study. *International Journal of Hydrogen Energy*, *40*(31), 9696–9703. https://doi.org/10.1016/j.ijhydene.2015.06.001

Bharati, B., Mishra, D., & Rath, C. (2018). Stabilization of anatase phase by uncompensated Ga-V codoping in TiO_2: A structural phase transition, grain growth and optical property study. *Ceramics International*, 44(18), 22166-22174.

Bharati, B., Sharma, S., & Rath, C. (2019). Stable Anatase Phase with a Bandgap in Visible Light Region by a Charge Compensated Ga–V (1:1) codoping in TiO_2. *Ceramics International*, 45(16), 20972-20979.

Bhullar, S., Goyal, N., & Gupta, S. (2021). Rapid Green-synthesis of TiO_2 nanoparticles for therapeutic applications. *RSC Advances*, *11*(48), 30343–30352. https://doi.org/10.1039/D1RA05588G

Bian, R., An, S., Wang, X., Xue, Y., Tian, J., Liang, Z., & Song, Z. (2023). Ca^{2+} doped TiO_2 Nano-sized Polygon Plates with Oxygen Vacancies for Photocatalytic Hydrogen Evolution. *International Journal of Hydrogen Energy*. https://doi.org/10.1016/j.ijhydene.2023.07.068

Biswas, M., & Rangari, V. (2022). Highly Porous Carbon Nanoparticles from Biowaste For Wastewater Treatment. In *Nano-Bioremediation: Fundamentals and Applications* (pp. 339–361). Elsevier. https://doi.org/10.1016/B978-0-12-823962-9.00009-X

Bitsos, D., Salepis, A., Orfanos, E., Coutsolelos, A., Kosheleva, I., Mitropoulos, A., & Ladomenou, K. (2025). Exploring Metal- and Porphyrin-Modified TiO_2-Based Photocatalysts for Efficient and Sustainable Hydrogen Production. *Inorganics*, *13*(4), 121. https://doi.org/10.3390/inorganics13040121

Borik, M., Korableva, G., Kulebyakin, A., Kuritsyna, I., Larina, N., Lomonova, E., Milovich, F., Myzina, V., Ryabochkina, P., Sidorova, N., Tabachkova, N., & Volkova, T. (2021). Phase Stability and Transport Properties of (ZrO2)0.91−x(Sc2O3)0.09(Yb2O3)x Crystals (x = 0–0.01). *Crystals*, *11*(2), 83. https://doi.org/10.3390/cryst11020083

Bulska, E., & Wagner, B. (2016). Quantitative aspects of inductively coupled plasma mass spectrometry. *Philosophical Transactions of the Royal Society A: Mathematical, Physical and Engineering Sciences*, *374*(2079), 20150369. https://doi.org/10.1098/rsta.2015.0369

Buonsanti, R., Grillo, V., Carlino, E., Giannini, C., Kipp, T., Cingolani, R., & Cozzoli, P. (2008). Nonhydrolytic synthesis of high-quality anisotropically shaped brookite TiO_2 nanocrystals. *Journal of the American Chemical Society*, 130(33), 11223-11233.

Cao, W. (2016). *Semiconductor Photocatalysis*. IntechOpen. https://doi.org/10.5772/61384

Cao, Z., An, S., & Song, X. (2022). Effect of Thermal Treatment at High Temperature on Phase Stability and Transformation of Yb_2O_3 and Y_2O_3 Codoped ZrO_2 Ceramics. *Scientific Reports*, *12*(1), 9955. https://doi.org/10.1038/s41598-022-13705-0

Chau, T., Kandasamy, S., Chinnathambi, A., Alahmadi, T., & Brindhadevi, K. (2023). Synthesis of Zirconia Nanoparticles Using Laurus Nobilis for Use As An Antimicrobial Agent. *Applied Nanoscience*, *13*(2), 1337–1344. https://doi.org/10.1007/s13204-021-02041-w

Chau, T., Veeraragavan, G., Narayanan, M., Chinnathambi, A., Alharbi, S., Subramani, B., Brindhadevi, K., Pimpimon, T., & Pikulkaew, S. (2022). Green Synthesis of Zirconium Nanoparticles Using Punica Granatum (pomegranate) Peel Extract and Their Antimicrobial and Antioxidant Potency. *Environmental Research*, *209*, 112771. https://doi.org/10.1016/j.envres.2022.112771

Chelliah, P., Wabaidur, S., Sharma, H., Majdi, H., Smait, D., Najm, M., Iqbal, A., & Lai, W. (2023). Photocatalytic Organic Contaminant Degradation of Green Synthesized ZrO_2 NPs and Their Antibacterial Activities. *Separations*, *10*(3), 156. https://doi.org/10.3390/separations10030156

Chen, D., Jiang, Z., Geng, J., & Zhu, J. (2016). Influences of Doping on Photocatalytic Properties of TiO_2 Photocatalyst. In D. Dongfang (Ed.), *Semiconductor photocatalysis: Materials, mechanisms and applications* (pp. 241-265). IntechOpen. https://doi.org/10.5772/63234

Chen, H., Li, X., Wan, R., Kao-Walter, S. & Lei, Y. (2017). A DFT Study of The Electronic Structures and Optical Properties of (Cr, C) Codoped Rutile TiO_2, *Chemical Physics* (2017), doi: https://doi.org/10.1016/j. chemphys.2017.11.021

Chen, H., Li, X., Wan, R., Kao-Walter, S., Lei, Y., & Leng, C. (2018). A DFT Study On Modification Mechanism of (N,S) Interstitial Codoped Rutile TiO_2. *Chemical Physics Letters*, *695*, 8–18. https://doi.org/10.1016/j.cplett.2018.01.044

Chen, T., Furubayashi, Y., Hirose, Y., Hitosugi, T., Shimada, T., & Hasegawa, T. (2007). Anatase Phase Stability and Doping Concentration Dependent Refractivity In Codoped Transparent Conducting TiO_2 Films. *Journal of Physics D: Applied Physics*, *40*(19), 5961–5964. https://doi.org/10.1088/0022-3727/40/19/026

Chen, X., Liu, L., & Huang, F. (2016). Formation of Oxygen Vacancies and Ti^{3+} State In TiO_2 Thin Film and Enhanced Optical Properties By Air Plasma Treatment. *Scientific Reports*, 6, 32355. https://doi.org/10.1038/srep32355

Chen, X., Liu, L., Yu, P., & Mao, S. S. (2013). Increasing Solar Absorption for Photocatalysis with Black Hydrogenated Titanium Dioxide Nanocrystals. *Science*, 331(6018), 746-750. https://doi.org/10.1126/science.1200448

Chen, Y., Ma, D., He, G., & Pan, S. (2024). Effects of pH on the Photocatalytic Activity and Degradation Mechanism of Rhodamine B over Fusiform Bi Photocatalysts Under Visible Light. *Water*, *16*(17), 2389. https://doi.org/10.3390/w16172389

Cheng, Q., Yang, W., Chen, Q., Zhu, J., Li, D., Fu, L., & Zhou, L. (2020). Fe-Doped Zirconia Nanoparticles with Highly Negative Conduction Band Potential for Enhancing Visible Light Photocatalytic Performance. *Applied Surface Science.* Volume 530, 15. 147291.Doi :1016/j.apsusc.2020.147291.

Chiang , L.,& Doong, R. (2014). Cu-TiO_2 Nanorods with Enhanced Ultraviolet- and Visible-Light Photo Activity for Bisphenol a Degradation. *J Hazard Mater*.277:84-92. doi: 10.1016/j.jhazmat.2014.01.047.

Chiara, G. Maria, C., Elio, G., Robertson, B., Christiana, D. & Gianfranco, P. (2014). Cerium-doped Zirconium Dioxide a Visible Light Sensitive Photoactive Material of Third Generation.*J. Phys.chem*5(3), pp 447-451.

Chowdhury, M., Hossain, N., Mostofa, M., Mia, M., Tushar, M., Rana, M., & Hossain, M. (2023). Green Synthesis and Characterization of Zirconium Nanoparticle for Dental Implant Applications. *Heliyon*, *9*(1), e12711. https://doi.org/10.1016/j.heliyon.2022.e12711

Colón, G., Maicu, M., Hidalgo, M., & Navío, J. (2006). Cu-doped TiO_2 Systems with Improved Photocatalytic Activity. *Applied Catalysis B: Environmental*, *67*(1), 41–51. https://doi.org/10.1016/j.apcatb.2006.03.019

Coronell, M., Toscano-Lucas, G., Solano, R., & Herrera, A. (2022). Green Synthesis of Silver-Doped Titanium Dioxide Nanostructures for Acetaminophen Degradation Under Solar Radiation. *Ingenieria y Universidad*, *26*. https://doi.org/10.11144/Javeriana.iued26.gsst

Cravansola, S., Federico, C., Gaziano, F. & Domenica, S. (2017). Sulphur-Doped TiO_2; Structural and Surface Properties *Research gate; Catalysts,* 7,214, doi:103390/catal7070214.

Daniel, M., & Astruc, D. (2004). Gold Nanoparticles: Assembly, Supramolecular Chemistry, Quantum-Size-Related Properties, and Applications Toward Biology, Catalysis, and Nanotechnology. *Chemical Reviews*, *104*(1), 293–346. https://doi.org/10.1021/cr030698+

De Souza, E., & Appel, L. (2021). Oxygen Vacancy Formation and Their Role In The CO_2 Activation On Ca Doped ZrO_2 Surface: An ab-initio DFT Study. *Applied Surface Science*, *553*, 149589. https://doi.org/10.1016/j.apsusc.2021.149589

Deák, P., Kullgren, J., Aradi, B., Frauenheim, T., & Kavan, L. (2019). Water Splitting and The Band Edge Positions of TiO_2. *Electrochimica Acta*, 199, 27-34.

Díaz-Reyes, J., Arias-Cerón, J., Álvarez-Ramos, M., Rodríguez-Vargas, B., Pérez-Benítez, A., Balderas-López, J., & Mendoza-Álvarez, J. (2023). Band Gap Narrowing Induced by Oxygen Vacancies in Reactively Sputtered TiO_2 Thin Films. *Thin Solid Films*, *767*, Article 139676. https://doi.org/10.1016/j.tsf.2023.139676

Dima, R., Maluta, N., & Maphanga, R. **(**2020) First-Principles Investigation of Ru- and Pt-Doped TiO_2 Brookite Surfaces. *Int. J. Electrochem. Sci.,* 15 1757 – 1770.Doi: 10.20964/2020.02.61

Dima, R., Phuthu, L., Maluta, N., Kirui, J., & Maphanga, R. (2021) Electronic, Structural, and Optical Properties of Mono-Doped and Co-Doped (210) TiO_2 Brookite Surfaces for Application in Dye-Sensitized Solar Cells—A First Principles Study. *Materials* 14, 3918. https://doi.org/10.3390/ma14143918.

Dominguez, R., Alarcón-Flores, G., Aguilar-Frutis, M., Sánchez-Alarcón, R., Falcony, C., Dorantes-Rosales, H., González-Velázquez, J., & Rivas-López, D. (2016). Effect on the Stabilization of the Anatase Phase and Luminescent Properties of Samarium-doped TiO_2 Nanocrystals Prepared by Microwave Irradiation. *Journal of Alloys and Compounds*, *687*, 121–129. https://doi.org/10.1016/j.jallcom.2016.06.083

Dong, J., Han, J., Liu, Y., Nakajima, A., Matsushita, S., Wei, S., & Gao, W. (2020). Defective Black TiO_2 Synthesized Via Anodization for Visible-Light Photocatalysis. *ACS Applied Materials & Interfaces*, 6(3), 1385-1388.

Doufar, N., Benamira, M., Lahmar, H., Trari, M., Avramova, I., & Caldes, M. (2020). Structural and Photochemical Properties of Fe-Doped ZrO_2 and Their Application as Photocatalysts with TiO_2 for Chromate Reduction. *Journal of Photochemistry and Photobiology A: Chemistry*, *386*, 112105. https://doi.org/10.1016/j.jphotochem.2019.112105

El-Dossoki, F., Atwee, T., Hamada, A., & El-Bindary, A. (2021). Photocatalytic Degradation of Remazol Red B and Rhodamine B Dyes Using TiO_2 Nanomaterial: Estimation of the Effective Operating Parameters. *Desalination and Water Treatment*, *233*, 319–330. https://doi.org/10.5004/dwt.2021.27519

Elmakki, T., (2024). One-Pot Green Synthesis of TiO_2 Nanoparticles Using Inula Viscosa Leaf Extract as an Efficient Photocatalyst for Organic Dyes Removal. *International Journal of Hydrogen Energy*, 91, 463-476.

El-Sayed, R., Khattab, R**.,** Rehim, S., Hassan, W., & El-Shazly, T. (2021). Band Structure Engineering and Optical Properties of Pristine and Doped Monoclinic Zirconia (*m*-ZrO_2): Density Functional Theory Theoretical Prospective. *American Chemical Society*. Doi: 10.1021/acsomega.1c04756.

Etafa Tasisa, Y., Kumar Sarma, T., Krishnaraj, R., & Sarma, S. (2024). Band Gap Engineering of Titanium Dioxide (TiO_2) Nanoparticles Prepared Via Green Route and Its Visible Light Driven for Environmental Remediation. *Results in Chemistry*, *11*, 101850. https://doi.org/10.1016/j.rechem.2024.101850

Fang, Y., Xu, T., Zhang, Y., Kong, X., Liu, J., Cui, S., & Wang, D. (2019). Structural, Electronic and Optical Properties of La, C-Codoped TiO_2 Investigated by First Principle Calculations. *Journal of Physics and Chemistry of Solids, 132*, 121–129. https://doi.org/10.1016/j.jpcs.2019.04.017

Fedorov, P., & Yarotskaya, G. (2021). *Zirconium dioxide. Review. 23*(2), 169–187. https://doi.org/10.17308/kcmf.2021.23/3427

Foo, C., Li, Y., Lebedev, K., Chen, T., Day, S., Tang, C., & Tsang, S. (2021). Characterisation of Oxygen Defects and Nitrogen Impurities In TiO_2 Photocatalysts Using Variable-Temperature X-Ray Powder Diffraction. *Nature Communications*, *12*(1), 661. https://doi.org/10.1038/s41467-021-20977-z

Fuentes-Cervantes, A., Ruiz Allica, J., Calderón Celis, F., Costa-Fernández, J., & Ruiz Encinar, J. (2023). The Potential of ICP-MS as a Complementary Tool in Nanoparticle–Protein Corona Analysis. *Nanomaterials*, *13*(6), 1132. https://doi.org/10.3390/nano13061132

Fujishima, A., & Honda, K. (1972). Electrochemical Photolysis of Water at a Semiconductor Electrode. *Nature*, 238(5358), 37-38.

Funahashi, T., Mineshige, A., Yoshioka, H., Kobayashi, K., Matsushita, Y., Katsuya, Y., Tanaka, M., Sakata, O., & Yazawa, T. (2016). Effect of Cation Doping On Ionic Conductivity and Crystal Structure of Oxyapatite-Type Lanthanum Silicates. *Solid State Ionics*, *289*, 106–112. https://doi.org/10.1016/j.ssi.2016.03.004

Ingale, A. (2013). Biogenic Synthesis of Nanoparticles and Potential Applications: An Eco- Friendly Approach. *Journal of Nanomedicine & Nanotechnology*, *04*(02). https://doi.org/10.4172/2157-7439.1000165

Gai, Y., Li, J., Li, S., Xia, J., & Wei, S. (2009). Design of Narrow-Gap TiO_2: A Passivated Codoping Approach for Enhanced Photoelectrochemical Activity. *Physical Review Letters*, 102(3), 036402.

Gallino, F., Di Valentin, C., & Pacchioni, G. (2011). Band Gap Engineering of Bulk ZrO_2 by Ti Doping. *Phys. Chem. Chem. Phys.*, *13*(39), 17667–17675. https://doi.org/10.1039/C1CP21987A

Gan , Q., Feng , G., Liu , X., Shang , H., & Feng , C.(2017).Self-Assembly of Mesoporous Bi-S-TiO 2 Composites for Degradation of Industrial Dinitrotoluene Solution Under UV Light. *Environ Sci Pollut Res Int*. 24(10):9585-9593. doi: 10.1007/s11356-017-8526

Garcia, G. & Scolfaro, L., Lino, A., Freire, V., Farias, G., Silva, C., Leite Alves, H., Rodrigues, S. & Silva, E. (2006). Structural, Electronic and Optical Properties of ZrO_2 from *Ab-initio* Calculations. *Journal of applied Physics*, Volume100,104103 (2006), doi10.1063/1.2386967.

Garcia, J., Scolfaro, L., R., Lino, A., Freire, V., Farias, G., Silva, C., Alves, H., Rodrigues, S., & da Silva, E. (2006). Structural, Electronic, and Optical Properties of ZrO_2 from Ab Initio Calculations. *Journal of Applied Physics*, *100*(10), 104103. https://doi.org/10.1063/1.2386967

Gharagozlou, M., & Bayati, R. (2014). Photocatalytic Activity and Formation of Oxygen Vacancies in Cation Doped Anatase TiO_2 Nanoparticles. *Ceramics International*,*40*(7),10247–10253. https://doi.org/10.1016/j.ceramint.2014.02.114

Ghazi, S. (2020). Photocatalytic Degradation of Organic Dyes Using Titanium Dioxide (TiO_2) and Mg-TiO_2 Nanoparticles. *Scientific Archives of Dental Sciences*, 3(4), 13-22.

Ghuman, K. & Singh, C. (2013). A DFT + U Study of (Rh, Nb)-Codoped Rutile TiO_2.*J Phy Condens Matter.*2013 Feb 27;25 (8):085501. doi:10.1088/0953-8984/25/8/085501.

Glover, E., Ellington, S., Sankar, G., & Palgrave, R. (2016). The Nature and Effects of Rhodium and Antimony Dopants On the Electronic Structure of TiO_2: Towards Design of Z-Scheme Photocatalysts. *J. Mater. Chem. A*, *4*(18), 6946–6954. https://doi.org/10.1039/C6TA00293E

Gong, J., Gao, P., Han, G., Ma, Q., Wang, X., Chen, S., & Yang, B. (2024). High-Temperature Phase Stability of Y_2O_3 and SiO_2 Co-Doped Zro2 Powder. *Journal of Sol-Gel Science and Technology*, *109*(3), 619–625. https://doi.org/10.1007/s10971-023-06274-9

Gong, S., Zhang, T., Liu, B., Liu, P., Niu, Y., Yang, Z., Jin, Y., Chen, W., Ji, G., Guo, S., & Zhang, L. (2025). Synthesizing Mixed-Phase TiO_2 Semiconductor Catalysts Via Microwave-Assisted Rutile Seed Crystal: A New Approach. *Ceramics International*, *51*(7), 8880–8896. https://doi.org/10.1016/j.ceramint.2024.12.319

Gorgani, M., & Kaleji, B. (2020). Structural, Photocatalytic and Surface Analysis of Nb/Ag Codoped TiO_2 Mesoporous Nanoparticles. *Journal of Sol-Gel Science and Technology*, *96*(3), 728–741. https://doi.org/10.1007/s10971-020-05403-y

Goudarzi, M. G., Bagherzadeh, M., Taheri, F., & Rostami-Vartooni, A. (2020). Preparation and Characterization of Magnetic Zirconium Oxide Nanocomposite as a Catalyst for Reduction of Methylene Blue. *SN Applied Sciences*, *2*(7), 1249. https://doi.org/10.1007/s42452-020-3034-3

Goyal, P., Bhardwaj, A., Mehta, B., & Mehta, D. (2021). Research Article Green Synthesis of Zirconium Oxide Nanoparticles (ZrO_2NPs) Using Helianthus Annuus Seed and Their Antimicrobial Effects. *Journal of the Indian Chemical Society*, *98*(8), 100089. https://doi.org/10.1016/j.jics.2021.100089

Graciani, J., Álvarez, L., Rodriguez, J., & Sanz, J. (2021). N doping of Rutile TiO_2 (110) Surface: A Theoretical DFT Study. *Journal of Physical Chemistry C*, 112(7), 2624-2630.

Groeneveld, I., Kanelli, M., Ariese, F., & Van Bommel, M. (2023). Parameters That Affect the Photodegradation of Dyes and Pigments in Solution and On Substrate an Overview. *Dyes and Pigments*, *210*, 110999. https://doi.org/10.1016/j.dyepig.2022.110999

Guan, S., Cheng, Y., Hao, L., Yoshida, H., Tarashima, C., Zhan, T., Itoi, T., Qiu, T., & Lu, Y. (2023). Oxygen Vacancies Induced Band Gap Narrowing for Efficient Visible-Light Response in Carbon-Doped TiO2. *Scientific Reports*, *13*(1), 14105. https://doi.org/10.1038/s41598-023-39523-6

Gul, S., Khan, M., Yi, Z., & Wu, B. (2017). Structural, Electronic and Optical Properties of Non-Compensated and Compensated Models of Yttrium Stabilized Zirconia. *Materials Research Express*, *4*(12), 126304. https://doi.org/10.1088/2053-1591/aa9bfa

Guo, C. (2024). Recent Progress of Ion-Modified TiO_2 for Enhanced Photocatalytic Hydrogen Production. *Molecules*, 29(10), 2162.

Guo, Y., Ma, W., Chong, M., Tang, C. Y., Zhou, Q., Nan, J., & Zhu, Y. (2024). Generation of Holes from Intra-Valence Band for Enhanced Oxidation Potentials Under Visible Light. *Chem*, *10*(4), 1252–1267. https://doi.org/10.1016/j.chempr.2024.01.022

Gupta, T., Cho, J., Rehman, F., Subramaniyam, C., Seo, H., Kim, S., Liu, Y., Zhang, L., Yu, J., & Lim, S. (2020). Machine Learning Band Gaps of Doped-TiO_2 Photocatalysts from Structural and Morphological Parameters. *ACS Omega*, *5*(24), 14487–14496. https://doi.org/10.1021/acsomega.0c01438

Gurkan, Y., Kasapbasi, E., & Cinar, Z. (2017). Influence of Se/N Codoping On the Structural, Optical, Electronic and Photocatalytic Properties of TiO_2 . *Molecules*, *22*(3), Article 414. https://doi.org/10.3390/molecules22030414

Gutiérrez-Moreno, J., Fernández-Álvarez, V., Medina-Rodríguez, S., & Hernández-Fenollosa, M. (2025). Synthesis and Characterization of Nitrogen-Doped Titanium Dioxide (TiO_2-N) For Photocatalytic Applications. *Materials Today Communications*, 38, 107850.

Hanaor, D., & Sorrell, C. (2011). Review of The Anatase to Rutile Phase Transformation. *Journal of Materials Science*, 46(4), 855-874.

Hanaor, D., Assadi, M., Li, S., Yu, A., & Sorrell, C. (2012). Ab initio Study of Phase Stability in Doped TiO_2. *Computational Mechanics*, *50*(2), 185–194. https://doi.org/10.1007/s00466-012-0728-4

Haque, F., Blanchard, A., Laipply, B., & Dong, X. (2024). Visible-Light-Activated TiO_2-Based Photocatalysts for the Inactivation of Pathogenic Bacteria. *Catalysts*, *14*(12), 855. https://doi.org/10.3390/catal14120855

Harahap, H. (2024). Bio-Synthesis of TiO_2 Photocatalyst: A Reduced Step Approach Using Leaf Extract. *Green Chemistry Letters and Reviews*, 17(1), 2433607.

Hassan, N. S., & Jalil, A. (2022). A Review On Self-Modification of Zirconium Dioxide Nanocatalysts with Enhanced Visible-Light-Driven Photodegradation of Organic Pollutants. *Journal of Hazardous Materials*, *423*, 126996. https://doi.org/10.1016/j.jhazmat.2021.126996

Heffner, H., Faccio, R., & López-Corral, I. (2022). Electronic Structure Properties of Boron–Doped and Carbon–Boron–Codoped TiO_2(B) For Photocatalytic Applications. *Journal of Physics and Chemistry of Solids*, *165*, 110685. https://doi.org/10.1016/j.jpcs.2022.110685

Henderson, M. (2011). A Surface Science Perspective On TiO_2 Photocatalysis. *Surface Science Reports*, 66(6-7), 185-297. https://doi.org/10.1016/j.surfrep.2011.01.001

Hussain, F., Imran, M., Khalil, R., Sattar, M., Niaz, N., Rana, A., Ismail, M., Khera, E., Rasheed, U., Mumtaz, F., Javed, T., & Kim, S. (2019). A First-Principles Study of Cu and Al Doping in ZrO_2 For Rram Device Applications. *Vacuum*, *168*, 108842. https://doi.org/10.1016/j.vacuum.2019.108842

Ibrahim, H., Mohamed, A., & Ibrahim, M. (2020). Origin of The Enhanced Photocatalytic Activity of (Ni, Se, and B) Mono- and Co-Doped Anatase TiO_2 Materials Under Visible Light: A Hybrid DFT Study. *RSC Advances*, *10*(70), 43092–43102. https://doi.org/10.1039/D0RA07781J

Idrissi, S., Ziti, S., Labrim, H., & Bahmad, L. (2021a). Sulfur Doping Effect On the Electronic Properties of Zirconium Dioxide ZrO_2. *Materials Science and Engineering: B*, *270*, 115200. https://doi.org/10.1016/j.mseb.2021.115200

Idrissi, S., Ziti, S., Labrim, H., & Bahmad, L. (2021b). Sulfur Doping Effect On the Electronic Properties of Zirconium Dioxide (ZrO_2). *Materials Science and Engineering: B*, *270*, 115200. https://doi.org/10.1016/j.mseb.2021.115200

Idrissi.S., Ziti, S., Labrim, H., & Bahmad, L. (2020). Doping Effect of Sulfur Substituting on Zirconium Dioxide. *Authorea.* DOI:10.22541/au.160322433.39186383/v1.

Ihara, T., Miyoshi, M., Iriyama, Y., Matsumoto, O., & Sugihara, S. (2003). Visible-Light-Active Titanium Oxide Photocatalyst Realized by an Oxygen-Deficient Structure and By Nitrogen Doping. *Applied Catalysis B: Environmental*, 42(4), 403-409.

Ikram, M., Aslam, S., Haider, A., Naz, S., Ul-Hamid, A., Shahzadi, A., Ikram, M., Haider, J., Ahmad, S., & Butt, A. (2021). Doping of Mg on ZnO Nanorods Demonstrated Improved Photocatalytic Degradation and Antimicrobial Potential with Molecular Docking Analysis. *Nanoscale Research Letters*, *16*(1), 78. https://doi.org/10.1186/s11671-021-03537-8

Jin-Gang, M., Zhang, C., Ji-Jun, G., You-Zhi, W., Sheng-Zhong, K., Hua, Y., Chen, Y., Liu, Z. & Chen, H. (2015). The Electronic and Optical Properties of Alkaline Earth Metal Doped Anatase TiO_2; A Comparative Study of Screened Hybrid Functional and Generalised Gradient Approximation. *Materials Journal*, 2015,8,5508-5525.

Jones, R. (2015). Density Functional Theory: Its Origins, Rise To Prominence, and Future. *Reviews of Modern Physics*, *87*(3), 897–923. https://doi.org/10.1103/RevModPhys.87.897

Joshi, N., Chaudhary, N., & Rai, N. (2021). Medicinal Plant Leaves Extract Based Synthesis, Characterisations and Antimicrobial Activities of ZrO_2 Nanoparticles (ZrO_2 NPs). *BioNanoScience*, *11*(2), 497–505. https://doi.org/10.1007/s12668-021-00829-2

Kambur, A., Pozan, S., & Boz, I. (2012). Preparation, Characterization and Photocatalytic Activity of TiO_2 – ZrO_2 Binary Oxide Nanoparticles. *Applied Catalysis B*: *Environmental* .115–116, 149–158. DOI: 10.1016/j.apcatb.2011.12.012

Kanoun, M. B., Ahmed, F., Awada, C., Jonin, C., & Brevet, P. (2024). Band Gap Engineering of Au Doping and Au – N Codoping into Anatase TiO_2 for Enhancing the Visible Light Photocatalytic Performance. *International Journal of Hydrogen Energy*, *51*, 907–913. https://doi.org/10.1016/j.ijhydene.2023.10.244

Katal, R., Eshkalak, S., Masudy-Panah, S., Kosari, M., Saeedikhani, M., Zarinejad, M., & Ramakrishna, S. (2024). Evaluation of Solar-Photocatalytic Degradation of Gaseous Multicomponent Volatile Organic Compounds Using TiO_2-Based Photocatalysts. *Journal of Cleaner Production*, 434, 140245.

Katal, R., Masudy-Panah, S., Tanhaei, M., Farahani, M., & Jiangyong, H. (2020). A Review On the Synthesis of The Various Types of Anatase TiO_2 Facets and Their Applications For Photocatalysis. *Chemical Engineering Journal*, 384, 123384.

Katal, R., Shen, T., Jafari, I., Masudy-Panah, S., & Farahani, M. (2023). An Overview On the Preparation and Photocatalytic Activity of Transparent TiO_2 Films. *Journal of Photochemistry and Photobiology C: Photochemistry Reviews*, 53, 100552.

Kaur, M., & Singh, K. (2007). Review On Titanium and Titanium Based Alloys As Biomaterials For Orthopaedic Applications. *Materials Science and Engineering: C*, 102, 844-862.

Kayani, Z., Abid, H., Nazli, H., Shahid, A., Riaz, S., & Naseem, S. (2023). Mg Doped TiO_2 Thin Films: Optical, Dielectric, Photocatalytic, Magnetic and Antibacterial Studies. *Materials Science and Engineering: B, 297*, 116674. https://doi.org/10.1016/j.mseb.2023.116674

Keerthana, S. P., Yuvakkumar, R., Senthil Kumar, P., Ravi, G., & Velauthapillai, D. (2022). Nd Doped ZrO_2 Photocatalyst for Organic Pollutants Degradation in Wastewater. *Environmental Technology & Innovation*, *28*, 102851. https://doi.org/10.1016/j.eti.2022.102851

Kenzhina, I., Kozlovskiy, A., Begentayev, M., Blynskiy, P., Tolenova, A., & Popov, A. (2025). Study of Phase Transformations in ZrO_2 Ceramics Stabilized by Y_2O_3 and Their Role in Changing Strength Characteristics and Heat Resistance. *Sustainability*, *17*(10), 4284. https://doi.org/10.3390/su17104284

Khan, H. (2025). Cerium-Doped Titanium Dioxide (CeT) Hybrid Material, Characterization and Spiramycin Antibiotic Photocatalytic Activity. *Catalysts*, *15*(6), 512. https://doi.org/10.3390/catal15060512

Khan, J., & Han, L. (2023). Oxygen Vacancy in TiO_2: Production Methods and Properties. In B. Bejaoui (Ed.), *Updates on Titanium Dioxide*. IntechOpen. https://doi.org/10.5772/intechopen.111545

Khan, M., Lan, Z., & Zeng, Y.(2018). Analysis of Indium Oxidation State on the Electronic Structure and Optical Properties of TiO_2. Materials *(Basel).* 11(6): 952.doi: 10.3390/ma11060952

Khan, M., Ansari, S., Pradhan, D., Ansari, M., Han, D., Lee, J., & Cho, M. (2016). Band Gap Engineered TiO2 Nanoparticles for Visible Light Induced Photoelectrochemical and Photocatalytic Studies. *Journal of Materials Chemistry A*, 2(3), 637-644.

Khan, M., Zeng, Y., Lan, Z., & Lin, M. (2019). Ab-initio Study of Indium, Nitrogen Codoping Effect On the Structure and Properties of TiO_2. *Materials Research Express*, *6*(8), 085517. https://doi.org/10.1088/2053-1591/ab1e0c

Khan, R., Rahman, N., Prasannan, A., Ganiyeva, K., Chakrabortty, S., & Sangaraju, S. (2025). Phase Transition and Bandgap Modulation in TiO_2 Nanostructures For Enhanced Visible-Light Activity and Environmental Applications. *Scientific Reports*, *15*(1), 20309. https://doi.org/10.1038/s41598-025-07000-x

Khattab, E., Abd El Rehim, S., Hassan, W., & El-Shazly, S. (2021). Band Structure Engineering and Optical Properties of Pristine and Doped Monoclinic Zirconia (m -ZrO_2): Density Functional Theory Theoretical Prospective. *ACS Omega*, *6*(44), 30061–30068. https://doi.org/10.1021/acsomega.1c04756

Khatun, N., Tiwari, S., Amin, R., Tseng, C., Biring, S., & Sen, S. (2020). Stable Anatase Phase with a Bandgap in Visible Light Region by a Charge Compensated Ga–V (1:1) Codoping in TiO_2. *Ceramics International*, *46*(7), 8958–8970. https://doi.org/10.1016/j.ceramint.2019.12.143

Kianfar, A., Arayesh, M., & Momeni, M. (2021). Degradation of MB and RhB by Modified ZrO_2 Nanoparticles Via Sunlight. *Applied Physics A*, *127*(2), 158. https://doi.org/10.1007/s00339-020-04257-z

Kim, W., Tachikawa, T., Kim, H., Lakshminarasimhan, N., Murugan, P., Park, H., Majima, T., & Choi, W. (2014). Visible Light Photocatalytic Activities of Nitrogen and Platinum-Doped TiO_2: Synergistic Effects of Codopants. *Applied Catalysis B: Environmental*, *147*, 642–650. https://doi.org/10.1016/j.apcatb.2013.09.034

Kumar, A. (2023). Microbial Synthesis of Titanium Dioxide Nanoparticles and Their Importance in Wastewater Treatment and Antimicrobial Activities: A Review. *Environmental Research*, 237, 116975.

Kumar, A., Kumar, P., & Dhaliwal, A. (2021). Structural Studies of Zirconia and Yttria Doped Zirconia for Analysing It Phase Stabilization Criteria. *IOP Conference Series: Materials Science and Engineering*, *1033*(1), 012052. https://doi.org/10.1088/1757-899X/1033/1/012052

Kumar, A., Singh, D., Singh, R. K., Kumar, P., & Kumar, R. (2024). Influence of Ti-Vacancies On The Site Occupancy of Amphoteric Calcium, Oxygen Vacancies, Dielectric, Optical, and Ferroelectric Behavior of $Ba_{0.8}Ca_{0.2}Ti_{1-x}O_{3-\delta}$. *Journal of Alloys and Compounds*, 1012, 176580. https://doi.org/10.1016/j.jallcom.2024.176580

Kumar, D., Singh, A., Kaur, N., Thakur, A., & Kaur, R. (2020a). Tailoring Structural and Optical Properties of ZrO_2 with Nickel Doping. *SN Applied Sciences*, *2*(4), 644. https://doi.org/10.1007/s42452-020-2491-z

Kumar, D., Singh, A., Kaur, N., Thakur, A., & Kaur, R. (2020b). Tailoring Structural and Optical Properties of ZrO_2 with Nickel Doping. *SN Applied Sciences*, *2*(4), 644. https://doi.org/10.1007/s42452-020-2491-z

Kumar, M., Basera, P., Saini, S., & Bhattacharya, S. (2020). Role of Defects in Photocatalytic Water Splitting: Monodoped vs Codoped $SrTiO_3$. *The Journal of Physical Chemistry C*, *124*(19), 10272–10279. https://doi.org/10.1021/acs.jpcc.9b11160

Kumar, M., Majumdar, J., & Manna, I. (2025). Phase Evolution, Densification Behaviour and Thermal and Mechanical Properties of Gd_2O_3 Co-Doped Y_2O_3 Stabilised ZrO_2. *Journal of Alloys and Compounds*, *1022*, 179851. https://doi.org/10.1016/j.jallcom.2025.179851

Kumar, S. (2024). A Review of Recent Developments in Green Synthesis of TiO_2 Nanoparticles Using Plant Extract: Synthesis, characterization and photocatalytic activity. *Inorganic Chemistry Communications*, 163, 112269.

Kumaravel, V., Rhatigan, S., Mathew, S., Michel, M., Bartlett, J., Nolan, M., Hinder, S. J., Gascó, A., Ruiz-Palomar, C., Hermosilla, D., & Pillai, S. C. (2020). Mo Doped TiO_2: Impact On Oxygen Vacancies, Anatase Phase Stability and Photocatalytic Activity. *Journal of Physics: Materials*, *3*(2), 025008. https://doi.org/10.1088/2515-7639/ab749c

Kumari, N., Anand, V., Sareen, S., Choudhary, P., Kondal, N., Aulakh, M., Sharma, A., Verma, M., Mehta, S., & Mutreja, V. (2023). Synthesis of Low-Band Gap Porous Zirconia Nanoparticles Via Greener-Route: Mechanistic Investigation and Their Applications. *Materials Chemistry and Physics*, *294*, 127004. https://doi.org/10.1016/j.matchemphys.2022.127004

Kunnamareddy, M., Diravidamani, B., Rajendran, R., Singaram, B., & Varadharajan, K. (2018). Synthesis of Silver and Sulphur Codoped TiO_2 Nanoparticles for Photocatalytic Degradation of Methylene Blue. *Journal of Materials Science: Materials in Electronics*, *29*(21), 18111–18119. https://doi.org/10.1007/s10854-018-9922-2

Kunnamareddy, M., Rajendran, R., Sivagnanam, M., Rajendran, R., & Diravidamani, B. (2021). Nickel and Sulfur Codoped TiO_2 Nanoparticles for Efficient Visible Light Photocatalytic Activity. *Journal of Inorganic and Organometallic Polymers and Materials*, *31*(6), 2615–2626. https://doi.org/10.1007/s10904-021-01914-5

Laghrib, S., Gherdaoui, C., Belgherbi, O., Benaskeur, N., Boudissa, M., Kanagaraj, A., & Aouffa, N. (2025). Photocatalytic Degradation of Methylene Blue Using TiO_2 Nanoparticles Synthesized Via the Sol–Gel Method in Acidic and Neutral Media. *Reaction Kinetics, Mechanisms and Catalysis*, *138*(3), 1725–1745. https://doi.org/10.1007/s11144-025-02816-0

Leong, K., Chu, H., Ibrahim, S., & Saravanan, P. (2015). Suppression of Anatase to Rutile Phase Transformation of Niobium Doped TiO_2 Synthesized by High Temperature Diffusion Technique. *International Journal for Innovation Education and Research*, 3(6), 69-78.

Li, B., Wu, S., & Gao, X. (2020). Theoretical Calculation of a TiO_2 -Based Photocatalyst in The Field of Water Splitting: A review. *Nanotechnology Reviews*, *9*(1), 1080–1103. https://doi.org/10.1515/ntrev-2020-0085

Li, D., Song, H., Meng, X., Shen, T., Sun, J., Han, W., & Wang, X. (2020). Effects of Particle Size On the Structure and Photocatalytic Performance by Alkali-Treated TiO_2. *Nanomaterials*, *10*(3), 546. https://doi.org/10.3390/nano10030546

Li, H., Shang, H., Li, Y., Cao, X., Yang, Z., Ai, Z., & Zhang, L. (2020). Interfacial Charging and Its Effects On the Photocatalytic Properties of $BaTiO_3$. *Nano Energy*, 69, 104376.

Li, J., Meng, S., Niu, J., & Lu, H. (2017). Electronic Structures and Optical Properties of Monoclinic ZrO_2 Studied by First-Principles Local Density Approximation + U Approach. *Journal of Advanced Ceramics*, *6*(1), 43–49. https://doi.org/10.1007/s40145-016-0216-y

Li, K., Zhang, Y., Lin, Y., Wang, K., & Liu, F. (2020). Machine Learning Band Gaps of Doped-TiO_2 Photocatalysts from Structural and Morphological Parameters. *ACS Omega*, 5(25), 15344-15352.

Li, L., Yan, J., Wang, T., Zhao, Z., Zhang, J., Gong, J., & Guan, N. (2015). Sub-10 Nm Rutile Titanium Dioxide Nanoparticles for Efficient Visible-Light-Driven Photocatalytic Hydrogen Production. *Nature Communications*, 6(1), 5881.

Li, M., Zhang, J., & Zhang, Y. (2023). Oxygen Vacancies In Black TiO_2: Enhancing Photocatalytic Performance Through Defect Engineering. *Journal of Materials Science & Technology*, 145, 178-192.

Li, S., Chen, G., Qiang, S., Yin, Z., Zhang, Z., & Chen, Y. (2020). Synthesis and Evaluation of Highly Dispersible and Efficient Photocatalytic TiO_2/Poly Lactic Acid Nanocomposite Films Via Sol-Gel and Casting Processes. *International Journal of Food Microbiology*, *331*, 108763. https://doi.org/10.1016/j.ijfoodmicro.2020.108763

Li, X., Liu, P., Mao, Y., Xing, M., & Zhang, J. (2015). Preparation of Homogeneous Nitrogen-Doped Mesoporous TiO_2 Spheres with Enhanced Visible-Light Photocatalysis. *Applied Catalysis B: Environmental*, 164, 352-359.

Li, X., Yu, J., Jaroniec, M., & Chen, X. (2019). Cocatalysts for Selective Photoreduction of CO_2 into Solar Fuels. *Chemical Reviews*, 119(6), 3962-4179.

Li, X., Zhu, W., Lu, X., Zuo, S., Yao, C., Ni, C., Chen, X. (2016). Integrated Black Phosphorus/TiO_2 Hybrid Nanostructure Solar Cells. *Small*, 12(5), 595-601.

Li, Y., Li, Y. L., Araujo, C. M., Luo, W., & Ahuja, R. (2013). Single-Atom CO/TiO_2 Nanostructures: A Comprehensive DFT Study. *Catalysis Science & Technology*, 3(9), 2214-2220.

Li, Y., Li, Y., Zhao, C., Fan, X., Li, D., & Chi, R. (2023). Oxygen Vacancies Induced Band Gap Narrowing for Efficient Visible-Light Response In Carbon-Doped TiO_2 . *Scientific Reports*, *13*, Article 14026. https://doi.org/10.1038/s41598-023-39523-6

Li, Y., Sun, Y., Dong, F., & Ho, W. K. (2014). Enhancing The Photocatalytic Activity of Bulk TiO_2 by Introducing Surface Disorder and F Substitution: The Case of TiO_2-xFx. *Journal of Colloid and Interface Science*, 436, 29-36.

Li, Y., Wang, B., Liu, S., Duan, X., & Hu, Z. (2015). Synthesis and Characterization of Cu_2O/TiO_2 Photocatalysts for H_2 Evolution From Aqueous Solution With Different Scavengers. *Applied Surface Science*, 324, 736-744.

Li, Z., Liu, Y., Xue, W., Li, C., Zhu, B., fang, Z., & Xu, J. (2025). Nitrogen-Doped TiO_2 For Enhanced CO_2 Photocatalytic Reduction: Combined DFT Calculation and Experimental Study. *Applied Catalysis B: Environmental*, 340, 123205.

Limbu, S. (2022). Investigation of Crystal Structure Confinement and Optical Attributes of Monoclinic–Tetragonal Zirconia Nanocrystals Via Chemical Co-Precipitation Technique. *Bulletin of Materials Science*, *45*(4), 182. https://doi.org/10.1007/s12034-022-02769-3

Lin, H., Long, X., Zhou, Y., Dang, C., Zhao, Y., Wang, W., & An, X. (2024). Synthesis of The Cu and P-Codoped TiO_2 Photocatalyst for Hydrogen Production from Seawater. *Energy & Fuels*, 38(24), 23845-23858.

Lin, Y., Jiang, Z., Zhu, C., Hu, X., Zhang, X., Zhu, H., Fan, J., & Lin, S. (2013). C/B Codoping Effect On Band Gap Narrowing and Optical Performance of TiO_2 Photocatalyst: A Spin-polarized DFT Study. *Journal of Materials Chemistry A*, *1*(14), 4516. https://doi.org/10.1039/c3ta01298k

Lin, Y., Zhu, S., Jiang, Z., Hu, X., Zhang, X., Zhu, H., Fan, J., Mei, T., & Zhang, G. (2013). Electronic and Optical Properties of S/I-Codoped Anatase TiO_2 from Ab Initio Calculations. *Solid State Communications*, *171*, 17–21. https://doi.org/10.1016/j.ssc.2013.06.002

Ling, M., Ong, S., & Lee, S. (2025). Recent Development of Surface-Modified Titanium Dioxide for Enhanced Oxidation Catalytic Activity: A Short Review. *Journal of Alloys and Compounds*, *1037*, 182226. https://doi.org/10.1016/j.jallcom.2025.182226

Liu, B., Zhao, X., Terashima, C., Fujishima, A., & Nakata, K. (2014). Thermodynamic and kinetic analysis of heterogeneous photocatalysis for semiconductor systems. *Physical Chemistry Chemical Physics*, 16(19), 8751-8760.

Liu, C., Mao, S., Shi, M., Hong, X., Wang, D., Wang, F., Wang, J. (2022). Enhanced Photocatalytic Degradation Performance of $BiVO_4$/BiOBr Through Combining Fermi Level Alteration and Oxygen Defect Engineering. *Chemical Engineering Journal*, 449, 137757.

Liu, J., Yu, S., Zhu, W., & Yan, X. (2019). Oxygen Vacancies In TiO_2: A Comprehensive Understanding From Quantum Dynamics. *Journal of Physical Chemistry C*, 123(6), 3505-3512.

Liu, R., Zhou, X., Yang, F., & Yua, Y. (2014) Combination Study of DFT Calculation and Experiment For Photocatalytic Properties of S-Doped Anatase TiO_2, *Appl. Surf. Sci.* http://dx.doi.org/10.1016/j.apsusc.(07)132.

Liu, X., Zheng, J., Peng, K., Qin, G., Yang, Y., & Huang, Z. (2022). The Intrinsic Effects of Oxygen Vacancy and Doped Non-Noble Metal In TiO_2(B) On Photocatalytic Oxidation Vocs By Visible Light Driving. *Journal of Environmental Chemical Engineering*, *10*(3), 107390. https://doi.org/10.1016/j.jece.2022.107390

Liu, Y., Liang, W., Zhang, W., Zhang, J., & Han, P. (2013). First Principle Study of Cu–N, Cu and N-doped Anatase TiO_2. *Solid State Communications.* 164 (2013) 27–31.doi: 10.1016/j.ssc.2013.04.005

Long, R., & English, N. (2010). Electronic Properties of F/Zr Co-Doped Anatase TiO_2 Photocatalysts from Gga +U Calculations. *Chemical Physics Letters*, *498*(4–6), 338–344. https://doi.org/10.1016/j.cplett.2010.09.006

Long, R., & English, N. (2009). First-Principles Calculation of Synergistic (N, P)-Codoping Effects On the Visible-Light Photocatalytic Activity of Anatase TiO2. *Journal of Physical Chemistry C*, 113(1), 303-307.

Long, R., & English, N. (2019). Dispelling The Myth of Passivated Codoping In TiO_2 . *Chemistry of Materials*, *31*(12), 4449–4460. https://doi.org/10.1021/acs.chemmater.9b00257

Long, R., & English, N. (2011). Tailoring The Electronic Structure of TiO_2 By Cation Codoping From Hybrid Density Functional Theory Calculations. *Physical Review B*, *83*(15), 155209. https://doi.org/10.1103/PhysRevB.83.155209

Long, R., English, N., & Prezhdo, O. V. (2012). Band Gap Narrowing of TiO_2 By Compensated Codoping For Enhanced Photocatalytic Activity. *Journal of the American Chemical Society*, *134*(34), 14238–14248. https://doi.org/10.1021/ja3051734

Lu, B., Zhang, J., Zhu, G., Liu, T., Chen, J., & Liang, X. (2023a). Highly Hydrophilic and Dispersed TiO_2 Nano-System with Enhanced Photocatalytic Antibacterial Activities and Accelerated Tissue Regeneration Under Visible Light. *Journal of Nanobiotechnology*, *21*(1), 491. https://doi.org/10.1186/s12951-023-02241-2

Lu, B., Zhang, J., Zhu, G., Liu, T., Chen, J., & Liang, X. (2023b). Highly Hydrophilic and Dispersed TiO_2 Nano-System with Enhanced Photocatalytic Antibacterial Activities and Accelerated Tissue Regeneration Under Visible Light. *Journal of Nanobiotechnology*, *21*(1), 491. https://doi.org/10.1186/s12951-023-02241-2

Luo, B., Chen, M., Zhang, Z., Xu, J., Li, D., Xu, D., & Shi, W. (2025). Dual Role of Oxygen Vacancies in TiO_2/Bi_2O_3 Composites: Band Alignment Regulation and Persulfate Activation for Enhanced Photocatalysis. *Chemical Engineering Journal*, 479, 147790.

Luo, H., Zeng, C., Tian, D., Wang, H., & Fu, Y. (2015). Adsorption of Co On M-Doped (M = Ca, Ce and Pr) Monoclinic Zirconia (111) Surface: A First-Principles Study. *Material, Energy and Environment Engineering.* (23) 4578-4830.

Lv, C., Lan, X., Wang, L., Yu, Q., Zhang, M., Sun, H., & Shi, J. (2019). Alkaline-Earth-Metal-Doped TiO_2 for Enhanced Photodegradation and H_2 Evolution: Insights into The Mechanisms. *Catalysis Science & Technology*, *9*(21), 6124–6135. https://doi.org/10.1039/c9cy01687b

Lyons, J., Wickramaratne, D., & Janotti, A. (2024). Dopants and Defects In Ultra-Wide Bandgap Semiconductors. *Current Opinion in Solid State and Materials Science*, *30*, 101148. https://doi.org/10.1016/j.cossms.2024.101148

Ma, X., Liang, P., Miao, L., Bie, S. W., Zhang, C., Xu, L., & Jiang, J. (2009). Pressure-Induced Phase Transition and Elastic Properties of TiO_2 Polymorphs. *Physica Status Solidi (b)*, *246*(9), 2132–2139. https://doi.org/10.1002/pssb.200945111

Mahmood, T., Cao, C., Ahmed, R., Ahmed, M., & Zafar, I. (2012). DFT Calculations: Stress Dependence Structural and Band Gap Study of Anatase and Rutile TiO_2. *2012 International Conference on Enabling Science and Nanotechnology*, 1–2. https://doi.org/10.1109/ESciNano.2012.6149663

Mahmood, T., Cao, C., Khan, W. S., Usman, Z., Butt, F. K., & Hussain, S. (2012). Electronic, Elastic, Optical Properties of Rutile TiO_2 Under Pressure: A DFT Study. *Physica B: Condensed Matter*, *407*(6), 958–965. https://doi.org/10.1016/j.physb.2011.12.114

Mai, N., Nga, N., Hue, D., Dung, T., Chinh, H., & Huy, T. (2021). Characterization of Co^{2+} and Fe^{3+} Codoped TiO_2 Nanomaterials for Photocatalytic Degradation of Organic Pollutants Under Visible Light Irradiation. *Adsorption Science & Technology*, *2021*, 1–12. https://doi.org/10.1155/2021/9193052

Mantravadi, H. (2017). Effectivity of Titanium Oxide Based Nano Particles on E. coli from Clinical Samples. *Journal of Clinical and Diagnostic Research*. https://doi.org/10.7860/JCDR/2017/25334.10278

Manurung, R., Low, F., Ting, C., Voon, C., Pung, S., Chiu, W., ... & Chia, C. (2020). Anatase to Rutile Phase Transformation of Iron-Doped TiO_2 Nanoparticles: Magnetic, Optical, and Photoelectrochemical Properties. *Nano-Structures & Nano-Objects*, 23, 100498.

Manzoor, M., Rafiq, M., Ikram, M., & Nabi, M. (2025). Density Functional Theory Study of Chlorine, Fluorine, Nitrogen, and Sulfur Doped Rutile TiO_2 For Photocatalytic Application. *Scientific Reports*, 15(1), 1-11.

Mardare, D., Frenti, M., Mita, C., Cornei, N., Bulai, G., Dobromir, M., Doroshkevich, A., & Yildiz, A. (2024). Electrical Conduction Mechanism of Mg-Doped ZrO_2 Thin Films. *Materials*, *17*(15), 3652. https://doi.org/10.3390/ma17153652

Mathew, S., Ganguly, P., Rhatigan, S., Kumaravel, V., Byrne, C., Hinder, S., Bartlett, J., Nolan, M., & Pillai, S. (2018). Cu-Doped TiO_2: Visible Light Assisted Photocatalytic Antimicrobial Activity. *Applied Sciences*, *8*(11), 2067. https://doi.org/10.3390/app8112067

Mattsson, A., Lejon, C., Bakardjieva, S., Štengl, V., & Österlund, L. (2013). Characterisation, Phase Stability and Surface Chemical Properties of Photocatalytic Active Zr and Y Co-Doped Anatase TiO_2 Nanoparticles. *Journal of Solid State Chemistry*, *199*, 212–223. https://doi.org/10.1016/j.jssc.2012.12.018

Mazarakioti, E. C., Zotos, A., Thomatou, A.-A., Kontogeorgos, A., Patakas, A., & Ladavos, A. (2022). Inductively Coupled Plasma-Mass Spectrometry (ICP-MS), a Useful Tool in Authenticity of Agricultural Products' and Foods' Origin. *Foods*, *11*(22), 3705. https://doi.org/10.3390/foods11223705

Mbae, J., & Muthui, Z. (2022). Ab initio Investigation of the Structural and Electronic Properties of Alkaline Earth Metal—TiO_2 Natural Polymorphs. *Advances in Materials Science and Engineering*, *2022*(1), 7629651. https://doi.org/10.1155/2022/7629651

Meermann, B., & Nischwitz, V. (2018). ICP-MS For The Analysis At The Nanoscale a Tutorial Review. *Journal of Analytical Atomic Spectrometry*, *33*(9), 1432–1468. https://doi.org/10.1039/C8JA00037A

Meng, D., Liu, X., Xie, Y., Du, Y., Yang, Y., & Xiao, C. (2019). Antibacterial Activity of Visible Light-Activated TiO_2 Thin Films with Low Level of Fe Doping. *Advances in Materials Science and Engineering*, *2019*, 1–8. https://doi.org/10.1155/2019/5819805

Mergenbayeva, S., Kumarov, A., Atabaev, T. Sh., Hapeshi, E., Vakros, J., Mantzavinos, D., & Poulopoulos, S. G. (2022). Degradation of 4-Tert-Butylphenol in Water Using Mono-Doped (M1: Mo, W) and Co Doped (M2-M1: Cu, Co, Zn) Titania Catalysts. *Nanomaterials*, *12*(14), 2326. https://doi.org/10.3390/nano12142326

Milman, V., Perlov, A., Gavartin, J., Refson, K., Clark, S., & Winkler, B. (2009). Structural, Electronic and Vibrational Properties of Tetragonal Zirconia Under Pressure: A Density Functional Theory Study. *Journal of Physics Condensed Matter*, *21*(48), 12.

Minchi, L., Cao, F., Xinni, Z., Youqiang, C., & Xuhua, L. (2019). Photocatalytic Activity of Ca-TiO_2 Nanofibers With Different Concentrations of Calcium. *Chemical Physics Letters*, *736*, 136807. https://doi.org/10.1016/j.cplett.2019.136807

Mobeen Amanulla, A., & Sundaram, R. (2019a). Green Synthesis of TiO_2 Nanoparticles Using Orange Peel Extract For Antibacterial, Cytotoxicity and Humidity Sensor Applications. *International Conference on Materials for Energy and Environment (ICMEE 2018), Loyola Institute of Frontier Energy (LIFE), Loyola College, Chennai-600 034*, *8*, 323–331. https://doi.org/10.1016/j.matpr.2019.02.118

Mobeen Amanulla, A., & Sundaram, R. (2019b). Green Synthesis of TiO_2 Nanoparticles Using Orange Peel Extract For Antibacterial, Cytotoxicity and Humidity Sensor Applications. *Materials Today: Proceedings*, *8*, 323–331. https://doi.org/10.1016/j.matpr.2019.02.118

Mohamed, M., & Ulrich, E. (2020). Electronic and Optical Properties of Metal-Doped TiO_2 Nanotubes: Spintronic and Photocatalytic Applications. *New J. Phys.* **22** 093028

Mondal, A., Islam, S., Zaman, Sk. M., Sultana, M., Abedin, Md. M., Chakraborty, A. K., Rahman, M. M., Rahaman, Md. H., Sumi, M. S. A., & Nur, A. S. M. (2025). Fabrication of Ca-doped TiO_2 for enhanced methylene blue degradation under UV-Vis irradiation. *Next Materials*, *7*, 100392. https://doi.org/10.1016/j.nxmate.2024.100392

Moon, S., Fujino, M., Yamashita, H.& Anpo, M. (1997). Characterization of Zirconium− Silicon Binary Oxide Catalysts Prepared by the Sol− Gel Method and Their Photocatalytic Activity for the Isomerization of 2-Butene. *The Journal of Physical Chemistry B*, *101*(3), 369-373.

Moradi, S., Sobhgol, S. A., Hayati, F., Isari, A. A., Kakavandi, B., Bashardoust, P., & Anvaripour, B. (2020). Performance and reaction mechanism of MgO/ZnO/Graphene ternary nanocomposite in coupling with LED and ultrasound waves for the degradation of sulfamethoxazole and pharmaceutical wastewater. *Separation and Purification Technology*, *251*, 117373. https://doi.org/10.1016/j.seppur.2020.117373

Mourdikoudis, S., Pallares, R., & Thanh, N. (2018a). Characterization Techniques For Nanoparticles: Comparison and Complementarity Upon Studying Nanoparticle Properties. *Nanoscale*, *10*(27), 12871–12934. https://doi.org/10.1039/C8NR02278J

Mourdikoudis, S., Pallares, R., & Thanh, N. (2018b). Characterization Techniques For Nanoparticles: Comparison and Complementarity Upon Studying Nanoparticle Properties. *Nanoscale*, *10*(27), 12871–12934. https://doi.org/10.1039/C8NR02278J

Mugumo, R., Ichipi, E., Tichapondwa, S., & Chirwa, E. (2023). Visible-Light-Induced Photocatalytic Degradation of Rhodamine B Dye Using a CuS/ZnS p-n Heterojunction Nanocomposite under Visible-Light Irradiation. *Catalysts*, *13*(8), 1184. https://doi.org/10.3390/catal13081184

Mukherjee, K., Acharya, K., Biswas, A., & Jana, N. (2020). TiO_2 Nanoparticles Co-doped with Nitrogen and Fluorine as Visible-Light-Activated Antifungal Agents. *ACS Applied Nano Materials*, *3*(2), 2016–2025. https://doi.org/10.1021/acsanm.0c00108

Nair, P., Justinvictor, V., Daniel, G., Joy, K., Ramakrishnan, V., Kumar, D., & Thomas, P. (2016). Influence of Plasma Gases On the Anatase-Rutile Phase Transformation of TiO_2 Nanoparticles. *Applied Surface Science*, 380, 48-52.

Nair, R. V., Gummaluri, V. S., Matham, M. V., & Vijayan, C. (2023). A review on optical bandgap engineering in TiO2 nanostructures via doping and intrinsic vacancy modulation towards visible light applications. *Journal of Physics D: Applied Physics*, 55(31), 313003

Naldoni, A., Allieta, M., Santangelo, S., Marelli, M., Fabbri, F., Cappelli, S., ... & Dal Santo, V. (2012). Effect of Nature and Location of Defects On Bandgap Narrowing in Black TiO2 Nanoparticles. *Journal of the American Chemical Society*, 134(18), 7600-7603.

Navas, J., Sánchez-Coronilla, A., Aguilar, T., Hernández, N., De Los Santos, D., Sánchez-Márquez, J., Zorrilla, D., Fernández-Lorenzo, C., Alcántara, R., & Martín-Calleja, J. (2014). Experimental and Theoretical Study of the Electronic Properties of Cu-Doped Anatase TiO2. *Physical Chemistry Chemical Physics*, *16*(8), 3835. https://doi.org/10.1039/c3cp54273d

Nguyen, T., Tran, V.& Bach, T. (2014). Influence of Metallic Doping on Anatase Crystalline TiO_2: From Electronic Structure Aspects to Efficiency of TiO_2 Based Dye Sensitized Solar Cell(DSSC). *Material Chemistry and Physics Journal*. (2014), doi./10.1016/j.matchemphys.2013.12.025.

Ni, M., Leung, M., Leung, D., & Sumathy, K. (2007). A Review and Recent Developments In Photocatalytic Water-Splitting Using TiO_2 For Hydrogen Production. *Renewable and Sustainable Energy Reviews*, 11(3), 401-425. https://doi.org/10.1016/j.rser.2005.01.009

Nisansala, B., Rohini, M., Damayanthi, D., Sunanda, G. & Kulatheepan, T. (2017). Is ZrO_2 Nano photocatalyst better Photocatalyst than Nano TiO_2 for Degradation of Plastics? *RSC Adv*, 2017,7,46155.

Nova, C., Reis, K., Pinheiro, A., Dalmaschio, C. J., Chiquito, A., Teodoro, M., Rodrigues, A., Longo, E., & Pontes, F. (2021). Synthesis, Characterization, Photocatalytic, and Antimicrobial Activity of ZrO_2 Nanoparticles and Ag_2ZroO_2 Nanocomposite Prepared By The Advanced Oxidative Process/Hydrothermal Route. *Journal of Sol-Gel Science and Technology*, *98*(1), 113–126. https://doi.org/10.1007/s10971-021-05488-z

Ortega Hernández, R., Escobedo Morales, A., Pal, U., & Rubio Rosas, E. (2011). Nitrogen/gold Codoping of the TiO_2(101) Anatase Surface. A Theoretical Study Based on DFT Calculations. *Physical Chemistry Chemical Physics*, 13(21), 9713-9720.

Pan, X., Yang, M. Q., Fu, X., Zhang, N., & Xu, Y. (2013). Defective TiO_2 With Oxygen Vacancies: Synthesis, Properties and Photocatalytic Applications. *Nanoscale*, 5(9), 3601-3614.

Pan, X., Yang, M., Fu, X., Zhang, N., & Xu, Y. (2023). Oxygen Vacancy in TiO_2: Production Methods and Properties. In *Defects in Advanced Electronic Materials and Novel Low Dimensional Structures*. IntechOpen. https://doi.org/10.5772/intechopen.111282

Panda, R., Shih, M., & Chi, T. (2018). Probing The Anatase To Rutile Transformation With Manganese In TiO_2 Using Electron, X-Ray and Gamma-Ray Spectroscopic Probes. *RSC Advances*, 8(18), 10134-10145.

Parrino, F., Pomilla, F., Camera-Roda, G., Loddo, V., & Palmisano, L. (2021). Properties of Titanium Dioxide.*Titanium Dioxide (TiO_2) and Its Applications* (pp. 13–66). Elsevier. https://doi.org/10.1016/B978-0-12-819960-2.00001-8

Patra, J., & Baek, K. (2014). Green Nanobiotechnology: Factors Affecting Synthesis and Characterization Techniques. *Journal of Nanomaterials*, *2014*, 1–12. https://doi.org/10.1155/2014/417305

Patra, S., Davoisne, C., Bouyanfif, H., Foix, D., & Sauvage, F. (2015). Phase Stability Frustration On Ultra-Nanosized Anatase TiO2. *Scientific Reports*, *5*(1), 10928. https://doi.org/10.1038/srep10928

Perumal, V., Hashim, U., Gopinath, S., Haarindraprasad, R., Foo, K., Balakrishnan, S., & Poopalan, P. (2019). Recent Progress in Metal-Doped TiO_2, Non-Metal Doped/Codoped TiO_2 and TiO_2 Nanostructured Hybrids For Enhanced Photocatalysis. *International Journal of Hydrogen Energy*, 44(58), 30153-30162.

Ponnusamy, D., Madurai Ramakrishnan, V., Rahuman, M., Balasubramani, K., Ramaraj, S., Sankar, R., Suganthi, S., Rajarajan, M., & Arunachalam, P. (2023). Impact of Metal Doping On the Physical Characteristics of Anatase Titanium Dioxide (TiO_2) films. *Journal of Materials Science: Materials in Electronics*, *34*(20), Article 1519. https://doi.org/10.1007/s10854-023-10948-z

Precious Ayanwale, A., & Reyes-López, S. (2019). ZrO2–ZnO Nanoparticles as Antibacterial Agents. *ACS Omega*, *4*(21), 19216–19224. https://doi.org/10.1021/acsomega.9b02527

Qiu, Y., Zhang, X., & Yang, S. (2020). Temperature-Dependent Structural and Electronic Properties of Anatase, Brookite, and Rutile Phase TiO_2 Nanoparticles From DFTB Calculations. *Nanoscale Advances*, 2(9), 3987-3996.

Quan, F., Hu, Y., Zhang, X., & Wei, C. (2014). Simple Preparation of Mn-N-Codoped TiO_2 Photocatalyst and The Enhanced Photocatalytic Activity Under Visible Light Irradiation. *Applied Surface Science*, *320*, 120–127. https://doi.org/10.1016/j.apsusc.2014.09.089

Rahman, K., & Kar, A. (2022). Influence of Catalyst Loading On Photocatalytic Degradation Efficiency of CTAB-Assisted TiO_2 Photocatalyst Towards Methylene Blue Dye Solution. *Bulletin of Materials Science*, *45*(1), 18. https://doi.org/10.1007/s12034-021-02600-5

Raja, P., Munusamy, K., Perumal, V., & Ibrahim, M. (2022). 5—Characterization of Nanomaterial Used In Nanobioremediation. In H. M. N. Iqbal, M. Bilal, & T. A. Nguyen (Eds.), *Nano-Bioremediation: Fundamentals and Applications* (pp. 57–83). Elsevier. https://doi.org/10.1016/B978-0-12-823962-9.00037-4

Rajaitha, P., Hajra, S., Sahu, M., Mistewicz, K., Kim, H., Panda, S., Dubal, D., & Nanda, S. (2024). Band Gap Engineering of Au Doping and Au–N Codoping Into Anatase TiO_2 For Enhancing The Visible Light Photocatalytic Performance. *International Journal of Hydrogen Energy*, *51*(Part D), 582–596. https://doi.org/10.1016/j.ijhydene.2023.06.285

Rajaraman, T. S., Parikh, S. P., & Gandhi, V. G. (2020). Black TiO_2: A Review of Its Properties and Conflicting Trends. *Chemical Engineering Journal*, 389, 123918.

Rajesh, G., Akilandeswari, S., Govindarajan, D., & Thirumalai, K. (2020). Enhancement of Photocatalytic Activity of $ZroO_2$ Nanoparticles By Doping With Mg For Uv Light Photocatalytic Degradation of Methyl Violet and Methyl Blue Dyes. *Journal of Materials Science: Materials in Electronics*, *31*(5), 4058–4072. https://doi.org/10.1007/s10854-020-02953-3

Ramos-Justicia, J., Ballester-andújar, J., Urbieta, A., & Fernández, P. (2023). Growth of Zr/ZrO2 Core–Shell Structures by Fast Thermal Oxidation. *Applied Sciences*, *13*(6), 3714. https://doi.org/10.3390/app13063714

Rasheed, P., Haq, S., Waseem, M., Rehman, S., Rehman, W., Bibi, N., & Shah, S. A. (2020). Green Synthesis of Vanadium Oxide-Zirconium Oxide Nanocomposite For The Degradation of Methyl Orange and Picloram. *Materials Research Express*, *7*(2), 025011. https://doi.org/10.1088/2053-1591/ab6fa2

Realpe Jimenez, A., Nuñez, D., Rojas, N., Ramirez, Y., & Acevedo, M. (2021). Effect of Fe–N Codoping on the Optical Properties of TiO_2 for Use in Photoelectrolysis of Water. *ACS Omega*, *6*(7), 4932–4938. https://doi.org/10.1021/acsomega.0c05981

Rehman, S., Mumtaz, A., & Hasanain, S. K. (2021). Characterisation of Oxygen Defects and Nitrogen Impurities In TiO_2 Photocatalysts Using Variable-Temperature X-Ray Powder Diffraction. *Journal of Materials Chemistry A*, 9(5), 3031-3040. https://doi.org/10.1039/D0TA09965H

Ren, Y., Han, Y., Li, Z., Liu, X., Zhu, S., Liang, Y., Yeung, K., & Wu, S. (2020). Ce and Er Co-Doped TiO_2 For Rapid Bacteria- Killing Using Visible Light. *Bioactive Materials*, *5*(2), 201–209. https://doi.org/10.1016/j.bioactmat.2020.02.005

Renuka, L., Anantharaju, K., Sharma, S., Nagaswarupa, H., Prashantha, S., Nagabhushana, H., & Vidya, Y. (2016). Hollow Microspheres Mg-Doped ZrO_2 Nanoparticles: Green Assisted Synthesis and Applications In Photocatalysis and Photoluminescence. *Journal of Alloys and Compounds*, *672*, 609–622. https://doi.org/10.1016/j.jallcom.2016.02.124

Ricca, C., Ringuedé, A., Cassir, M., Adamo, C., & Labat, F. (2015). A Comprehensive DFT Investigation of Bulk and Low-index Surfaces of ZrO_2 Polymorphs. *Journal of Computational Chemistry*, *36*(1), 9–21. https://doi.org/10.1002/jcc.23761

Ruíz-Santoyo, V., Marañon-Ruiz, V., Romero-Toledo, R., González Vargas, O., & Pérez-Larios, A. (2021). Photocatalytic Degradation of Rhodamine B and Methylene Orange Using TiO_2-ZrO_2 as Nanocomposite. *Catalysts*, *11*(9), 1035. https://doi.org/10.3390/catal11091035

Safeen, K., Ullah, R., Safeen, A., Zulfiqar, Kabeer, M., Khan, R., Ullah, H., Zaman, A., Shafique Ahmad, K., Ullah Shah, M., Elansary, H., Mohamed Moussa, I., Casini, R., & Mahmoud, E. A. (2023). Structure Phase-Dependent Dielectric and Photodegradation Properties of Co-Doped TiO_2 Nanoparticles Synthesized Via Co-Precipitation Route. *Journal of Saudi Chemical Society*, *27*(5), 101711. https://doi.org/10.1016/j.jscs.2023.101711

Sagadevan, S., Imteyaz, S., Murugan, B., Anita Lett, J., Sridewi, N., Weldegebrieal, G. K., Fatimah, I., & Oh, W. (2022). A Comprehensive Review On Green Synthesis of Titanium Dioxide Nanoparticles and Their Diverse Biomedical Applications. *Green Processing and Synthesis*, *11*(1), 44–63. https://doi.org/10.1515/gps-2022-0005

Sahni, V. (2004). The Hohenberg-Kohn Theorems and Kohn-Sham Density Functional Theory. In V. Sahni, *Quantal Density Functional Theory* (pp. 99–123). Springer Berlin Heidelberg. https://doi.org/10.1007/978-3-662-09624-6_4

Sajjadi, S., & Hosseinzadeh, G. (2025). Utilization of Green Synthesized Calcium Doped TiO2 Photocatalysts for the Solar-Light-Driven Degradation of Dyes in Aqueous Solution. *Journal of Nanostructures*, *15*(2). https://doi.org/10.22052/JNS.2025.02.027

Saka, A., Shifera, Y., Jule, L., Badassa, B., Nagaprasad, N., Shanmugam, R., Priyanka Dwarampudi, L., Seenivasan, V., & Ramaswamy, K. (2022). Biosynthesis of TiO_2 Nanoparticles By Caricaceae (Papaya) Shell Extracts For Antifungal Application. *Scientific Reports*, *12*(1), 15960. https://doi.org/10.1038/s41598-022-19440-w

Salari, S., & Ghodsi, F. (2017a). A Significant Enhancement In The Photoluminescence Emission of The Mg Doped ZrO_2 Thin Films By Tailoring The Effect of Oxygen Vacancy. *Journal of Luminescence*, *182*, 289–299. https://doi.org/10.1016/j.jlumin.2016.10.035

Salari, S., & Ghodsi, F.(2017b). A Significant Enhancement In The Photoluminescence Emission of The Mg Doped ZrO_2 Thin Films By Tailoring The Effect of Oxygen Vacancy. *Journal of Luminescence*, *182*, 289–299. https://doi.org/10.1016/j.jlumin.2016.10.035

Samat, M., Ali, A., Taib, M., Hassan, O., & Yahya, M. (2019). Structural and Electronic Properties of TiO_2 Polymorphs With Effective On-Site Coulomb Repulsion Term: DFT+U Approaches. *Materials Today: Proceedings*, *17*, 472–483. https://doi.org/10.1016/j.matpr.2019.06.482

Sandhya, G., & Babu, R. (2018). Synthesis and Characterization Co and Mg Co-Doped TiO_2 Nanoparticles. *Asian Journal of Research in Chemistry*, *11*(3), 645. https://doi.org/10.5958/0974-4150.2018.00115.3

Santiago, M., Rivera, D., & Torres, A. (2023). Green Synthesis of Titanium Oxide Nanoparticles Using Natural Extracts. *Journal of Materials Science and Chemical Engineering*, *11*(02), 29–40. https://doi.org/10.4236/msce.2023.112003

Sasani, A., Baktash, A., Mirabbaszadeh, K., & Khoshnevisan, B. (2016). Structural and Electronic Properties of Mg and Mg-Nb Co-doped TiO2 (101) Anatase Surface. *Applied Surface Science*, *384*, 298–303. https://doi.org/10.1016/j.apsusc.2016.05.040

Sayama, K. & Arakawa, H. (1993). Photocatalytic Decomposition of Water and Photocatalytic Reduction of Carbon dioxide over Zirconia Catalyst. *The Journal of Physical Chemistry*, *97*(3), 531-533.

Schneider, J., Matsuoka, M., Takeuchi, M., Zhang, J., Horiuchi, Y., Anpo, M., & Bahnemann, D. W. (2014). Understanding TiO_2 photocatalysis: Mechanisms and materials. *Chemical Reviews*, 114(19), 9919-9986.

Seema, K., & Kumar, R. (2015). Effect of Dopant Concentration on Electronic and Magnetic Properties of Transition Metal-Doped ZrO_2. *Journal of superconductivity and novel magnetism.* 28 (9),2735–2742.Doi: 10.10007/s109– 3086 – 6.

Selvam, K., Sudhakar, C., Selvankumar, T., Senthilkumar, B., Kim, W., Al-Ansari, M. M., & Al-Humaid, L. (2023). Photocatalytic Degradation of Malachite Green and Antibacterial Potential of Biomimetic-Synthesized Zirconium Oxide Nanoparticles Using Annona Reticulata Leaf Extract. *Applied Nanoscience*, *13*(4), 2837–2843. https://doi.org/10.1007/s13204-021-02148-0

Serpone, N. (2006). Is The Band Gap of Pristine TiO_2 Narrowed By Anion-and Cation-Doping of Titanium Dioxide In Second-Generation Photocatalysts? *Journal of Physical Chemistry B*, 110(48), 24287-24293.

Sethy, N., Arif, Z., Mishra, P., & Kumar, P. (2020). Green Synthesis of TiO_2 Nanoparticles From Syzygium Cumini Extract For Photo-Catalytic Removal of Lead (Pb) In Explosive Industrial Wastewater. *Green Processing and Synthesis*, *9*(1), 171–181. https://doi.org/10.1515/gps-2020-0018

Setiawati, E., & Kawano, K. (2008). Stabilization of Anatase Phase In The Rare Earth; Eu and Sm Ion Doped Nanoparticle TiO_2. *Journal of Alloys and Compounds*, *451*(1–2), 293–296. https://doi.org/10.1016/j.jallcom.2007.04.059

Shaikh, S., Ubaidullah, M., Mane, R., & Al-Enizi, A.(2024). Nitrogen and Sulfur Co-Doped Tio2 Nanoparticles: Structural, Optical and Photocatalytic Properties With DFT Insights. *Inorganic Chemistry Communications*, 161, 112025

Shanavas, S., Priyadharsan, A., Karthikeyan, S., Dharmaboopathi, K., Ragavan, I., Vidya, C., Acevedo, R., & Anbarasana, P. (2020). Green Synthesis of Titanium Dioxide Nanoparticles Using Phyllanthus Niruri Leaf Extract and Study On Its Structural, Optical and Morphological Properties. *Materials Today: Proceedings*, *26*, 3531–3534. https://doi.org/10.1016/j.matpr.2019.06.715

Shang, D., & Ching, W. (1995). Electronic and Optical Properties of Three Phases of Titanium Dioxide: Rutile, Anatase, and Brookite. *Physical Review B,*51(19).

Shannon, R. (1976). Revised Effective Ionic Radii and Systematic Studies of Interatomic Distances In Halides and Chalcogenides. *Acta Crystallographica Section A*, *32*(5), 751–767. https://doi.org/10.1107/S0567739476001551

Shao, G., Imran, S., Jeon, S., Engole, M., Abbas, N., Haider, M. & Kim, H. (2014). Sol–gel Synthesis of Photoactive Zirconia–Titania from Metal Salts and Investigation of their Photocatalytic Properties in the Photodegradation of Methylene Blue. *Powder Technology*, *258*, 99-109.

Sharaf, I., Laifi, J., Alraddadi, S., Saad, M., Koubesy, I., Elewa, N., Almohiy, H., Ismail, Y., Soldatov, A., & Aboraia, A. (2024). Unraveling The Effect of Cu Doping On The Structural and Morphological Properties and Photocatalytic Activity of ZrO2. *Heliyon*, *10*(1), e23848. https://doi.org/10.1016/j.heliyon.2023.e23848

Shikha, P. & Ritu, V. (2013). Use of Undoped and Doped Zirconium Dioxide in Photocatalytic Degradation of Malachite Green.*Sci. Revs.Chem. Commun*3(4),2013, 190-197.

Shimi, A., Ahmed, H., Wahab, M., Katheria, S., Wabaidur, S., Eldesoky, G., Islam, M., & Rane, K. (2022). Synthesis and Applications of Green Synthesized TiO2 Nanoparticles for Photocatalytic Dye Degradation and Antibacterial Activity. *Journal of Nanomaterials*, *2022*, 1–9. https://doi.org/10.1155/2022/7060388

Shukla, G., & Angappane, S. (2022). Dimensional Constraints Favour High Temperature Anatase Phase Stability In TiO_2 Nanorods. *Applied Surface Science*, *577*, 151874. https://doi.org/10.1016/j.apsusc.2021.151874

Singh Jassal, P., Kaur, D., Prasad, R., & Singh, J. (2022). Green Synthesis of Titanium Dioxide Nanoparticles: Development and Applications. *Journal of Agriculture and Food Research*, *10*, 100361. https://doi.org/10.1016/j.jafr.2022.100361

Singh, P., Kumar, P., Sharma, S., Kumar, A., Prasad, M., Jha, P., & Mehta, B. (2016). Formation of Oxygen Vacancies and Ti^{3+} State In TiO_2 Thin Film and Enhanced Optical Properties By Air Plasma Treatment. *Scientific Reports*, 6(1), 32355.

Singh, S., Maurya, I., Tiwari, A., Srivastava, P., & Bahadur, L. (2022). Green Synthesis of TiO_2 Nanoparticles Using Citrus Limon Juice Extract As a Bio-Capping Agent For Enhanced Performance of Dye-Sensitized Solar Cells. *Surfaces and Interfaces*, *28*, 101652. https://doi.org/10.1016/j.surfin.2021.101652

Slimani, Y., Almessiere, M., Mohamed, M., Hannachi, E., Caliskan, S., Akhtar, S., Baykal, A., & Gondal, M. (2023). Synthesis of Ce and Sm Co-Doped TiO_2 Nanoparticles With Enhanced Photocatalytic Activity For Rhodamine B Dye Degradation. *Catalysts*, *13*(4), 668. https://doi.org/10.3390/catal13040668

Solano, R., Herrera, A., Maestre, D., & Cremades, A. (2019). Fe-TiO_2 Nanoparticles Synthesized by Green Chemistry for Potential Application in Waste Water Photocatalytic Treatment. *Journal of Nanotechnology*, *2019*, 1–11. https://doi.org/10.1155/2019/4571848

Song, K., Zhou, J., Bao, J., & Feng, Y. (2021). Photocatalytic Water Splitting Based On C-Doped TiO_2 Nanoparticles: First-Principles Prediction and Experiment. *Journal of Alloys and Compounds*, 881, 160585.

Song, S., Wei, J., He, X., Yan, G., Jiao, M., Zeng, W., Dai, F., & Shi, M. (2021). Oxygen Vacancies Generated By Sn-Doped ZrO_2 Promoting The Synthesis of Dimethyl Carbonate From Methanol and CO_2. *RSC Advances*, *11*(56), 35361–35374. https://doi.org/10.1039/D1RA07060F

Sonkusare, V., Chaudhary, R., Bhusari, G., Mondal, A., Potbhare, A., Mishra, P., Rai, A., & Juneja, H. (2024). A Mesoporous Mo and N Co-Doped TiO_2 Nanocomposite With Enhanced Photocatalytic Activity. *RSC Advances*, *14*(6), 4267–4283. https://doi.org/10.1039/D3RA07258D

Soussi, A., Ait Hssi, A., Boujnah, M., Boulkadat, L., Abouabassi, K., Asbayou, A., Elfanaoui, A., Markazi, R., Ihlal, A., & Bouabid, K. (2021). Electronic and Optical Properties of TiO_2 Thin Films: Combined Experimental and Theoretical Study. *Journal of Electronic Materials*, *50*(8), 4497–4510. https://doi.org/10.1007/s11664-021-08976-8

Sugata, C., Nacole, K. & Winnie, W. (2018). Rutile TiO_2 Bulk Structural and Vibrational Properties: A DFT Study On The Importance of Pseudopotentials *Materials Measurement Division*, MD, 20899.

Sultana, M., Mondal, A., Islam, S., Khatun, Most., Rahaman, Md., Chakraborty, A., Rahman, Md., Rahman, M., & Nur, A. (2023). Strategic Development of Metal Doped TiO_2 Photocatalysts For Enhanced Dye Degradation Activity Under Uv–Vis Irradiation: A review. *Current Research in Green and Sustainable Chemistry*, *7*, 100383. https://doi.org/10.1016/j.crgsc.2023.100383

Sun, M., Liu, H., Sun, Z., & Li, W. (2020a). Donor-Acceptor Codoping Effects On Tuned Visible Light Response of TiO_2. *Journal of Environmental Chemical Engineering*, *8*(5), 104168. https://doi.org/10.1016/j.jece.2020.104168

Sun, M., Liu, H., Sun, Z., & Li, W. (2020b). Donor-acceptor codoping effects on tuned visible light response of TiO2. *Journal of Environmental Chemical Engineering*, *8*(5), 104168. https://doi.org/10.1016/j.jece.2020.104168

Suryawanshi, A., Dhanasekaran, P., Mhamane, D., Kelkar, S., Ogale, S., & Gupta, D. (2023). Oxygen Vacancy In TiO_2: Production Methods and Properties. In *Titanium Dioxide: Advances and Applications* (pp. 1-28). IntechOpen.

Suter, T., Hunault, M., Foteinopoulou, K., Montemore, M., & Ganduglia-Pirovano, M.(2021). Characterisation of Oxygen Defects and Nitrogen Impurities In TiO_2 Photocatalysts Using Variable-Temperature X-Ray Powder Diffraction. *Nature Communications*, 12(1), 1-12.

Takata, T., & Domen, K. (2009). Defect Engineering of Photocatalysts by Doping of Aliovalent Metal Cations for Efficient Water Splitting. *The Journal of Physical Chemistry C*, *113*(45), 19386–19388. https://doi.org/10.1021/jp908621e

Tana, F., De Giglio, E., Cometa, S., D'Agostino, A., Serafini, A., Variola, F., Bono, N., Chiesa, R., & De Nardo, L. (2020). Ca-Doped Zirconia Mesoporous Coatings for Biomedical Applications: A Physicochemical and Biological Investigation. *16th European Inter-Regional Conference on Ceramics (CIEC16)*, *40*(11), 3698–3706. https://doi.org/10.1016/j.jeurceramsoc.2019.10.024

Tana, F., Giglio, E., Cometa, S., D_Agostino, A., Serafini, A., Variola, F., Bono, N., Chiesa, R., & Nardo, L. (2020). Ca-Doped Zirconia Mesoporous Coatings For Biomedical Applications: A Physicochemical and Biological Investigation. *Journal of The European Ceramic Society*, *40*, 3698–3706.

Tekin, S., Karatay, A., Yildiz, E., Donar, Y., Sınağ, A., Dulkadir, H., & Elmali, A. (2022). Tuning The Energy Bandgap and Nonlinear Absorption Coefficients of Wox/ ZrO2 Nanocomposite Thin Films With The Role of Weight and Doping Concentration. *Journal of Luminescence*, *247*, 118869. https://doi.org/10.1016/j.jlumin.2022.118869

Terki, R., Bertrand, G., Aourag, H. & Coddet, C. (2006). Structural and Electronic Properties of Zirconia Phases: A FP-LAPW Investigations. *Material Science in Semiconductor Processing*,9(2006), 1006-1013.

Thambiliyagodage, C., & Usgodaarachchi, L. (2021). Photocatalytic Activity of N, Fe and Cu Co-Doped TiO_2 Nanoparticles Under Sunlight. *Current Research in Green and Sustainable Chemistry*, *4*, 100186. https://doi.org/10.1016/j.crgsc.2021.100186

Thamir, A., Jubier, N., & Odah, J. (2021). Antimicrobial Activity of Zirconium Oxide Nanoparticles Prepared by the Sol-Gel Method. *Journal of Physics: Conference Series*, *2114*(1), 012058. https://doi.org/10.1088/1742-6596/2114/1/012058

Thilagam, A., Simpson, D., & Gerson, A. (2010). A First-Principles Study of The Dielectric Properties of TiO_2 Polymorphs. *Journal of Physics: Condensed Matter*, *23*(2), 025901. https://doi.org/10.1088/0953-8984/23/2/025901

Thongyong, N., Thongbai, P., & Srepusharawoot, P. (2023). DFT Calculations and Giant Dielectric Responses In (Ni1/3Nb2/3)xTi1−xO2. *RSC Adv.*, *13*(45), 31844–31854. https://doi.org/10.1039/D3RA06541C

Tijani, J., Odeh, E., Mustapha, S., Egbosiuba, T., Daniel, A., Abdulkareem, A., & Muya, F. (2022). Photocatalytic, Electrochemical, Antibacterial and Antioxidant Behaviour of Carbon-Sulphur Co-Doped Zirconium (Iv) Oxide Nanocomposite. *Cleaner Chemical Engineering*, *3*, 100034. https://doi.org/10.1016/j.clce.2022.100034

Tobaldi, D., Tucci, A., Camera-Roda, G., Baldi, G., & Esposito, L. (2016). Surface Energy Effects On The Stability of Anatase and Rutile Nanocrystals: A Predictive Diagram For Nb_2 O_5 -doped-TiO_2 . *Applied Surface Science*, *393*, 251–259. https://doi.org/10.1016/j.apsusc.2016.10.018

Torrado, A., Cortés, S., Salgado, J., Max, B., Rodríguez, N., Bibbins, B., Converti, A., & Domínguez, J. (2011). Citric Acid Production From Orange Peel Wastes By Solid-State Fermentation. *Brazilian Journal of Microbiology*, *42*(1), 394–409. https://doi.org/10.1590/S1517-83822011000100049

Tropea, A. (2022). Microbial Contamination and Public Health: An Overview. *International Journal of Environmental Research and Public Health*, *19*(12), 7441. https://doi.org/10.3390/ijerph19127441

Tumbelaka, R., Istiqomah, N., Kato, T., Oshima, D., & Suharyadi, E. (2022). High Reusability of Green-Synthesized Fe3O4/TiO2 Photocatalyst Nanoparticles For Efficient Degradation of Methylene Blue Dye. *Materials Today Communications*, *33*, 104450. https://doi.org/10.1016/j.mtcomm.2022.104450

Umebayashi, T., Yamak, T., Itoh, H. &Asai, K. (2002). Band Gap Narrowing of TiO_2 By Sulphur Doping. *AIP Journals*.81, 454, doi:10.1063/1.1493647.

Vásquez, G. C., Karazhanov, S., Maestre, D., Cremades, A., Piqueras, J., & Foss, S. (2016). Oxygen Vacancy Related Distortions In Rutile TiO_2 Nanoparticles: A Combined Experimental and Theoretical Study. *Physical Review B*, *94*(23), 235209. https://doi.org/10.1103/PhysRevB.94.235209

Verma, V., Al-Dossari, M., Singh, J., Rawat, M., Kordy, M., & Shaban, M. (2022). A Review On Green Synthesis of TiO_2 Nps: Photocatalysis and Antimicrobial Applications. *Polymers*, *14*(7), 1444. https://doi.org/10.3390/polym14071444

Wang, B., Li, C., Cui, Y., Closed, B., Lausch, D., Peng, J., Mao, J. (2020). Enhanced Photocatalytic Degradation of Organic Dyes By B/N Co-Doped TiO_2. *Environmental Science and Pollution Research*, 27(36), 45545-45556.

Wang, H., Liang, Y., Liu, L., Hu, J., & Cui, W. (2023). Reduced TiO_2: From Preparation To Photocatalytic Application. *Materials Chemistry Frontiers*, 7(12), 2607-2637.

Wang, X., Liu, T., Li, H., Han, C., Su, P., Ta, N., Jiang, S., Kong, B., Liu, J., Huang, Z. (2023). Balancing Mass Transfer and Active Sites to Improve Electrocatalytic Oxygen Reduction by B,N Codoped C Nanoreactors. *Nano Letters*, *23*(11), 4699–4707. https://doi.org/10.1021/acs.nanolett.3c00202

Wang, X., Sø, L., Su, R., Wendt, S., Hald, P., Mamakhel, A., Ooi, B. (2014). The Influence of Crystallite Size and Crystallinity of Anatase Nanoparticles On The Photo-Degradation of Phenol. *Journal of Catalysis*, 310, 100-108.

Wang, Y., Wang, J., Liu, Y., Li, Y., & Zhang, Q. (2023). Ca^{2+} doped TiO_2 Nano-Sized Polygon Plates With Oxygen Vacancies For Photocatalytic Hydrogen Evolution. *International Journal of Hydrogen Energy*, 48(73), 28347-28358. https://doi.org/10.1016/j.ijhydene.2023.04.086

Wang, Z., Wang, L., Jiang, T., Sun, S., & Jones, M. (2020). Surface Modification of TiO_2 With Pt Improves Photocatalytic CO_2 Reduction: Role of Oxygen Vacancies and Schottky Barrier. *Applied Catalysis B: Environmental*, 264, 118478.

Wang, Z., Yu, H., & Liu, Z. (2023). Oxygen Vacancies Defective $La_2Ti_2O_7$ Nanosheets Enhanced Photocatalytic Activity of Hydrogen Evolution under Visible Light Irradiation. *Molecules (Basel, Switzerland)*, *28*(15), 5792. https://doi.org/10.3390/molecules28155792

Whangchai, K., Shanmugam, S., Van Le, Q., Chau, T., Al-Kheraif, A., Brindhadevi, K., & Duc, P. (2023). Study of Antimicrobial Activity of Thespesia Populnea-Coated Nanozirconium On Cotton Gauze Fabrics. *Applied Nanoscience*, *13*(1), 605–611. https://doi.org/10.1007/s13204-021-01867-8

Wilschefski, S., & Baxter, M. (2019). Inductively Coupled Plasma Mass Spectrometry: Introduction To Analytical Aspects. *Clinical Biochemist Reviews*, *40*(3), 115–133. https://doi.org/10.33176/AACB-19-00024

Xie, K., Jia, Q., Wang, Y., Zhang, W., & Xu, J. (2018).The Electronic Structure and Optical Properties of Anatase TiO_2 With Rare Earth Metal Dopants From First-Principles Calculations. *Materials Basel*. 11(2): 179. doi: 10.3390/ma11020179.

Yadav, P., Dwivedi, P., Tonda, S., Boukherroub, R., & Shelke, M. (2020). Metal and Non-metal Doped Metal Oxides and Sulfides. In Mu. Naushad, S. Rajendran, & E. Lichtfouse (Eds.), *Green Photocatalysts* (Vol. 34, pp. 89–132). Springer International Publishing. https://doi.org/10.1007/978-3-030-15608-4_4

Yanyu, L., Wei, Z. & Ping W. (2014). Room-Temperature Ferromagnetism and Optical Properties In Mg-Doped TiO_2: A Density Functional Theory Investigation. *Journal of Applied Physics* 115. 123913

Yasin, A., Mohamed, I., Mousa, H., Park, C., & Kim, C. (2018). Facile Synthesis of TiO_2/ZrO_2 Nanofibers/Nitrogen Co-Doped Activated Carbon To Enhance The Desalination and Bacterial Inactivation Via Capacitive Deionization. *Scientific Reports*, *8*(1), 541. https://doi.org/10.1038/s41598-017-19027-w

Yin, W., Chen, S., Yang, J., Gong, X., Yan, Y., & Wei, S. (2010). Effective Band Gap Narrowing of Anatase TiO_2 By Strain Along a Soft Crystal Direction. *Applied Physics Letters*, *96*(22), 221901. https://doi.org/10.1063/1.3430005

Yu, X., Hou, T., Sun, X., & Li, Y. (2012). The Influence of Defects on Mo-Doped TiO_2 by First-Principles Studies. *Chemphyschem*. 13(6):1514-21. doi: 10.1002/cphc.201101012

Yuan, Y., Wu, Y., Suganthy, N., Shanmugam, S., Brindhadevi, K., Sabour, A., Alshiekheid, M., Lan Chi, N., Pugazhendhi, A., & Shanmuganathan, R. (2022). Biosynthesis of Zirconium Nanoparticles (ZrO_2 Nps) By Phyllanthus Niruri Extract: Characterization and Its Photocatalytic Dye Degradation Activity. *Food and Chemical Toxicology*, *168*, 113340. https://doi.org/10.1016/j.fct.2022.113340

Yuvakkumar, R., Suresh, J., Hong, S., Ramkumar, J., Nathanael, A., Ravi, G., & Kumar Elango, T. (2020). Synthesis and Characterization of Various Doped Tio_2 Nanocrystals For Dye-Sensitized Solar Cells. *ACS Omega*, *5*(22), 12564–12576. https://doi.org/10.1021/acsomega.0c01614

Zare, M., & Mehrabani-Zeinabad, A. (2022). Photocatalytic Activity of $ZrO_2/TiO_2/Fe_3O_4$ Ternary Nanocomposite For The Degradation of Naproxen: Characterization and Optimization Using Response Surface Methodology. *Scientific Reports*, *12*(1), 10388. https://doi.org/10.1038/s41598-022-14676-y

Zarzzeka, C., Goldoni, J., De Paula De Oliveira, J., Lenzi, G., Bagatini, M., & Colpini, L. (2024). Photocatalytic Action of Ag/TiO_2 Nanoparticles To Emerging Pollutants Degradation: A Comprehensive Review. *Sustainable Chemistry for the Environment*, *8*, 100177. https://doi.org/10.1016/j.scenv.2024.100177

Zeng, Z., Zheng, G., Wang, X., He, K., Yu, L. & Wang, Q. (2010). First-principles Study on the Structural and Electronic Properties of Double N Atoms Doped-Rutile TiO_2. *J. At. Mol. Sci.***1** (2) 177-184.

Zhan, C., Chen ,F., Yang, J., Dai ,D., Cao, X., & Zhong, M.(2013). Visible Light Responsive Sulfated Rare Earth Doped TiO_2 @Fumed SiO_2 Composites with Mesoporosity: Enhanced Photocatalytic Activity for Methyl Orange Degradation. *J Hazard Mater*.267:88-97 doi: 10.1016/j.jhazmat.2013.12.038

Zhang, H., Liu, J., Tian, Z., Li, Y., & Wang, X. (2023). Recent Progress of Ion-Modified TiO2 for Enhanced Photocatalytic Hydrogen Production. *Catalysts*, 13(5), 858. https://doi.org/10.3390/catal13050858

Zhang, J., Zhou, P., Liu, J., & Yu, J. (2014). New understanding of the difference of photocatalytic activity among anatase, rutile and brookite TiO2. *Physical Chemistry Chemical Physics*, 16(38), 20382-20386.

Zhang, S., Liu, X., Liu, C., Luo, S., Wang, L., Cai, T., ... & Chen, S. (2018). Nitrogen and fluorine codoped, colloidal TiO2 nanoparticle: Tunable doping, large red-shifted band edge, visible light induced photocatalysis, and cell death. *ACS Applied Materials & Interfaces*, 10(2), 2172-2180.

Zhang, X., Wu, Y., Li, S., He, Y., Li, Y., & Zhou, X. (2023). Oxygen vacancy-mediated band gap engineering via B-doping for enhanced Z-scheme anatase/rutile TiO2 heterojunction photocatalyst. *Journal of Alloys and Compounds*, 933, 167779.

Zhang, Y.-F., Ren, H., & Hou, Z.-T. (2014). First-principles calculations of electronic and optical properties of C-doped and F, C-codoped cubic ZrO2. *Journal of Alloys and Compounds*, *617*, 86–92. https://doi.org/10.1016/j.jallcom.2014.07.215

Zhang, Z., Pilger, F., Alxneit, I., Carino, A., Tarik, M., Müller, E., Cervellino, A., Mühlmann, A., Ludwig, C., Gubler, L., & Testino, A. (2025). Pt/$Ce_x Zr_{1-x} O_2$ Bi-Functional Catalyst for Gas Recombination and Radical Scavenging in PEM Water Electrolysis Cells. *ACS Catalysis*, *15*(7), 5577–5588. https://doi.org/10.1021/acscatal.4c07426

Zhao, H., Zhang, Y., Li, Y., Huang, P., Zhang, H., Li, H., & Deng, R. (2025). An efficient and fast catalyst for Rhodamine B photodegradation: SnO_2/g-C3N4/Bi2WO6 heterojunction. *Chemical Engineering Science*, *306*, 121243. https://doi.org/10.1016/j.ces.2025.121243

Zhao, Y., Wang, W., & He, L. (2017). The effects of Co/N dopants on the electronic, redox potential, optical, and photocatalytic water-splitting properties of TiO_2: First principles calculations. *Chemical Physics Letters*, *685*, 108–113. https://doi.org/10.1016/j.cplett.2017.07.046

Zheng, J., Li, J., Wei, H., Yu, J., Su, H. & Wang, X. (2015). The Investigation of Gold/Zirconia as a Photocatalyst for the Direct Synthesis of Imines from Alcohols and Aniline. *Materials Science in Semiconductor Processing*, *32*, 131-136.

Zhou, J., Ren, C., Tian, C., Omran, M., Tang, J., Zhang, F., & Chen, G. (2024). The phase-stabilized behavior of Sc_2O_3–Y_2O_3 codoped ZrO_2 nanopowders by co-precipitation synthesis. *Ceramics International*, *50*(13), 24823–24834. https://doi.org/10.1016/j.ceramint.2024.04.218

Zhou, X., Ji, H., & Huang, X. (2012).Photocatalytic Degradation of Methyl Orange Over Metalloporphyrins Supported on TiO_2 Degussa P25.*Molecules*.; 17(2): 1149–1158.

Zhu, H., Wang, X., Zhou, D., Jiang, H., & Liu, M. (2020). First Principles Study on Electronic, Magnetic Properties and Optical Absorption of Vanadium Doped Rutile TiO_2.*Physical letters A*.126637. Doi: 10:1016/jphysleta.2020.126637.

APPENDICES

Appendix 1: Anatase TiO_2 (2x2x2) Supercell Poscar

TiO_2_(anatase)
1.0

7.5700001717	0.0000000000	0.0000000000
0.0000000000	7.5700001717	0.0000000000
0.0000000000	0.0000000000	19.0279998779

O Ti
64 32
Direct

0.000000000	0.750000000	0.228300005
0.250000000	0.500000000	0.478300005
0.250000000	0.250000000	0.353300005
0.000000000	0.000000000	0.603299975
0.250000000	0.750000000	0.146699995
0.000000000	0.500000000	0.896700025
0.000000000	0.250000000	0.021699995
0.250000000	0.000000000	0.771700025
0.750000000	0.000000000	0.771700025
0.500000000	0.250000000	0.021699995
0.500000000	0.000000000	0.603299975
0.750000000	0.250000000	0.353300005
0.250000000	0.000000000	0.478300005
0.000000000	0.250000000	0.228300005
0.000000000	0.000000000	0.896700025
0.250000000	0.250000000	0.146699995
0.000000000	0.750000000	0.728299975
0.250000000	0.500000000	0.978299975
0.250000000	0.250000000	0.853299975
0.000000000	0.000000000	0.103300005
0.250000000	0.750000000	0.646700025
0.000000000	0.500000000	0.396699995
0.000000000	0.250000000	0.521700025
0.250000000	0.000000000	0.271699995
0.750000000	0.000000000	0.271699995
0.500000000	0.250000000	0.521700025
0.500000000	0.000000000	0.103300005
0.750000000	0.250000000	0.853299975
0.250000000	0.000000000	0.978299975
0.000000000	0.250000000	0.728299975
0.000000000	0.000000000	0.396699995
0.250000000	0.250000000	0.646700025
0.500000000	0.750000000	0.228300005
0.750000000	0.500000000	0.478300005
0.250000000	0.750000000	0.353300005
0.000000000	0.500000000	0.603299975
0.750000000	0.750000000	0.146699995
0.500000000	0.500000000	0.896700025
0.000000000	0.750000000	0.021699995

0.250000000	0.500000000	0.771700025
0.750000000	0.500000000	0.771700025
0.500000000	0.750000000	0.021699995
0.500000000	0.500000000	0.603299975
0.750000000	0.750000000	0.353300005
0.750000000	0.000000000	0.478300005
0.500000000	0.250000000	0.228300005
0.500000000	0.000000000	0.896700025
0.750000000	0.250000000	0.146699995
0.500000000	0.750000000	0.728299975
0.750000000	0.500000000	0.978299975
0.250000000	0.750000000	0.853299975
0.000000000	0.500000000	0.103300005
0.750000000	0.750000000	0.646700025
0.500000000	0.500000000	0.396699995
0.000000000	0.750000000	0.521700025
0.250000000	0.500000000	0.271699995
0.750000000	0.500000000	0.271699995
0.500000000	0.750000000	0.521700025
0.500000000	0.500000000	0.103300005
0.750000000	0.750000000	0.853299975
0.750000000	0.000000000	0.978299975
0.500000000	0.250000000	0.728299975
0.500000000	0.000000000	0.396699995
0.750000000	0.250000000	0.646700025
0.000000000	0.750000000	0.125000000
0.250000000	0.500000000	0.375000000
0.250000000	0.250000000	0.250000000
0.000000000	0.000000000	0.500000000
0.250000000	0.750000000	0.250000000
0.000000000	0.500000000	0.000000000
0.000000000	0.250000000	0.125000000
0.250000000	0.000000000	0.875000000
0.750000000	0.000000000	0.875000000
0.500000000	0.250000000	0.125000000
0.500000000	0.000000000	0.500000000
0.750000000	0.250000000	0.250000000
0.250000000	0.000000000	0.375000000
0.000000000	0.000000000	0.000000000
0.000000000	0.750000000	0.625000000
0.250000000	0.500000000	0.875000000
0.250000000	0.250000000	0.750000000
0.250000000	0.750000000	0.750000000
0.000000000	0.500000000	0.500000000
0.000000000	0.250000000	0.625000000
0.750000000	0.000000000	0.375000000
0.500000000	0.250000000	0.625000000
0.500000000	0.000000000	0.000000000
0.750000000	0.250000000	0.750000000
0.500000000	0.750000000	0.125000000

Appendix 2: Ecutwfc Convergence

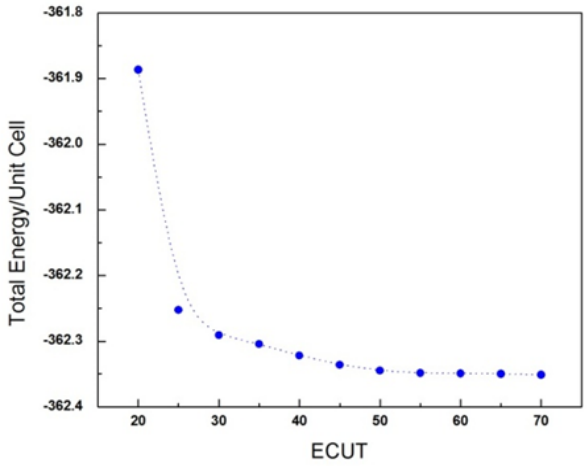

Appendix 3: Kpoints Convergence

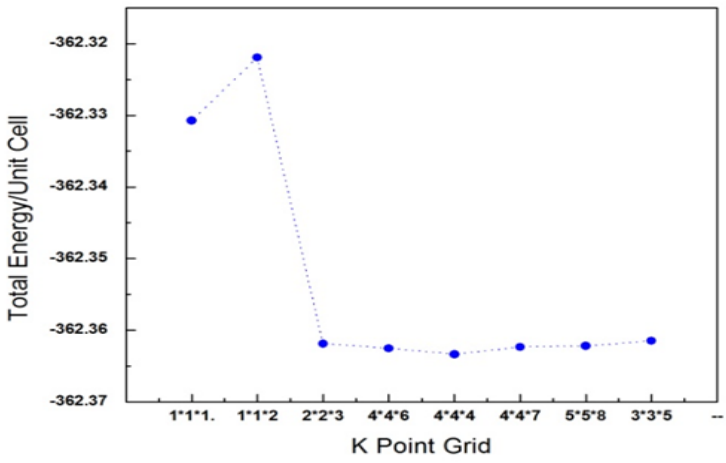

Appendix 4: RhB Calibration Curve

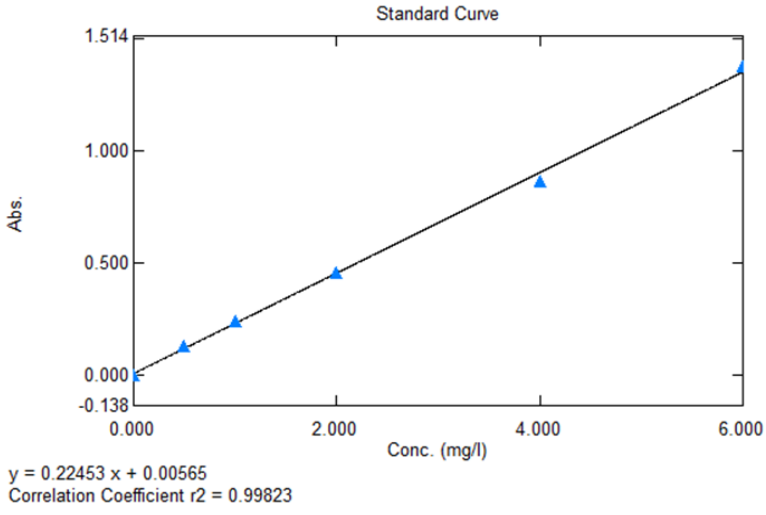

Appendix 5: NACOSTI Permit

REPUBLIC OF KENYA

NATIONAL COMMISSION FOR SCIENCE,TECHNOLOGY & INNOVATION

Ref No: **270598**

Date of Issue: **10/February/2025**

RESEARCH LICENSE

This is to Certify that Ms,. Jane Kathure Mbae of Chuka University, has been licensed to conduct research as per the provision of the Science, Technology and Innovation Act, 2013 (Rev.2014) in Tharaka-Nithi on the topic: PHASE & OXYGEN VACANCY PREDICTION OF GREEN SYNTHESISED Ca-Mg CO-DOPED TITANIA AND ZIRCONIA FOR PHOTOCATALYTIC DEGRADATION AND DISINFECTION for the period ending : 10/February/2026.

License No: **NACOSTI/P/25/415778**

270598

Applicant Identification Number

Director General
NATIONAL COMMISSION FOR SCIENCE,TECHNOLOGY & INNOVATION

Verification QR Code

NOTE: This is a computer generated License. To verify the authenticity of this document, Scan the QR Code using QR scanner application.

See overleaf for conditions